Search for Dark Matter Produced in *pp* Collisions with the ATLAS Detector

by

Danika MacDonell
B.Sc., University of Victoria, 2016
M.Sc., University British Columbia, 2018

A Dissertation Submitted in Partial Fulfillment of the
Requirements for the Degree of

DOCTOR OF PHILOSOPHY

in the Department of Physics and Astronomy

Search for Dark Matter Produced in *pp* Collisions with the ATLAS Detector

by

Danika MacDonell
B.Sc., University of Victoria, 2016
M.Sc., University British Columbia, 2018

Supervisory Committee

Dr. R. Kowalewski, Supervisor
(Department of Physics and Astronomy)

Dr. R. Sobie, Supervisor
(Department of Physics and Astronomy)

Dr. M. Roney, Departmental Member
(Department of Physics and Astronomy)

Dr. I. Paci, Outside Member
(Department of Chemistry)

ABSTRACT

Longstanding evidence from observational astronomy indicates that non-luminous “dark matter” constitutes the majority of all matter in the universe, yet this mysterious form of matter continues to elude experimental detection. This dissertation presents a search for dark matter at the Large Hadron Collider using 139 fb^{-1} of proton-proton collision data at a centre-of-mass energy of $\sqrt{s} = 13\,\text{TeV}$, recorded with the ATLAS detector from 2015 to 2018. The search targets a final state topology in which dark matter is produced from the proton-proton collisions in association with a pair of W bosons, one of which decays to a pair of quarks and the other to a lepton-neutrino pair. The dark matter is expected to pass invisibly through the detector, resulting in an imbalance of momentum in the plane transverse to the beam line. The search is optimized to test the Dark Higgs model, which predicts a signature of dark matter production in association with the emission of a hypothesized new particle referred to as the Dark Higgs boson. The Dark Higgs boson is predicted to decay to a W boson pair via a small mixing with the Standard Model Higgs boson discovered in 2012. Collisions that exhibit the targeted final state topology are selected for the search, and an approximate mass of the hypothetical Dark Higgs boson is reconstructed from the particles in each collision. A search is performed by looking for a deviation between distributions of the reconstructed Dark Higgs boson masses and Standard Model predictions for the selected collisions. The data is found to be consistent with the Standard Model prediction, and the results are used to constrain the parameters of the Dark Higgs model. This search complements and extends the reach of existing searches for the Dark Higgs model by the ATLAS and CMS collaborations.

Contents

List of Tables

List of Figures

DECLARATION

Analysis contributions

- Initiated and served as analysis co-contact for the mono-s(WW) semileptonic analysis presented in this thesis (2020-present).
  - Defined, delegated, documented and ensured timely completion of studies and tasks for the analysis.
  - Liaised with conveners, experts and performance groups to ensure that analysis choices were widely understood and endorsed.
  - Organized and facilitated regular analysis group meetings.
  - Delivered regular updates and presentations to communicate the progress of the analysis to ATLAS collaborators.
  - Facilitated and contributed to all stages of analysis approval within the ATLAS collaboration by presenting at approval meetings, interfacing with conveners, and addressing feedback from reviewers.
- Editor and primary developer of the supporting documentation for the publication of the mono-s(WW) semileptonic analysis.
- Primary analyst for the mono-s(WW) semileptonic analysis.
  - Collaborated on the design and optimization of selections used to define signal and control regions for the analysis.
  - Optimized and implemented the binning strategy in the signal region.
  - Developed a framework to evaluate and implement all systematic uncertainties considered in the analysis.
  - Designed and optimized the statistical interpretation of the analysis within the HistFitter [1] framework.
  - Contributed to the development and release of ATLAS-wide recommendations for the calibration of small-radius ($R = 0.2$) jets, and for the evaluation of their associated systematic uncertainties. $R = 0.2$ jets are used to construct large-radius TAR jets [2] used in the analysis (see Section 5.1.4 for details).
  - Prepared requests for Monte Carlo samples used by the analysis to model signal and Standard Model background processes, and processed all data and Monte Carlo samples through the full analysis chain.

- Contributed to control region studies and the evaluation of theoretical systematic uncertainties for the mono-s(WW) analysis in the fully hadronic channel.

Computing infrastructure contributions

- Developed infrastructure to automate the creation and deployment of a kubernetes cluster as an ATLAS computing site using cloud computing infrastructure at the University of Victoria.
- Implemented and tested tools for cluster federation and resource monitoring.

Analysis preservation contributions

- Analysis preservation contact person for all searches for new physics within the ATLAS collaboration (Feb. 2020 to Oct. 2021).
  - Provided technical assistance and liaison to support analysis teams with the development of automated analysis preservation workflows in the RECAST framework [3].
  - Maintained central documentation of RECAST tools.
  - Reviewed RECAST workflows for completeness, and ensured centralized storage of workflows.
  - Organized hands-on training events to familiarize analysts with the tools involved with analysis preservation.
  - Facilitated the integration of the REANA data analysis platform [4] as a central tool for the development and execution of RECAST analysis preservation workflows.
- Contributed to workshop planning and ran tutorials on analysis preservation and related tools for numerous ATLAS workshops.
- Developed and currently maintain the RECAST framework for the ATLAS $E_{\mathrm{T}}^{\mathrm{miss}}$ +jets search published in 2021 [5], which continues to be used regularly within the collaboration to constrain new models of physics beyond the Standard Model.
- Developed the RECAST frameworks for the mono-s(WW) analysis in both the fully hadronic and semileptonic channels.

ACKNOWLEDGEMENTS

I would like to thank:

Dr. Robert Kowalewski for giving me the opportunity to work on the ATLAS experiment and pursue my interests within it, vastly improving the quality of this work through your advice and expertise, and being the most supportive supervisor I could have asked for.

Dr. Randall Sobie for the interesting and very rewarding work on ATLAS computing, and the support throughout.

Dr. Kenji Hamano for the guidance and advice, which was invaluable to the mono-s analysis.

Dr. Philipp Mogg for graciously teaming up with me as analysis co-contact, and sharing your impressive expertise and insight throughout.

Dr. Rolf Seuster for supporting my ATLAS computing work, and the many delightful conversations.

Dr. Richard Keeler for your generosity in offering me an inspiring first exposure to physics research as an undergraduate student at a time when I wasn't really sure I was cut out for the field, and for your continued support and encouragement since then.

My parents and sisters for encouraging me to carve my own path, and for your unwavering love and support at every twist and turn.

Struan Eamer for being crazy enough to hike the Juan de Fuca trail in the middle of winter so I could meet you, and for changing my life ever since.

My friends for reminding me that there's more to life than my computer.

DEDICATION

To Paul

Chapter 1

Introduction

With the discovery of the Higgs boson in 2012 [6, 7], the final piece of the Standard Model fell into place. Developed during the latter half of the 20th century, the Standard Model describes all known particles and their interactions. The model has demonstrated remarkable predictive power, and can account for nearly all phenomena observed in particle physics detectors to date, with no firmly established deviations from its predictions. Yet, it is known to be incomplete. Among the observed phenomena that it fails to explain [8, 9, 10] are multiple lines of astronomical observation that collectively point to the existence of a new form of non-luminous matter in the universe known as "dark matter" (DM).

While the nature of DM remains a mystery, the observational data strongly suggest that it will take the form of one or more new particles beyond the Standard Model. In addition to its gravitational interactions with massive particles, theoretical considerations give good reason to expect that the new particle(s) could experience additional, albeit weak, couplings to particles of the Standard Model by mechanisms yet to be determined. The study presented in this thesis is part of a multi-pronged international effort to search for evidence of particle DM by means of its non-gravitational interactions in particle physics experiments. In particular, this study probes new ground in the search for DM production in high-energy particle collisions at the Large Hadron Collider (LHC) at CERN.

This chapter introduces the Standard Model, focusing on aspects that are particularly relevant to the presented search, and discusses the astronomical evidence for the existence of DM in the universe. It also introduces the range of experimental strategies that are currently employed to search for evidence of DM in particle physics detectors, and how this search fits into the wider DM search programme at the LHC.

1.1 Introduction to the Standard Model

The Standard Model (SM) describes all known elementary particles and three of the four known forces by which they interact with one another - the strong, the electromagnetic (EM), and weak forces. The theory of general relativity [8], which describes the gravitational force, has yet to be incorporated into the SM.

The known particles, illustrated in Figure 1.1 are divided into two classes known as “fermions” and “bosons” on the basis of an intrinsic form of angular momentum known as “spin”. Fermions carry spin $\frac{1}{2}$, and bosons carry integer spin.

The specific forces by which particles in the SM interact with one another are determined by the charge(s) that they carry. Particles that carry electric charge interact with other particles carrying this charge via the EM force. Similarly, particles that carry weak and colour charge interact via the weak and strong forces, respectively.

Each fermion has a corresponding anti-particle with the same mass, but with opposite values of the charges it carries - for example, the electron e^- carries negative electric charge and its antiparticle, the positron e^+, carries positive electric charge.

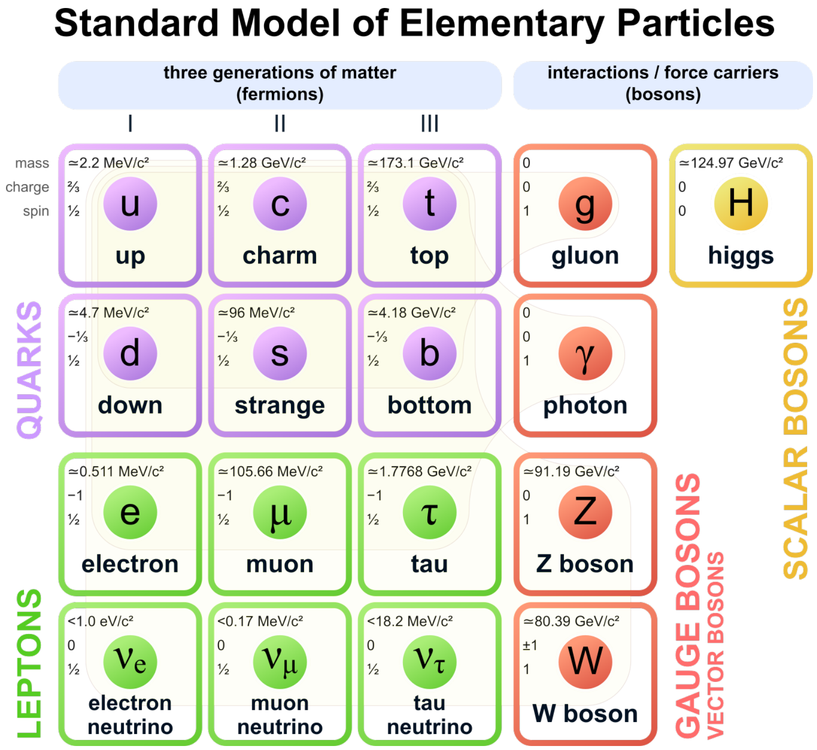

Figure 1.1: Names and fundamental properties of particles in the Standard Model. Figure from © [11].

1.1.1 Fermions

Fermions are further sub-divided into leptons and quarks, depending on the charges they carry, and hence by the forces with which they interact. There are three known generations of fermions, labelled I, II and III in Figure 1.1, each with significantly larger mass than the last. Each generation contains a pair of quarks and a pair of leptons, along with their associated antiparticles. The quark pair consists of one "up-type" quark with positive electric charge and one "down-type" with negative charge. The lepton pair consists of one charged lepton and one charge-neutral "neutrino".

Leptons carry electric charge and weak isospin, and as a result interact with one another and with other particles carrying these charges via the EM and weak forces, respectively.

Like leptons, quarks also carry electric charge and weak isospin, and additionally carry colour charge. The colour charge allows quarks to interact via the strong force. As a result, quarks interact by all three forces described by the SM. Unlike charged leptons, which carry an electric charge of ±1, quarks carry fractional electric charge; up-type (down-type) quarks carry a charge of $+\frac{2}{3}\ \left(-\frac{1}{3}\right)$.

Due to an effect known as "colour confinement", quarks cannot exist as stable particles in isolation, and must instead combine with other quarks to form stable "colour-neutral" states called "hadrons". The two major forms of hadrons are "mesons" formed by a quark-antiquark pair and "baryons" formed by three quarks. Although the intrinsic strength (i.e. probability) with which particles couple via the strong interaction is 3 (14) orders of magnitude greater than via the EM (weak) interaction [12], the range of strong force interactions is limited by colour confinement to the approximate size of the proton (10^{-15}m). The LHC collides protons with sufficient energy to probe interactions between their constituent quarks and gluons at length scales smaller than the size of the proton. Due to the large strong force coupling at this scale, there is a relatively high probability that the interactions initiated by these collisions will proceed via the strong force compared with other forces.

1.1.2 Bosons

Bosons in the SM are divided into "gauge bosons" and "scalar bosons". The gauge bosons are spin 1 force carriers that mediate interactions between particles. The photon mediates EM interactions between electrically charged particles. The gluon mediates the strong interaction between quarks. Unlike charge-neutral photons, the gluon itself carries colour charge, which allows it to self-interact via the strong force. The weak force is mediated by three particles: the electrically neutral Z boson, and two W bosons ($W^{\pm}$) with opposite electric charges of ±1.

Scalar bosons are defined as spin 0 particles. There is only one scalar boson in the SM, namely the Higgs boson (or, simply, the "Higgs") [13, 14, 15] . Particles in the SM acquire mass via their interaction with the Higgs field. As such, the Higgs only interacts with massive SM particles, which includes all particles except the photon and the gluon. The more massive the particle, the stronger its coupling with the Higgs. Neutrinos are a possible exception; there is at present no mechanism in the SM by which neutrinos could interact with the Higgs field, so the origin of their tiny masses remains an open question.

1.1.3 Collision and Decay Processes at Colliders

The high-energy counter-rotating proton beams at the LHC are brought into head-on collisions at four interaction points around the ring, each of which is surrounded by a detector[1]. At each interaction point, constituents of the colliding protons known as "partons"[2] can pair annihilate to form observable collision products via one or more "virtual mediators"[3], and the collision products are subsequently measured by the detector.

Each process that describes a physically allowed mechanism by which partons may annihilate to form observable particles has a certain probability of taking place relative to other possible annihilation and production processes. The probability that a given process will take place is quantified by its "cross section" σ. The beam luminosity $\mathcal{L}$ relates the rate of collisions $\frac{dN}{dt}$ that proceed via a given process to the cross section of the process:

$$\frac{dN}{dt} = \mathcal{L}\sigma \tag{1.1}$$

The luminosity can be integrated over a period of time t_1 to t_2, such that the total number of events expected to be produced via a process with cross section σ over the given period is related to the "integrated luminosity" $\mathcal{L}_{\text{int}}$ by:

---

[1] See Chapter 3 for a detailed discussion of the LHC and the detectors that surround the four interaction points.

[2] See Section 3.1 for an introduction to the parton model.

[3] See Section 1.1.5 for a discussion of virtual particles.

$$N = \sigma \int_{t_1}^{t_2} \mathcal{L}(t)dt = \sigma \mathcal{L}_{\text{int}} \tag{1.2}$$

1.1.4 Unstable Particles

The lowest-mass "first-generation" quarks and charged leptons located in column I in Figure 1.1 are, along with neutrinos and the massless photons and gluons, the only stable particles in the SM. All other particles are unstable, and will decay to less-massive particles after they are produced.

The decay of an unstable particle occurs randomly with respect to the time elapsed since the particle was produced, with the elapsed time governed by Poisson statistics. The probability $P(t)$ that an unstable particle will have decayed after a time t has elapsed in its rest frame is given by the following cumulative exponential distribution:

$$P(t) = 1 - e^{-\frac{t}{\tau}} \tag{1.3}$$

where τ is the mean lifetime of the particle.

Unstable Resonance and the Breit-Wigner Formula

Due to their finite lifetime, the Heisenberg uncertainty principle implies that unstable particles will not be produced with a well-defined mass, but rather with a mass distribution peaked at a central value m_0. The probability density function $p(m)$ associated with measuring an unstable particle to have a mass m is given by the Breit-Wigner formula [16]:

$$p(m) \propto \frac{1}{(m - m_0)^2 + \frac{\Gamma_E^2}{4}} \tag{1.4}$$

which exhibits a resonant peak of width Γ_E centred at m_0. The lifetime of the unstable particle is related to the width of its Breit-Wigner resonance by $\tau = \frac{\hbar}{\Gamma_E}$.

For unstable mediators produced in high-energy colliders which decay to a pair of detectable particles, the mediator mass can be reconstructed as the combined invariant mass[4] of its measured decay products. Neglecting detector resolution effects, the cross section $\sigma(m)$ associated with producing an unstable particle with a given reconstructed mass is expected to be proportional to its Breit-Wigner distribution:

---

[4] The invariant mass m of two particles with four-momenta p_1 and p_2 is in general given by: $m^2 = (p_1 + p_2)^2 = (E_1 + E_2)^2 - (\mathbf{p}_1 + \mathbf{p}_2)^2$

$\sigma(m) \propto p(m)$. This results in a characteristic resonant peak in the reconstructed invariant mass distribution of the mediator's decay products, which can be used to identify the unstable mediator, and to measure its mass and lifetime.

1.1.5 Feynman Diagrams

The interaction mechanisms by which observable collision products are produced from the annihilation of two partons can be represented by Feynman diagrams, which are described in detail in Chapter 2 of Ref. [12] and summarized here. As an example, the Feynman diagram for the Drell Yan process in which a $q\bar{q}$ pair annihilate to form a lepton pair $\ell\bar{\ell}$ via the exchange of a virtual photon (γ^*)[5] or Z^* boson mediator is shown in Figure 1.2.

The particles involved in the interactions are represented as lines in a Feynman diagram, with different particle types represented by different line styles - fermions are generally represented by solid straight lines, and bosons (with the exception of gluons) are generally represented by wavy lines. Particle interactions are represented by vertices at which lines in the diagram intersect. The annihilation of a $q\bar{q}$ pair to form the virtual γ^*/Z^* mediator is represented in Figure 1.2 by the vertex at which the q and $\bar{q}$ fermion lines meet the γ^*/Z^* boson line, and the subsequent decay of the γ^*/Z^* to $\ell\bar{\ell}$ is represented by the vertex to the right at which the γ^*/Z^* line meets the ℓ and $\bar{\ell}$ lines. Note that time flows horizontally from left to right in Feynman diagrams, so the colliding $q\bar{q}$ pair are shown on the left and the observable decay products $\ell\bar{\ell}$ on the right.

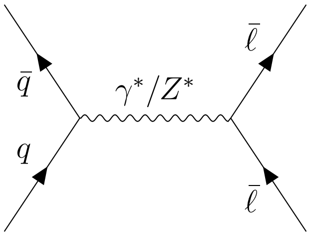

Figure 1.2: Feynman diagram for the Drell Yan process.

---

[5] The * indicates that mass of the virtual particle may be off-shell (see discussion of virtual particles below).

Virtual Particles

In general, ingoing and outgoing lines in a Feynman diagram represent real observable particles, and internal lines represent so-called virtual particles. Virtual particles are not observable, but are rather a representation of the mechanism involved with producing the observable final-state particles. Importantly, virtual particles can take on any mass needed to satisfy energy and momentum conservation at each interaction vertex.

Matrix Element

The final-state observables (momenta of outgoing particles) associated with a process of particle production from *pp* collisions at the LHC, such as the Drell-Yan process shown in Figure 1.2, depend in general on both the phase space and dynamics of the process. The phase space represents the full space of available kinematics (masses and momenta) for the incoming and outgoing particles. The dynamics are encoded in the matrix element $\mathcal{M}$, which is calculated on the basis of the internal structure of the process as represented by the Feynman diagram.

1.1.6 Mathematical Formulation of the Standard Model

The SM is formulated mathematically as a quantum field theory, in which particles of the SM are represented as excitations of quantum fields. The mathematical formulation of the SM is presented in detail in standard texts [12, 17], and briefly summarized in this section, with focus placed on aspects that are relevant to later discussions in this thesis.

Lagrangian Densities

As in classical field theories, the quantum fields of the SM and their interactions are powerfully described by the formalism of Lagrangian densities, which are functions of the quantum fields and their derivatives. For example, interactions between photons and electrically charged fermions are described in quantum electrodynamics (QED) by the following Lagrangian density term:

$$\mathcal{L}_{\text{QED, interaction}} = -q\psi^{\dagger}(x)\gamma^{0}\gamma^{\mu}\psi(x)A_{\mu}(x) \tag{1.5}$$

where $\psi(x)$, a function of the four spacetime coordinates represented by x, is the quantum spinor field of the spin-$\frac{1}{2}$ fermions in the SM. $A_\mu(x)$ represents the vector field of the massless spin-1 photon and γ^μ are the Dirac matrices [12]. The index μ runs over the four spacetime coordinates. The factor q represents the electric charge of the fermion involved in the interaction and its value[6] determines the strength of the interaction.

Symmetries and Group Theory Description

Symmetries in the Lagrangian density function associated with each fundamental interaction are described in the language of group theory by classifying the fundamental interactions into gauge groups that describe their symmetries. For example, QED exhibits a symmetry under local phase transformations, described by the unitary local gauge group U(1). This means that the Lagrangian $\mathcal{L}_{\text{QED}}$ is invariant under the multiplication of the fermion spinor $\psi(x)$ by a unitary function $U = e^{i\theta(x)}$ (unitarity implies that $U^\dagger U = 1$), where $\theta(x)$ can be any function of the spacetime coordinates x. It is found that this symmetry can be ensured by the inclusion of the vector field $A_\mu(x)$ in the QED Lagrangian, which is identified with the physical photon. Because it ensures invariance under the U(1) gauge group, the vector field $A_\mu(x)$ is referred to as a "gauge field", and the corresponding boson (the photon) as a "gauge boson". The symmetries in the SM are described by the direct product[7] of the U(1)×SU(2)×SU(3) gauge groups.

Quantum Chromodynamics

The theory of quantum chromodynamics (QCD), presented in standard texts such as Ref. [19], describes the strong interactions mediated by gluons between particles with colour charge (quarks and gluons). Its symmetries are described by the SU(3) gauge group. The quarks are represented by a three-component vector of spinors: $\psi_c = \{\psi_r, \psi_g, \psi_b\}$, where the subscripts refer to the three colours - red, green and blue - that constitute the charges of the strong interaction. The QCD Lagrangian (see eg. Eq. 10.88 in Ref. [12]) is symmetric under a transformation of the vector of quark spinors ψ_c by a 3×3 SU(3) matrix, which is unitary with determinant 1. The SU(3) symmetry is ensured by the inclusion of an eight-component set $\boldsymbol{A_\mu}$ of vector gauge

---

[6] The electric charges of all fermions in the SM are as follows: ± 1 for charged leptons, $+\frac{2}{3}$ $(-\frac{1}{3})$ for up (down) type quarks and 0 for neutrinos.

[7] General definitions in group theory can be found, for example, in Section 1.1 of Ref. [18].

fields in the QCD Lagrangian. The associated gauge bosons are identified as the eight physical gluons, each of which possesses a unique superposition of rgb colour states [12].

Electoweak Theory and the Higgs Mechanism

The mathematical descriptions of the weak and EM forces are unified into a single "electroweak" theory (for a review, see [20]) whose symmetries are described by the SU(2)×U(1) product of gauge groups.

Developed in 1954, Yang-Mills theory [21] showed that a set of three massless vector gauge bosons, referred to as the "isospin triplet" $\boldsymbol{W}$ are needed to satisfy the SU(2) symmetry, and a fourth massless vector gauge boson B is needed to satisfy the U(1) symmetry. Despite satisfying the SU(2) symmetry of the weak interaction, the weak isospin triplet predicted by Yang-Mills theory falls short of fully describing the physical $W^{\pm}$ and Z bosons that mediate the weak interaction, which are known to be massive [22].

The U(1)×SU(2)×SU(3) symmetry of the SM Lagrangian does not admit mass terms of the form $m_X^2 X^\dagger X$, where X is an arbitrary field. Proposed in 1964, the "Higgs mechanism" [13, 14, 15] provides a means of generating the masses of the physical $W^{\pm}$ and Z bosons, as well as all other massive particles (with the exception of neutrinos), by adding the following term to the SM Lagrangian:

$$\mathcal{L}_{\text{Higgs}} = (D^\mu H)^\dagger (D_\mu H) - V(H) \tag{1.6}$$

where

$$H = \frac{1}{\sqrt{2}} \begin{pmatrix} 0 \\ h + v \end{pmatrix} \tag{1.7}$$

$h(x)$ is interpreted as the scalar field of the physical Higgs boson, and v as the so-called "vacuum expectation value". With H in this form, $\mathcal{L}_{\text{Higgs}}$ is described by the U(1) symmetry group but not the SU(2) group, and is thus said to "break" the electroweak symmetry SU(2)×U(1) to the QED gauge symmetry U(1).

The covariant derivative $D_\mu H$ in Eq. 1.6 takes the form:

$$D_\mu H = \big(\partial_\mu + i\frac{1}{2} g \sigma_k W^k_\mu + i\frac{1}{2} g' B_\mu\big) H \tag{1.8}$$

where σ_k are the Pauli matrices, and g and g' are the coupling constants between the Higgs field and the $\boldsymbol{W}$ and $\boldsymbol{B}$ fields, respectively.

The Higgs potential $V(H)$ takes the form:

$$V(H) = -\mu^2 H^\dagger H + \lambda(H^\dagger H)^2 \tag{1.9}$$

where the second term describes quartic self-interactions of the Higgs field.

The emergence of the massive physical $W^\pm$, Z bosons and the massless photon comes from the interactions of the electroweak $\boldsymbol{W}$ and B fields with the Higgs field to produce "mass" terms in the Lagrangian of the form $m_X^2 X^\dagger X$. This can be seen by expanding Equations 1.6 and 1.8, considering only the terms involving the vacuum expectation value v:

$$\mathcal{L}_{\text{Higgs}} = \frac{v^2}{8}\Big[g^2\big((W_\mu^1)^2 + (W_m u^2)^2\big) + (gW_\mu^3 - g'B_\mu)^2\Big] + [...] \tag{1.10}$$

with the physical vector boson fields and masses defined as:

$$\begin{aligned}
W_\mu^\pm &\equiv \frac{1}{2}(W_\mu^1 \mp W_\mu^2) && \text{with mass} && m_W = \frac{gv}{2} \\
Z_\mu &\equiv \frac{1}{\sqrt{g^2+g'^2}}(gW_\mu^3 - g'B_\mu) && \text{with mass} && m_Z = \frac{v}{2}\sqrt{g^2+g'^2} \\
A_\mu &\equiv \frac{1}{\sqrt{g^2+g'^2}}(g'W_\mu^3 + gB_\mu) && \text{with mass} && m_A = 0
\end{aligned} \tag{1.11}$$

Inserting the definitions of the physical vector boson fields from Eq. 1.11 back into Eq. 1.10, it can be readily confirmed that Eq. 1.10 takes the form $\mathcal{L}_{\text{Higgs}} = \big[m_W^2 (W^\pm)_\mu^\dagger (W^\pm)^\mu + m_Z^2 Z_\mu^\dagger Z^\mu + m_A^2 A_\mu^\dagger A^\mu\big] + [...]$. Masses of fermions are likewise generated by so-called Yukawa couplings [23] between the fermion and Higgs fields. The dark Higgs model used to optimize and interpret the DM search presented in this thesis postulates that DM, as well as any hypothetical new bosons that mediate its interactions with SM particles, would acquire their masses by means of their interaction with the dark Higgs field S, as discussed in Chapter 2.

1.2 Evidence for Dark Matter from Observational Astronomy

Looking beyond the SM, many independent astronomical observations collectively provide compelling evidence for the presence and abundance of a new form of matter in the universe that is not directly observable because it neither emits nor absorbs light. Some of the earliest and clearest evidence for this so-called "dark matter" (DM) came in 1978, when Rubin et al. [24] reported systematic anomalies in measured rotation speeds of spiral galaxies. In particular, distributions of the rotation speed as a function of the radial distance from the galactic centre differed in shape from what would be expected on the basis of the distribution of galactic mass measured from the observed luminosity profile.

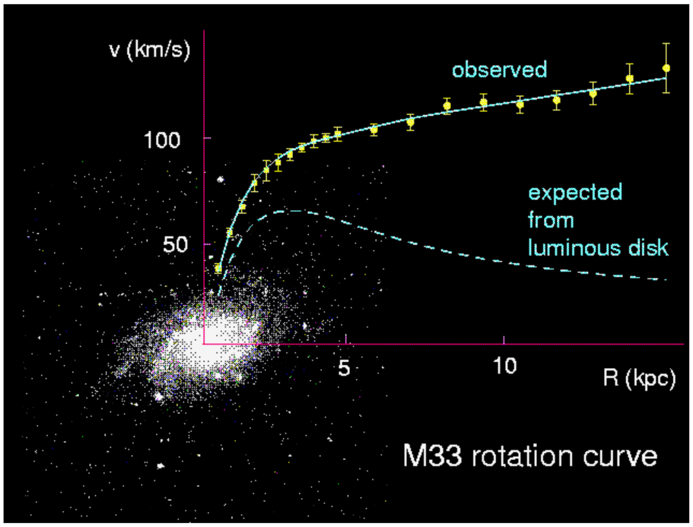

Figure 1.3: Observed rotation speed of the nearby dwarf galaxy M33, overlaid on an optical image of the galaxy. Yellow data points show observed rotational speed of the galaxy as a function of the radial distance from the galactic centre (in kpc). Dashed line shows the expected rotational speed on the basis of the calculated mass of the luminous stellar disk. Figure from © [25].

Spiral galaxies were known at the time to be comprised of a central spheroidal "galaxy bulge" that contains the majority of luminous matter in the galaxy, in addition to a "disk" extending out to larger radii from the galactic centre, within which the density of luminous matter falls off exponentially with radius. If one assumes that the distribution of mass in the spiral galaxy follows its luminosity profile, application of Newtonian gravitational mechanics[8] would predict the rotation speed to peak near the edge of the central galaxy bulge, as illustrated in the blue dashed line in Figure 1.3 for the dwarf galaxy M33, and fall off at larger radii due to the exponentially

---

[8] Rotation speeds of spiral galaxies are in general non-relativistic (typically $v_{\mathrm{rot}}/c < 1\%$ [26]). Since Newtonian gravitational mechanics represents an accurate approximation of general relativity in this macroscopic non-relativistic regime, it is generally assumed to provide an appropriate framework for the mathematical description of galactic rotation curves.

decaying matter density of the disk. However, the observed galactic rotation speed, shown as yellow data points in Figure 1.3, is generally observed to continue increasing well beyond the luminous galactic bulge. These anomalies in galactic rotation curves, which have since been observed in hundreds of spiral galaxies [26], can be explained by postulating an additional source of non-luminous matter density in galaxies, DM, which extends well beyond the luminous bulge and provides the necessary gravitational potential to prevent the rotation speeds from falling off beyond the bulge.

In the years following the early reports by Rubin et al., modifications to the laws of Newtonian gravity at galactic scales [27] were considered as an alternative to explain the anomalies without invoking the need for DM. However, while the proposed modifications to gravity were successful in describing the observed galactic rotation curves, numerous astronomical observations in other contexts have independently turned up results that indicate a need for DM in the universe, many of which cannot be easily explained by modifying Newtonian gravity. Additional evidence at galactic scales comes from significant differences between the spatial distributions of matter density, measured using gravitational lensing, and of luminous matter following collisions of galaxy clusters, such as the Bullet cluster identified in 1995 [28], which indicate that the majority of the matter density in the colliding galaxies is non-luminous. Studies of the relative contribution to the masses of galaxy clusters from luminous matter using data from the Chandra X-ray observatory [29] suggest that only 15-20% of the mass composition of the galaxies studied is comprised of luminous matter, with DM comprising the remaining 80-85%.

Because of their stability and EM interactions, protons and neutrons comprised of bound quarks, as well as their bound electrons - collectively known as "baryonic matter" - comprise by mass the overwhelming majority of known luminous matter in the universe. The theory of Big Bang nucleosynthesis (BBN) (for a review, see Section 24 of Ref. [22]) predicts that the production of light nuclei - D, ^{2}He, ^{4}He, and ^{7}Li - took place in the early universe following the Big Bang (see Ref. [30] for a review of the Big Bang theory), as the universe expanded and cooled sufficiently to allow their formation by means of nuclear fusion reactions. BBN theory predicts that the abundances of these light nuclei in the universe were fixed during BBN, following which the rate of the nuclear fusion reactions became negligibly small due to the continued expansion and cooling of the universe. Importantly, the theory also predicts that the relative abundances of the light nuclei are highly sensitive to the density of baryonic matter in the universe, which was fixed prior to their formation. As a result, their relative abundance can be used to infer the density of baryonic matter in the universe in the context of BBN theory. Using this approach, precision measurements of the abundances of light nuclei inferred from observational data indicate that baryonic matter constitutes approximately 5% [22] of the energy density of the universe. Current measurements of anisotropies in the cosmic microwave background (CMB) [31] measured by the Planck collaboration [32], interpreted in the context of the ΛCDM model of cosmology (for a review, see Section 25 of [22]), indicate that approximately 30% of the energy density of the universe is comprised of matter, with the missing 25% identified as non-baryonic DM. This result implies that 85% of all matter in the universe is comprised of non-luminous DM, consistent with the findings discussed above from measurements of galaxy clusters.

1.3 Dark Matter Composition Hypotheses

The previous section presented a diverse range of astronomical observations that collectively point to the need for DM in the universe. While active research continues within the theoretical community (see, for example, Refs. [33, 34]) into the possibility of modifying the laws of gravitation at astronomical scales to explain these observations without the need for DM, there are significant theoretical challenges involved with designing modifications that can consistently explain the range of observational anomalies at scales ranging from individual galaxies to galaxy clusters, while simultaneously addressing the apparent need for DM at cosmological scales from the discrepancy between measurements of the baryonic mass density from BBN and the much larger total mass density inferred from anisotropies in the CMB. As a result, DM is widely considered the leading hypothesis to explain the full range of observational data.

While the astronomical observations provide a wealth of information regarding the composition of DM in the universe by means of its gravitational effects on visible matter, they provide relatively few clues as to what actually comprises the DM. Its abundance in the present day universe indicates that it must be stable on cosmological timescales (i.e. billions of years). The evidence from BBN and CMB anisotropies indicates that the DM must be non-baryonic. Its non-luminous nature further implies that it neither emits nor absorbs photons, and therefore has negligible or no charge under the EM force. Besides baryons, neutrinos - with their tiny but nonzero masses[9] - represent the only other massive stable particles currently known to the SM, and satisfy the requirement of being electrically neutral. However, the possibility of neutrinos constituting any appreciable fraction of the DM was ruled out by studies published in the 1980's [35], which demonstrated that the large scale structure of the universe would differ significantly from what is observed today if the mass density of the universe were dominated by neutrinos due to their ultra-relativistic velocity. More generally, analysis of the measured anisotropies in the CMB measured by the Planck collaboration [32] is found to strongly favour the standard ΛCDM model in which the DM is predominantly comprised of "cold" particles, so called because they travel at non-relativistic velocities.

With the stable particles of the SM ruled out, the current most widely accepted hypothesis is that DM is comprised of a new form of cold non-baryonic matter that is not currently described by the SM.

1.3.1 Origin and Interactions of Particle Dark Matter

Despite the observable effects of its gravitational interactions at astronomical scales, the strength of gravitational couplings between massive particles is ~ 30 orders of magnitude weaker than any of the other three known forces [12]. As a result, gravitational interactions between DM and SM particles are far too weak to be observable in particle detectors. Given that there have not yet been any conclusive indications of DM in particle detectors, it can be further deduced that any non-gravitational interactions between DM and particles of the SM are relatively weak compared with the strong, weak and EM couplings between SM particles. However, most theories that aim to describe the origin of the observed abundance of DM in the present day universe imply the existence of non-gravitational couplings between DM and SM particles, and in many cases predict that the couplings could be strong enough to be probed by modern particle detection methods. This produces a generic class of DM candidates known as weakly-interacting[10] massive particles (WIMPs).

A positive detection of WIMPs would not only confirm the hypothesis of particle DM, but would also allow physicists to begin to study its properties as a particle, and test theoretical extensions of the SM that incorporate particle DM.

---

[9] Current constraints from cosmology place an upper limit on the sum of neutrino masses from all generations of 0.17 eV, 3×10^6 times smaller than the electron mass.

[10] The "weak" interactions of the WIMP DM candidates are in general not necessarily associated with the weak force, but are simply too weak to have produced a measurable signature in particle detectors to date

Dark Matter Origin from Thermal Freeze-out

A review of the existing hypotheses for the origin of DM can be found in Section 27.3 of Ref. [22]. Of these, the so-called "thermal freeze-out" scenario is a popular candidate, because it postulates that the observed DM density in the present day universe originated from the same process of thermal decoupling that produced the primordial abundances of light nuclei in the well-tested BBN scenario discussed earlier. The hypothesis postulates that in the very early universe, matter was sufficiently dense and energetic to establish thermal equilibrium between DM and SM particles due to interactions between DM and SM particles (so-called "DM-SM interactions"). As the universe expanded and cooled, eventually the rate of DM-SM interactions became too low to maintain thermal equilibrium between the two species. At this point, known as "thermal freeze-out", DM became decoupled from SM particles, thus fixing the relic abundance of DM observed in the present-day universe.

For cold DM relics ($v/c \lesssim 0.1$ at the time of freeze-out), and assuming that the relic abundance is predominantly set by direct DM-SM interactions, analysis of the observed relic abundance of DM in the context of the thermal freeze-out hypothesis (see, for example, Section B of Ref. [36]) implies that the cross section for SM-DM interactions should be $\sigma_{\text{SM-DM}} \gtrsim 1$ pb, comparable to typical cross sections for interactions mediated by the weak force. Searches for DM in particle detectors (for a review, see [37]) have yet to turn up any hints of a DM candidate with interaction cross sections with the SM near the weak scale. However, the cross section constraint can be significantly relaxed by considering a scenario in which the relic abundance of DM is set not by direct interactions between the DM and the SM, but rather by interactions between DM and an unstable mediator, which subsequently decays to SM particles (see, for example, Ref. [38]). The DM search presented in this thesis is interpreted in the context of such a scenario, wherein the unstable mediator is the Dark Higgs boson [39, 40].

1.4 Dark Matter Search Strategies

There are three complementary approaches used to search for particle DM by means of its non-gravitational interactions. Direct detection searches (for a review, see [41]) aim to detect evidence of a recoil induced by elastic scattering between a DM particle in the galactic halo and a target particle in the detector. Indirect searches (for a review, see [42]) use observational data to search for evidence of particles produced by DM annihilation or decay in particular regions of the observable universe that are expected to have a high DM density. Searches for DM at colliders (for a review, see [43]), of which the work in this thesis is an example, study the decay products from high-energy collisions of subatomic particles to search for an above-background excess of events that could be consistent with DM having been produced in some of the collisions.

1.4.1 Direct Detection

Direct detection searches operate in very low-background environments, typically in underground facilities such as SNOLAB (for a review, see Ref. [44]), in order to minimize scattering events in the detectors from non-DM sources such as cosmic rays and radioactivity, and detailed studies are performed to determine the expected rate of events from all possible background sources. As a result, a significant excess of elastic scattering events, particularly if observed in multiple direct detection experiments, would offer a clear signature of interactions with DM in the galactic halo.

If no evidence of excess scattering events is found, experiments place upper bounds on DM-nucleon interaction cross section with a largely standard set of methods and assumptions (most notably the local DM density and the relative speed with which the DM passes through Earth) - see, for example, Ref. [45] - which facilitates comparison between different experiments. Figure 1.4 summarizes the current upper bounds on the spin-independent[11] DM-nucleon interaction cross section from all direct detection searches. The searches probe down to many orders of magnitude below the weak scale ($\sigma \sim 10^{-36}\text{cm}^{-2}$) over ~ 4 orders of magnitude of candidate DM masses. However, current direct detection strategies generally suffer practical limitations to the ranges of DM masses and interaction cross sections that can be probed. The lower bound on accessible DM masses is in general dictated by the signal to noise ratio of the detector, referred to as the "noise wall", which is quite difficult to overcome. The range of accessible cross sections is also bounded from below for most direct detection experiments by the so-called "solar neutrino floor", below which the measured event rate becomes dominated by the irreducible flux of solar neutrinos passing through the Earth.

---

[11] Spin-dependent vs. spin-independent DM-nucleon interactions differ according to whether the coupling is sensitive to the spin state of the target nucleon [41].

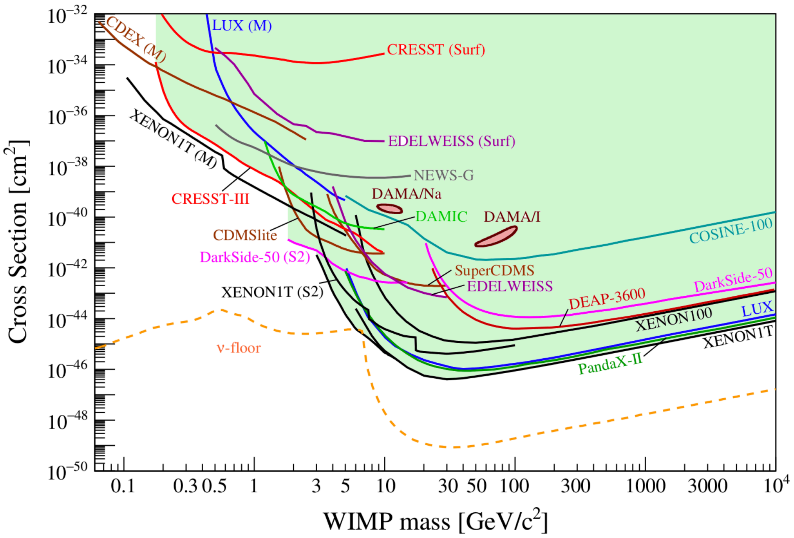

Figure 1.4: Summary of upper bounds from direct detection searches on the interaction cross section for spin-independent WIMP-nucleon scattering, over a range of hypothetical WIMP masses. Upper bounds from individual searches are shown as solid lines. Results labelled “M” were obtained assuming the Migdal effect [46]. Shaded green region shows combined exclusion from all searches, excluding results obtained assuming the Migdal effect. Yellow dashed line shows the solar neutrino floor for a Ge target, computed using the assumptions and methodology presented in Refs. [47, 48]. Figure from © [41].

1.4.2 Indirect Detection

By searching for excesses of several potential DM annihilation products in observational data - gamma rays, charged leptons and antimatter - in addition to neutrinos, indirect detection searches (reviewed in Refs. [42, 49, 22]) can avoid the limitation of the solar neutrino floor. Depending on the target species, these searches can also target a wider range of candidate DM masses compared with direct detection searches. Due to the many potential processes that could produce the target particles in observational data - both within and beyond the SM - indirect searches generally contend with relatively large uncertainties associated with modelling the expected flux from these background sources.

1.4.3 Searches for DM at Colliders

Rather than searching for non-gravitational interactions of relic DM on Earth or in the observable universe, searches for DM at colliders (for a review, see [43]) instead look for evidence of DM production from high-energy particle collisions. Like neutrinos, DM would be expected to pass invisibly through any detector surrounding the collision point due to its very low interaction cross section, producing a momentum imbalance transverse to the beam line referred to as $E_{\mathrm{T}}^{\mathrm{miss}}$[12]. An excess of collision events with large final-state $E_{\mathrm{T}}^{\mathrm{miss}}$ above the rate expected from SM processes with final-state neutrinos would be consistent with the production of DM in the high-energy collisions. Given that other hypothetical new physics processes (see, for example, Refs. [50, 51]) could also produce an excess of high-$E_{\mathrm{T}}^{\mathrm{miss}}$ events from non-DM sources, any such findings would benefit from corroborating DM detections in direct and/or indirect detection experiments.

Despite operating in a very high background environment, colliders offer numerous advantages that allow DM searches performed using collider data to complement and potentially extend the reach of direct and indirect searches. First, the detectors used by particle colliders are often designed to measure all final-state particles produced by the collisions and their kinematic information with high precision. This detailed final-state information allows DM searches to target specific final-state topologies, which can lead to substantial reductions in SM background processes and considerably enhance the sensitivity to hypothetical DM production processes that predict events with the targeted topology. Second, by targeting DM produced in the collisions and adopting a search strategy that does not require the DM to interact with the detector, searches at colliders are insensitive to the neutrino floor that will challenge the sensitivity of next-generation direct detection searches. Third, while the range of DM masses is bound from above by the centre of maximum centre-of-mass energy of the particle collisions (∼TeV for proton-proton collisions at the LHC), DM searches at colliders do not suffer the noise wall that limits the sensitivity of direct detection searches below ~ 1 GeV (see Figure 1.4).

Even if particle DM is first discovered at a non-collider experiment, the detailed final-state information available in particle collision data will enable detailed measurements of its properties and interactions, provided that it can be produced at colliders.

---

[12] See Section 3.4.4 for a detailed introduction to missing transverse momentum in the ATLAS detector.

1.4.4 Searching for Dark Matter at Particle Accelerators

Approaches used to Search for DM at Colliders

The concept of searching for evidence of DM production in high-energy particle collisions is currently being pursued by numerous collaborations. The particular energy scales and detector technologies available to each experiment can be exploited to target specific mass ranges and possible DM production mechanisms, thus allowing for a rich programme of complementary searches.

The proton-proton collision experiments at the Large Hadron Collider (LHC)[13] [52] - ATLAS [53], CMS [54] and LHCb [55] - benefit from the world-leading 13 TeV centre-of-mass energy of the pp collisions to probe models with massive mediators (m_{med} up to a few TeV) of the DM-SM interactions that could be produced in the collisions. The hermetic[14] coverage and precise event reconstruction available with the ATLAS and CMS general-purpose detectors make it possible to probe a wide range of hypothetical DM production models and final-state signatures, typically targeting DM candidates with masses in the $\sim$GeV-TeV range (see Ref. [56] for a review of DM searches performed with the ATLAS and CMS detectors). Meanwhile, DM searches at LHCb (for a review, see [57]) take advantage of the detector's excellent forward-angle coverage and vertex resolution to target signatures with lower-mass DM ($\sim$MeV-GeV) and displaced vertices.

In addition to proton-proton collisions at the LHC, production of DM in electron-positron e^+e^- collisions has been probed with the BABAR experiment [58] at the Stanford Linear Accelerator Centre (SLAC), as well as the Belle experiment [59] and its recent Belle II upgrade [60] at the SuperKEKB collider [61]. With a 10.6 GeV centre-of-mass collision energy, the Belle II experiment is particularly well suited to study DM with masses in the range of a few MeV to $\sim$10 GeV. Searches at e^+e^- colliders benefit in precision both from the well-defined initial state afforded by colliding fundamental particles, and from the vastly reduced background of QCD activity[15] in the final state compared with pp collision events. Searches performed with early Belle II data, reviewed in Ref. [62], are already showing promising sensitivity to a number of low-mass DM candidates, with significant sensitivity improvements

---

[13] See Section 3 for a general introduction to the LHC and its major detectors.

[14] Hermetic detectors, of which ATLAS and CMS are examples, are designed to detect all SM decay products from a collision with the exception of neutrinos.

[15] See Section 3.4.5 for a more detailed discussion of the QCD background in the context of the ATLAS triggering system.

expected as more data is collected in the coming years.

The most direct way to search for DM at pp and e^+e^- colliders is to look for evidence of the so-called "$E_{\mathrm{T}}^{\mathrm{miss}}$ +X" events introduced above, in which the DM is produced along with detectable SM particles, thus producing a signature of SM particles recoiling against $E_{\mathrm{T}}^{\mathrm{miss}}$ in the final state. An alternative and less direct approach, known as a "resonance search", is to look for evidence of the production of new massive mediators which could potentially mediate DM-SM interactions by looking for resonant peaks in the invariant mass distribution of one or more pairs of final-state particles. Such a peak, if not associated with any known SM mediators, would be indicative of the production and subsequent decay of a new massive mediator to a pair of SM particles.

DM in the ∼MeV-GeV mass range can also be probed with competitive sensitivity at fixed-target experiments in which a beam of energetic electrons or protons is directed at a fixed target, and downstream detectors search for evidence of DM produced from the electron-nucleon or proton-nucleon collisions. A variety of approaches are employed by different experiments to search for signatures of DM production. Some searches re-purpose neutrino detectors, such as MiniBooNE [63] and NOvA [64] at Fermilab, to directly detect any DM that may be produced in the collisions by means of DM-nucleon or DM-electron collisions with the detector material, placing additional shielding between the fixed target and the detector to reduce the background flux of neutrinos (see, for example, Refs. [65, 66]). Others such as NA64 [67] at CERN employ a fully hermetic detector to search for a $E_{\mathrm{T}}^{\mathrm{miss}}$ +X signature of DM in the downstream collision products.

Models of DM Production

Models of DM production in colliders can range in complexity from an effective field theory (EFT), where the DM production mechanism is completely unspecified, to a complete model such as supersymmetry, which predicts viable DM candidates as part of a hypothesized extension to the SM designed to address a range of phenomena unexplained by the SM (see Ref. [68] for a review of supersymmetric DM candidates).

In principle, complete theories of physics beyond the SM, such as the minimal supersymmetric SM (MSSM) (for a review, see [71]) can offer theoretically motivated and experimentally accessible models that specify the details of candidate processes by which the colliding partons may annihilate to produce DM. However, these theories

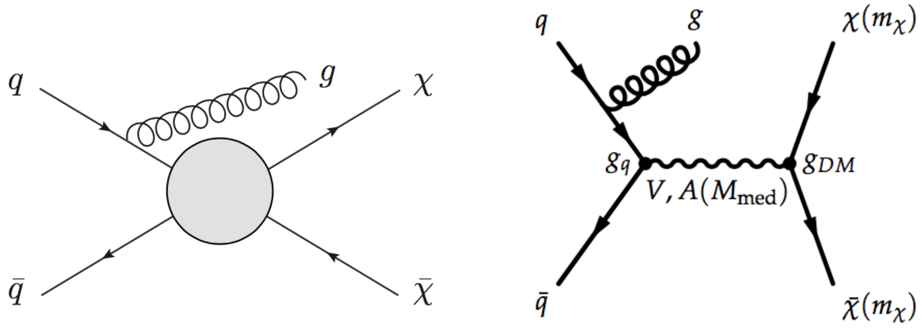

Figure 1.5: Left: $E_{\mathrm{T}}^{\mathrm{miss}}$ +jets process in the EFT framework (figure from © [69]). Right: $E_{\mathrm{T}}^{\mathrm{miss}}$ +jets process in a simplified model framework, where the pair production of DM occurs via a new vector or axial-vector (V, A) mediator of mass M_{med}, which couples to quarks and DM with coupling constants g_q and g_{DM}, respectively (figure from © [70])

.

tend to be quite complex, with many free parameters - over 100 in the case of MSSM - most of which need to be fixed to generate a reasonably testable model. Relying on complete theories alone to guide experimental signatures may run the risk of missing important parameter space of new physics for which a complete theory has not yet been developed.

Simplified models, widely used in recent and ongoing DM searches at the LHC (see, for example, the 2015 report of the ATLAS/CMS Dark Matter Forum [70]), are designed to bridge the gap between EFT and complete theories. They provide a "first-order" description of theoretically motivated new physics scenarios that could be accessible at collider energies. They provide guidance for experimental searches without fully specifying the details of any additional new physics at energies above the collider scale that would be needed for a complete theory. In terms of DM production at the LHC, one or more new "portal mediators" associated with new physics scenarios may be considered, which allow for mixing between SM particles and DM. The process by which the mixing occurs is represented with a tree-level diagram whose experimental signature would be accessible at LHC energies, such as the diagram shown in Figure 1.5, which represents a DM benchmark model featured in Ref. [70].

Many simplified models predict the so-called $E_{\mathrm{T}}^{\mathrm{miss}}$ +X final-state signature discussed above, in which the DM is produced in association with detectable SM particles (X). Depending on the details of the hypothesized DM production mechanism and the parameter ranges considered, different models can vary widely in terms of the identity and topology of the detectable final-state particles (X) predicted in $E_{\mathrm{T}}^{\mathrm{miss}}$ +X final states. Therefore, a broad-based program has been undertaken at the LHC to search for DM production in a variety of $E_{\mathrm{T}}^{\mathrm{miss}}$ +X final states to ensure maximal coverage of potential DM production scenarios. Results from a selection of recent DM searches in $E_{\mathrm{T}}^{\mathrm{miss}}$ +X final states can be found in Refs. [72, 5, 73, 74, 75, 76, 77, 78, 79].

The search presented in this thesis, which targets a final state of DM produced in association with a pair of W bosons ($E_{\mathrm{T}}^{\mathrm{miss}}$ +WW), is interpreted with the "Dark Higgs" simplified model [40] discussed in Chapter 2. Searches for DM at the LHC, interpreted in the context of this model, are sensitive to DM with mass in the range of ~ 100 GeV.

1.5 Summary of the Thesis

Following a brief introduction to the Standard Model (SM) of particle physics, this chapter presented multiple lines of evidence from observational astronomy for the abundance of DM in the universe, and for its hypothesized composition as one or more new particles beyond the SM. This was followed by a discussion of the ongoing worldwide effort to search for evidence of particle DM using particle detectors, and how the search presented in this thesis fits into the wider effort.

The following chapter discusses the "Dark Higgs" model that is used to interpret the search. Chapter 3 introduces the LHC machine and the ATLAS detector used to collect the particle collision data. Chapter 4 introduces the Monte Carlo method and its application to modelling the expected yields of events in the ATLAS detector, both from the Dark Higgs signal process and from known Standard Model processes that constitute a background in the search. The reconstruction and analysis of the ATLAS collision data is discussed in Chapter 5, and Chapter 6 presents the methods used to quantify the impacts of uncertainties from theoretical and experimental sources. Chapter 7 discusses the statistical framework used to interpret the results of the search. Chapter 8 presents the range of Dark Higgs model parameters excluded by the search. Chapter 9 concludes with a discussion of the experimental strategy and results.

Chapter 2

The Dark Higgs Model

The dark matter (DM) search presented in this thesis is motivated by and interpreted with the "Dark Higgs" (DH) model [40]. The DH model predicts a mechanism for DM production from proton-proton collisions at the LHC by means of portal interactions with the "dark sector". The dark sector, which is predicted as part of various BSM models, represents a collection of quantum fields and associated particles that are assumed to interact gravitationally, but which do not couple via any of the other known forces - electromagnetic, strong and weak - of the SM. Non-gravitational couplings between the dark sector and the SM proceed instead via one or more so-called "portal mediators".

In the DH model, the DM is a particle in the dark sector, and is produced from high-energy $q\bar{q}$ collisions at the LHC via a hypothetical spin 1 vector boson portal mediator referred to as the Z'. The model introduces an additional Higgs boson in the dark sector called the "Dark Higgs" (DH), which acts as a portal mediator by decaying to SM particles via a small mixing with the SM Higgs boson.

Figure 2.1 shows three Feynman diagrams, which illustrate some of the dominant modes by which the DH model could produce a measurable signature of DM production at the LHC. In all cases, the DM pair is produced via the Z' mediator, along with the emission of a DH boson s, which decays to a pair of SM particles.

2.1 Theoretical Motivation for the Dark Higgs Model

Given that the particles of the SM acquire mass via their interaction with the Higgs field [13, 14, 15], the existence of a hypothetical "Dark Higgs" (DH) field - and its associated particle the DH boson - is motivated by the need to likewise generate the masses of particles in the dark sector. More generally, the existence of so-called portal

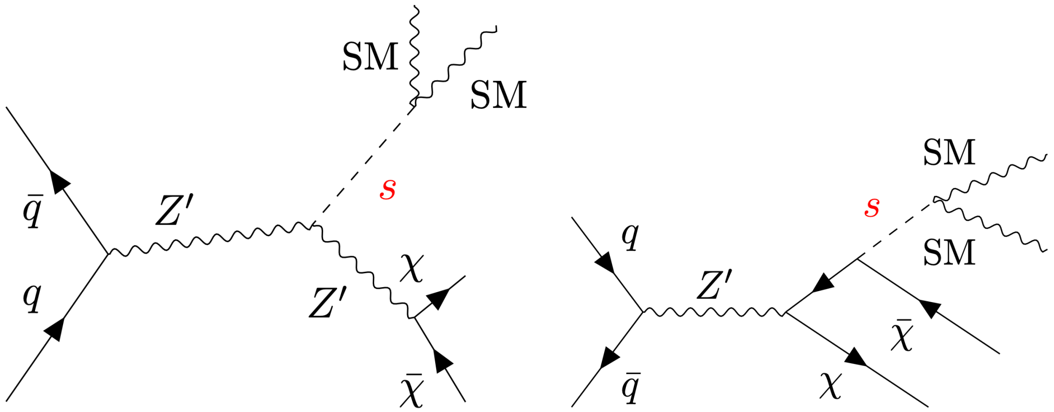

(a) s-channel (DH and DM emitted from the Z')

(b) s-channel (DM emitted from the Z', DH emitted from the DM)

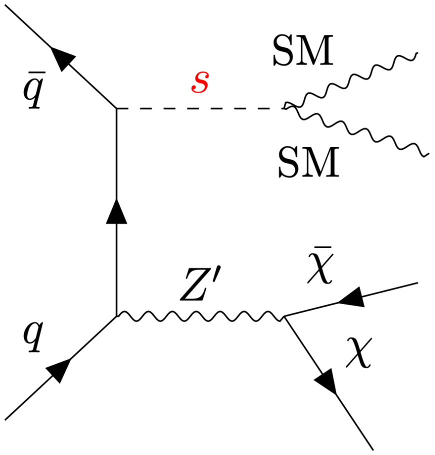

(c) t-channel (DH radiated off q, DM emitted from the Z')

Figure 2.1: Feynman diagrams with leading contributions to the cross section of hypothetical DM production at the LHC by means of the DH model.

mediators that enable interactions between dark sector and SM particles is motivated by theoretical arguments, discussed in Section 1.3.1, for the presence of thermal equilibrium between DM and SM particles in the early Universe, which would be established by creation and annihilation processes between particles in the two sectors. The present-day relic abundance of DM, set at the time of thermal freeze-out, places constraints on the details of these creation and annihilation processes. The hypothesized DH boson would open up a new mechanism for portal interactions between DM and SM particles. As discussed in the following section, this new mechanism allows for a relaxation of constraints from the DM relic abundance compared with simpler models in which portal interactions are limited to those mediated by a vector boson mediator (the so-called Z').

2.1.1 Constraints on Generic Z' Mediator Models

In addition to providing a mechanism by which particles acquire mass in the dark sector, the introduction of a new Higgs boson in the dark sector is motivated by strong theoretical and experimental constraints on the more generic simplified model in which portal interactions between the dark sector and the DM are mediated exclusively by the Z' vector boson mediator (see Ref. [80] for a review of the Z' portal mediator model, and Refs. [81, 82] for reviews of experimental constraints on the model). Removing the emission of the DH s from the contributing Feynman diagrams of the DH model in Figure 2.1 reduces all three to the generic "s-channel" mechanism by which SM particles would pair-annihilate to form DM via the Z' mediator, shown in Figure 2.2a.

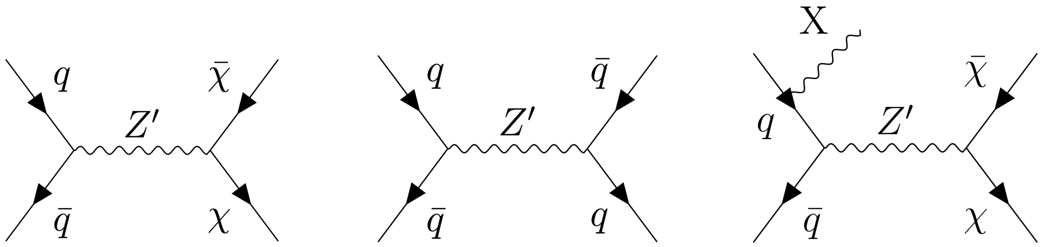

(a) Generic DM production (b) Dijet resonance (c) Mono-X signature

Figure 2.2: Signatures for DM production and detection via a Z' vector boson mediator at the LHC.

The Z' mediator model is probed at the LHC using either dijet resonance searches, which search for a signature of a Z' being created and subsequently decaying back into a pair of quarks as shown in Figure 2.2b, or with so-called "$E_{\mathrm{T}}^{\mathrm{miss}}$ +X" searches in which a SM particle "X" is emitted as initial state radiation from one of the colliding quarks, as shown in Figure 2.2c, to produce a signature of SM particles recoiling against missing transverse momentum due to the undetected DM pair.

Dijet resonance searches probe the model by searching for the presence of a resonant peak in the dijet invariant mass spectrum over the SM background of QCD-induced dijet events, where this above-background peak would be induced by the process in Figure 2.2b. Ref. [81] presents a statistical combination of several dijet searches that were performed with the ATLAS and CMS detectors, as well as an interpretations of the observed absence of any such above-background resonance peaks in the context of the Z' mediator model. It is found that for typical choices of the coupling strengths g_q (g_χ) between the Z' and quarks (DM), the model is excluded over a wide range of Z' masses (500 GeV $< m_{Z'} <$ 3 TeV) for nearly all DM masses up to 2 TeV, as shown in Figure 2.3a. A statistical combination of monojet searches performed by ATLAS and CMS, in which the radiated particle X in Figure 2.2c is a quark or gluon, is presented in Ref. [82]. As shown in Figure 2.3b, the monojet searches likewise exclude a large region of DM and vector boson mediator masses for a range of choices for the coupling constants g_q and g_χ.

2.1.2 Implications of a Dark Higgs Portal

The implications of introducing a new portal interaction mediated by a spin 0 boson (the DH) - which couples to the SM via a mixing with the SM Higgs boson - to the generic Z' mediator portal model are studied in detail by Duerr et al. in Ref. [39]. In this study, it is found that within various regimes of the coupling strengths and masses of the hypothetical particles - the Z', DH and DM - in this two-mediator model, referred to as the DH model, it is possible to relax or evade some of the constraints described above that are placed on the generic Z' mediator model by a combination of experimental results and the observed relic DM density in the Universe. As a result, in addition to providing a mechanism by which particles acquire mass in the dark sector, the DH also introduces new parameter space to the model that is not yet excluded by existing constraints. In particular, for $m_s < 2m_\chi$ and provided there are no other lighter particles in the dark sector, the only available decay route for the s is to SM particles via mixing with the SM Higgs, regardless of the mixing strength. In this case, the DM relic abundance is predominately set by the process $\chi\chi \rightarrow ss$

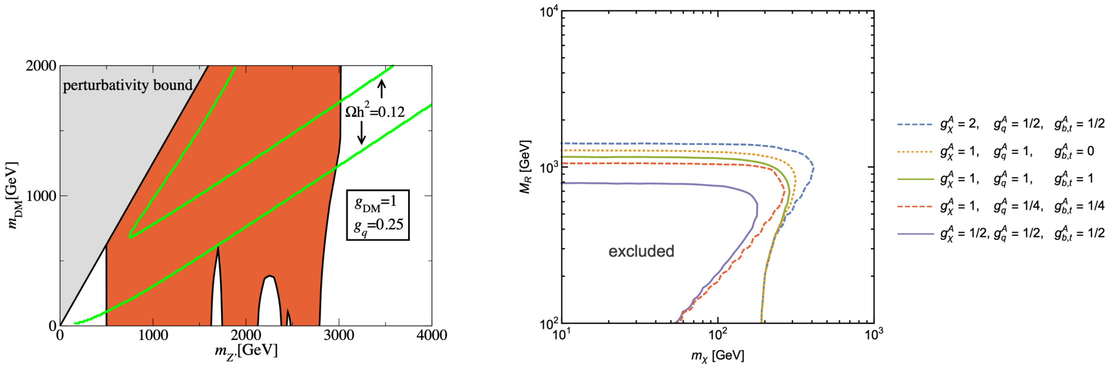

(a) Dijet resonance. Figure from © [81].

(b) Monojet. Figure from © [82].

Figure 2.3: Constraints on the masses of the Z' vector boson mediator (labelled $m_{Z'}$ in 2.3a and M_R in 2.3b) and DM (labelled $m_{\rm DM}$ in 2.3a and m_χ in 2.3b) from combined ATLAS and CMS dijet searches [82] (left) and monojet searches [82] (right). The results are shown for typical coupling choices of the Z' to DM ($g_{\rm DM}$ in 2.3a and g_χ^A in 2.3b), and of the Z' to quarks (g_q in 2.3a and g_q^A or $g_{b,t}^A$ in 2.3b, where $g_{b,t}^A$ specifies the coupling to heavy quarks, which may be 0 for models that prohibit heavy quark couplings). Green lines in 2.3a contain the region of $m_{Z'}$, m_χ that reproduces the observed relic density of DM in the Universe. In the grey region perturbative unitarity is violated.

followed by decays of s into SM particles, which allows for a significant relaxation of relic density constraints.

For various choices of m_χ, Duerr et al. [39] consider a range of m_s, $m_{Z'}$ and m_χ, and perform global scans over all other free parameters in the DH model (see Section 2.2 below), as shown in Figure 2.4, to identify regions in which the model has not yet been excluded by existing constraints. Particularly for $m_\chi \geq 200$ GeV, it is found that the model evades all existing constraints for a large region of m_s and $m_{Z'}$ (up to ~ 1000 GeV in m_s and up to ~ 2500 GeV in $m_{Z'}$).

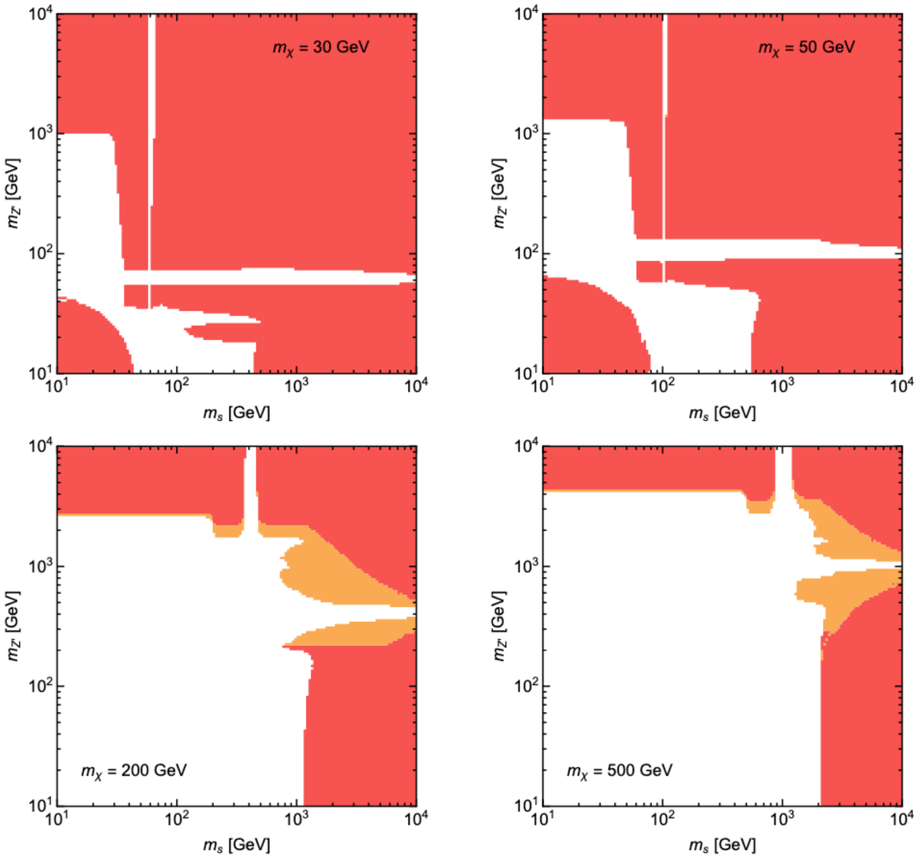

Figure 2.4: Global scans of the DH model, with Z' and DH as portal mediators, performed by Duerr et al. in Ref. [39]. The red shaded region is excluded for all possible combinations of couplings, while in the white region all constraints can be evaded. In the orange shaded region it is not possible to exclude large values of g_q corresponding to $\Gamma'_Z/m_{Z'} > 0.3$, where Γ'_Z is the decay width of the Z' mediator. Figure from © [39].

2.2 Model Description

The Dark Higgs (DH) model presented in Refs. [40] and [39] belongs to a wider class of simplified dark sector models, which hypothesize that DM interacts with particles of the SM via the exchange of one or more new mediators that act as so-called "portals" between the SM and the dark sector. Candidate portals are broadly categorized according to the portal mediator into vector-, neutrino-, Higgs- and axion-mediated portals (for reviews, see Refs. [83, 84], [85], [86] and [87], respectively). In the DH model, DM is assumed to be a Majorana fermion, which means that - like the photon, for example - it is its own antiparticle. The model postulates that DM interacts with the SM via both vector-mediated and Higgs-mediated portals.

A new gauge group called the U(1)', with an associated vector gauge boson referred to as the Z', is introduced as an extension of the SM gauge group presented in Chapter 1. Both the DM and the Z' are assumed to acquire their mass from a new Higgs field with vaccum expectation value w, which gives rise to a new physical Higgs boson, referred to as the DH boson s. The DM acquires an axial coupling to the Z', such that all three dark sector particles interact with one another.

The interactions of the U(1)' gauge group within the dark sector are expressed by the interaction Lagrangian (of which more details can be found in Appendix A of Ref. [39]):

$$\mathcal{L}_{U(1)'} = -\frac{1}{2} g_\chi Z'^\mu \bar{\chi}\gamma^5\gamma_\mu\chi - g_\chi \frac{m_\chi}{m_{Z'}} s\bar{\chi}\chi + 2g_\chi Z'^\mu Z'_\mu (g_\chi s^2 + m_{Z'} s) \tag{2.1}$$

Considering each term in $\mathcal{L}_{U(1)'}$ individually:

$$\mathcal{L}_{\chi,Z'} = -\frac{1}{2} g_\chi Z'^\mu \bar{\chi}\gamma^5\gamma_\mu\chi \tag{2.2}$$

describes the axial coupling between the DM χ and the Z', with coupling strength g_χ.

$$\mathcal{L}_{\chi,\mathrm{DH}} = -g_\chi \frac{m_\chi}{m_{Z'}} s\bar{\chi}\chi = -\frac{y_\chi}{2\sqrt{2}} s\bar{\chi}\chi \tag{2.3}$$

describes the coupling between the DM χ and the DH field S, where the associated coupling strength y_χ on the right-hand side of Eq. 2.3 has the following dependence on the masses and coupling strength of the DM and the Z': $y_\chi = 2\sqrt{2} g_\chi \frac{m_\chi}{m_{Z'}}$.

$$\mathcal{L}_{Z',\mathrm{DH}} = 2g_\chi Z'^\mu Z'_\mu (g_\chi s^2 + m_{Z'} s) \tag{2.4}$$

describes the interaction between the Z' and the DH field.

Motivated by models of gauged baryon number [40, 39, 88], the SM quarks are charged under the U(1)' gauge group, and as a result have vector couplings with the Z', which are described by the following interaction Lagrangian:

$$\mathcal{L}_{q,Z'} = -g_q Z'^{\mu} \bar{q}\gamma_\mu q \tag{2.5}$$

The quark-Z' coupling provides a mechanism for vector-mediated portal interactions between the SM and the dark sector. Axial vector couplings of the Z' to quarks would also be expected to produce a signature at the LHC, but are neglected in the model for simplicity [40].

The most general Lagrangian describing the scalar couplings of the SM Higgs h and the DH s is given by (see, for example, Ref. [89]):

$$\mathcal{L}_{\text{scalar}} = -\lambda_h\Big(H^\dagger H - \frac{v^2}{2}\Big) - \lambda_s\Big(S^\dagger S - \frac{w^2}{2}\Big) - \lambda_{hs}\Big(H^\dagger H - \frac{v^2}{2}\Big)\Big(S^\dagger S - \frac{w^2}{2}\Big) \tag{2.6}$$

where $H = \frac{1}{\sqrt{2}}(0, h+v)$ represents the SM Higgs field with vacuum expectation value v, and $S = \frac{1}{\sqrt{2}}(s+w)$ represents the DH field. The third term with coupling λ_{hs} mixes the DH and SM Higgs fields, such that the physical mass eigenstates h' and s' are a superposition of the scalars h and s:

$$\begin{pmatrix} h' \\ s' \end{pmatrix} = \begin{pmatrix} \cos\theta & \sin\theta \\ \sin\theta & \cos\theta \end{pmatrix} \begin{pmatrix} h \\ s \end{pmatrix} \tag{2.7}$$

where the “mixing angle” θ is related to SM and DH field couplings λ_h and λ_s and the vacuum expectation values v and w by:

$$\tan 2\theta = \frac{\lambda_{hs} v w}{\lambda_h v^2 - \lambda_s w^2} \tag{2.8}$$

Therefore, if the mixing between the SM and DH fields is nonzero ($\sin\theta > 0$), the physical Higgs eigenstate in the SM Lagrangian becomes $h\cos\theta + s\sin\theta$. This opens up the possibility for interactions between the physical DH and SM particles, with coupling strengths scaled by $\sin\theta$. For example, the decays of the DH to SM fermions f and vector bosons V are described by the following Lagrangians [39, 22]:

$$\mathcal{L}_{hf\bar{f}} = -g_{hf\bar{f}} \bar{f} f h \sin\theta \tag{2.9}$$

and

$$\mathcal{L}_{hVV} = -\delta_V g_{hVV} V_\mu V^\mu h \sin\theta \tag{2.10}$$

where (from SM physics):

$$g_{hf\bar{f}} = \frac{f}{v},\ g_{hVV} = \frac{2m_V^2}{v},\ \delta_W = 1,\ \delta_Z = \frac{1}{2} \tag{2.11}$$

2.2.1 Free Parameters in the Model

The free parameters in the DH model are as follows:

- $\mathbf{m}_\chi$: The mass of the DM particle χ.
- $\mathbf{m}_{\mathbf{Z'}}$: The mass of the hypothetical Z' boson in the dark sector, which mediates interactions between SM quarks q and the DM χ.
- $\mathbf{m}_\mathbf{s}$: The mass of the hypothetical DH boson, whose associated Higgs field provides a mechanism for particles in the dark sector to acquire mass, and which can decay to SM particles via a small mixing with the SM Higgs boson.
- $\mathbf{g}_\mathbf{q}$: Strength of the vector coupling between SM quarks and the Z' boson.
- $\mathbf{g}_\chi$: The coupling strength between DM and the Z' boson.
- θ: The mixing angle between the DH and the SM Higgs boson. The coupling strength associated with the decay of the DH to SM particles scales with $\sin\theta$.

Some of these parameters are already constrained by other results. Mixing between the DH and the SM Higgs in the model would introduce unobservable decay modes of the SM Higgs to dark sector particles, which would modify the yield of events observed at the LHC in which a Higgs boson is produced from the SM expectation. Given the agreement between the observed yield and the SM expectation [90, 91], an upper limit of $|\sin\theta| < 0.25$ can be placed (assuming that no other appreciable unobservable decay channels exist), as discussed in Section 4.2.1 of Ref. [92].

Dijet resonance searches, discussed in Section 2.1.1, also place upper bounds on the coupling strength g_q of the Z' to SM quarks by searching for a resonant peak in the dijet spectrum associated with the scenario shown in Figure 2.2b in which a Z' is produced by high-energy $q\bar{q}$ collisions at the LHC, and decays immediately back to a pair of quarks. Based on the agreement with SM predictions observed in the most recent dijet resonance searches performed by the ATLAS and CMS experiments, [93, 94, 95, 96] upper bounds on g_q ranging from 0.04 to 0.4, depending on $m_{Z'}$, have been established. Figure 2.5 shows upper bounds on g_q from two recent dijet searches, one of which (Figure 2.5a) uses “trigger-level jets” [94] to boost sensitivity in the low-$m_{Z'}$ range.

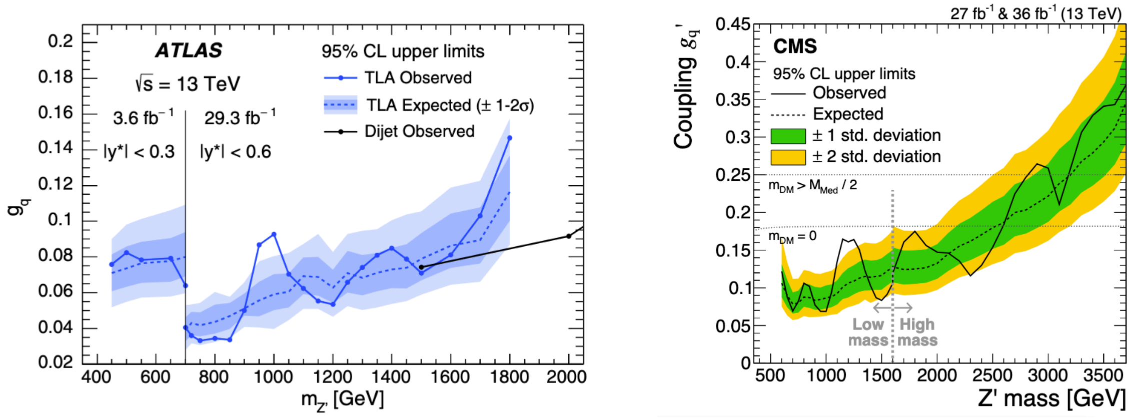

(a) Limits from ATLAS low-mass dijet resonance search [94]. Black solid line shows observed limits from a previous dijet resonance search [97]. Limits for $m_{Z'} < 700$ GeV are obtained using a subset of ATLAS data collected with non-standard trigger (see Ref. [94] for details). Figure from © [94].

(b) Limits from a recent CMS dijet resonance search [95]. The high-mass (low-mass) region is performed with $m_{jj} > 1.25$ TeV ($m_{jj} > 0.49$ TeV). See Section 5.1 of Ref. [95] for details pertaining to the horizontal dotted lines. Figure from © [95].

Figure 2.5: Upper bounds on the g_q coupling between the Z' and quarks, as reported by recent dijet resonance searches performed by ATLAS (left) and CMS (right).

2.3 Search for the Dark Higgs Model at the LHC

For certain choices of the model parameters discussed in Section 2.2.1, the DH model predicts a unique and measurable signature by which it could be detected at the LHC. This LHC signature, of which some of the most contributing Feynman diagrams are shown in Figure 2.1, would occur when a q in one of the colliding protons pair-annihilates with a $\bar{q}$ in the other proton to produce a Z', which subsequently decays to DM. A DH s is emitted either from an initial-state q or from the Z' mediator, and subsequently decays to a pair of SM particles. This produces a final state with the SM products from the s decay recoiling against $E_{\mathrm{T}}^{\mathrm{miss}}$ in the detector due to the undetected

DM pair. In particular, assuming that the Z' is relatively low in mass compared with the centre of mass energy of the $q\bar{q}$ collision, the Z' may be imparted with a large momentum (a.k.a. boost). As a result, the diagrams shown in Figures 2.1a and 2.1b in which the s is emitted from the Z' can produce highly boosted, collimated SM decay products. These boosted SM decay products make the signature distinct from typical $E_{\mathrm{T}}^{\mathrm{miss}}$ +X final states in which the SM products ('X') recoiling against the DM are assumed to be produced exclusively as initial state radiation, as in Figure 2.1c.

2.3.1 Dark Higgs Decay Channels

As discussed in Section 2.2, since the DH decays to SM particles via mixing with the SM Higgs boson, its decay mechanisms - including the branching fractions for its decay channels to various SM particles - would be analogous to that of the SM Higgs. As a result, the signature of boosted SM decay products recoiling against $E_{\mathrm{T}}^{\mathrm{miss}}$ may be used to probe various ranges of m_s in the model depending on the particular choice of SM products (a.k.a. "decay channel", or simply "channel") from the s decay that the search targets. Figure 2.6 shows the branching fraction that the SM Higgs - and consequently the DH s - would be expected to have to SM particles if its mass were allowed to float in the SM. For low m_s, the decay to $b\bar{b}$ is dominant. At $m_s \approx 160$ GeV, the decay to WW becomes kinematically accessible[1], and is the dominant s decay channel for $m_s \gtrsim 160$ GeV. The decay to ZZ also becomes kinematically accessible at $m_s \approx 180$ GeV, though its branching fraction remains sub-dominant compared with the WW decay channel. The decay to SM Higgs bosons $s \to HH$ opens up at $m_s \approx 250$ GeV, and for $m_s > 250$ GeV the branching fraction for this HH decay channel becomes appreciable, though still smaller than the WW channel. This suggests that searches in all four of these s decay channels could complement one another to collectively probe the full available m_s range, as summarized in Table 2.1.

2.3.2 Completed and Ongoing Searches for the Dark Higgs Model

The search presented in this thesis is one of several ongoing and completed searches for the DH model at the LHC, which target different decay channels of the DH after it is emitted in the model's LHC signature, of which some of the most contributing Feynman diagrams are shown in Figure 2.1.

---

[1] A particular decay mode $X \to YY$ generally becomes kinematically accessible for $m_X > 2m_Y$, because in this regime the on-shell parent particle X has a sufficient rest mass energy to decay to the daughter products YY while satisfying energy conservation.

Table 2.1: Summary of DH decay channels to SM particles that could be targeted to probe various m_s ranges in DH model.

$\mathbf{m_s}$ Range	**Sensitive DH Decay Channels**
$m_s < 160$ GeV	$s \to bb$
160 GeV $< m_s <$ 180 GeV	$s \to WW$
180 GeV $< m_s <$ 250 GeV	$s \to WW$, $s \to ZZ$
$m_s > 250$ GeV	$s \to WW$, $s \to ZZ$, $s \to HH$

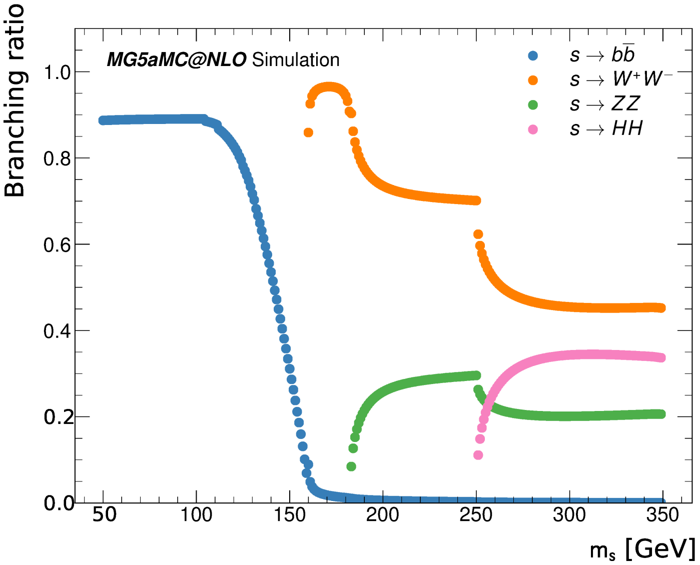

Figure 2.6: m_s dependence of the branching fraction for decays of the DH boson to SM particles. The branching fractions of the $s \to WW$ and $s \to ZZ$ decay channels experience a drop-off at $m_s = 2m_H (= 250$ GeV), above which the decay to $s \to HH$ to SM Higgs becomes kinematically accessible. Note that the branching fraction for $s \to WW$ decays is only simulated for $m_s \geq 160$ GeV, but remains appreciable ($\gtrsim 0.1$) for $m_s \gtrsim 120$ GeV. Figure from © [98].

Model Parameters Probed by LHC Searches

Given the number of parameters in the DH model, computational resource limitations make it impractical to scan over all parameters when performing dedicated searches for the model at the LHC. Therefore, in the search presented in this thesis - and in all other searches for the model performed to date at the LHC - the coupling constants and mixing angle θ are fixed as follows:

- $g_q = 0.25$
- $g_\chi = 1$
- $\sin\theta = 0.01$

The choice of $\sin\theta = 0.01$ is well within the range $|\sin\theta| < 0.25$ required by measurements of the SM Higgs - see above discussion in Section 2.2.1. The values of the coupling constants g_χ and g_q are chosen to be consistent with other searches performed at the LHC for dark sector benchmark models [99] involving a Z' mediator, which facilitates comparisons with these existing searches. It is worth noting that the choice of $g_q = 0.25$ is in fact ruled out in the approximate range 500 GeV $< m_{Z'} <$ 3000 GeV by the recent dijet searches discussed above in Section 2.2.1. However, the choice of $g_q = 0.25$ is maintained in this search because it is considered important to maintain consistency with other searches performed with this benchmark choice. In particular, it allows for the search results to be easily compared with other searches for the DH model, which used the same parameter choices. It is also worth noting that the computational procedure required to interpret the analysis with an arbitrary BSM physics model has been preserved and automated in the RECAST framework [3]. Using this framework, it should be straightforward to re-interpret the search results in the future, if needed, for a DH model with alternative choices of the fixed parameters.

In the search for the DH model presented in this thesis, the DM mass m_χ is fixed to 200 GeV, consistent with the choice used by the other two published searches for the DH model [98, 100] performed by the ATLAS collaboration. This choice of $m_\chi = 200$ GeV was found in early sensitivity studies undertaken by the search in the $s \to WW(q\bar{q}q\bar{q})$ channel [100] to predict a relatively large measurable yield of events in the ATLAS detector from the DH process, which allows the searches to probe a large range of the remaining model parameters relative to other m_χ choices. The recently-published search by the CMS collaboration in the $s \rightarrow WW(\ell\nu\ell\nu)$ channel [101] considered four candidate m_χ: 100, 150, 200 and 300 GeV.

The mediator masses m_s and $m_{Z'}$ are left as floating parameters in the searches. The m_s range covered by the search depends on the range to which the s decay channel considered in each search is sensitive on the basis of the predicted branching ratios in Figure 2.6, as summarized in Table 2.1. In addition, the sensitivity of searches for the DH model using this boosted SM+$E_{\mathrm{T}}^{\mathrm{miss}}$ signature drops off sharply for $m_s > 2m_\chi$, because in this m_s range the decay mode $s \rightarrow \chi\chi$ becomes kinematically accessible, and the radiated s would be expected to decay predominantly via this invisible channel, rather than to visible SM particles via mixing with the SM Higgs.

The available $m_{Z'}$ range to which these searches may be sensitive covers the approximate range of 500 to 3500 GeV. This range is bound from above by the fall-off in cross section for producing such a massive Z' mediator from $q\bar{q}$ collisions at the LHC. The production rate of the model begins to fall off quite rapidly for $m_{Z'}$ below $\sim$ 500 GeV due to the minimum virtual mediator mass required to produce to a pair of 200 GeV DM particles (in addition to radiating the DH as shown in the contributing Feynman diagrams in Figures 2.1a and 2.1b).

$s \rightarrow bb$ Channel

The $s \rightarrow bb$ decay channel was probed by the search presented in Ref. [98]. The search used the RECAST framework [3] to re-interpret an earlier DM search [102], which targeted a signature of DM produced in association with a Higgs boson decaying to b quarks, in the context of the DH model. This re-interpretation was possible because the model that was used to optimize and interpret the original search, for which the most contributing Feynman diagram is shown in Figure 2.7a, is very similar in structure to the DH model, and predicts the same final state of a boosted $b\bar{b}$ pair recoiling against $E_{\mathrm{T}}^{\mathrm{miss}}$ in the detector. As shown in Figure 2.7b, this re-interpretation was able to place upper limits on the $m_{Z'}$ in the DH model ranging from $\sim$ 2000 GeV to 3200 GeV, with the given choices of coupling strengths and $\sin\theta$, for m_s in the range 50 GeV $< m_s <$ 150 GeV.

There is also a dedicated search in the $s \rightarrow bb$ channel under development within the ATLAS collaboration. In addition to optimizing the search strategy to maximize sensitivity to the DH model, this search also plans to improve upon the earlier search performed in the $s \rightarrow bb$ channel by scanning over additional model parameters such

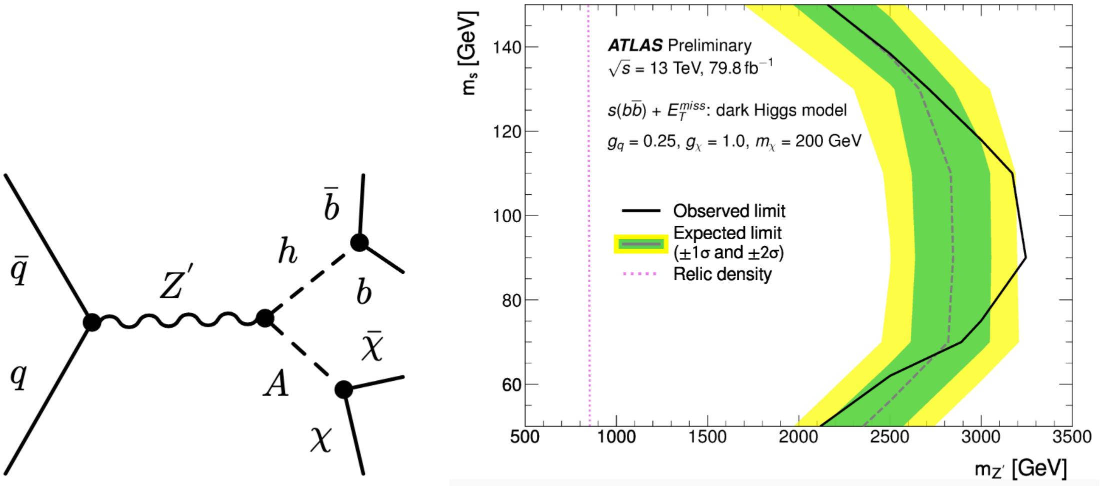

(a) Figure from © [102].

(b) Figure from © [95].

Figure 2.7: Left: Most important Feynman diagram for the original DM search [102] that was re-interpreted in Ref. [98] to probe the DH model in the $s \to bb$ channel. Figure from © [102]. Right: Exclusion limits on the mediator masses m_s and $m_{Z'}$ in the DH model from the search in the $s \to bb$ channel. Values of m_s and $m_{Z'}$ to the left of the solid black line are excluded by the search. The dashed pink line reproduces the relic density of DM observed in the Universe for the choices of coupling constants $g_\chi = 1$ and $g_q = 0.25$ used in the search. Figure from © [98].

as g_q and m_χ that were fixed in the earlier search, targeting values for these parameters that would maximize the sensitivity of the search to the DH model while reproducing the observed relic abundance of DM in the Universe.

$s \to WW$ and $s \to ZZ$ Channels

The $s \to WW$ and $s \to ZZ$ ($s \to VV$) channels, which collectively dominate the branching fraction of s decays for $m_s > 160$ GeV, are somewhat more complex in terms of their final state in the detector compared with the $s \to bb$ channel. This is because, whereas the $b\bar{b}$ pair in the latter decay channel produce a characteristic signature of either two distinct b-tagged jets[2] or one two-pronged large-radius jet[3] in the calorimeter, the vector bosons in the $s \to WW$ and $s \to ZZ$ final states can decay via several possible channels, which leads to a number of distinct final states in the detector for these $s \to VV$ channels. For this reason, a number of different LHC searches in the $s \to VV$ channels have been completed or are ongoing, each of which targets only a subset of the VV decay channels.

Table 2.2 summarizes the available decay channels for the WW and ZZ final states, as well as the branching fraction of each channel and information regarding any completed or ongoing efforts to search for the DH model in each VV decay channel. Figure 2.8 shows the range of mediator masses ($m_s, m_{Z'}$) that are excluded, for $m_\chi = 200$ GeV, by completed searches performed by ATLAS in the $s \to VV(q\bar{q}q\bar{q})$ channel [100], and by CMS in the $s \to WW(\ell\nu\ell\nu)$ channel [101]. As would be expected on the basis of the branching fractions in Figure 2.6, these searches exclude parameter space roughly in the range $m_s > 160$ GeV. The search presented in this thesis, which covers the $s \to WW$ decay channel in the semileptonic final state ($WW \to q\bar{q}\ell\nu$), complements these existing searches, and extends the excluded range of m_s and $m_{Z'}$.

---

[2] See Section 5.1.2 for a description of the method used to tag jets in the calorimeter as having originated from a b quark.

[3] see Section 3.4.2 for more details on hadronic jets in the calorimeter

Table 2.2: Summary of decay channels for WW and ZZ pairs and their branching fractions.

Decay channel	**Branching fractions [22] (from WW or ZZ pair)**	**Search effort(s)**
$WW \to q\bar{q}q\bar{q}$	0.45	ATLAS published search: Ref. [100]
$ZZ \to q\bar{q}q\bar{q}$	0.49	
$WW \to q\bar{q}\ell\nu$ ($\ell = e$ or μ)	0.29	This thesis
$ZZ \to q\bar{q}\ell\ell$ ($\ell = e$ or μ)	0.094	Ongoing within ATLAS collaboration
$ZZ \to q\bar{q}\nu\nu$	0.14	N/A (expected sensitivity too low)
$WW \to \ell\nu\ell\nu$ ($\ell = e$ or μ)	0.046	CMS published search: Ref. [101]. Effort also ongoing within ATLAS collaboration.
$ZZ \to LLLL$ ($L = \ell$ or ν)	0.071	N/A (expected sensitivity too low)

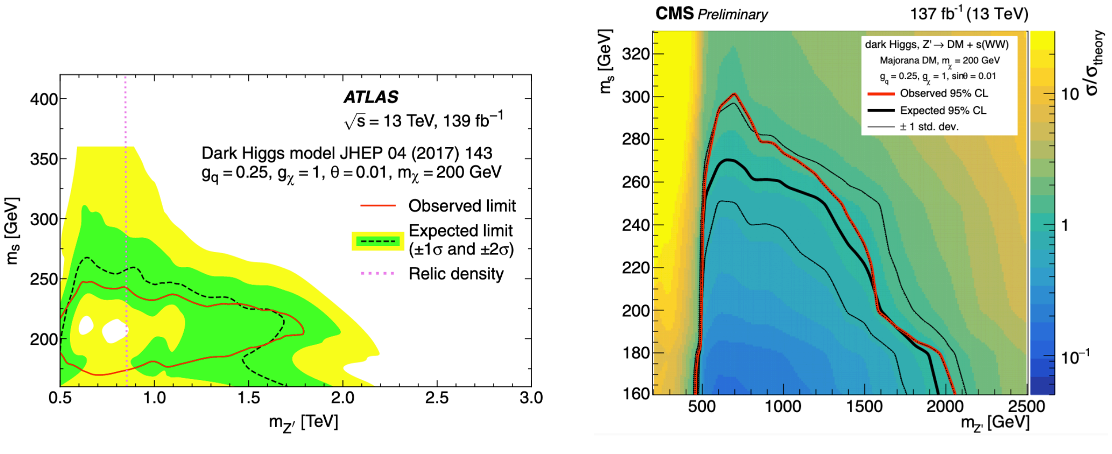

(a) Exclusion limits from search in $s \to VV(q\bar{q}q\bar{q})$ channel. Figure from © [100].

(b) Exclusion limits from search in $s \to WW(\ell\nu\ell\nu)$ channel. Figure from © [101].

Figure 2.8: Range of $(m_s, m_{Z'})$ in the DH model excluded by searches performed by ATLAS in the $s \to VV(q\bar{q}q\bar{q})$ channel (left), and by CMS in the $s \to WW(\ell\nu\ell\nu)$ channel (right), for the following choices of remaining parameters in the model: $g_q = 0.25$, $g_\chi = 1$, $\sin\theta = 0.01$, $m_\chi = 200$ GeV.

Chapter 3

Introduction to the LHC and the ATLAS Detector

The Large Hadron Collider (LHC) [52] is a circular proton-proton (pp) collider, which resides in a 27 km tunnel near the European Organization for Nuclear Research (CERN). Superconducting magnets are used to accelerate counter-rotating bunched proton beams to near the speed of light, and direct the beams into head-on collisions at four interaction points around the ring. The collisions take place at a world-leading centre of mass energy of up to 13 TeV. Each interaction point is surrounded by a detector, which measures the energetic debris of particles produced by the high energy collisions to perform precision measurements of the SM and search for new physics.

The large 13 TeV centre of mass energy of the collisions makes it possible for the colliding proton constituents, known as "partons", to pair annihilate and subsequently produce massive unstable particles such as the Higgs boson, which cannot presently be produced by any other experimental means. Experiments at the LHC can study hypothetical models of physics beyond the SM ("BSM physics") by searching for evidence of the production of the massive particles involved in these models from their subsequent decay to SM particles.

The LHC collides protons at an approximate rate of 1 billion collisions per second, $\sim$100 times higher than the proton collision rate at the Tevatron collider [103], which operated from 1983-2011 and collided protons and anti-protons ($p\bar{p}$) at a peak centre of mass energy of 1.8 TeV. Over several years of data-taking, the high collision rate at the LHC has enabled experiments to collect rich data sets. The large data sets can be used to probe new phenomena in highly selective final states.

3.1 The Parton Model

Before discussing *pp* collisions at the LHC in detail, it is important to first introduce the parton model, which describes the substructure of protons involved in the collisions.

The proton has an internal structure comprised of constituent quarks, antiquarks and gluons - collectively known as “partons” - and their interactions (for a review of the parton model and its applications, see [104]). When a proton collides with another particle in particle colliders such as the LHC, the probability density $f(x, Q^2)$ that a particular species of parton, for example a quark with “up” flavour u, will be involved in the collision is a function of both the fraction x of the proton’s momentum carried by the parton, and the squared momentum scale Q^2 of the collision. Detailed parametrized models of the parton distribution function (PDF), such as MSHT20 [105] have been developed using combined fits to data from deep inelastic scattering (DIS) experiments at proton colliders. MSHT20 PDF models at Q^2 of 10 GeV^2 and 10^4 GeV^2 are shown in Figure 3.1.

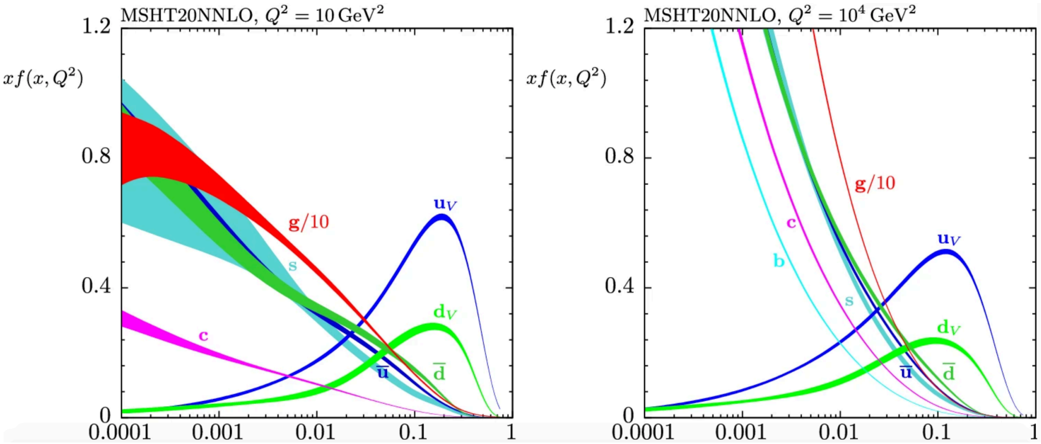

Figure 3.1: Parton distribution functions, with respect to the proton momentum fraction x carried by the parton, modelled with MSHT20 at $Q^2 = 10$ GeV^2 and 10^4 GeV^2. Figure from © [105].

Based on the PDFs shown in Figure 3.1, u and d quarks carry the highest probability density for parton momentum fractions above ∼10%, with the u carrying approximately double the probability density of the d. These dominant quarks are known as the proton’s “valence” quarks, of which there are two u and one d, and they carry the proton’s quantum numbers.

3.2 Decay Processes from Parton Collisions

As discussed in Section 1.1.3, each process by which colliding partons may annihilate to form observable products proceeds with a certain cross section σ, which is related to the production rate $\frac{dN}{dt}$ of the process by the beam luminosity $\mathcal{L}$:

$$\frac{dN}{dt} = \mathcal{L}\sigma \tag{3.1}$$

Figure 3.2 shows a summary of cross sections for the production of SM particles - or particle combinations (eg. "Wt" represents the production of a W boson along with a top quark) - from pp collisions at the LHC, as measured by the ATLAS detector.

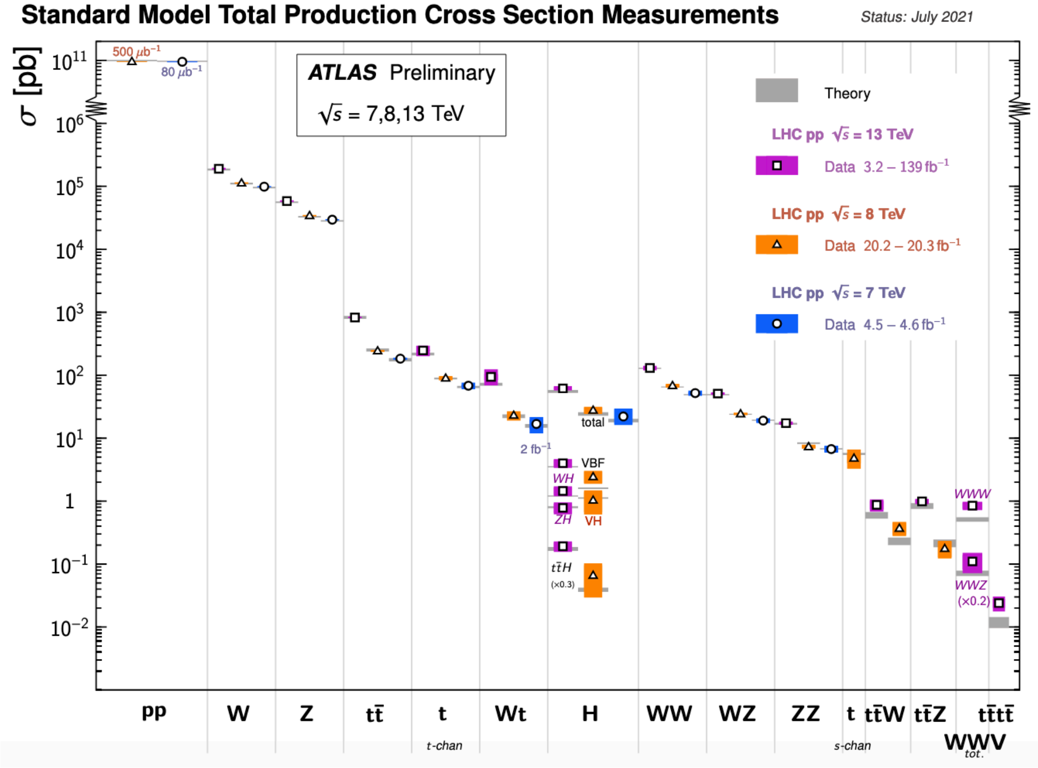

Figure 3.2: Summary of SM cross sections for particle production processes measured by the ATLAS detector. Figure from © [106].

3.2.1 Branching Fractions and W Boson Decays

Unstable particles produced by the parton collisions will subsequently decay to less-massive particles, typically with multiple possible mechanisms, also known as "channels", by which the decay can occur. Each such channel has an associated "branching fraction", which quantifies the relative probability with which the decay will proceed by the given channel. The search presented in this thesis focuses on DM production in association with a pair of oppositely-charged W bosons. Figure 3.3 shows the two W boson decay routes. Due to energy and momentum conservation, W bosons can only decay to a pair of particles whose combined mass is smaller than the W mass. Charge conservation additionally requires that the decay products have a combined charge equal to that of the parent W boson. These two requirements allow the W to decay either "hadronically" to a quark-antiquark pair with one up-type quark/antiquark (U) and one down-type (D), or "leptonically" to a charged lepton (L) and a neutrino (ν).

(a) Hadronic decay mode (b) Leptonic decay mode

Figure 3.3: W boson decay mechanisms.

3.3 Detectors at the LHC

The DM search presented in this thesis uses data collected from the ATLAS (A Toroidal LHC ApparatuS) detector [53]. ATLAS is one of four particle detectors at the LHC, which are designed to measure the energetic debris of particles produced by high energy particle collisions to perform precision measurements of the SM and search for new physics using the resulting particle collision data. This section briefly introduces each of the four particle detectors at the LHC, and what each contributes to the LHC physics programme.

The two largest, **ATLAS** (A Toroidal LHC ApparatuS) [53] and **CMS** (Compact Muon Solenoid) [54], are both general-purpose detectors designed to record all SM decay products from the collisions, with the exception of neutrinos, which pass through due to their very low interaction cross sections. Thanks to their near-complete detection of decay products, data from these detectors can be used to study a wide range of physics processes resulting from the collisions, including both measurements of the SM and searches for new physics beyond the SM. By taking a general-purpose approach, rather than specializing in the study of one particular collision or decay process, these experiments seek to maintain sensitivity to the broadest possible range of particle processes, in the hopes of allowing physicists to detect and measure new physics processes in whatever form they may take. While the physics goals of these two detectors are very similar, they are accomplished using different detector designs and technologies, and as such they are able to produce complementary physics results.

The Large Hadron Collider beauty (LHCb) detector [55] is designed to measure heavy quark (b and c) decays resulting from pp collisions. Precise measurement of heavy quark decays are of particular interest for the study of CP violation in the SM, and in the search for potential sources of CP violation beyond the SM. Rather than providing full coverage of all collision products, the LHCb detector is comprised of a series of sub-detectors that provide "forward angle" coverage to detect particles produced with a large boost along the direction of one of the two proton beams. This forward region is of particular interest for measurements of heavy quark decays, because this is the angular region in which heavy quark pairs are predominantly produced by high-energy collisions.

A Large Ion Collider Experiment (ALICE) [107] is designed to measure the products of heavy-ion collisions produced during special LHC runs in which the proton beams are replaced by Pb beams, which are collided at a centre of mass energy of 5 TeV. The high-energy Pb collisions produce a sufficiently high temperature and density to form an unbound state of quarks and gluons known as "quark-gluon plasma" that would have occurred in the early universe. The study of this exotic state could give novel insights into the theory of quantum chromodynamics[1], including the phenomena of quark colour confinement and chiral-symmetry restoration (for reviews, see Refs. [108, 109]).

3.4 Introduction to the ATLAS detector

The ATLAS detector [53], shown schematically in Figure 3.5, is the largest detector by volume to have been built at any particle collider, with a length of 44 m and a height of 25 m, constituting a total weight of approximately 7,000 tonnes. The tremendous amount of detector material is needed to absorb and measure the highly energetic decay products of the pp collisions with sufficient resolution to enable a detailed reconstruction of the particles involved and their kinematic properties. Such a

---

[1] The theory of quantum chromodynamics (QCD), introduced in Section 1.1.6, describes interactions that proceed via the strong force.

complete and detailed reconstruction of the collisions and subsequent decay processes enable physicists to carry out the impressive range of physics goals shared by the ATLAS and CMS collaborations. These goals include precision measurements of the SM, which profit both from the enormous collision rate, and from the large centre of mass collision energy that enables on-shell production of all known SM particles. The detector is also designed to be sensitive to as wide a range of new physics signatures as possible. Particular emphasis was placed on designing the detector to be sensitive to the anticipated production modes of the Higgs boson, which was jointly discovered by the ATLAS and CMS collaborations in 2012 [6, 7].

The detector provides full 4π coverage around the pp interaction point, with the exception of the beam pipe. It consists of several layers of sub-detectors, each of which is specialized for recording specific kinematic information and particle types.

The ATLAS detector is described spatially using the standard coordinate system of (x, y, z) coordinates and $(\theta,\ \phi)$ angles shown in Figure 3.5b. The origin of the coordinate system is placed at the nominal interaction point of the colliding proton beams, and the z axis lies along the beam line. The angle of a particle or detector component in the plane transverse to the beam line is given by the angle ϕ, and its angle relative to the beam line is given by θ. The "pseudorapidity" η is a quantity related θ according to:

$$\eta = -\ln\left[\tan\left(\frac{\theta}{2}\right)\right] \tag{3.2}$$

Pseudorapidity is often used rather than θ because differences $\Delta\eta$ in pseudorapidity are invariant under Lorentz boosts along the z axis.

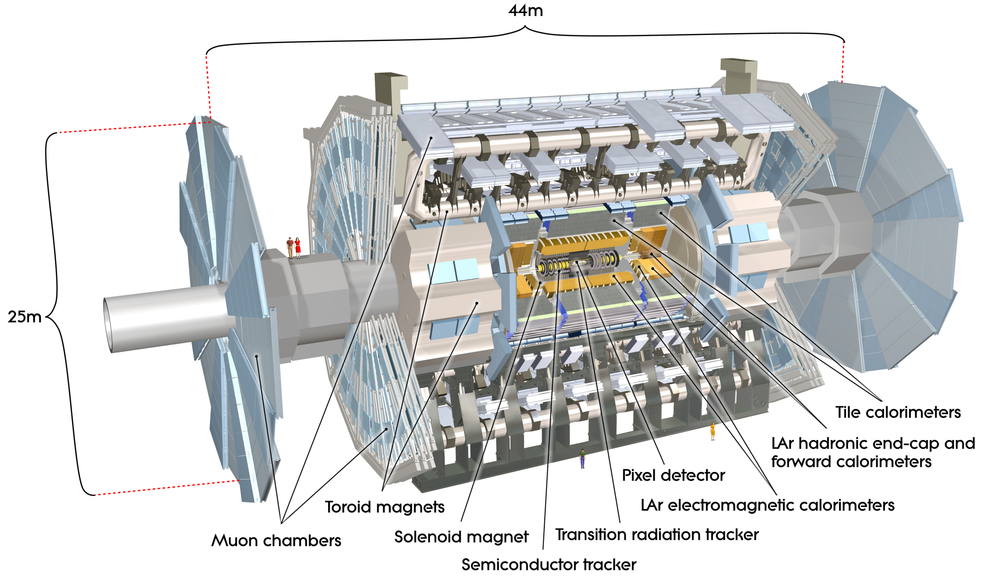

Figure 3.4: Schematic diagram of the ATLAS detector. Figure from © [53]

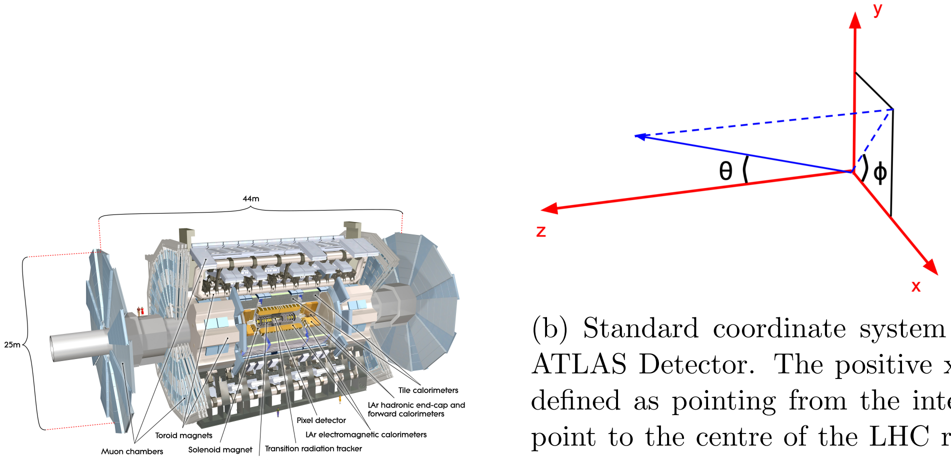

(a) ATLAS Detector

(b) Standard coordinate system for the ATLAS Detector. The positive x-axis is defined as pointing from the interaction point to the centre of the LHC ring and the positive y-axis is defined as pointing upwards.

Figure 3.5: Left: Schematic diagram of the ATLAS detector (figure from © [53]). Right: Standard coordinate system used for the ATLAS detector.

.

The ATLAS sub-detectors are described in some detail in the following sections.

3.4.1 The Inner Detector

The inner detector (ID) [110], located nearest the beam pipe, is specialized for charged particle tracking. It is immersed in a 2T magnetic field oriented parallel to the beam pipe, which bends the trajectories ("tracks") of electrically charged particles as they pass through the field. Three distinct but complementary high-resolution tracking technologies are employed along with pattern recognition tools to map the trajectories of charged particles passing through the ID. The tracking is accomplished with as little material as possible in the ID, such that the particle trajectories can be mapped with minimal scattering and energy loss before they reach the calorimeters.

Tracks from the inner detector are reconstructed by assembling clusters of "hits" in channels of the ID tracking layers. The reconstructed tracks are a critical component of vertex reconstruction, and the degree of bending and direction of the bent tracks at the production vertex provide information about the momentum, charge, and identity of the charged particles that produced them.

3.4.2 The Calorimeters

The calorimeter is designed to measure the energy of all particles that pass through it by initiating cascades of secondary particle production in the high-density detector material known as "showers", and fully absorbing the energy of each shower. The only particles that cannot be absorbed by the calorimeter are muons and neutrinos, which pass through without showering. The calorimeter is divided into two sub-detectors, the electromagnetic and hadronic calorimeters. Both are "sampling calorimeters", which means they are comprised of repeated layers of dense absorbing material with "sampling" layers in between. The sampling layers track the location of the shower and record a small fraction of its energy, to which a calibration factor is applied to infer the full shower energy.

The Electromagnetic Calorimeter

The electromagnetic (EM) calorimeter forms the inner calorimeter layer, and is designed to fully absorb and measure the energies of electrons, positrons and photons. Energy is primarily deposited in the lead absorbing layers in the form of EM showers [111], in which the initial electron or photon interacts via bremsstrahlung with the absorbing material to produce a cascade of photon radiation and electron pair production (see, for example, Ref. [112] for a review of the physics of EM and hadronic showers). The sampling layers are filled with liquid argon (LAr), which absorbs relatively little energy compared with the lead absorbing layers due to its lower density. Ionization is produced when a charged particle passes through the LAr [113] layer, which drifts through an electric field generated by a high voltage placed between absorber plates and readout electrodes on either end of the LAr layer to produce a triangular current pulse [114].

Candidate EM showers are reconstructed into clusters from energy deposits in calorimeter cells using a "seed-cluster" algorithm described in Ref. [115]. The seed-cluster algorithm works by dividing the $\eta \times \phi$ space of the EM calorimeter into a grid of $\eta \times \phi = 0.025 \times 0.025$ solid angle elements called "towers". For each such element, the energy detected in all calorimeter layers that lie within the given patch of solid angle is summed to form the energy of the tower. A sliding window algorithm of size 3×5 towers is used to construct the energy clusters that constitute EM clusters from localized energy deposits.

Reconstruction and selection of electron candidates is performed with the use of a complex matching algorithm (details of which can be found in Section 5 of Ref. [115]) to match candidate reconstructed tracks in the ID with EM clusters in the calorimeter based on their proximity in $\eta \times \phi$ space. This matching is complicated by the fact that electrons may radiate photons via bremsstrahlung in the ID prior to reaching the calorimeters. The radiated photons can subsequently decay into an electron-positron pair, which themselves can generate tracks in the ID. As a result, it is possible to reconstruct multiple tracks in the ID, all originating from the same electron, and match these tracks to EM clusters in the calorimeter. In case several tracks in the ID can be matched to the same EM cluster, the track considered to be associated with the primary electron is selected by an algorithm that accounts for, among other quantities, the number of hits in the ID and the distance in (η, ϕ) between the extrapolated track position in the calorimeter and the barycentre of the EM cluster.

Reconstructed objects selected as electron candidates are subsequently passed through a likelihood-based electron identification algorithm, described in detail in Section 6 of Ref. [115], which uses as a discriminant the ratio

$$d_L = \frac{L_S}{L_S + L_B} \tag{3.3}$$

where the likelihood function $L_S(B)$ is a product of signal (background) PDFs for various quantities related to the reconstructed object such as track conditions, details of the track-cluster matching, and reconstructed EM shower widths for the EM cluster in various layers of the EM calorimeter. The signal S is "prompt" electrons, which originate from the primary interaction, and the background B is a combination of jets that mimic prompt electron signatures, electrons from photon conversions in the detector and non-prompt electrons originating from hadron decays.

The Hadronic Calorimeter

As discussed in Section 1.1.1, the vast majority of collision events that occur in the ATLAS detector ultimately result in the production of quarks and gluons. Due to the phenomenon of colour confinement, quarks and gluons cannot exist in isolation, and immediately "hadronize" to form colour-neutral combinations of quarks called "hadrons". As these hadrons pass through the detector, they eventually undergo a showering process similar in principle to the EM showers described in Section 3.4.2. In the case of these "hadronic showers", the shower is initiated by the strong interaction of a hadron with the detector material to produce a cascade of secondary hadrons (see, for example, Ref. [112] for a review of the physics of EM and hadronic showers). Unlike the EM showers, which proceed exclusively via electromagnetic interactions, hadronic showers proceed via both the strong and EM interactions, where the EM interactions are primarily induced by electromagnetic decays of neutral pions (π^0) [112]. Because hadronic showers involve strong interactions, they are in general much more complex in terms of the variety of particles and mechanisms involved in the showering, and as a result are in general more variable and less localized compared with EM showers.

The hadronic calorimeter surrounds the EM calorimeter, and is designed to fully absorb and measure hadronic showers. The primary hadrons that initiate these hadronic showers generally pass through the EM calorimeter without showering due to their relatively long interaction length [53]. The hadronic calorimeter is comprised of a tile calorimeter, which encircles the EM calorimeter barrel, and a LAr calorimeter with copper and tungsten absorbers in the end-cap region that encloses the two ends of the barrel. The tile calorimeter uses steel as the absorber material and scintillators read out by photomultiplier tubes (PMTs) in the sampling layers.

Hadronic showers are reconstructed as "jets" using clusters of energy deposited in the hadronic calorimeter cells (for a review of jet reconstruction and calibration with the ATLAS detector, see [116]). The jets can be reconstructed using a variety of different reconstruction algorithms depending on the use case.

Most jet reconstruction algorithms use clusters of topologically connected calorimeter cells known as "topo-clusters" as basic building blocks for jet reconstruction. Topo-clusters are designed with the goal of extracting significant signals of energy deposition originating from energetic hadrons from the background of detector noise and other sources of fluctuation in the calorimeter cells. Candidate clusters are formed from "seed cells" in which the deposited energy E is $E > S\sigma_{\text{cell}}$, where σ_{cell} is the average noise for the given cell and S is the "seed threshold" significance, set to 4 by default [117]. Cluster construction proceeds by collecting neighbouring cells with energy $E > N\sigma_{\text{cell}}$, where N is the "growth threshold", set to 2 by default. If a neighbouring cell passes the $E > N\sigma_{\text{cell}}$ requirement, its neighbours will also be added to the cluster if their energy significance exceeds the growth threshold, and this process repeats until there are no remaining neighbouring cells with significance above the growth threshold. Lastly, one set of neighbouring cells that satisfy $E > P\sigma_{\text{cell}}$ are added to the cluster, where p is the "principal cell filter", set to 0 by default.

Jets are reconstructed from these topo-clusters using the anti-k_t clustering algorithm described in Ref. [118] in a cone with an angular radius R in (η, ϕ) space, given by:

$$R = \sqrt{\eta^2 + \phi^2} \tag{3.4}$$

The jet radius R determines the angular radius within which the anti-k_t algorithm will include calorimeter deposits in the vicinity of a topo-cluster or a set of topo-clusters and attempt to group the energy deposits into jets. Different choices of R can be used in the algorithm depending on the identity and kinematics of the shower parent particle(s) that one is interested in reconstructing [116]. Jets produced by quarks and gluons that either originate from different parent particles, or whose shared parent particle has a relatively low momentum in the lab frame (a.k.a. "low boost"), generally have sufficient angular separation that they can be individually reconstructed using relatively small radius parameters such as $R = 0.2$ or $R = 0.4$.

Jets that originate from boosted massive particles, such as the hadronically decaying W boson in the search presented in this paper, generally contain two or more significant topo-clusters (a.k.a. "prongs") in close angular proximity, each having been induced by the hadronization of a strongly interacting daughter particle produced by the hadronic decay of the massive parent particle. In this latter case, the angular proximity of these significant topo-clusters can make it challenging to usefully reconstruct them as individual small-radius jets due to the resulting jet overlap. In these cases, it may be more useful to capture all the decay products in a single jet reconstructed with a larger radius parameter such as $R = 0.8$ or $R = 1.0$, such that the resulting large-radius jet fully reconstructs the massive parent particle. Methods such as the TAR algorithm [2] employed in this analysis are subsequently applied to the reconstructed large-radius jet to obtain useful jet sub-structure information, including the likely number of prongs contained within the jet.

3.4.3 The Muon Spectrometer

The muon spectrometer [119] surrounding the calorimeter is specialized for tracking muons and measuring their momentum. It employs the same principle used in the inner detector of applying a strong magnetic field and measuring the resulting bent trajectories of the electrically charged muons passing through to infer their momenta. Details of muon reconstruction and identification using the ATLAS muon spectrometer can be found in Ref. [120].

The magnetic field is generated by rectangular superconducting “toroid magnets” arranged azimuthally in radial planes around the beam axis, which set up a toroidal field concentric to the beam axis. In the region containing the strong field established by the toroid magnets, muon tracks are recorded by three cylindrical layers of muon tracking chambers in the barrel region and three layers of chambers arranged in wheels perpendicular to the beam axis in the end-cap region. Additional layers of fast trigger chambers deliver muon track information to the ATLAS trigger system (see Section 3.4.5) so it can be incorporated into the event readout decision.

Precise measurements of muon track coordinates are provided by monitored drift tubes (MDTs) in the barrel region, which cover a pseudorapidity range of $|\eta| < 2.0$), and by cathode strip chambers (CSCs) in the end-cap region ($2.0 < |\eta| < 2.7$). The CSCs are designed to withstand the relatively high flux of energetic particles that bombard the detector in the end-cap region. These MDTs and CSCs measure track coordinates with nominal resolutions of 60 μm and 80μm, respectively, in the magnetic bending plane [120].

High precision tracking is needed both to achieve the design performance goal of reconstructing muon transverse momenta with at most 10% resolution for 1 TeV tracks [53], and to distinguish prompt muons that originate from the primary interaction from the background of non-prompt muons that arise from secondary interactions in the detector. Reconstruction and identification of prompt muons is performed by combining tracking information from the muon spectrometer and the inner detector, along with energy deposition measurements from the calorimeters. Various muon reconstruction strategies are employed, which attempt to match tracks between the muon spectrometer and the inner detector, or to match inner detector tracks with calorimeter deposits [120].

3.4.4 Missing Transverse Momentum

Many signatures of hypothesized processes involving physics beyond the SM - including the DH model considered in this thesis - involve the production of particles that would pass through the ATLAS detector without being detected due to their extremely low interaction cross section with SM particles. Similarly, neutrinos produced in weak interactions will also pass undetected for the same reason.

The law of momentum conservation, which requires the vector sum of momenta of all measured particles produced by a collision to match that of the initial state quarks, can be used to infer the presence of undetected particles in the collision. Because the fraction of proton momentum carried by each of the initial state quarks - described by the PDFs presented in Section 3.1 - is statistical in nature, the momenta in the direction of the pp beam line cannot be known precisely. However, initial state quark momenta in the plane transverse to the beam line are in general negligibly small compared with the collision energy, so it can be expected to a high degree of precision that the final state particle momenta in this transverse plane will sum to zero. This expectation implies that collision events that produce undetected particles with an appreciable momentum in the transverse plane can be expected to exhibit a signature of high missing transverse momentum in the final state.

This two dimensional missing transverse momentum vector for a collision event is typically denoted “$\vec{E}_{\mathrm{T}}^{\mathrm{miss}}$ ”, and its magnitude “$E_{\mathrm{T}}^{\mathrm{miss}}$ ”. A detailed description of $E_{\mathrm{T}}^{\mathrm{miss}}$ reconstruction with the ATLAS detector can be found in Section 3 of Ref. [121]. The components of $\vec{E}_{\mathrm{T}}^{\mathrm{miss}}$ lie in the transverse (x, y) plane of the detector, and are given by:

$$E_{x(y)}^{\mathrm{miss}} = -\sum_{i} p_{x(y),i} \tag{3.5}$$

where the sum is over all fully reconstructed electrons, muons, photons, hadronically-decaying tau leptons and jets (a.k.a. "hard objects"), and additionally over all other detector signals that were recorded as part of the event, but were not used as part of the construction of the hard objects (a.k.a the "soft term").
$\vec{E}_{\mathrm{T}}^{\mathrm{miss}}$ and $E_{\mathrm{T}}^{\mathrm{miss}}$ are constructed from the components $E_{x(y)}^{\mathrm{miss}}$ as follows:

$$\vec{E}_{\mathrm{T}}^{\mathrm{miss}} = (E_x^{\mathrm{miss}}, E_y^{\mathrm{miss}}) \tag{3.6}$$

$$E_{\mathrm{T}}^{\mathrm{miss}} = |\vec{E}_{\mathrm{T}}^{\mathrm{miss}}| = \sqrt{(E_x^{\mathrm{miss}})^2 + (E_y^{\mathrm{miss}})^2} \tag{3.7}$$

3.4.5 The Trigger System

The majority of collision events in the ATLAS detector result in "soft quantum chromodynamics" (soft QCD) interactions, which proceed via the strong force and produce only quarks and gluons with a relatively low momentum in the lab frame - and hence are referred to as "soft" - and which do not result in the production of any high-mass ($\mathcal{O}$(GeV)) particles. Figure 3.5 compares the overall cross section of all interactions resulting from pp collisions with the cross sections of processes that produce various massive SM particles. The overall collision cross section is ∼6 orders of magnitude larger than the highest cross section for producing a massive particle, namely that of the W boson. The soft QCD interactions that dominate the total cross sections are in general not of interest for the ATLAS physics programme. It would be impossible to process and save all collision events produced in the ATLAS detector, as the massive flux of these soft QCD interaction events would very quickly overwhelm the bandwidth of the data acquisition system and fill up the available offline data storage capacity.

The ATLAS trigger [122] is designed to efficiently select a tiny minority of collision events to be read out, processed and saved to offline storage (a.k.a. "recorded") based on a set of criteria applied to preliminary event information from the sub-detector. The criteria are designed to select for signatures from the sub-detectors that are considered likely to represent processes that will be of interest to the various analyses that study the data either to measure parameters of the SM, or to search for evidence of BSM physics.

The trigger system is divided into a hardware-based "first level trigger" (L1 trigger) and software-based "high-level trigger" (HLT), which collectively select events at an average rate of ∼1000 Hz from the total collision rate of 40 MHz [122]. Events must be accepted by both the L1 trigger and the HLT in order to be recorded.

The L1 trigger is based on candidate objects identified within regions of interest ("RoIs") defined by their η and ϕ ranges. Candidate objects are divided into muons, EM calorimeter clusters, jets in the hadronic calorimeter and taus. In addition, the sums of missing transverse momentum ($E_{\mathrm{T}}^{\mathrm{miss}}$) and total energy are also constructed. Hardware level trigger decisions are designed using combinations of these reconstructed objects and sums. Events that pass the L1 trigger are subsequently processed by the HLT. The L1 trigger is designed to form the "trigger decision" of whether to reject the event or accept it for processing by the HLT within at most 2.5 μs per event [122].

Thanks to the reduction in event rate by the L1 trigger selections, the HLT is able to use software-based algorithms to produce more complex reconstructions of the candidate objects and sums compared with the L1 trigger, and can apply more sophisticated selections on these objects. The HLT trigger decision is typically formed within 300 ms per event [122]. Objects reconstructed and considered in the HLT trigger decision include muons measured by the muon spectrometer, electrons, photons, jets, $E_{\mathrm{T}}^{\mathrm{miss}}$ and tau leptons.

The L1 trigger and the HLT each have their own "trigger menu", which represents the compilation of all sets of selection criteria, or "triggers", that are considered for each event. Any event that satisfies the criteria of any of the triggers in the trigger menu is kept. Both the L1 trigger and the HLT trigger menus include both triggers applied to individual objects, such as the "$E_{\mathrm{T}}^{\mathrm{miss}}$ trigger" or the "photon trigger", as well as triggers applied to combinations of different objects.

Importantly for the analysis presented in this thesis, the $E_{\mathrm{T}}^{\mathrm{miss}}$ that is reconstructed for each event by the L1 trigger and the HLT is based on calorimeter measurements, which register very little energy deposition from muons, and does not incorporate the momenta of muons detected by the muon spectrometer. As a result, in cases where the majority of $E_{\mathrm{T}}^{\mathrm{miss}}$ in the event is recoiling against one or more energetic muons, the $E_{\mathrm{T}}^{\mathrm{miss}}$ reconstructed for the triggers will underestimate the actual $E_{\mathrm{T}}^{\mathrm{miss}}$ in the event due to the absence of muon momentum information. Because this analysis includes many events with an energetic muon in the final state, it was found that requiring events to have passed the $E_{\mathrm{T}}^{\mathrm{miss}}$ trigger as part of the analysis selections removes some events with energetic muons in the final state that would have passed the other event selections. These analysis selections include a stringent lower bound on the offline-reconstructed $E_{\mathrm{T}}^{\mathrm{miss}}$, which accounts for muon momenta. The solution, presented in more detail in Section 5.3, was to additionally allow for events that pass the “single muon” trigger.

Chapter 4

Modelling of Signal and Background Processes

To search for evidence of new physics in the ATLAS data, it is necessary to develop an accurate model of the expected yield of both SM events (a.k.a. "background") and hypothesized BSM events (a.k.a. "signal") in the data, as well as their kinematic distributions. The yields and kinematic distributions of events in the data are then compared with those in the signal and background models to check for any "above-background" significant excesses in the data that could point to the presence of BSM physics. If no significant excesses are observed, the search can exclude the signal model over the range of parameters for which the model predicts a significant above-background excess in the data.

4.1 Introduction to the Monte Carlo Method

Like many collider experiments, the ATLAS collaboration uses the "Monte Carlo" (MC) method to model the expected yield and kinematic distributions of SM and hypothesized BSM events in the data collected by the detector. The MC method is a computational algorithm that uses repeated sampling of random variables, where each set of randomly sampled variables represents a randomly generated "event".

To simulate the predicted behaviour of any given process using the MC method, a parametric model for the process is needed. The parametric model receives as input a set of variables associated with a single event (eg. kinematic information describing the partons involved in a high-energy parton-parton collision at the LHC, prior to the collision), and predicts the values of all variables of interest for the event after it has undergone the process being modelled (eg. the energy and momentum of the massive particle that would be produced from the parton-parton collision for a given particle production process). The MC method proceeds as follows: for each randomly generated event, the random variables associated with the event are passed into the model to produce a resulting set of output variables. For physical models, one is particularly interested in the set of "observable" output variables, meaning those that can be measured experimentally in the modelled system. Given a set of these so-called "MC simulated events", the associated set of values for each observable, which were generated by passing the events through the model, represents a random sampling of the underlying probability density distribution for that observable according to the model. The method is useful for complex models with many free parameters, for which it would be unfeasible to develop analytical formulations of the distributions of observables predicted by the model.

The MC simulated events can then be binned into histograms in one or more observables. Assuming that, for each event, the sampling of random variables is performed "independently" - i.e. in a manner such that the sampling of random variables for each event is unaffected by that of any other event - the number N_i of events in each bin i will vary randomly according to Poisson statistics with, on average, a standard deviation of $\sigma_{N_i} = \sqrt{N_i}$. Consequently, as the number of MC simulated events is increased by a factor of α, the relative size $\frac{\sigma_{N_i}}{N_i}$ of fluctuations in each bin will, on average, decrease according to $\frac{1}{\sqrt{\alpha}}$. As a result, as one increases the number of MC simulated events, the shapes of histograms binned in the model's observables for the simulated events will become an increasingly precise approximation of the underlying probability distributions for these observables according to the model.

4.2 Monte Carlo Simulation of Events in the ATLAS Detector

Signal and SM background models used to perform searches for BSM physics with the ATLAS detector are produced using sophisticated MC simulation of both the passage of the final-state particles through the ATLAS detector and of the physical production mechanisms for the particle collision, production and decay processes involved. For a given process, "truth-level" information for each MC simulated event generated to simulate the process is first obtained from a random proton-proton collision by simulating the physical production mechanism for the process. An example of such a process would be the dominant W+jets SM background in this DM search, shown in Figure 4.3a.

The set of simulated final state particles, along with their kinematic information, are collectively known as the "truth-level" event. Truth-level events can subsequently be passed through a highly detailed simulation of the ATLAS detector [123] produced using the Geant4 toolkit [124], which models how these events would actually be measured by the detector at this so-called "reconstruction-level". ATLAS requires very large MC generated data sets (millions of simulated events per process) to adequately model the predicted probability distributions for kinematic observables over their full range of interest for the SM measurements and BSM searches that use the ATLAS data.

4.2.1 Use of Alternative MC Generators

ATLAS uses various MC simulation packages (also known as "generators") to perform truth-level MC simulation of different physics processes. For many processes, particularly SM background processes, independent MC simulations have been performed using several different packages, and the yields and distributions of events predicted by the different packages can be compared to evaluate a systematic uncertainty associated with the choice of generator used to simulated the process. The specific generators used to model the physics processes considered in this search will be discussed in Sections 4.3 and 4.4.

4.2.2 Weighting and Normalization of MC Simulated Processes

Given a set of MC simulated events for a given process, it is often necessary to apply multiplicative "weights" to the simulated events in order to correct their distributions and amplitude before comparing with the measured data. The weights are designed to modify the amount that a given event contributes to the amplitude of the bin to which it is assigned when the MC simulated events are binned into histograms. Rather than simply summing the number of simulated events that fall into a given bin, the simulated amplitude, or "yield", of each bin is evaluated instead as the sum of event weights w for all events that fall into the bin:

$$\text{simulated yield in bin } k = \sum_{\text{event } i \text{ in bin k}} w_i \tag{4.1}$$

The weights are broadly categorized into "event-level" weights and "scaling factors". Event-level weights may differ between one event and the next, and are designed to modify the shapes of simulated yield distributions in one or more observables to better represent their expected distributions in the measured data. These shape modifications may be motivated by a variety of factors, such as to account for data-taking conditions that were not known or incorporated at the time of simulation. Individual sources of event-level weights for processes simulated in the ATLAS detector are discussed in more detail in Section 4.2.2 below.

After applying event-level weights to correct the shapes of the distributions, scaling factors are applied identically to all the events generated for a given process. The scaling factors are designed to scale the total simulated yield of events such that it matches the total number of events that are expected to have been produced by the simulated process in the actual measured data set.

Weighting of MC Simulated Events of Particle Collision Processes

Event-level weights are applied to events generated by the MC method to model particle collision and decay processes in the ATLAS detector. For a given process, the overall event-level weight applied to each event is a product individual weights arising from various sources:

$$\begin{aligned}\text{event-level weight } i = (\text{generator weight})_i \times (\text{pileup reweighting weight})_i \times \\ \times \prod_j (\text{reconstruction weight j}) \end{aligned} \tag{4.2}$$

The “generator weight” is a weight applied by some generators during the generation of truth-level events for various purposes. These purposes may include correcting for the generation of duplicate events at various stages of the calculation and correcting leading-order calculations to achieve the expected distributions that a more precise “next-to-leading-order” calculation would be expected to produce.

The “pileup reweighting weight” is designed to account for the effects of “pileup” (see Ref. [125] for a description of the methods currently used to model pile-up in the ATLAS detector). Due to the oscillatory electric fields used to accelerate protons in the counter-rotating LHC beams, protons in the beams do not form a continuous stream of particles, but are instead concentrated into regularly-spaced “bunches” in the longitudinal beam direction [126]. Superconducting magnets are used to direct proton bunches in the counter-rotating beams into head-on collisions, known as “bunch crossings”, at the centre of the ATLAS detector. Pileup constitutes the soft QCD collision events that take place in the same (or closely-surrounding) bunch crossings as the “hard interaction” that actually triggered the event readout. The nominal procedure of simulating the “hard interactions” that would produce the process being modelled does not account for the presence of these pileup interactions that would be measured by the detector as part of the readout for the triggered event.

To correctly model the actual pileup conditions during data-taking, the soft QCD collision events that constitute these pileup interactions are either simulated or collected from actual LHC collisions as so-called “zero-bias data”[1] (see Refs. [128] and [127], respectively, for recent discussions of these alternative pileup modelling methods). Each simulated hard interaction event is then overlaid with a variable number of the simulated pileup events, and the hard interaction and pileup events are weighted to produce the distribution of pileup events in the data. Since the MC simulated datasets were in many cases produced before or during data-taking, it is necessary to reweight the MC simulated events using the so-called pileup reweighting weight such that the distribution of pileup events accurately reflects the actual pileup distribution during the data-taking. To do so, the full ATLAS data-taking period is divided into “luminosity blocks”, and the average rate of pileup interactions is measured within each such luminosity block. MC simulated events are then associated with specific luminosity blocks. The pileup reweighting weights are evaluated for MC simulated events within each luminosity block to match the pileup rate in the simulated events to the average pileup rate measured during the associated data-taking period.

The “reconstruction weights” collectively refer to weights assigned to apply corrections to quantities such as data-driven measurements of efficiency or resolution associated with the reconstruction of objects such as electrons, muons and jets that are produced in the simulated passage of events through the ATLAS detector.

Scaling Distributions for Comparison with Data

In addition to the event-level weights described in Section 4.2.2 above, scaling factors are applied to each signal and background process such that the predicted yield of events per bin in the MC simulated distributions for each process properly predicts the actual yield of events expected in the ATLAS data based on the integrated luminosity of the collected data set.

---

[1] Zero-bias data is collected using a dedicated trigger, which fires one LHC turn after a high-p_{T} L1 trigger fires [127]. This method ensures that the rate at which the zero-bias events are triggered is proportional to the instantaneous luminosity of the collisions. Since no other triggers are applied, the event readout for this zero-bias data is expected to be representative of the pileup background conditions.

Sum of Weights Normalization

While the event-level weights can adjust the shapes of distributions of MC simulated events to match those expected in the data, the sum of these weights does not in general have any particular physical significance, and depends on the number of events that were simulated. Prior to scaling the sum of weights to the predicted yield in the data, it is therefore necessary to first normalize the sum of weights to unity by dividing by the sum over all event weights for the process:

$$\text{event-level weight (normalized) } i = \frac{\text{event-level weight } i}{\sum_j \text{event-level weight } j} \tag{4.3}$$

where the index j runs over all MC simulated events for the given process.

Scaling to Expected Data Yield

As discussed in Section 3.2, the total predicted yield N of events for a given process of particle production and decay initiated by a proton-proton collision in the LHC is given by the total integrated luminosity:

$$N = \sigma \int_{t_1}^{t_2} \mathcal{L}(t)dt = \sigma \mathcal{L}_{\text{int}} \tag{4.4}$$

where $\int_{t_1}^{t_2} \mathcal{L}(t)dt$ is the integrated beam luminosity over the full data-taking period from t_1 to t_2 and σ is the cross section for the process, which quantifies the rate at which the proton-proton collisions will produce events via the process for a given beam luminosity $\mathcal{L}$.

Therefore, the final step in weighting the MC simulated events for comparison with data is to scale all the normalized weights in Eq. 4.3 by the product of the cross section σ for the given process and the integrated ATLAS luminosity $\mathcal{L}_{\text{int}}$ such that they sum to the total predicted yield N of events for the process:

$$\text{event-level weight (normalized, scaled) } i = \big[\text{event-level weight (normalized) } i\big] \times \sigma \times \mathcal{L}_{\text{int}} \tag{4.5}$$

The following calculation confirms that summing all event weights in Eq. 4.5, and combining with 4.3 and 4.4 produces the total predicted yield N for the given process:

$$\sum_i \text{event-level weight (normalized, scaled) } i = \frac{\sum_i \text{event-level weight } i}{\sum_j \text{event-level weight } j} \times \sigma \times \mathcal{L}_{\text{int}}$$
$$= \sigma \mathcal{L}_{\text{int}} = N \quad (4.6)$$

4.2.3 Comparing Data and MC Simulation to Search for New Physics

With the MC simulated data properly weighted and normalized as described in Section 4.2.2 above, event selections are applied to both data and MC simulated events based on their final-state observables, such as the identity, momenta and directions of final-state particles measured by the detector. The selections, which are discussed in more detail in Section 5.2, are designed to define one or more regions of the data, known as "signal regions" within which the MC simulation of the signal process predicts a relatively large yield of the hypothesized BSM process compared with the MC prediction of SM background processes. Within each signal region, the data and MC simulated events may be additionally binned in one or more final-state observables, and the resulting distributions of ATLAS data are compared with those of the total MC simulated SM background yields to check for any significant yield excesses or shape differences in ATLAS data that could be indicative of new physics.

4.3 Simulation of the DH Signal Model

The DH signal model presented in Chapter 2 is simulated using a program called MadGraph 5 [129][2], which generates proton-proton collision events and calculates the matrix element at leading order to produce events associated with the Lagrangian for a given process. The Lagrangian for the DH signal model is encoded in MadGraph, with the coupling constants g_q, g_χ, the mixing angle θ, and the DM mass m_χ fixed to the values specified in Section 2.2.1. The DH and Z' masses m_s and $m_{Z'}$ are left as floating parameters in the search. Therefore, MC simulated data sets are generated over a grid of m_s and $m_{Z'}$. The grid was designed to cover masses for which the search is expected to be reasonably sensitive to the model. Figure 4.1 shows the m_s and $m_{Z'}$ masses for which MC simulated data sets were generated for the DH signal process.

---

[2] MadGraph5_aMC@NLO 2.7.2 (ATLAS, LCG) [130] is the particular version of MadGraph 5 used to generate the MC simulated signal events used in this search.

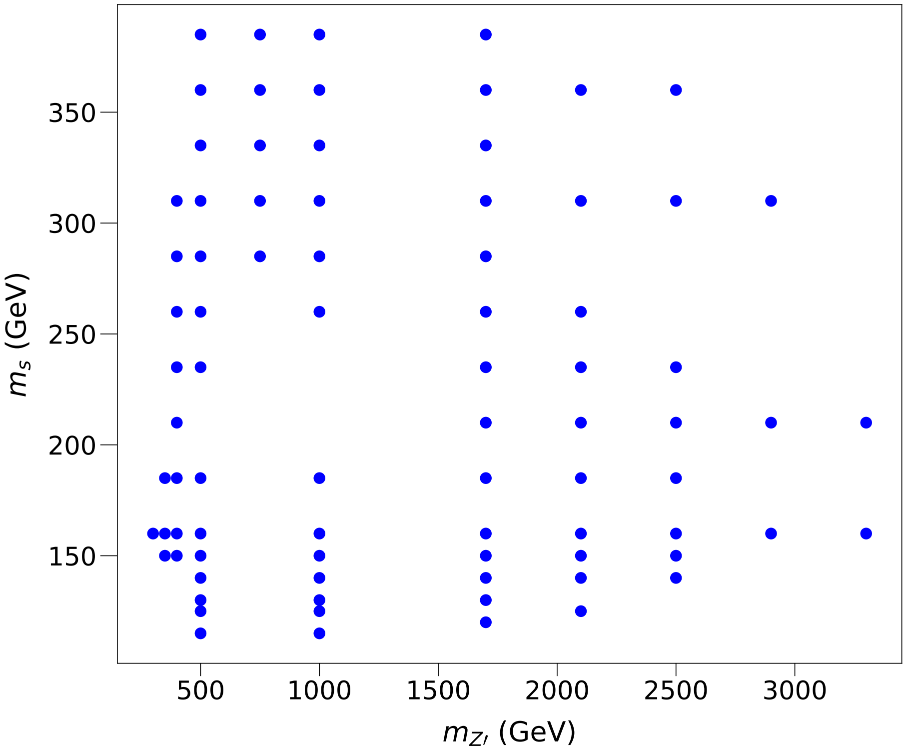

Figure 4.1: Grid of produced signal samples with different choices of $m_{Z'}$, m_s and the other parameters fixed to $g_q = 0.25$, $g_\chi = 1.0$, $m_\chi = 200$ GeV, $\theta = 0.01$.

As discussed in Chapter 2, the signal model considered in this search produces two final-state partons from the $s \to WW(qq\ell\nu)$ decay. MadGraph also includes production mechanisms in the matrix element calculation for which up to one additional parton is radiated in the final state. These final-state partons initiate cascades of radiation produced by QCD processes, which are modelled using the Pythia8 [3] [131] program.

4.4 Simulation of SM Background Processes

The selection criteria applied to final-state observables in the ATLAS and MC simulated events are designed to define signal regions, which contain events that exhibit the final-state signature of the DH signal model, namely of a WW pair that decays semileptonically and recoils against missing transverse momentum produced by the DM pair in the final state. However, some SM processes can produce final state

---

[3] The PYTHIA 8.230 [131] is the particular version of Pythia8 used to generate the MC simulated signal events used in this search.

observables that are similar enough to that of the signal model as to create an appreciable yield of events in the signal regions. In addition to targeting the signal model, the selections are also optimized to minimize the predicted yield of SM background processes in the signal regions. This section presents the background processes that have a non-negligible yield in the signal regions even with the optimized signal region selections.

Dominant backgrounds to the search are the W+jets, Diboson and $t\bar{t}$ processes described in Section 4.4.1. Figure 4.2 shows the yield breakdowns in the signal regions of all SM background processes considered in the analysis.

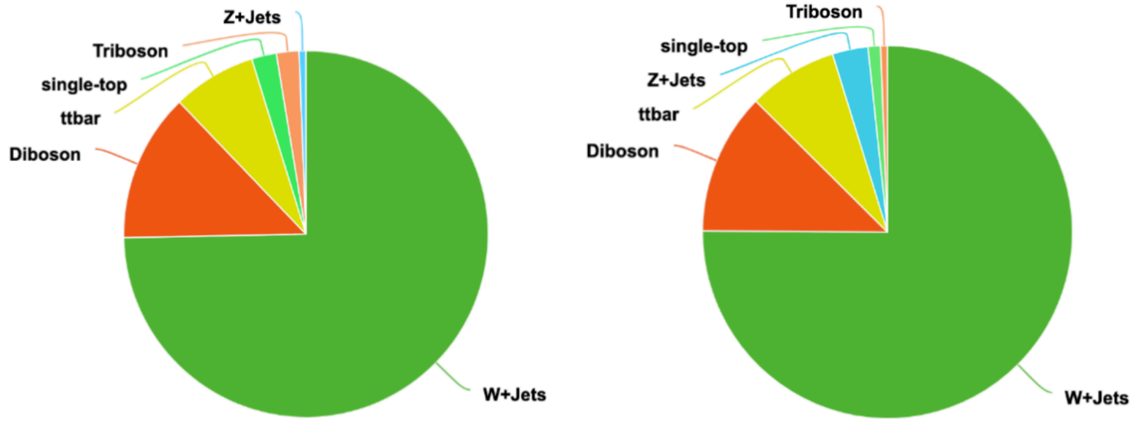

(a) “merged” SR (b) “resolved” SR

Figure 4.2: Relative contributions of all SM background processes considered in the signal regions.

4.4.1 Dominant Background Processes

W+jets

The dominant SM background in the signal regions comes from the W+jets process, wherein a leptonically decaying W is produced from the initial parton-parton collision, along with hadronic activity that fakes the hadronically decaying W in the signal model. A leading Feynman diagram for the W+jets background is shown in Figure 4.3a.

The Sherpa 2.2 [132] MC generator is used to model both the hard W+jets process, as well as the parton shower initiated by the final-state partons in the process.

Statistical Enhancement in W+jets Samples for $m_W > 120$ GeV

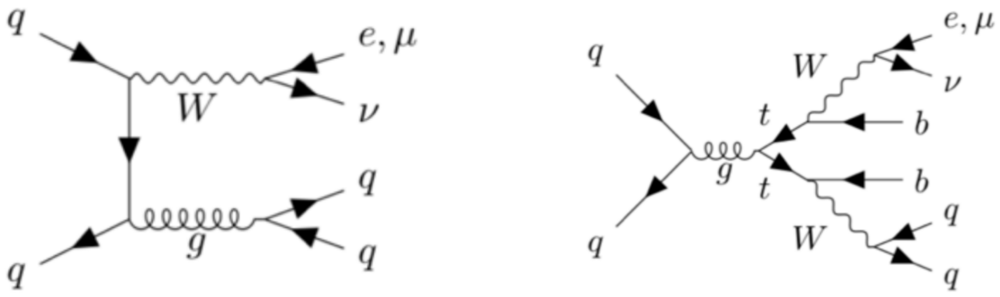

(a) W+jets

(b) $t\bar{t}$

Figure 4.3: Feynman diagrams for W+jets and $t\bar{t}$ SM background processes.

Due to application of a high $m_{\mathrm{T}}(\ell, E_{\mathrm{T}}^{\mathrm{miss}})$ requirement, described in Section 5.2, to reduce the W+jets background in the signal region, it was found that the majority of MC simulated events simulated for the W+jets process that make it into the signal regions are generated with a very high off-shell mass of the leptonically decaying W boson in the process. The default SHERPA 2.2 generator is not optimized to produce large MC statistics in this high-m_W regime. Therefore, in addition to using samples produced by the default SHERPA 2.2 generator, this search also makes use of a recently-developed set of specialized SHERPA 2.2 W+jets MC generated samples[4] that are generated with enhanced MC statistics for large off-shell masses ($m_W > 120$ GeV) of the leptonically decaying W.

Diboson

The next-leading SM background after W+jets comes from the diboson process, in which a pair of vector bosons - WW, ZZ or WZ - are produced from the initial parton-parton collision. The diboson events that make it into the signal region are dominated by the production mechanism in which both bosons decay leptonically ($W \to \ell\nu$, $Z \to \nu\nu$ or $Z \to \ell\ell$) to produce a final-state lepton in addition to missing transverse momentum from the neutrino production, and one or more partons are radiated as part of the diboson production process to produce QCD activity that fakes the hadronically decaying W in the signal model.

The diboson process, as well as the parton showers initiated by partons produced in the process, is modelled using the SHERPA 2.2 MC generator.

---

[4] The specialized samples generated with enhanced MC statistics for large off-shell m_W are not yet discussed in any published work, but are described in the following internal ATLAS document: ATL-COM-PHYS-2021-063

$\mathbf{t\bar{t}}$

The $t\bar{t}$ process represents the third-leading SM background in the signal regions. A leading Feynman diagram for the process is shown in Figure 4.3b. In this process, two t quarks are produced from the initial parton-parton collision, both of which decay to a b quark and a W boson. The WW pair decays semileptonically, thus faking the semileptonically decaying WW pair produced in the signal model. The final-state ν from the leptonic W decay produces the missing transverse momentum required in the signal region selection. The signal region selection includes a veto on the presence of b-tagged quarks in the final state to reduce the yield of $t\bar{t}$ events, but some events from the process pass the veto and make it into the signal region due to the limited efficiency of the b quark tagging algorithm [133].

The production of $t\bar{t}$ events is modelled using the POWHEG BOX v2 [134, 135, 136, 137] generator, which calculates matrix elements for the process. Parton showers initiated by final-state partons produced in the $t\bar{t}$ process are modelled using PYTHIA 8.230 [131].

4.4.2 Sub-dominant Background Processes

Z+jets

The Z+jets process is analogous to the W+jets process, but with the leptonically decaying W boson replaced by a Z boson, which also decays leptonically. For the majority of Z+jets events that are classified into the signal region, the Z boson decays to a $\ell\ell$ pair, of which one of the ℓs is not properly identified as a e or μ during event reconstruction.

Triboson

The triboson process is similar in structure to the diboson, except that three vector bosons rather than two are produced from the initial parton-parton collision. Triboson events that pass the signal region selection predominantly exhibit a "$VVjj$" final state, in which two of the vector bosons decay leptonically to produce a final-state e or μ in addition to missing transverse momentum from ν production, and the third vector boson decays hadronically. The triboson process, as well as parton showers initiated by final-state partons in the process, is modelled using the SHERPA 2.2 MC generator.

single-top

The single-top process in the signal region is dominated by "Wt" events, in which a single t quark is produced in association with a W boson from the initial collision of a quark and a gluon. The t quark subsequently decays to Wb to produce the signature WW final state of the signal model. As with the $t\bar{t}$ background, the yield of single-top events in the signal region is reduced by the application of a b-veto in the event selection for the signal region.

Single-top Wt associated production is modelled using the Powheg Box [138, 135, 136, 137] v2 generator, which provides matrix elements for the process. Parton showers initiated by final-state partons produced in the single-top Wt process are modelled using Pythia 8.230 [131].

Chapter 5

Data Reconstruction, Selection and Triggers

This chapter describes the physics objects that are reconstructed on an event-by-event basis using collision data from the ATLAS detector, and used in this DM search. It also discusses the triggers and event selection cuts that are applied to define the subsets of collision data and MC simulated data, also known as "analysis regions", used for the search.

5.1 Object Definitions

The goal of the ATLAS detector is to identify particles that are produced by the proton-proton collisions that take place in the centre of the detector, and to reconstruct their kinematic properties. The particle identification and reconstruction is performed using collections of measured signals in the detector sub-systems, which are broadly referred to as "physics objects" (See Ref. [139] for a review of physics object reconstruction with the ATLAS detector). The physics objects used to reconstruct all particles considered in this search are described in the following sections.

5.1.1 Charged Leptons

The final state charged lepton produced from the leptonic decay of a W in the DH model could with approximately equal probability [22] be an electron e, a muon μ or a tau τ. Electrons are stable and as such do not decay before depositing their energy in the ATLAS detector. This allows them to be reconstructed directly using information from the inner tracker and the EM calorimeter, as discussed in Sections 3.4.1 and 3.4.2. Muons are unstable and will ultimately decay to a ν_μ and a $e\bar{\nu}_e$ pair via a virtual W boson mediator, as shown in Figure 5.1a. However, their mean lifetime of $2.2\mu s$, which is the average time after they are produced before they undergo the decay to $\nu_\mu + e\bar{\nu}_e$, is long enough that muons do make it through the ATLAS detector before they decay, and are reconstructed using information from the inner tracker and the muon spectrometer, as discussed in Sections 3.4.1 and 3.4.2. Only the $W \to e\bar{\nu}_e$ decay is possible in the 3-body muon decay, because any other particles that a virtual W could otherwise decay to are too massive to be produced from the initial 106 MeV rest mass energy of the muon.

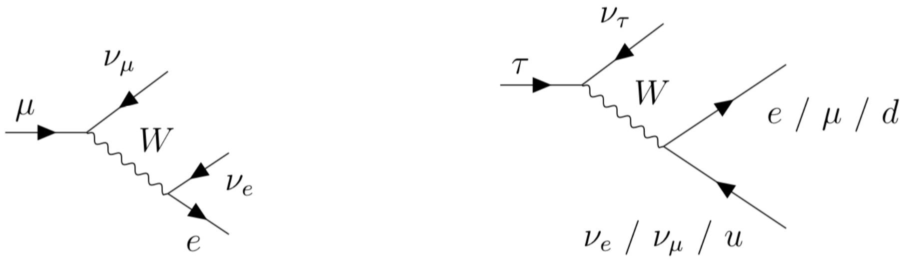

(a) Muon decay (b) Tau decay

Figure 5.1: Decay mechanisms for muons and taus.

Due to the relatively large tau mass of 1.8 GeV, the virtual W boson in the 3-body tau decay can itself decay either leptonically to $e\bar{\nu}_e$ or $\mu\bar{\nu}_\mu$, or hadronically to $d\bar{u}$, as shown in Figure 5.1b. As a result of the additional decay channels, tau decays proceed with a much shorter mean lifetime of 0.3ps compared with that of the muon. Because of this relatively short lifetime, taus will decay before passing through the ATLAS detector, and as such it is their leptonic or hadronic decay products that are actually measured in the detector [140]. As will be discussed in Section 5.2 below, the selections applied for this analysis require that events have exactly one electron or muon in the final state in order to be considered for the search. As a result, the search is sensitive to $s \to WW$ decays in which the leptonically decaying W decays to $\tau\nu_\tau$ only in the case where the τ decays leptonically to produce a single energetic electron or muon in the final state. This leptonic τ decay mode occurs with a 35% branching fraction [140].

Electrons

As discussed in Section 3.4.2, electron objects are reconstructed from clusters of energy deposits in the electromagnetic calorimeter that are associated with tracks in the inner detector, and calibrated to the EM scale. Detailed information about electron reconstruction, identification, and calibration can be found in Refs. [141],

[142] and [143]. To accommodate the differing needs of the various studies that make use of electron objects, ATLAS reconstructs these objects at several levels of identification and isolation efficiency, where the various efficiency levels are referred to as "working points", the names of which are typically variants of *Loose*, *Medium* and *Tight* for reasons that will be discussed in the following paragraphs.

The identification efficiency refers to the probability that an electron passing through the detector will be correctly reconstructed and identified as such. In general, a higher efficiency is achieved by loosening electron identification criteria, which comes at the cost of an increased background acceptance. The increased background acceptance means that reconstructed objects have a higher probability of being incorrectly identified as having originated from an electron.

Electron isolation tackles a slightly different, though related, challenge in comparison with identification. The goal of isolation is to separate the so-called "prompt" electrons that are produced from the primary decay processes of heavy mediators produced in the pp collisions from background processes such as semileptonic quark decays, hadrons misidentified as leptons and photons that convert into e^+e^- pairs before reaching the EM calorimeter. It is generally found that reconstructed objects that originate from prompt electrons can be characterized by a relative absence of (i.e. isolation from) significant activity in a small angular radius R around the object in the space of $\eta \times \phi$. In analogy with the identification efficiency, a high isolation efficiency is achieved by loosening the criteria for defining an object as isolated. As such, loosening isolation criteria will improve the probability that the prompt electrons targeted by the isolation requirement are identified as isolated objects, at the cost of an increase in the rate at which objects that originate from background processes are also identified as isolated.

Two types of electrons are defined for the search based on different sets of criteria.

Baseline electrons use the *Loose* working point for both identification and isolation. Isolation is measured within a fixed angular radius of $\Delta R = 0.2$ around the reconstructed electron object [142]. The *Loose* identification working point is measured in dedicated studies performed within the ATLAS collaboration to have an efficiency of 93% [142] for identifying prompt electrons with $E_T = 40$ GeV. The *Loose* isolation working point has a total measured efficiency of 98% [142]. Because of their relatively high efficiency, *baseline* electrons are used to veto the presence of additional electrons in the final state.

Signal electrons are designed to reconstruct prompt electrons with high purity.

They are required to satisfy the *Medium* identification criteria, which are measured to have an 88% efficiency [142], and *Loose* isolation criteria.

Both types of electrons are required to have $p_{\mathrm{T}} > 7$ GeV and a pseudorapidity in the range of $|\eta| < 2.47$.

Muons

As described in Section 3.4.3, muons are reconstructed using information from the the inner detector and the muon spectrometer. Detailed information about muon reconstruction, identification and calibration can be found in Refs. [144] and [145]. As is the case with electron objects, muon objects are reconstructed at several identification and isolation working points, and two definitions for muons are considered for this analysis:

Baseline muons do not have any isolation requirement, but are required to satisfy the *Loose* identification criteria, with a measured efficiency of 98% for 20 GeV $< p_{T,\mu} <$ 100 GeV [144].

Signal muons are designed to have a relatively high purity, and must satisfy the *Medium* identification criteria, with a 96% efficiency for 20 GeV $< p_{T,\mu} <$ 100 GeV [144]. Signal muons are additionally required to pass a set of tight isolation criteria referred to as *TightTrackOnly_VarRad* [145]. These tight isolation criteria use information from the inner tracker, and are defined within an angular radius ΔR around the reconstructed muon object that depends on the p_{T} of the muon object.

Both types of muons use a threshold of $p_{\mathrm{T}} > 7$ GeV.

Baseline muons are required to have pseudorapidity in the range of $|\eta| < 2.7$. For signal muons, a tighter pseudorapidity range of $|\eta| < 2.5$ is required to ensure that the muons are well measured in the inner detector as well as the muon spectrometer.

5.1.2 Small-radius anti-k_t $(R = 0.4)$ jets

As discussed in detail in Section 3.4.2, quarks and gluons induce showers of energy deposits in the calorimeter known as jets. This search uses the "particle flow algorithm" [146] to reconstruct objects associated with the energy deposits in the hadronic calorimeter. The particle flow algorithm matches signals from the inner tracker with topologically connected clusters of energy deposits in the calorimeter known as "topoclusters" with the aim of forming objects that represent individual charged particles. The energy deposited in the calorimeter by these identified charged particle objects is removed, leaving behind an ensemble of "particle flow objects" that consist of the remaining calorimeter energy and tracks. The anti-k_t algorithm described in Ref. [118] is then used to reconstruct jets using these particle flow objects. A range of jet radii R[1] may be chosen within which the anti-k_t algorithm should include particle flow objects for jet reconstruction. The choice of R depends on the kinematics, and on anticipated origins of the quark or gluon that initiated the shower (see discussion in Section 3.4.2 for more details).

As discussed in Chapter 2, the final state signature of the DH model targeted in this search involves a pair of energetic W bosons in the final state, one of which decays leptonically to a $\ell\nu$ pair, and the other hadronically to a pair of quarks. If the boost of the hadronically decaying W is sufficiently low, the angular separation between the two quarks may be large enough that the quarks are most effectively reconstructed as two separate jets, each with a small jet radius R. In the so-called "resolved" regime of the search, the two sets of energy deposits in the calorimeter produced by the $W \to qq$ decay are so separated that it is not even possible to reconstruct the two quarks within a single large-radius jet. For this search, these so-called "small-R " jets are reconstructed with a jet radius of $R = 0.4$.

After all small-R jets in the final state are reconstructed and fully calibrated, as described in Ref. [147], only jets with $p_{\mathrm{T}} > 20$ GeV and $|\eta| < 2.5$ are considered for the search. Jet cleaning [148] with the *TightBad* working point is applied to suppress noise in the calorimeter, as well as background jets that are not produced from the primary pp collision. The jet vertex tagger [149] is applied with the *Tight* working point to suppress pileup jets (see Ref. [125] for a discussion of pileup and its simulation in the ATLAS detector) from other pp interactions in the same and neighbouring bunch crossings - see Section 4.2.2 for a more detailed discussion of pileup events.

b-tagging

When b quarks are produced by pp collisions in the ATLAS detector, they immediately form "b-hadrons" due to colour confinement. The b-hadrons subsequently decay primarily via the weak force to form lighter hadrons. The so-called secondary decays of b-hadrons occur with a typical lifetime of $\sim$ 1.5ps [22], and as a result the b-hadrons can travel several millimeters from the primary pp interaction point

---

[1] See Eq. 3.4 for the definition of the angular radius R.

[150] before undergoing secondary decay. The displaced secondary vertex represents a signature of b-hadron decay in the ATLAS detector. It can be reconstructed using precision tracking of charged particles provided by the inner detector, and used to assign a "b tag" to hadronic jets in the ATLAS calorimeter to identify them as having originated from the decay of a b-hadron. This so-called "b-jet tagging" is performed with the `DL1r` algorithm [150], which uses a deep learning method for the identification. A fixed working point with a 77% efficiency is used. b-tagged jets are vetoed in the signal region to reduce the background of SM $t\bar{t}$ and single-top processes (see Section 4.4.1 for details).

5.1.3 Resolved W Candidate

As described in Section 5.1.2 above, the pair of quarks produced by the hadronic decay of the W boson in the signal model are reconstructed as two resolved small-R jets in the less-boosted resolved regime. The parent W boson can then be reconstructed from small-R jets induced by its daughter quarks using the combined energy and momentum of the small-R jet pair. Given that small-R jets can also be produced by, for example, initial-state radiation and pileup, it is quite common for there to be more than two small-R jets reconstructed in the final state. These additional jet sources complicate the task of identifying which of the reconstructed small-R jets in a given event should be associated with the $W \to qq$ in the signal model. For events with more than two small-R jets in the final state, the pair of small-R jets whose combined invariant mass is closest to the W boson mass is assumed to have originated from the W decay, and used to reconstruct the W boson candidate. The algorithm for this jet identification and W boson reconstruction is as follows:

- Construct all possible combinations of two small-R jets (a.k.a. "dijet pairs") in the final state.

- For each such candidate dijet pair, j_1 and j_2, sum the four-momenta of the reconstructed jets, $\mathbf{p}_{j_1,j_2} = \mathbf{p}_{j_1} + \mathbf{p}_{j_2}$, and calculate their combined invariant mass:

$$M_{j_1,j_2} = \sqrt{\mathbf{p}_{j_1,j_2} \cdot \mathbf{p}_{j_1,j_2}} \tag{5.1}$$

- Select the dijet pair whose invariant mass is closest to the W boson mass of 80.4 GeV [22] as the small-R jets to be associated with the $W \to q\bar{q}$ decay.

- Reconstruct the hadronically decaying W boson candidate using the dijet pair with four-momentum $\mathbf{p}_{j_1,j_2}$.

Figure 5.2 shows distributions of the reconstructed W boson candidate mass for MC simulated events generated for a range of m_s and $m_{Z'}$ after application of the baseline event selections presented in Section 5.2, with the additional requirement that there be at least two small-R jets in the final state. The distributions are in general well centred around the W boson mass.

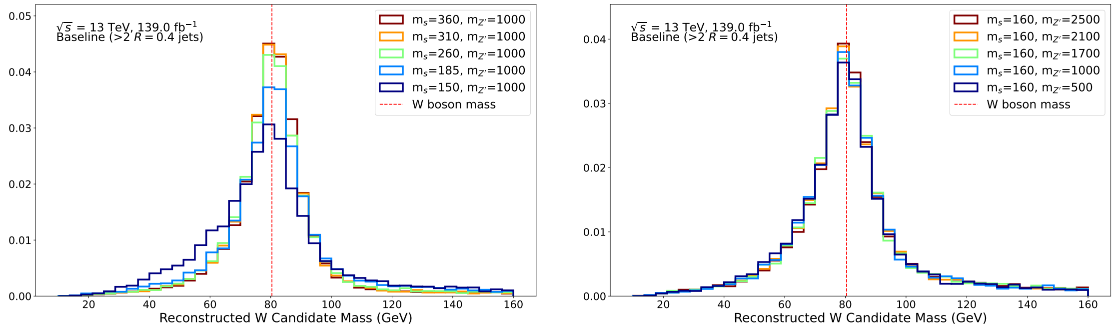

(a) $m_{Z'}$ fixed, m_s varied

(b) m_s fixed, $m_{Z'}$ varied

Figure 5.2: Distributions of the reconstructed W candidate mass for MC simulated events produced with the DH signal model over a range of m_s and $m_{Z'}$. All events included in the distributions are required to have passed the baseline event selection described in Section 5.2, and to have at least two small-R jets in the final state. The red dashed vertical line is placed at the W boson mass of 80.4 GeV. Distributions are normalized to unit area.

5.1.4 Track-Assisted Reclustered Jets (Merged W Candidate)

If the hadronically decaying W boson is produced with a sufficiently large momentum (i.e. boost), the jets produced by the $q\bar{q}$ pair may be sufficiently collimated (i.e. "merged") that they are most effectively reconstructed as a single multi-pronged large-R jet, as opposed to the resolved small-R jets used for W reconstruction in the resolved regime (see Sections 5.1.2 and 5.1.3 above for details).

Since the signal model predicts that charged particle tracks and energy deposits in the detector will have originated primarily from the two quarks produced by the $W \to q\bar{q}$ decay in the signal model, it is important to reconstruct the large-radius jet in this so-called merged regime with as much detailed kinematic and substructure information as possible. This information is used in the search to help identify whether the hadronic activity contained within a large-R jet is consistent with having been induced by two energetic quarks originating from a W parent, as predicted by the signal model. Such features include the combined invariant mass $m^{\text{TAR Jet}}$ of all particles associated with the jet, which would be expected to be consistent with the W boson mass within detector resolution. Important substructure information includes variables that aim to quantify the number of distinct "prongs" of localized energy deposition within the jet, which can be correlated to the number of high-p_{T} strongly interacting particles whose energy deposits are included in the jet (two such prongs would be expected for the signal model).

This search uses the track-assisted reclustered (TAR) jet algorithm [2] for large-R jet reconstruction in the merged regime. In this regime, the highest-p_{T} TAR jet reconstructed with a radius parameter of $R = 1.0$ is used to reconstruct the hadronically decaying W boson (W_{had}) in the DH signal model. Whereas most large-R jet reconstruction techniques rely on energy deposits in the calorimeter to reconstruct the jet substructure information, TAR jets are designed to profit from the superior resolution of the inner tracker for improved substructure reconstruction by matching charged particle tracks with energy deposits in the calorimeter.

TAR Algorithm

For this search, $R = 0.2$ small-R jets are used to reconstruct energy deposits in the calorimeter, and are input to the TAR algorithm along with tracks measured by the inner detector that satisfy a set of quality criteria summarized in Table 5.1. The TAR algorithm [2] is as follows: the input $R = 0.2$ small-R "subjets" are reclustered using the anti-k_t algorithm with $R = 1.0$ to form large-R jets. A trimming procedure is applied to mitigate the effects of pileup and background QCD processes within the triggered event that do not originate from the hard interaction. The trimming procedure removes any of the input subjets that carry less than a fraction $f_{\text{cut}} = 0.05$ of the total transverse momentum of the large-R jet: $p_{\text{T}}^{\text{subjet}}/p_{\text{T}}^{\text{large-}R\text{ jet}} < 0.05$. The tracks from the inner detector are then matched to the remaining small-R subjets using the ghost association procedure described in Ref. [151], if possible. Any tracks that cannot be matched to subjets using ghost association are instead matched to the nearest subjet, provided that there is a jet within an angular radius $\Delta R = 0.3$ of the track. To account for the energy of the neutral hadronic jet components, which do not leave tracks in the inner detector, the p_{T} of each track is scaled such that the summed p_{T} of all tracks matched to a given subjet will evaluate to the energy of the subjet as measured by the calorimeter:

$$p_{\mathrm{T}}^{\text{track, new}} = p_{\mathrm{T}}^{\text{track, old}} \times \frac{p_{T,j}^{\text{subjet}}}{\sum_{i\in j} p_{T,i}^{\text{track, old}}} \tag{5.2}$$

where the index i runs over all tracks matched to the subjet j. The rescaled tracks and remaining subjets are again reclustered using the anti-k_t algorithm to form the final large-R TAR jet.

While the kinematic properties of the TAR jets are calculated from the constituent small-R jets, the jet substructure and mass m^{TAR} are calculated from the constituent tracks. Figure 5.5 shows a visual summary of the basic TAR algorithm.

TAR-lepton Disentanglement

The analysis applies the TAR algorithm to $R = 0.2$ small-R jets and tracks that have undergone a "TAR-lepton disentanglement" preselection to remove tracks associated with any reconstructed baseline electrons or muons, as well as any $R = 0.2$ jets that overlapped with the baseline electron tracks. This preselection is helpful given the final state targeted in the search, because the charged lepton produced by the leptonic $W \to \ell\nu$ decay often falls within the $R = 1.0$ cone of the TAR jet, as illustrated in Figure 5.3. This TAR-lepton overlap disrupts the jet reconstruction, particularly due to the additional jet energy induced by calorimetric clusters created in the large-R jet by the overlapping electron.

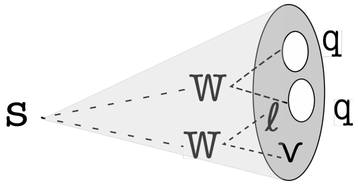

Figure 5.3: Illustration of the final state scenario in which the charged lepton produced by the leptonic $W \to \ell\nu$ decay overlaps with the large-R TAR jet reconstructed from the hadronic $W \to qq$ decay.

Figure 5.4 shows a comparison of the distributions of reconstructed TAR jet mass $m^{\text{TAR Jet}}$ either without or with the TAR-lepton disentanglement preselection applied, for MC simulated events produced with the DH signal model at several representative m_s and $m_{Z'}$, in which the reconstructed electron in the final state overlaps with the highest-p_{T} reconstructed TAR jet. For all the signal points, the TAR-lepton disentanglement preselection is found to substantially improve the ability of the TAR algorithm to reconstruct TAR jets with $m^{\text{TAR Jet}}$ near the W boson mass, as would be expected for the signal model.

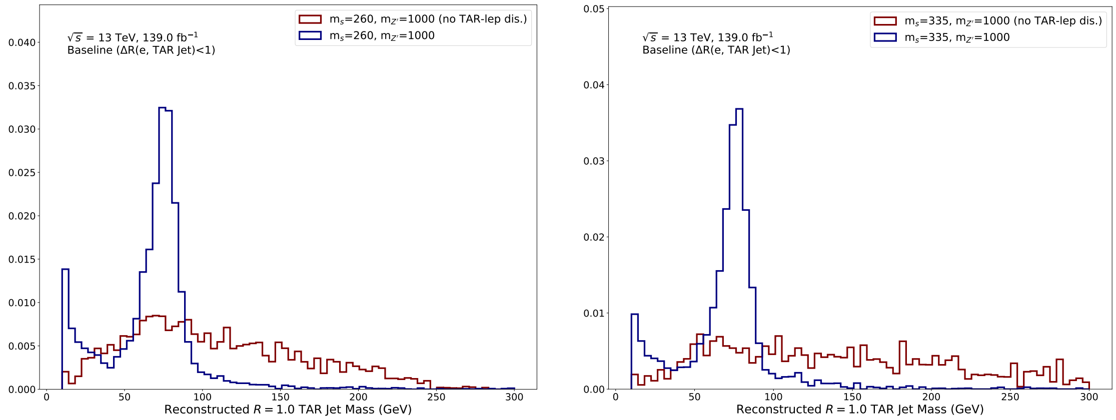

(a) $(m_s, m_{Z'}) = (260, 1000)$ GeV

(b) $(m_s, m_{Z'}) = (335, 1000)$ GeV

Figure 5.4: Distributions of $m^{\text{TAR Jet}}$ for the leading-p_{T} TAR jet in MC simulated events generated for the DH signal model process with semileptonic WW decay at several representative m_s and $m_{Z'}$, with and without application of the lepton disentanglement preselection. Events included in the distributions are required to have one signal electron and at least one reconstructed TAR jet, both within an angular radius of $\Delta R = 1.0$. Distributions are normalized to unit area.

Summary of the TAR Procedure

The following steps summarize the algorithm used to construct the TAR jets used in this search (steps with a * are included to disentangle leptons):

- Tracks and calibrated anti-k_t $R = 0.2$ jets are chosen as input to the algorithm.
- Tracks associated with a baseline muon or electron are removed from the input collection (*).
- $R = 0.2$ jets overlapping with a baseline electron ($\Delta R < 0.2$) are removed from the input collection (*).
- The remaining $R = 0.2$ subjets are reclustered using the anti-k_t algorithm into $R = 1.0$ jets, and trimmed using the p_T fraction $f_{\text{cut}} = 0.05$.

- Input tracks are matched to $R = 0.2$ subjets that remain after trimming, if possible, using ghost association.
- Tracks that remain unassociated are matched to the nearest anti-k_t $R = 0.2$ jet within $\Delta R < 0.3$.
- The p_{T} of each track is rescaled using the p_{T} of the jet to which it is matched using Eq. 5.2. This rescaling accounts for the missing neutral momentum, which is measured at calorimeter level but is not present at tracker level.
- Finally, jet substructure variables and m^{TAR} are calculated using the rescaled matched tracks.

The parameters of the TAR algorithm used are summarized in Table 5.1.

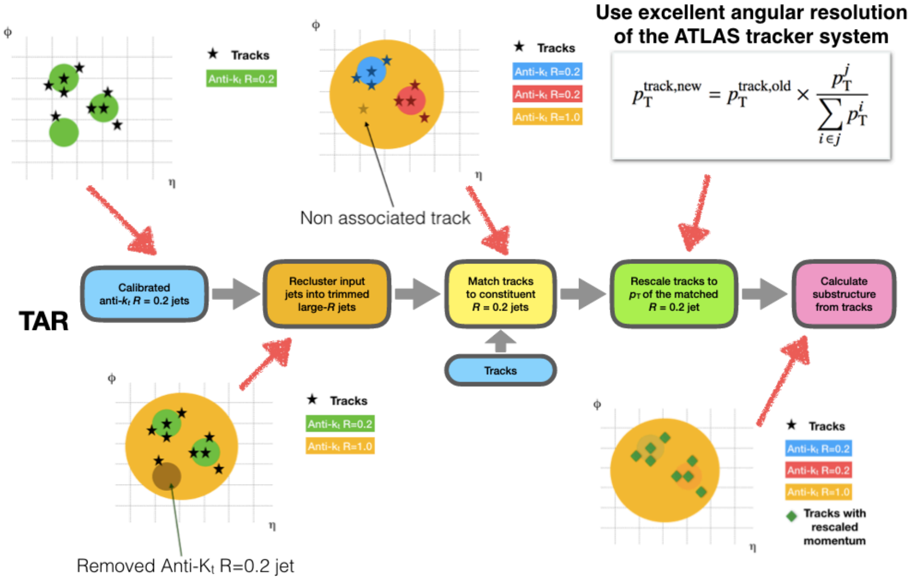

Figure 5.5: TAR jet reconstruction algorithm depicted without lepton disentanglement. Figure adapted from © [2]

5.1.5 $E_{\mathrm{T}}^{\mathrm{miss}}$

The missing transverse momentum $E_{\mathrm{T}}^{\mathrm{miss}}$, introduced in Section 3.4.4, quantifies the imbalance of momentum in the plane transverse to the beam line. In the event that all particles produced in a pp collision are fully detected, conservation of momentum implies that the transverse momenta of all objects produced by the event should sum

Table 5.1: TAR jet reconstruction parameters.

Track selection	`Loose` quality $p_{\mathrm{T}} > 0.5$ GeV $\lvert\eta\rvert < 2.5$
Tracks removed if associated to	electrons, muons
Input jet selection	$R = 0.2$ anti-k_t jets $p_{\mathrm{T}} > 20$ GeV $\lvert\eta\rvert < 2.5$
Reclustering radius	$R = 1.0$
TAR jet p_{T}	$p_{\mathrm{T}}^{\mathrm{TAR}} > 100$ GeV
Trimming radius	$R = 0.2$
Trimming p_{T} fraction	$f_{\mathrm{cut}} = 0.05$
Track-to-jet association	$\Delta R(\text{jet, track}) < 0.3$
jet-electron overlap removal	$\Delta R(\text{jet, electron}) < 0.2$

to zero within detector resolution. As a result, large $E_{\mathrm{T}}^{\mathrm{miss}}$ in an event is indicative of the production of undetected energetic particles. The semileptonic $s \to WW(qq\ell\nu)$ decay channel of the LHC signature for the DH model probed in this DM search (see Chapter 2 for details) predicts large (i.e. above-detector-resolution) $E_{\mathrm{T}}^{\mathrm{miss}}$ in the final state. The large $E_{\mathrm{T}}^{\mathrm{miss}}$ would be due both to the DM pair produced from the decay of the hypothetical Z', and to the neutrino produced by the leptonic decay of one of the W bosons in the final state. Both the DM pair and the neutrino would be expected to pass through the detector without any appreciable interactions due to their very low interaction cross sections with SM particles, and hence constitute undetected (i.e. missing) momentum in the event.

The $E_{\mathrm{T}}^{\mathrm{miss}}$ is calculated using fully calibrated and reconstructed physics objects (for details, see Ref. [152]). For this search, baseline electrons and muons (see Section 5.1.1) and $R = 0.4$ jets (see Section 5.1.2) are used to construct the $E_{\mathrm{T}}^{\mathrm{miss}}$. A soft term is additionally included, which uses tracks that are not associated with any of these reconstructed objects.

This search also makes use of the object-based $E_{\mathrm{T}}^{\mathrm{miss}}$ significance $\mathcal{S}$ [153], which is designed to be positively correlated with the likelihood that the measured $E_{\mathrm{T}}^{\mathrm{miss}}$ was actually produced by undetected particles in the event, rather than by fluctuations arising from the limited detector resolution. The $E_{\mathrm{T}}^{\mathrm{miss}}$ significance is calculated on an event-by-event basis using the uncertainties associated with the reconstructed objects involved in the $E_{\mathrm{T}}^{\mathrm{miss}}$ calculation for the given event.

5.1.6 Overlap Removal

To avoid double-counting any physics objects in an event, a priority-based overlap removal (OR) strategy is employed, which eliminates any overlap between the physics objects. This is accomplished by removing all but the highest-priority object from any region in which objects overlap. The strategy presented in this section resolves any overlap between electrons, muons and $R = 0.4$ small-R jets. The overlap removal between leptons and TAR jets is described in Section 5.1.4. No overlap removal between $R = 0.4$ jets and TAR jets is applied, as they are not used in the same selection (see Section 5.2 for details). Table 5.2 summarizes the criteria under which overlap is removed between a given pair of objects.

Overlap removal is performed for baseline objects, and only the remaining objects are considered as candidate signal objects. Note that the calorimeter-tagged (CT) muons listed in Table 5.2, details of which can be found in Section 4 of Ref. [120], are identified and reconstructed using only inner detector tracks and calorimeter energy deposits consistent with a minimum-ionizing particle, and do not have any associated hits identified in the muon spectrometer. Due to the absence of any associated signal in the muon spectrometer, these CT muons are given a relatively low priority in the OR procedure compared with non-CT muons, which do activate the muon spectrometer.

Table 5.2: Object priorities and overlap removal criteria for each pair of physics objects considered in the OR procedure. Object pairs and removal criteria are listed in the sequence by which they are considered for OR, with the top row considered first.

Removed Object	**Retained Object**	**Criteria for OR**
Electron (lower p_{T})	Electron (higher p_{T})	shared inner detector track
Muon	Electron	shared ID track, and muon is CT
Electron	Muon	shared ID track, and muon is not CT
anti-k_t 4 Jet	Electron	Angular separation $\Delta R < 0.2$
Electron	anti-k_t 4 Jet	$\Delta R < \min\left(0.4, 0.04 + 10\ \mathrm{GeV}/p_{\mathrm{T}}(e)\right)$
anti-k_t 4 Jet	Muon	fewer than 3 tracks in jet, and (muon is ghost-associated to jet, or $\Delta R < 0.2$)
Muon	anti-k_t 4 Jet	$\Delta R < \min\left(0.4, 0.04 + 10\ \mathrm{GeV}/p_{\mathrm{T}}(\mu)\right)$

5.1.7 Dark Higgs Candidate Mass

In principle, the four-momentum of the Dark Higgs boson s in the DH signal model is simply the sum of the four-momenta of the WW pair that it decays to:

$$\mathbf{p}_s = \mathbf{p}_{W_{\mathrm{had}}} + \mathbf{p}_{W_{\mathrm{lep}}} \tag{5.3}$$

where W_{had} (W_{lep}) denotes the hadronically (leptonically) decaying W boson. The W_{had} four-momentum is reconstructed in the resolved regime using the pair of anti-k_t 4 jets whose invariant mass is closest to the on-shell W mass of 80.4 GeV (see Section 5.1.3), or in the merged regime as the four-momentum of the highest-p_{T} $R = 1.0$ TAR jet (see Section 5.1.4). The four-momentum of the W_{lep} is the sum of four momenta of its lepton and neutrino daughters:

$$\mathbf{p}_{W_{\mathrm{lep}}} = \mathbf{p}_\ell + \mathbf{p}_\nu \tag{5.4}$$

If the neutrino were the only anticipated source of "true $E_{\mathrm{T}}^{\mathrm{miss}}$ " (i.e. $E_{\mathrm{T}}^{\mathrm{miss}}$ arising from undetected particles rather than limited detector resolution) in the final state, the final state $E_{\mathrm{T}}^{\mathrm{miss}}$ could be unambiguously assigned to the neutrino, i.e. $(p_{x,\nu}, p_{y,\nu}) = (E_x^{\mathrm{miss}}, E_y^{\mathrm{miss}})$, at which point the only missing information would be the z-component $p_{\nu,z}$ of the neutrino momentum. However, since the DH signal model additionally predicts $E_{\mathrm{T}}^{\mathrm{miss}}$ originating from the DM pair in the final state, there is some ambiguity involved with assessing how much of the measured $E_{\mathrm{T}}^{\mathrm{miss}}$ is accounted for by the neutrino vs. the DM pair.

An approximate solution is obtained by determining the minimum m_s that would be required in order for the s decay to have produced a lepton and W_{had} with the observed momenta, subject to the constraint that the invariant mass of the reconstructed $m_{W_{\mathrm{lep}}}$ be equal to the on-shell W mass of 80.4 GeV. Although this minimum m_s may not necessarily evaluate to the actual modelled m_s, by providing an absolute lower bound on the possible range of m_s that could produce the observed final state, it is expected to at least be positively correlated with the actual modelled m_s.

To simplify the math involved in determining the minimum m_s, the coordinate system is rotated without loss of generality such that the lepton is strictly traveling along the z axis, and the hadronically decaying W boson W_{had} is in the xz plane, as shown in Figure 5.6.

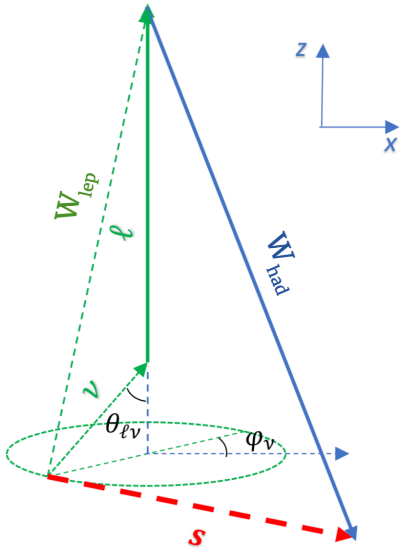

Figure 5.6: Coordinate system used to evaluate the minimum DH mass m_s that is kinematically required to produce the observed final state, subject to the constraint that $m_{W_{\mathrm{lep}}} = 80.4$ GeV.

In this rotated coordinate system, the four-momenta $\mathbf{p}_\nu$, $\mathbf{p}_\ell$ of the neutrino, lepton and hadronically decaying W boson, respectively, are given by:

$$\mathbf{p}_\nu = E_\nu(1, \sin\theta_{\ell\nu}\cos\phi_\nu, \sin\theta_{\ell\nu}\sin\phi_\nu, \cos\theta_{\ell\nu}) \tag{5.5}$$

$$\mathbf{p}_\ell = E_\ell(1, 0, 0, 1) \tag{5.6}$$

and

$$\mathbf{p}_{W_{\text{had}}} = (E_{W_{\text{had}}}, p_{W_{\text{had}},x}, 0, p_{W_{\text{had}},z}) \tag{5.7}$$

where $\theta_{\ell\nu}$ is the angular separation between the lepton and the neutrino, and ϕ_ν is the angle of the neutrino relative to the x axis in the xy plane. The m_s is then obtained by squaring the four-momenta in Eq. 5.3:

$$\begin{aligned} m_s^2 &= (\mathbf{p}_{W_{\text{had}}} + \mathbf{p}_{W_{\text{lep}}})^2 = (\mathbf{p}_{W_{\text{had}}} + \mathbf{p}_\ell + \mathbf{p}_\nu)^2 \\ &= (E_{W_{\text{had}}}+E_\ell+E_\nu)^2-(p_{W_{\text{had}},x}+E_\nu\sin\theta_{\ell\nu}\cos\phi_\nu)^2-(E_\nu\sin\theta_{\ell\nu}\sin\phi_\nu)^2-(E_\ell+p_{W_{\text{had}},z}+E_\nu\cos\theta_{\ell\nu})^2 \end{aligned} \tag{5.8}$$

It can be shown by taking derivatives of Eq. 5.8 that the minimum m_s occurs when $\phi_v = 0$ (i.e. when the neutrino is in the same plane as the $\mathbf{p}_{W_{\text{had}}}$).

Setting $\phi_v = 0$ in Eq. 5.8 and using the Pythagorean identity $\sin\theta = \sqrt{1-\cos^2\theta}$:

$$\begin{aligned} m_s^2 = (E_{W_{\text{had}}} + E_\ell + E_\nu)^2 - \left(p_{W_{\text{had}},x} + E_\nu\sqrt{1-\cos^2\theta_{\ell\nu}}\right)^2 \\ - (E_\ell + p_{W_{\text{had}},z} + E_\nu\cos\theta_{\ell\nu})^2 \end{aligned} \tag{5.9}$$

This leaves an equation for m_s with two unknowns: the energy E_ν of the neutrino, and the cosine $\cos\theta_{\ell\nu}$ of the angle between the lepton and the neutrino. The neutrino energy is determined as a function of $\cos\theta_{\ell\nu}$, by imposing the constraint that the mass $m_{W_{\text{lep}}}$ of the leptonically decaying W boson be set to the on-shell W boson mass of $m_W = 80.4$ GeV:

$$m_{W_{\text{lep}}}^2 = m_W^2 = (p_\ell + p_\nu)^2 = 2p_\ell p_\nu = 2E_\ell E_\nu(1-\cos\ \theta_{\ell\nu}) \tag{5.10}$$

Solving for E_ν:

$$E_\nu = \frac{m_W^2}{2E_\ell(1 - \cos\ \theta_{\ell\nu})} \tag{5.11}$$

With this independent determination of E_ν, the minimum m_s in Eq. 5.9 is evaluated numerically by scanning over $\cos\ \theta_{\ell\nu} \in [-1, 1]$ and identifying the value of $\cos\ \theta_{\ell\nu}$ that minimizes m_s (excluding $\cos\ \theta_{\ell\nu} = 1$ to avoid a singularity in Eq. 5.11).

Figure 5.7 shows distributions of this minimized "min(m_s)" for MC simulated events produced with the DH signal model over a range of m_s (left column) or $m_{Z'}$ (right column). The distributions are more sharply peaked for lower m_s, and for higher m_s the location of peak in min(m_s) becomes increasingly shifted to the left of (i.e. below) the actual modelled m_s. The minimal variation between the different modelled values of $m_{Z'}$ presented in distributions in the right-hand column of Figure 5.7, which scan over a range of $m_{Z'}$ for the same m_s, offers an encouraging indication that the value of the min(m_s) variable is primarily a function of the m_s parameter in the model that it is designed to approximate.

Despite the shifted location of the peaks at higher m_s, the presence of distinct peaks in the approximate vicinity of the modelled m_s imply that the min(m_s) variable can be a valuable tool to aid in discriminating events in the data that could be consistent with the DH signal process from the SM background processes. For this reason, events in the signal regions are binned in m_s when searching for evidence of the signal model in the ATLAS collision data. The binning in min(m_s) is presented in detail in Section 7.2.

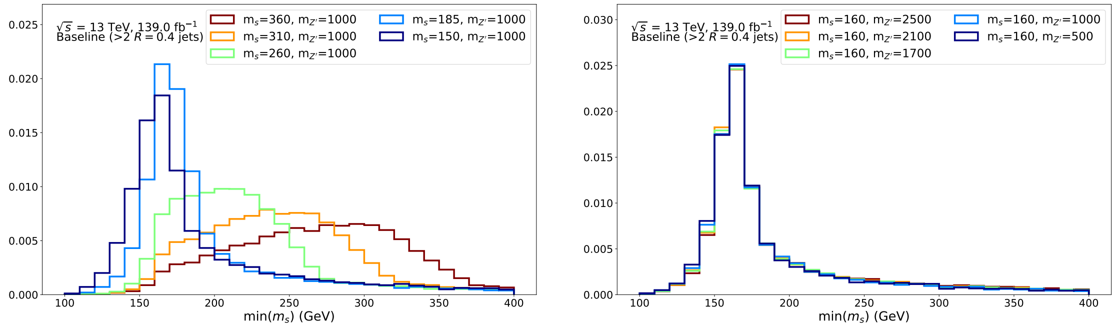

(a) $m_{Z'}$ fixed, m_s varied (b) m_s fixed, $m_{Z'}$ varied

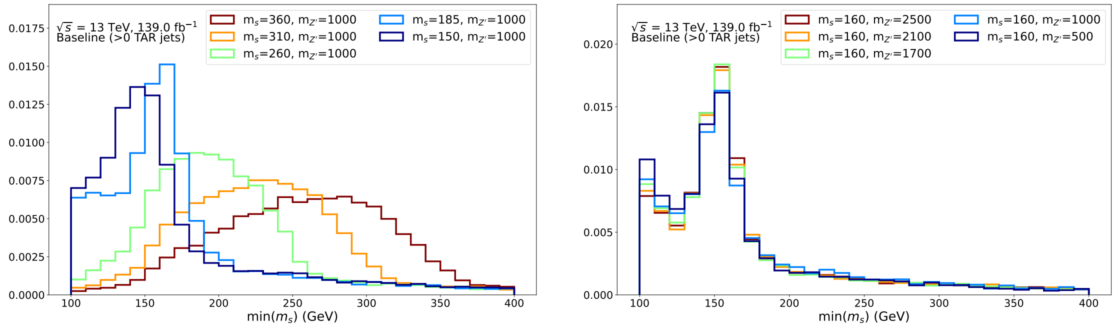

(c) $m_{Z'}$ fixed, m_s varied (d) m_s fixed, $m_{Z'}$ varied

Figure 5.7: Distributions of the DH candidate mass $\min(m_s)$, reconstructed using the minimization strategy presented in Section 5.1.7, for MC simulated events produced for the DH signal model over a range of m_s and $m_{Z'}$. Distributions are normalized to unit area. Events included in all distributions are required to pass the baseline selection requirements presented in Section 5.2. For the distributions shown in the top (bottom) row, the W_{had} is reconstructed as a resolved candidate (TAR jet) using the strategy presented in Section 5.1.3 (5.1.4), and events are required to have ≥ 2 $R = 0.4$ small-R jets (≥ 1 $R = 1.0$ TAR jets) reconstructed in the final state.

5.1.8 Transverse Mass

The transverse mass $m_T(E_{\mathrm{T}}^{\mathrm{miss}}, \ell)$ between the lepton and $E_{\mathrm{T}}^{\mathrm{miss}}$ is considered in this search because it is sensitive to the presence of additional $E_{\mathrm{T}}^{\mathrm{miss}}$ beyond that arising from the neutrino in the leptonic decay of the W_{lep}. It is computed for events measured in the ATLAS detector as:

$$m_T(\ell, E_{\mathrm{T}}^{\mathrm{miss}}) = \sqrt{2 p_{T,\ell} E_{\mathrm{T}}^{\mathrm{miss}} (1 - \cos\theta_{\ell, E_{\mathrm{T}}^{\mathrm{miss}}})} \tag{5.12}$$

which is derived from the more general transverse mass definition found in Section 48.6.1 of Ref. [22].

$$m^2_{T,\text{ full}}(\ell, E_{\mathrm{T}}^{\mathrm{miss}}) = (p_{T,\ell} + p_{T,E_{\mathrm{T}}^{\mathrm{miss}}})^2$$
$$= m_\ell^2 + m^2_{E_{\mathrm{T}}^{\mathrm{miss}}} + 2E_{T,\ell}, E_{T,E_{\mathrm{T}}^{\mathrm{miss}}}(1 - \cos\theta_{\ell,E_{\mathrm{T}}^{\mathrm{miss}}}) \quad (5.13)$$

under the assumptions that the masses associated with the lepton and $E_{\mathrm{T}}^{\mathrm{miss}}$ are negligibly small compared with their momenta. The assumption of negligible lepton mass is in general justified given the high energy of the *pp* collisions at the LHC. The assumption of negligible mass associated with $E_{\mathrm{T}}^{\mathrm{miss}}$ is justified if the true $E_{\mathrm{T}}^{\mathrm{miss}}$ arises only from the neutrino in the leptonic W_{lep} decay, as it would in the leading SM backgrounds. In the signal model, however, there is additional mass associated with the $E_{\mathrm{T}}^{\mathrm{miss}}$, which arises from the decay of the massive Z' mediator to an invisible DM pair. The result, shown in figure 5.8 after applying the baseline selection, is that the bulk of the SM background has $m_{\mathrm{T}}(\ell, E_{\mathrm{T}}^{\mathrm{miss}})$ below the W mass peak, but the signal distribution tends to be peaked closer to $\sim$ 250 GeV.

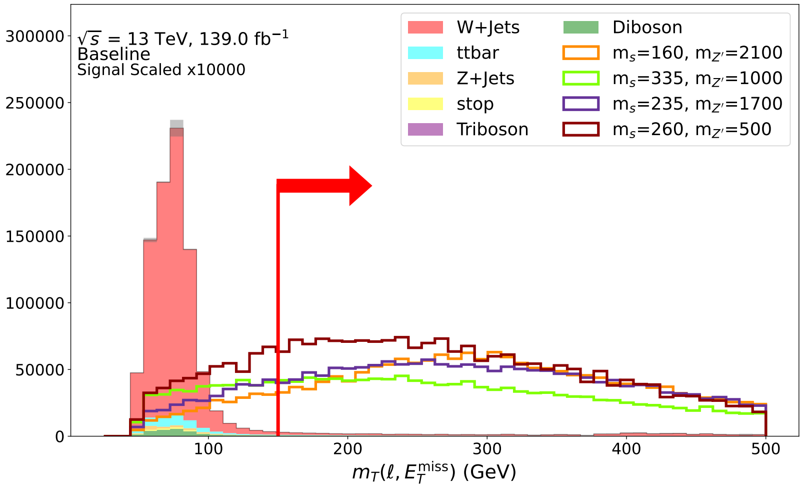

Figure 5.8: Transverse mass distribution for SM background and several signal points with baseline selections, excluding the lower bound on $m_{\mathrm{T}}(\ell, E_{\mathrm{T}}^{\mathrm{miss}})$. The red line and arrow indicate the placement of the baseline selection on $m_{\mathrm{T}}(\ell, E_{\mathrm{T}}^{\mathrm{miss}})$.

5.2 Event Selections

Selections are applied to the ATLAS collision data and MC simulated events with the aim of defining subsets, or “regions” of data that are enriched in a particular process of interest for the search. The regions are designed and optimized using MC simulated data (see Chapter 4 for a detailed discussion of MC simulation and its application to simulating data produced by the ATLAS detector). The use of MC simulated data makes it possible to quantify the relative contribution to the expected yield of events in the region arising from each physics process predicted in the data.

Selections that define the "signal regions" (SRs) are optimized to produce an enriched yield of MC simulated events produced using the DH signal model (referred to as "signal events"), with a minimal yield of simulated events generated to model SM background processes (referred to as "background events"). A discrepancy between the ATLAS collision data and the predicted yield of SM backgrounds in the signal regions would indicate the presence of a BSM physics process with a production mechanism at the LHC consistent with that of the signal model. "Control regions" (CRs) are optimized to have an enriched yield of MC simulated events modelled for one particular SM background process. W+jets and $t\bar{t}$ CRs are defined for this DM search to obtain data-driven constraints on the total yields of these SM background processes in the signal region.

5.2.1 Kinematic Categories

Within each of the SRs and CRs, the analysis selection is divided into two kinematic regimes, referred to as "categories". The "merged" category is designed to target the merged regime discussed in Section 5.1.4 in which the hadronic decay products are sufficiently boosted as to be reconstructed as a single $R = 1.0$ TAR jet. The leading p_{T} TAR jet is then used to reconstruct the candidate hadronically decaying W boson W_{had} in the signal model. The "resolved" category targets the lower-p_{T} regime in which the hadronic decay products have a sufficient angular separation that they cannot be reclustered into a TAR jet, and are instead reconstructed as resolved small-R anti-k_t $R = 0.4$ jets. As described in Section 5.1.3, the W_{had} is reconstructed in the resolved category using the two small-R jets whose combined invariant mass is nearest to $m_W = 80.4$ GeV.

Figure 5.9 illustrates the two kinematic categories.

Within each of the signal and control regions, the selection is divided into the merged and resolved kinematic categories presented in Section 5.2.1. Events are classified into the merged category if there is at least one reconstructed $R = 1.0$ TAR jet in the final state ($N(\text{TAR Jets}) > 0$), and the resolved category if there are at least two reconstructed $R = 0.4$ small-R jets ($N(\text{Jets}) > 1$). Selections are

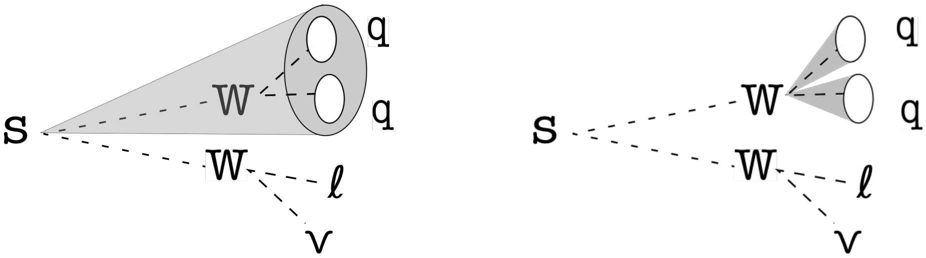

Figure 5.9: A graphical representation of the two kinematic categories used in the search based on the characteristics of the final state. Left: merged category, in which the jets produced by the $w \rightarrow q\bar{q}$ are sufficiently boosted as to be reconstructed within a single large-R TAR jet. Right: resolved category, in which the two quarks are reconstructed separately as two small-R anti-k_t $R = 0.4$ jets.

further refined and optimized separately within each category. It is worth noting that, as is, the requirements for events to be classified into the merged or resolved categories are not mutually exclusive - i.e. there are events that have least one $R = 1.0$ TAR jet **and** at least two small-R jets. To avoid double-counting the same events in the search, orthogonality between the merged and resolved categories is therefore enforced in all of the signal and control regions by explicitly requiring events that pass the requirements to be classified into the resolved category in any region to have additionally failed the merged category selection in all regions.

5.2.2 Baseline selection

The baseline preselection is common to all analysis regions and categories used in the search, and is used to roughly define the region of interest for the search prior to any detailed optimization of selection requirements or sub-division into separate analysis regions. The baseline selection is defined as follows:

- (1 signal muon or 1 signal electron) and no additional baseline muons or electrons
- ($E_{\mathrm{T}}^{\mathrm{miss}}$ trigger passed) OR ((single muon trigger passed) AND (signal muon matched to muon trigger))
- $E_{\mathrm{T}}^{\mathrm{miss}} > 200$ GeV
- $\mathcal{S} > 5$
- $m_{\mathrm{T}}(\ell, E_{\mathrm{T}}^{\mathrm{miss}}) > 150$ GeV
- N(TAR Jets) > 0 or N(Jets) > 1

See Section 5.1.1 for the definitions of baseline and signal muons and electrons, and Section 5.3 for details of the $E_{\mathrm{T}}^{\mathrm{miss}}$ and single muon triggers as well as the single muon trigger matching requirement. The veto on baseline muons or electrons in addition to requirement of a single signal lepton is designed to improve the purity of the single lepton final state predicted by the signal model by removing events in which an additional lepton was produced from the hard scatter and reconstructed as a baseline lepton, yet failed the criteria to be identified as a signal lepton.

5.2.3 Signal Region Definition

In addition to the baseline selection, a veto on jets identified as having been induced by a b quark (a.k.a. a b-jet veto) is applied in the SR to reduce the yield of SM $t\bar{t}$ and single-top processes discussed in Section 4.4. See Section 5.1.2 for details of the b-jet tagging algorithm.

Within each category, the baseline selection is further refined by optimizing the exact placements of upper or lower bounds, also referred to as "cuts", on variables for which the distributions of MC simulated events generated according to the signal model differs appreciably from MC simulated distributions of the SM background processes.

Broadly, the cut placements are optimized to maximize the predicted yield of MC simulated events that model the DH signal process relative to the predicted yield of events that model the SM background processes. However, this basic benchmark fails to account for the fact that, as discussed in Section 4.1, the relative "statistical uncertainty" associated with the limited number of MC simulated events used to calculate yield predictions will increase as the selections are tightened (i.e. as lower bounds are increased or upper bounds are reduced) due to the resulting reduction in the number of MC simulated events that pass the selections. As the relative statistical uncertainty of the predicted yields increases, the ability of the search to confidently identify an excess of ATLAS collision events above the predicted yield of SM background processes - which would be indicative of additional events produced by a BSM process - is reduced. Furthermore, as the predicted yield of events is reduced, the relative statistical uncertainty associated with the number of observed events, derived from the Poisson distribution, will also increase and similarly impact the sensitivity of the search. Therefore, while if is often valuable to tighten certain selections in order to increase the relative predicted yield of the signal process, it is also important to avoid over-tightening them to the point that the statistical uncertainty of the predicted and observed event yields begins to reduce the sensitivity of the search.

A metric known as the "Asimov discovery significance" [154] Z is used as a means of quantifying the sensitivity of a signal region given the predicted yields s and b of the signal and background processes, respectively, while also accounting for the statistical uncertainty σ_b associated with the limited number of MC simulated events used to predict b:

$$Z(s,b,\sigma_b) = \left[2(s+b)\left(\ln\left[\frac{(s+b)(b+\sigma_b^2)}{b^2+(s+b)\sigma_b^2}\right] - \frac{b^2}{\sigma_b^2}\ln\left[1+\frac{\sigma_b^2 s}{b(b+\sigma_b^2)}\right]\right)\right]^{\frac{1}{2}} \tag{5.14}$$

Optimization Strategy for Signal Region Definition

After applying the baseline selections and b-jet veto, the placement of upper and lower bounds is optimized for the selection variables listed in Table 5.3. The SR was kept "blinded" during optimization, which means that only the MC simulated signal and background events were considered, and not the ATLAS collision data. Blinding is done in order to avoid biasing the cut choices on the basis of any trends or fluctuations that may be present in the distributions of ATLAS data in the SR.

The choice of selection variables was made based on a visual assessment of the impact of cuts on all the variables considered as candidate selection variables on the Asimov discovery significance Z. Visualization of Z with respect to the cut placement on each variable is done using so-called "N-1" plots, which are shown for the finalized selections in the merged and resolved SRs, respectively, in Figures 5.10 and 5.11. The N-1 plots are produced for a given variable v and a given set of candidate selections on all other variables as follows:

- Place the candidate selections on all variables except for v.
- In the upper panel, plot the distributions of the background and signal processes, binned in v.
- In the lower panel, plot the distributions of the Asimov discovery significance Z for each signal process plotted in the upper panel.
    - If comparing the placement of an **upper bound** v_u on the variable v: calculate the Asimov significance $Z(v_u)$ for all events with $v < v_u$:

$$\begin{aligned} s_u &= \sum_{i\in\{\text{signal},v(i)<v_u\}} w(i) \\ b_u &= \sum_{i\in\{\text{SM backgrounds},v(i)<v_u\}} w(i) \\ \sigma_{b_u} &= \sqrt{\sum_{i\in\{\text{SM backgrounds},v(i)<v_u\}} \big[w(i)\big]^2} \end{aligned} \tag{5.15}$$

where each event i is implicitly required to have passed all the other candidate selections for the given process (signal or SM backgrounds) in addition to $(v < v_u)$, and $w(i)$ is the event weight associated with event i (see discussion of event weights in Section 4.2.2). The statistical variance $(\sigma_b)^2$ is evaluated in Eq. 5.16 as the sum of squared weights for events in the background process that pass all other candidate selections in addition to $(v < v_u)$. Inserting s_u, b_u and σ_{b_u} into Eq. 5.14:

$$Z(v_u) = Z(s_u, b_u, \sigma_{b_u}) \tag{5.16}$$

- Conversely, if comparing the placement of a **lower bound** v_d: calculate the Asimov significance $Z(v_d)$ for all events with $v > v_d$ by replacing "$v < v_u$" in Eq. 5.16 with "$v > v_d$".

The optimization was performed first in the merged category of the SR, after placing an additional requirement of at least one $R = 1.0$ TAR jet. Once the selections defining the merged SR were finalized, optimization was subsequently performed in the resolved category, with the $N(\text{TAR Jets}) > 0$ requirement replaced by $N(\text{Jets}) > 1$ in addition to a veto on any events that pass the finalized merged SR selections.

Since the optimal placement of selections was found to vary to some extent for MC simulated signal data sets with different m_s and $m_{Z'}$, the cut placements were initially optimized with the aim of maximizing the average Asimov discovery significance for MC simulated data sets at the following four mass points, which cover most of the m_s range considered in the search: $(m_s, m_{Z'}) = \{(210, 2100), (285, 1700), (310, 500), (335, 1000)\}$ GeV. The $m_{Z'}$ values of these four mass points were chosen because they are near the edge of the so-called "exclusion range", which represents the range of m_s and $m_{Z'}$ within which the search was expected to be sensitive to the presence (or absence) of events produced by the DH signal model in the ATLAS data, at a 95% confidence level on the basis of sensitivity projections obtained using the method presented in Section 7.3.3 with the Asimov data set. It is particularly desirable to optimize the cut placements for mass points near the edge of the exclusion range in order to extend this range as much as possible.

An iterative approach was used to optimize cut placements at the four signal points, which combined:

- repeated grid searches, which scanned over 1, 000, 000 candidate multi-dimensional combinations of cut placements on some or all of the optimized variables to identify combinations that maximized Z, and

- visual analysis of N-1 plots such as those shown in Figures 5.10 and 5.11 to visually validate the optimal placements found by the grid searches.

It is worth noting that, inspecting Eq. 5.14, the Asimov discovery significance does not account for the statistical uncertainty σ_s arising from limited MC simulated events in the signal sample. Therefore, in order to ensure that there were sufficient events in the signal samples, the grid search included an option to avoid cut combinations that reduced the predicted signal yield below some acceptable minimum set by the user. After some testing, it was found that setting a minimum acceptable predicted yield of 15 for the signal point $(m_s, m_{Z'}) = (210, 2100)$ GeV was adequate to ensure that the signal samples of interest for cut optimization had a sufficient number of events as to prevent their statistical uncertainty from becoming appreciable compared with other sources of uncertainty. The signal point $(m_s, m_{Z'}) = (210, 2100)$ GeV was chosen to define the minimum yield because, at the time of optimization, it was among the mass points with the lowest predicted yield over the set of $m_{Z'}$ and m_s masses for which MC simulated datasets were produced for the search (also referred to as the "signal grid").

After an optimized set of selections were determined for the four signal points considered in the iterative optimization procedure described above, these selections were validated and further refined by examining the projected sensitivity of the search over the signal grid. Some minor refinements were made to cut placements with the aim of maximizing the exclusion range. See Section 7.3.3 for a description of how the sensitivity is quantified for each MC simulated signal data set, and visualized over the full signal grid. For expediency, only the statistical uncertainties associated with the MC simulation of signal and background processes were considered when evaluating the Asimov discovery significance and the sensitivity projections used for optimization, and the systematic uncertainties presented in Chapter 6 were neglected. The choice to neglect systematic uncertainties was justified by the fact that, following initial efforts to include the dominant theoretical sources of systematic uncertainty in evaluation of the Asimov discovery significance, their inclusion was found to have a negligible impact on the evaluation of optimal cut placements.

Figures 5.10 and 5.11 show N-1 plots with the finalized selections, as well as the placements of cuts, for the $m^{\text{TAR Jet}}$ and $\Delta R(\text{TAR Jet}, \ell)$ ($m(W_{\text{Cand}})$ and $\Delta R(W_{\text{Cand}}, \ell)$)

Table 5.3: List of selection variables, with descriptions, for which the placements of cuts were optimized when designing the merged and resolved signal regions. The third and fourth columns indicate whether the variable is used in the merged category, the resolved category, or both.

Variable	**Description**	**Mgd**	**Res**
$E_{\mathrm{T}}^{\mathrm{miss}}$	A **lower bound** is placed on $E_{\mathrm{T}}^{\mathrm{miss}}$ to select for the production of undetected energetic particles.	✓	✓
$\mathcal{S}$	A **lower bound** is placed on $\mathcal{S}$ to select for a high likelihood that the measured $E_{\mathrm{T}}^{\mathrm{miss}}$ arises from undetected particles rather than limited detector resolution.	✓	✓
$m_{\mathrm{T}}(\ell, E_{\mathrm{T}}^{\mathrm{miss}})$	A **lower bound** is placed on $m_{\mathrm{T}}(\ell, E_{\mathrm{T}}^{\mathrm{miss}})$ to select for a high likelihood of there being sources of $E_{\mathrm{T}}^{\mathrm{miss}}$ in the final state in addition to the neutrino produced by a leptonic $W \to \ell\nu$ decay (See Section 5.1.8 for details).	✓	✓
$m^{\mathrm{TAR\ Jet}}$	Reconstructed mass of the highest-p_{T} $R = 1.0$ TAR jet. A **window cut** around the W boson mass of 80.4 GeV is placed on $m^{\mathrm{TAR\ Jet}}$ to select for events in which the highest-p_{T} $R = 1.0$ TAR jet actually reconstructs the hadronic decay of a boosted W boson, rather than other potential sources of strongly interacting particles.	✓	×
$D_2^{\beta=1}$(TAR Jet)	Energy correlation function of the highest-p_{T} $R = 1.0$ TAR jet. Used to discriminate large-R jets with a two-pronged substructure from those with a single-pronged substructure using the angular separation and transverse momenta of combinations of the jet constituents [155, 156]. An **upper bound** is placed on $D_2^{\beta=1}$(TAR Jet), because the $D_2^{\beta=1}$(TAR Jet) distribution for two-pronged signal events is found to be peaked at lower $D_2^{\beta=1}$(TAR Jet) compared with the SM background events.	✓	×
$\Delta R(\mathrm{TAR\ Jet}, \ell)$	Angular separation in $\eta \times \phi$ space between the TAR jet and lepton. An **upper bound** is placed on $\Delta R(\mathrm{TAR\ Jet}, \ell)$ to select for the expected signal topology in which the TAR jet and the $\ell\nu$ form a collimated system, having originated from the decay of the boosted s.	✓	×
$p_{\mathrm{T}}(W_{\mathrm{Cand}})$	p_{T} of the reconstructed W candidate in the resolved regime. A **lower bound** is placed on the $p_{\mathrm{T}}(W_{\mathrm{Cand}})$ to select for the signal topology in which the W is produced with a large momentum from the decay of a boosted s.	×	✓
$m(W_{\mathrm{Cand}})$	Mass of the reconstructed W candidate in the resolved regime. A **window cut** is placed around the W boson mass of 80.4 GeV.	×	✓
$\Delta R(W_{\mathrm{Cand}}, \ell)$	Angular separation in $\eta \times \phi$ space between the reconstructed W candidate and lepton in the resolved regime. An **upper bound** is placed on $\Delta R(W_{\mathrm{Cand}}, \ell)$ to select for the expected signal topology in which the W candidate and the $\ell\nu$ form a collimated system, having originated from the decay of the boosted s.	×	✓

variables in the merged (resolved) SR. N-1 plots for the other selection variables listed in Table 5.3 can be found in Appendix A. The finalized selections are summarized in Table 5.4 for the merged and resolved SRs, respectively. The lower bound on $E_{\mathrm{T}}^{\mathrm{miss}}$ in the merged SR was ultimately kept at the same value of 200 GeV applied in the baseline selection, because it was found that with the other optimized selections applied there were very few signal and background events with $E_{\mathrm{T}}^{\mathrm{miss}} <$ 250 GeV, and explicitly increasing the lower bound was not found to produce any appreciable improvements in sensitivity.

Table 5.4: Optimized selection criteria for the signal region in the merged and resolved categories.

Merged Selection	**Resolved Selection**
Passes baseline selection	
	Fails merged selection
$N(\text{TAR Jets}) > 0$	$N(\text{Jets}) > 1$
$m_{\mathrm{T}}(\ell, E_{\mathrm{T}}^{\mathrm{miss}}) > 220$ GeV	$m_{\mathrm{T}}(\ell, E_{\mathrm{T}}^{\mathrm{miss}}) > 200$ GeV
$E_{\mathrm{T}}^{\mathrm{miss}} > 200$ GeV	$E_{\mathrm{T}}^{\mathrm{miss}} > 250$ GeV
$\mathcal{S} > 16$	$\mathcal{S} > 16$
68 GeV $< m^{\text{TAR Jet}} <$ 89 GeV	68 GeV $< m(W_{\text{Cand}}) <$ 89 GeV
$\Delta R(\text{TAR Jet}, \ell) < 1.2$	$\Delta R(W_{\text{Cand}}, \ell) < 1.4$
$D_2^{\beta=1}(\text{TAR Jet}) < 1.1$	$p_{\mathrm{T}}(W_{\text{Cand}}) > 150$ GeV

Tables 5.5 and 5.6 show the predicted yields of MC simulated events for the three dominant SM backgrounds after successive application of selections in the merged and resolved SRs respectively, beginning with the baseline selection. Tables 5.5 and 5.6 show the same information for the DH signal model at three sample mass points in $(m_s, m_{Z'})$.

5.2.4 Control regions

There are in general numerous uncertain theoretical parameters involved in modelling signal and SM background processes produced by pp collisions at the LHC, and it is necessary to fix their values when generating the MC simulated events and weights used to predict the yields of these processes in the ATLAS collision data. These include, for example, parameters associated with the parton distribution function used to model the protons involved in the high-energy collisions. A recent review of progress in the determination of parton distribution functions can be found in Ref.

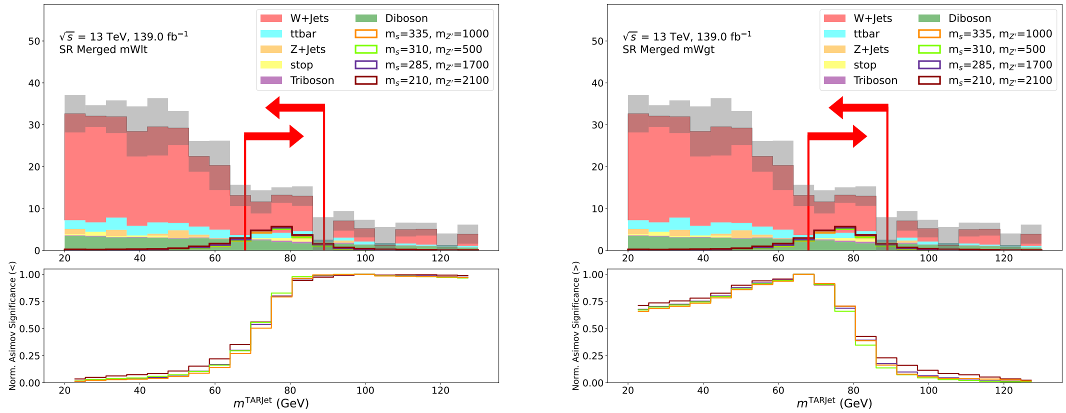

(a) $m^{\text{TAR Jet}}$ Cut (Z evaluated for upper bound)

(b) $m^{\text{TAR Jet}}$ Cut (Z evaluated for lower bound)

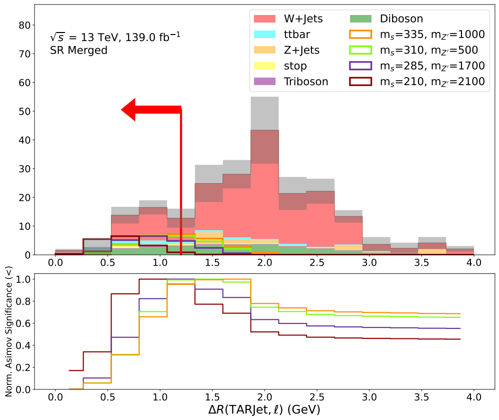

(c) $\Delta R(\text{TAR Jet}, \ell)$

Figure 5.10: N-1 Distributions for the $m^{\text{TAR Jet}}$ and $\Delta R(\text{TAR Jet}, \ell)$ variables used in the merged signal region definition. Grey bands show statistical uncertainty on background estimate. The lower panel shows the cumulative Asimov significance normalized to unit peak, where the direction ($>$ or $<$) specified in the y label indicates whether the significance is being summed from above ($>$) or from below ($<$). Red vertical line and arrow show placement and direction of selection on the given variable in this region.

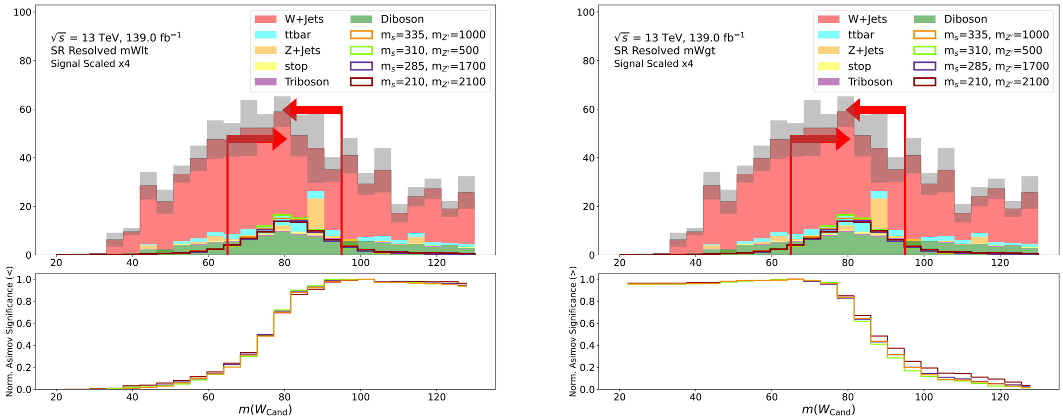

(a) $m(W_{\rm Cand})$ Cut (Z evaluated for upper bound)

(b) $m(W_{\rm Cand})$ Cut (Z evaluated for lower bound)

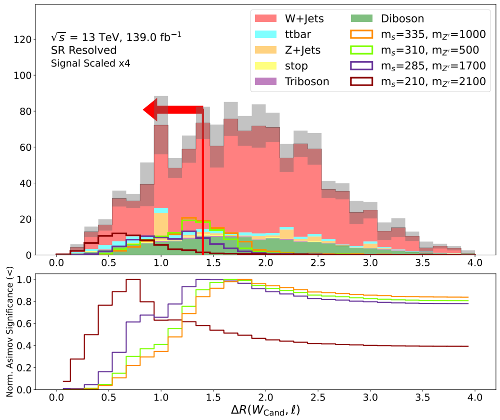

(c) $\Delta R(W_{\rm Cand}, \ell)$

Figure 5.11: N-1 Distributions for the $m(W_{\rm Cand})$ and $\Delta R(W_{\rm Cand}, \ell)$ variables used in the resolved signal region definition. Grey bands show statistical uncertainty on the background estimate. The lower panel shows the cumulative Asimov significance normalized to unit peak, where the direction (> or <) specified in the y label indicates whether the significance is being summed from above (>) or from below (<). Red vertical line and arrow show placement and direction of selection on the given variable in this region.

Table 5.5: Cutflow yields after application of preselection cuts for the dominant SM backgrounds in the merged SR. Percent passage is reported relative to the number of weighted events after application of the baseline selection.

Cut	**W+jets**	$t\bar{t}$	**Diboson**
None	11352445.72	101404110.82	1270378.37
baseline selection	93740.14 (100.00%)	51263.07 (100.00%)	8469.92 (100.00%)
N(TAR Jets) ≥ 1	36957.80 (39.43%)	44993.63 (87.77%)	6887.00 (81.31%)
b-jet veto	34077.64 (36.35%)	5082.68 (9.91%)	6199.93 (73.20%)
$m_{\mathrm{T}}(\ell, E_{\mathrm{T}}^{\mathrm{miss}}) > 220$ GeV	21927.98 (23.39%)	2994.69 (5.84%)	3450.61 (40.74%)
$m^{\mathrm{TAR\ Jet}} \in (68, 89)$ GeV	942.31 (1.01%)	165.13 (0.32%)	206.63 (2.44%)
$\mathcal{S} > 16$	437.27 (0.47%)	21.52 (0.04%)	85.00 (1.00%)
$\Delta R(\mathrm{TAR\ Jet}, \ell) < 1.2$	65.79 (0.07%)	10.30 (0.02%)	21.46 (0.25%)
$D_2^{\beta=1}(\mathrm{TAR\ Jet}) < 1.1$	24.29 (0.03%)	4.29 (0.01%)	7.61 (0.09%)

[157], and recommendations for the evaluation of uncertainties associated with parton distribution function parameters in the context of studies performed with LHC data can be found in Ref. [158].

In some cases, the range of plausible choices for an uncertain parameter, or a set of related uncertain parameters, can produce an associated uncertain range of yield predictions that is non-negligible compared with the statistical yield uncertainties. The resulting uncertainties in predicted yields in the SR can be reduced by constraining the predicted yields using the ATLAS collision data in a kinematically similar region.

W+jets and $t\bar{t}$ control regions (CRs), with enriched yields of these respective SM background processes, are defined in this search with the aim of providing data-driven constraints on the total yield of the W+jets and $t\bar{t}$ backgrounds in the SRs within each of the merged and resolved kinematic categories. As discussed in detail in Section 7.3, the data-driven constraints are obtained within each category by comparing the total yield of MC simulated SM background events to the observed yield of data in the CRs for the given category, and scaling the total predicted yield of the W+jets and $t\bar{t}$ backgrounds in both the CRs and the SRs by multiplicative “normalization factors”, $\mu_{W\text{+jets},\mathrm{category}}$ and $\mu_{t\bar{t},\mathrm{category}}$, such that the total predicted yield of SM background processes within each control region is in close agreement with the observed yield of

Table 5.6: Cutflow yields after application of preselection cuts for the dominant SM backgrounds in the resolved SR. Percent passage is reported relative to the number of weighted events after application of the baseline selection.

Cut	**W+jets**	$\boldsymbol{t\bar{t}}$	**Diboson**
None	11352445.72	101404110.82	1270378.37
baseline selection	93740.14 (100.00%)	51263.07 (100.00%)	8469.92 (100.00%)
Fails merged selection	93552.83 (99.80%)	51178.42 (99.83%)	8435.36 (99.59%)
$N(\text{Jets}) \geq 2$	41566.23 (44.34%)	49150.32 (95.88%)	6624.88 (78.22%)
b-jet veto	38106.85 (40.65%)	5696.57 (11.11%)	5888.39 (69.52%)
$m_{\mathrm{T}}(\ell, E_{\mathrm{T}}^{\mathrm{miss}}) > 200$ GeV	30794.06 (32.85%)	4053.26 (7.91%)	4045.52 (47.76%)
$E_{\mathrm{T}}^{\mathrm{miss}} > 250$ GeV	14965.69 (15.97%)	1639.75 (3.20%)	2366.03 (27.93%)
$m(W_{\mathrm{Cand}}) \in (65, 95)$ GeV	5214.91 (5.56%)	816.93 (1.59%)	941.15 (11.11%)
$\mathcal{S} > 16$	3041.82 (3.24%)	166.35 (0.32%)	429.93 (5.08%)
$\Delta R(W_{\mathrm{Cand}}, \ell) < 1.4$	771.85 (0.82%)	58.37 (0.11%)	114.24 (1.35%)
$p_{\mathrm{T}}(W_{\mathrm{Cand}}) > 150$ GeV	242.64 (0.26%)	21.19 (0.04%)	51.12 (0.60%)

ATLAS collision data.

The selections for the W+jets and $t\bar{t}$ CRs were designed with the following aims in order to provide effective and reliable constraints on the total yield of the respective SM background processes in the SR:

- To obtain a **high purity** of the background process of interest in the CR, as evaluated by its MC simulated yield in the CR relative to other MC simulated background processes. It is important that the predicted event yield in the CR be dominated by the background process of interest, to ensure that the ratio of total MC simulated yield from all SM background processes, $\sum\limits_{\text{process } i} (N_{\mathrm{MC}})_{i,\text{ CR}}$ to the observed yield of ATLAS collision events $(N_{\mathrm{data}})_{\text{observed, CR}}$ in the CR represents a reasonable approximation of the equivalent ratio for the background process $p_{\text{constraint}}$ of interest:

$$\frac{\sum\limits_{\text{process } i} (N_{\mathrm{MC}})_{i,\text{ CR}}}{(N_{\mathrm{data}})_{\text{total observed, CR}}} \approx \frac{(N_{\mathrm{MC}})_{p_{\text{constraint}},\text{ CR}}}{(N_{\mathrm{data}})_{p_{\text{constaint}},\text{ CR}}} \tag{5.17}$$

  where the index i runs over all simulated SM background processes.

Table 5.7: Cutflow yields after application of preselection cuts for three sample signal points in the merged SR. Signal points are labelled in column headers as ($m_{Z'}$, m_s) (units of GeV). Percent passage is reported relative to the number of weighted events after application of the baseline selection.

Cut	**(1000, 360)**	**(1700, 335)**	**(2100, 210)**
None	798.61	396.57	537.03
baseline selection	168.35 (100.00%)	111.66 (100.00%)	143.64 (100.00%)
N(TAR Jets) ≥ 1	147.88 (87.84%)	98.12 (87.87%)	124.98 (87.01%)
b-jet veto	131.89 (78.34%)	87.51 (78.37%)	111.32 (77.50%)
$m_{\mathrm{T}}(\ell, E_{\mathrm{T}}^{\mathrm{miss}}) > 220$ GeV	102.83 (61.08%)	70.82 (63.42%)	92.86 (64.65%)
$m^{\mathrm{TAR\ Jet}} \in (68, 89)$ GeV	45.00 (26.73%)	30.85 (27.63%)	31.88 (22.19%)
$\mathcal{S} > 16$	33.84 (20.10%)	23.97 (21.47%)	24.34 (16.95%)
$\Delta R(\mathrm{TAR\ Jet}, \ell) < 1.2$	15.80 (9.39%)	13.33 (11.94%)	23.20 (16.15%)
$D_2^{\beta=1}$(TAR Jet) < 1.1	11.10 (6.59%)	9.50 (8.51%)	16.19 (11.27%)

- The CR should contain a **relatively large number of MC simulated events** (and consequently a lower relative statistical uncertainty) for the background process of interest compared with the SR. This requirement is designed to ensure that the normalization factors $\mu_{W\text{+jets,category}}$ and $\mu_{t\bar{t}\text{,category}}$ will be constrained predominantly in the overall fit of MC simulated yields to the observed data (see Section 7.3 for details on the fitting strategy) by the comparison with data in the CRs, and also to minimize the statistical uncertainties of the fitted normalization factors associated with the limited number of MC simulated events in the CRs.

- To ensure **orthogonality with the SR**. In order for the CR to provide an unbiased data-driven constraint on the amplitude of a simulated SM background used in the signal region, it must be defined in such a way that no events are shared between these two regions.

- To obtain a **negligibly small contamination of MC simulated signal events**. Negligible signal contamination is needed to ensure that the constraints on normalization factors are obtained purely from known physics processes in the data.

Table 5.8: Cutflow yields after application of preselection cuts for three sample signal points in the resolved SR. Signal points are labelled in column headers as ($m_{Z'}$, m_s) (units of GeV). Percent passage is reported relative to the number of weighted events after application of the baseline selection.

Cut	**(1000, 360)**	**(1700, 335)**	**(2100, 210)**
None	798.61	396.57	537.03
baseline selection	168.35 (100.00%)	111.66 (100.00%)	143.64 (100.00%)
Fails merged selection	152.86 (90.80%)	100.58 (90.08%)	127.22 (88.57%)
$N(\text{Jets}) \geq 2$	138.08 (82.02%)	90.56 (81.10%)	110.52 (76.94%)
b-jet veto	121.13 (71.95%)	79.35 (71.06%)	96.14 (66.93%)
$m_{\mathrm{T}}(\ell, E_{\mathrm{T}}^{\mathrm{miss}}) > 200$ GeV	101.11 (60.06%)	68.49 (61.34%)	84.25 (58.65%)
$E_{\mathrm{T}}^{\mathrm{miss}} > 250$ GeV	78.78 (46.80%)	55.43 (49.64%)	67.87 (47.25%)
$m(W_{\mathrm{Cand}}) \in (65, 95)$ GeV	55.87 (33.19%)	39.09 (35.01%)	42.40 (29.52%)
$\mathcal{S} > 16$	40.37 (23.98%)	28.77 (25.77%)	29.22 (20.34%)
$\Delta R(W_{\mathrm{Cand}}, \ell) < 1.4$	16.84 (10.00%)	14.51 (12.99%)	23.77 (16.55%)
$p_{\mathrm{T}}(W_{\mathrm{Cand}}) > 150$ GeV	13.35 (7.93%)	11.35 (10.16%)	15.87 (11.05%)

- Events in the CR should occupy a **kinematic phase space that is as similar as possible to the SR**. This is important to ensure that the ratio of the MC simulated yield of SM background events to the observed yield of ATLAS collision data in the CR is representative of the equivalent ratio in the SR.

Table 5.9 summarizes the CRs used in the analysis and the cut changes relative to the SR that are used to define each CR. The CRs are discussed in more detail in Section 5.2.4.

W+jets **Control Region Definition**

A W+jets CR (a.k.a. CRW) is defined to obtain a high purity and yield of the W+jets background process by reversing the cut on ΔR (W, ℓ). Orthogonality with the SR is ensured by the reversal of the ΔR (W, ℓ) cut. The lower bound on $E_{\mathrm{T}}^{\mathrm{miss}}$ significance is also reduced to 12 in the merged category of the CR in order to reduce the relative statistical uncertainty by boosting the number of MC simulated events in the region. In addition, after some study the cut on ΔR (W, ℓ) in the merged CRW was tightened

Table 5.9: Summary of control regions.

Control region	**Modified selections relative to the SR**
Merged W+jets CR	$(\Delta R(\text{TAR Jet}, \ell) < 1.2) \rightarrow (\Delta R(\text{TAR Jet}, \ell) > 1.8)$ $(\mathcal{S} > 16) \rightarrow (\mathcal{S} > 12)$
Resolved W+jets CR	$(\Delta R(W_{\text{Cand}}, \ell) < 1.4) \rightarrow (\Delta R(W_{\text{Cand}}, \ell) > 1.4)$
Merged $t\bar{t}$ CR	(N(b-tagged jets) < 1) → N(b-tagged jets) ≥ 2 $(\mathcal{S} > 16) \rightarrow (\mathcal{S} > 12)$
Resolved $t\bar{t}$ CR	(N(b-tagged jets) < 1) → N(b-tagged jets) ≥ 2

from a simple reversal - ($\Delta R(\text{TAR Jet}, \ell) < 1.2$) $\rightarrow$ ($\Delta R(\text{TAR Jet}, \ell) > 1.2$) - to a slightly increased lower bound of ($\Delta R(\text{TAR Jet}, \ell) > 1.8$) in order to reduce the predicted yield of signal processes in the CR to an acceptable level.

The motivation for reversing the ΔR selection is that, as shown schematically in Figure 5.12, a ΔR reversal would largely reverse the directions of the lepton and neutrino in the W+jets process described in Section 4.4.1, without modifying the kinematic details of the hadronic activity that fakes a hadronically-decaying W candidate for this process in the SR. As a result, the modelling of W+jets events in this ΔR-reversed region would be expected to be similar to W+jets events in the SR, with the exception of the reversed lepton and neutrino directions in the $W \rightarrow \ell\nu$ decay.

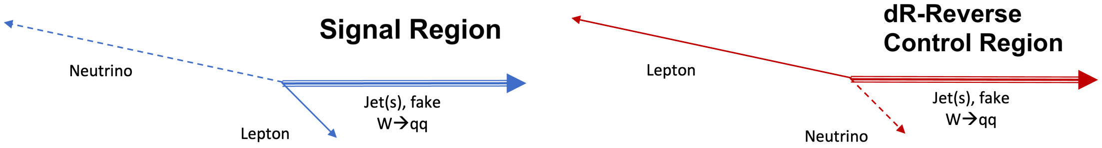

Figure 5.12: Comparison of typical event topologies between the SR and the W+jets CR, showing that the typical directions of the lepton and neutrino relative to hadronic activity faking the hadronically-decaying W boson are simply reversed.

Kinematic distributions of interest are compared between the W+jets CRs and the SRs in Figures B.1 and B.2 in Appendix B.1.

A comparison of the $E_{\mathrm{T}}^{\mathrm{miss}}$ distributions between the merged SR and CRW in Figures B.1i and B.1j indicates some bias towards lower $E_{\mathrm{T}}^{\mathrm{miss}}$ for events that pass the merged CRW selection. This difference is attributable to two factors. First, because the $\mathcal{S}$ is in general expected to be positively correlated with $E_{\mathrm{T}}^{\mathrm{miss}}$, the loosened $\mathcal{S}$ cut of $\mathcal{S} > 12$ in the merged CRW compared with $\mathcal{S} > 16$ in the SR would be expected to allow a larger proportion of low-$E_{\mathrm{T}}^{\mathrm{miss}}$ events into the region. The impact of the loosened $\mathcal{S}$ selection in the merged CRW is shown in Figure 5.13 by comparing the $E_{\mathrm{T}}^{\mathrm{miss}}$ distribution between the merged SR and the merged CRW, either with or without the loosened $\mathcal{S}$ selection in the merged CRW. Tightening the $\mathcal{S}$ lower bound is seen to remove most of the low-$E_{\mathrm{T}}^{\mathrm{miss}}$ bias in the merged CRW. The small remaining bias towards low $E_{\mathrm{T}}^{\mathrm{miss}}$ in the merged CRW even after tightening the $\mathcal{S}$ selection is attributed to the expected reversal of the neutrino direction in the ΔR-reversed topology of W+jets background in the CRW, such that it becomes approximately aligned with the high-pt TAR jet rather than recoiling against both the TAR jet and the lepton. The neutrino p_{T} required to conserve momentum in the ΔR-reversed topology will on average be somewhat smaller due to the approximately opposing momenta of the lepton and the TAR jet. Since the neutrino constitutes the only source of true $E_{\mathrm{T}}^{\mathrm{miss}}$ in the W+jets background, this implies that the $E_{\mathrm{T}}^{\mathrm{miss}}$ distribution would be expected to become somewhat biased to lower values in the CRW topology, as observed.

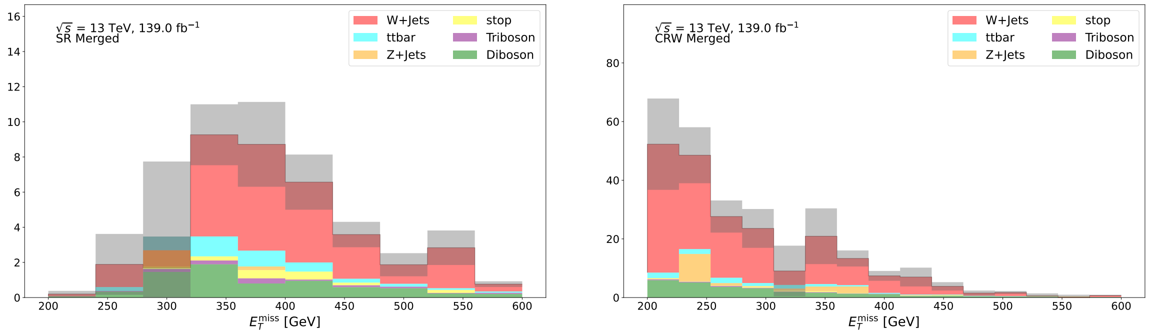

(a) merged SR

(b) merged CRW ($\mathcal{S} > 12$)

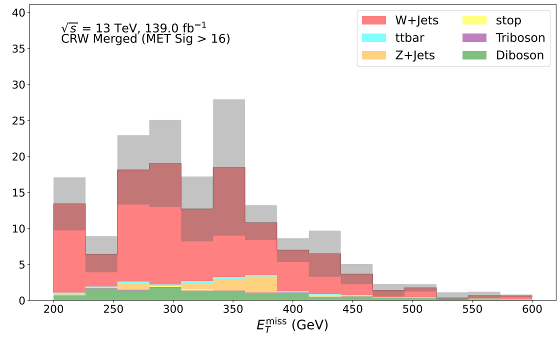

(c) merged CRW ($\mathcal{S} > 16$)

Figure 5.13: Comparison of N-1 distributions between the merged SR (top left) and the merged CRW, with the lower bound on $\mathcal{S}$ in the merged CRW either kept at its nominal value of 12 (upper right), or tightened (bottom) to match the $\mathcal{S} > 16$ cut applied in the merged SR.

A comparison of Figures B.1i and B.1j shows that, though present, this bias in the $E_{\mathrm{T}}^{\mathrm{miss}}$ distribution is much more subtle in the resolved SR. This is attributed to the fact that the lower bound on $\mathcal{S}$ is not loosened compared with the SR in the resolved category, in addition to the relatively low p_{T} of the hadronic activity that the neutrino is approximately aligned with in the CRW.

Based on the comparable shapes of the other kinematic distributions in the merged and resolved categories, it is concluded that the kinematics of events in the W+jets CRs are sufficiently similar to those in the SR of the corresponding category that the constraints on normalization of the W+jets background evaluated in the W+jets CRs can be reasonably applied in the SR.

Table 5.10 compares the yield and relative composition of the W+jets background in the SRs with the W+jets CRs. Figures 5.14 and 5.15 compare the signal yield and signal/background between the SR and the W+jets CR in the merged and resolved categories, respectively. The W+jets background constitutes over 75% of the predicted yield of SM background processes in both CRs, making it the dominant SM background process, with signal contamination below 2.5% for all signal points. Thanks to the boost in the number of MC simulated events in the CRs afforded by the reversal of the ΔR cut, as well as the reduced lower bound on $\mathcal{S}$ in the merged CR, the relative statistical uncertainties of the predicted W+jets yields are reduced by factors of 2 and 1.5 in the CRW compared with the SR in the merged and resolved categories, respectively. This ensures that the normalization of the W+jets background process can be predominantly established in the W+jets CR with a reasonably low statistical uncertainty.

The benchmark used to evaluate the maximum acceptable level of signal contamination in a given CR is as follows: if the predicted yield of the signal process is negligibly small (i.e. less than ~half as large) compared with the statistical uncertainty associated with the predicted yield of all SM background processes in the CR, then the level of signal contamination is considered acceptably small, since the presence or absence of the signal process would not be detectable given the statistical uncertainty of the total predicted yield. In the merged W+jets CR, the predicted signal yield is at most 5.1 (from Figure 5.14a, which is negligibly small compared with the total background yield uncertainty of 24.5 (from the third row in Table 5.10). The signal yields in the resolved CRW are similarly small compared with the statistical uncertainty of the total background yield.

$t\bar{t}$ Control Region Definition

Given that b-tagged jets are vetoed in the SR to reduce the yield of events produced by the $t\bar{t}$ process, a reversal of this veto presents a straightforward opportunity to define an orthogonal CR enriched with $t\bar{t}$ events. Early studies found that while a simple reversal of the b-jet veto in the SR selection to instead require at least one b-tagged jet was sufficient to obtain a $t\bar{t}$-enriched region with a substantially larger sample of simulated $t\bar{t}$ events compared with the SR, the contamination of signal

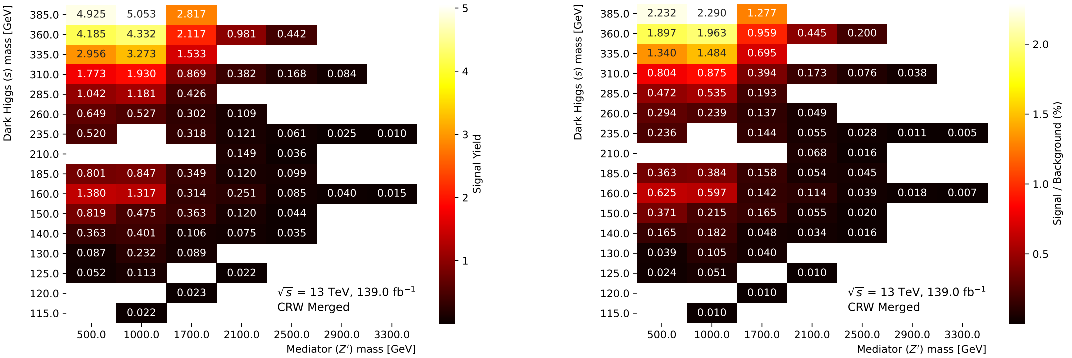

(a) Signal yield in merged W+jets control region

(b) Signal / background in merged $W+$ jets control region

Figure 5.14: Predicted yields of MC simulated events (left), and ratio of predicted signal / SM background yields (right) for all signal points in the merged $W+$jets control region.

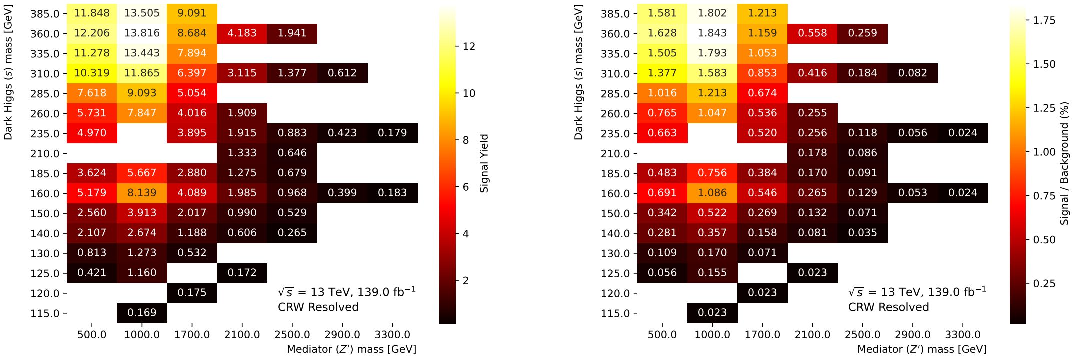

(a) Signal yield in resolved W+jets control region

(b) Signal / background in resolved $W+$ jets control region

Figure 5.15: Predicted yields of MC simulated events (left), and ratio of predicted signal / SM background yields (right) for all signal points in the resolved $W+$jets control region.

Table 5.10: Comparison of the W+jets background yield, total background yield, and the composition of the W+jets background relative to the total background. Uncertainties on the relative composition are obtained from the sum of squared event weights.

Region	**W+jets Yield**	**Total Background Yield**	**Relative W+jets Composition**
Merged SR	24.3±7.2	40.1±7.3	(60.6±21.1)%
Resolved SR	243.5±19.6	339.9±24.0	(71.6±7.7)%
Merged CRW	164.0±23.6	220.6±24.5	(74.3±13.5)%
Resolved CRW	598.1±30.4	749.5±31.0	(79.8±5.2)%

events in the region was found to be too high for a control region.

Further tightening the b-jet veto reversal to require at least two b-tagged jets was found to reduce the signal contamination in this $t\bar{t}$ CR to a reasonable level on the basis of the benchmark requirement of negligible signal yield compared with the statistical uncertainty of the total background yield discussed above in the context of the W+jets CR. However, due to the associated reduction in the number of MC simulated $t\bar{t}$ events that pass this tightened requirement, it was deemed necessary to reduce the lower bound on $\mathcal{S}$ in the merged $t\bar{t}$ CR to $\mathcal{S} > 12$, as is done in the merged W+jets CR, in order to increase the number of simulated events admitted for the $t\bar{t}$ process.

Table 5.11 summarizes the modifications made to the SR selections to define the $t\bar{t}$ CR in both the merged and resolved categories.

Table 5.12 compares the yield and relative composition of the $t\bar{t}$ background in the SRs with those in the $t\bar{t}$ CRs. Figures 5.16 and 5.17 compare the signal yield and signal/background between the SR and the $t\bar{t}$ CR in the merged and resolved categories, respectively. As expected, the reversal of the $t\bar{t}$ veto produces a region that is highly enriched in $t\bar{t}$ events, which constitute 90% of the predicted yield in the $t\bar{t}$ CR. The merged and resolved $t\bar{t}$ CRs admit comparable yields of $\sim 65-70$ $t\bar{t}$ events, which in both categories constitutes a several-fold increase in the predicted yield compared with the SR. Comparing the predicted signal yields in the merged and resolved CRTT, shown in Figures 5.16a and 5.17a respectively, with the statistical uncertainties associated with the total yield of events in these CRTTs from Table 5.11, the predicted signal yields are in all cases well below the statistical uncertainty of the background yield, and thus constitute a reasonably low level of signal contamination in the CRTT.

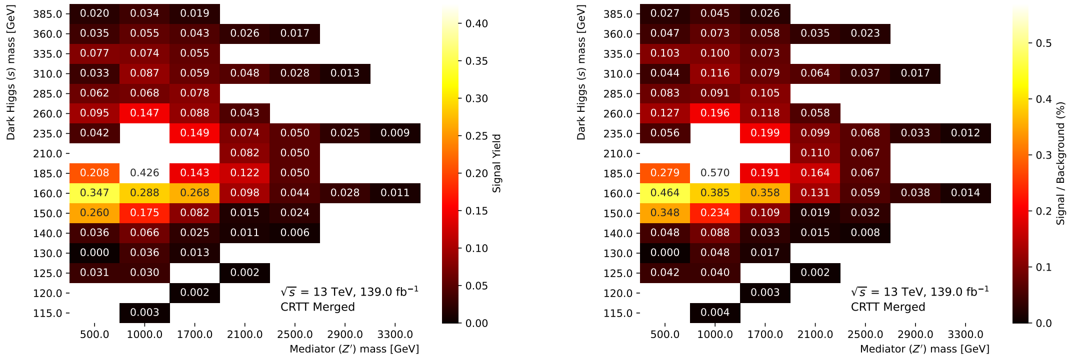

(a) Signal yield in merged $t\bar{t}$ control region

(b) Signal / background in merged $t\bar{t}$ enriched control region

Figure 5.16: Predicted yields of MC simulated events (left), and ratio of predicted signal / SM background yields (right) for all signal points in the merged $t\bar{t}$ control region.

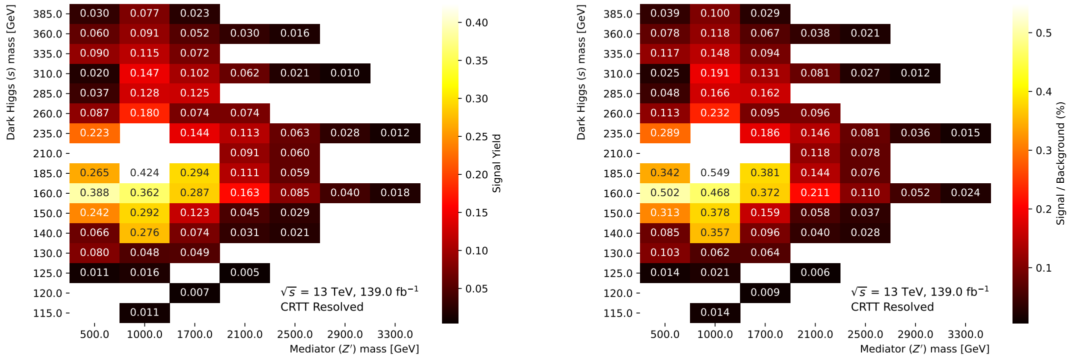

(a) Signal yield in resolved $t\bar{t}$ control region

(b) Signal / background in resolved $t\bar{t}$ enriched control region

Figure 5.17: Predicted yields of MC simulated events (left), and ratio of predicted signal / SM background yields (right) for all signal points in the resolved $t\bar{t}$ control region.

Table 5.11: Summary of differences in selections on $N(b\text{-jet})$ and $\mathcal{S}$ between signal regions and $t\bar{t}$ control regions.

Region	**b-tagged Jet Veto/Requirement**	**$\mathcal{S}$ Cut**
Merged SR	$N(b\text{-jet}) = 0$	$\mathcal{S} > 16$
Resolved SR	$N(b\text{-jet}) = 0$	$\mathcal{S} > 16$
Merged CRTT	$N(b\text{-jet}) > 1$	$\mathcal{S} > 12$
Resolved CRTT	$N(b\text{-jet}) > 1$	$\mathcal{S} > 16$

Table 5.12: Comparison of the $t\bar{t}$ background yield, total background yield, and the composition of the $t\bar{t}$ background relative to the total background. Uncertainties on the relative composition are obtained from the sum of squared event weights.

Region	**$t\bar{t}$ Yield**	**Total Background Yield**	**$t\bar{t}$ Relative Composition**
Merged SR	4.3±0.3	40.1±7.3	(10.7±2.1)%
Resolved SR	21.2±0.7	339.9±24.0	(6.2±0.5)%
Merged CRTT	70.5±1.7	74.8±5.0	(94.2±6.7)%
Resolved CRTT	64.2±1.2	73.3±4.9	(83.1±3.4)%

Kinematic distributions of interest are compared between the $t\bar{t}$ CRs and the SRs in Figures B.3 and B.4 in Appendix B.2. A similar bias towards lower $E_{\mathrm{T}}^{\mathrm{miss}}$ that was discussed in the context of the merged W+jets CR is also seen in the merged CRTT, and is similarly attributable to the loosened lower bound on $\mathcal{S}$ in this region. The level of shape agreement in the other distributions is considered to be close enough to conclude that events in the $t\bar{t}$ CR occupy a sufficiently similar region of kinematic phase space as events in the SR to justify applying data-driven $t\bar{t}$ normalization constraints obtained in this CR to the SR.

5.2.5 Background Yields

Tables 5.13 and 5.14 show the overall background yields in the merged and resolved analysis regions, respectively, after application of all the analysis selections described in this section.

Table 5.13: Background yields after application of all analysis cuts in the merged analysis regions. Uncertainty on the yields is statistical.

Background	**Merged SR**	**Merged CRW**	**Merged CRTT**
W+jets	24.2 ± 7.2	164.0 ± 23.6	-1.3 ± 4.6
$t\bar{t}$	4.3 ± 0.3	9.9 ± 0.6	70.4 ± 1.6
Diboson	7.6 ± 0.3	26.8 ± 1.5	0.2 ± 0.0
Triboson	1.2 ± 0.1	1.9 ± 0.1	0.0 ± 0.0
Z+jets	1.1 ± 0.9	15.2 ± 6.3	0.0 ± 0.0
single t	1.6 ± 0.5	2.7 ± 0.6	5.4 ± 0.9
Total	40.1 ± 7.3	220.6 ± 24.5	74.8 ± 5.0

Table 5.14: Background yields after application of all analysis cuts in the resolved analysis regions. Uncertainty on the yields is statistical.

Background	**Resolved SR**	**Resolved CRW**	**Resolved CRTT**
W+jets	243.5 ± 19.6	598.1 ± 30.4	1.5 ± 2.2
$t\bar{t}$	21.2 ± 0.7	20.0 ± 0.7	64.2 ± 1.2
Diboson	51.1 ± 1.1	105.5 ± 1.5	0.6 ± 0.0
Triboson	3.0 ± 0.2	5.6 ± 0.3	0.0 ± 0.0
Z+jets	17.4 ± 13.7	17.1 ± 6.0	0.0 ± 0.0
single t	3.7 ± 0.8	3.2 ± 0.7	11.0 ± 1.2
Total	339.9 ± 24.0	749.5 ± 31.0	77.3 ± 2.8

5.3 Triggers

As discussed in Section 3.4.5, the ATLAS trigger system only saves collision events that pass both the hardware-based level-1 (L1) trigger and the software-based high-level trigger (HLT). The L1 trigger and the HLT are each comprised of numerous sets of selection criteria, which are also referred to as triggers. Any collision event that satisfies at least one of the triggers that comprise the L1 trigger is processed by the HLT. Likewise, if the event satisfies any of the triggers that comprise the HLT, it will be saved for later analysis.

The search presented in this thesis is interested in events that produce a single energetic lepton due to the $s \to WW(q\bar{q}\ell\nu)$ decay, in addition to high $E_{\mathrm{T}}^{\mathrm{miss}}$ due both to the undetected boosted DM in the final state, and to the undetected ν from the $W \to \ell\nu$ decay. It is important to determine the efficiency with which the ATLAS trigger system accepts events in the region of phase space defined by the event selections described in Section 5.2 above. This efficiency quantifies the probability that an event that the triggers are designed to accept successfully passes the trigger criteria and gets accepted. If the trigger efficiency is $< 100\%$ in any area of the phase space considered in the analysis, it is in general necessary to apply scale factors to any MC simulated events that fall into this phase space to account for the fact that some of these events would have been rejected by the trigger during actual data-taking. It is also then necessary to evaluate and propagate uncertainties associated with these scale factors.

To simplify the trigger efficiency analysis and determine whether any scale factors may be needed, it is helpful to identify a minimal list of triggers that all events considered in the analysis would be expected to pass. One of the event selection criteria for the analysis, presented in Section 5.2, requires all events to have $E_{\mathrm{T}}^{\mathrm{miss}} > 200$ GeV. Since the ATLAS $E_{\mathrm{T}}^{\mathrm{miss}}$ trigger, described in Refs. [159] and [160], is designed to efficiently select events with $E_{\mathrm{T}}^{\mathrm{miss}} > 150$ GeV, it is reasonable to expect events that pass the event selection criteria to have also passed the $E_{\mathrm{T}}^{\mathrm{miss}}$ trigger with a high efficiency. The specific $E_{\mathrm{T}}^{\mathrm{miss}}$ triggers in the ATLAS trigger menu that are considered in this study are chosen following ATLAS recommendations, and vary between different data collection periods defined by ATLAS. The full list of $E_{\mathrm{T}}^{\mathrm{miss}}$ triggers used, along with the associated data collection period for each, is listed in Table 5.15.

The ATLAS trigger system also includes single-muon and single-electron triggers, which are designed to pass events in which a single muon (electron) is reconstructed in the final state and satisfies some minimum p_{T} requirement. Since all events considered in the search are required to have a single lepton in the final state, events which pass the event selection would also be expected to pass these charged lepton triggers with high efficiency. The specific single muon and electron triggers considered in this study, along with the ATLAS data-taking period(s) in which they were applied and the minimum lepton p_{T} requirement associated with each trigger, are listed in Tables 5.16 and 5.17, respectively.

The lepton triggers are known to be $< 100\%$ efficient, but the resulting scale factors and associated systematic uncertainties are in general well calibrated by ded-

Table 5.15: Summary of $E_{\mathrm{T}}^{\mathrm{miss}}$ triggers from the ATLAS trigger menu used for the search, along with the associated data collection period for each trigger.

Period	**MET Trigger**
2015	HLT_xe70_mht
2016 (A-D3)	HLT_xe90_mht_L1XE50
2016 (D4-F1)	HLT_xe100_mht_L1XE50
2016 (F2-)	HLT_xe110_mht_L1XE50
2017 (B-D5)	HLT_xe110_pufit_L1XE55
2017 (D6-K)	HLT_xe110_pufit_L1XE50
2018 (B-C5)	HLT_xe110_pufit_xe70_L1XE50
2018 (C5-)	HLT_xe110_pufit_xe65_L1XE50

icated measurements performed within the ATLAS collaboration. As a result, the charged lepton triggers are useful as a means of independently quantifying the efficiency of the $E_{\mathrm{T}}^{\mathrm{miss}}$ trigger, as will be shown in a moment. However, if the $E_{\mathrm{T}}^{\mathrm{miss}}$ trigger can be shown to pass the events considered in this search with 100% efficiency then there is no need to apply scaling factors or evaluate related uncertainties.

The efficiency of the $E_{\mathrm{T}}^{\mathrm{miss}}$ trigger for a set of event selection criteria that define a given region "X" is defined equivalently for ATLAS data ("data") and MC simulated events ("MC"). Events considered for the calculation of trigger efficiency are also required to have passed the single lepton trigger (defined as the logical OR of the single muon trigger and the single electron trigger), to independently ensure that all data events considered passed a trigger that is relevant to the final state of interest. The trigger efficiency is given by:

$$\mathrm{eff}_{E_{\mathrm{T}}^{\mathrm{miss}},\ \mathrm{region\ X}} = \frac{\sum_i w_i \ \text{passing } (E_{\mathrm{T}}^{\mathrm{miss}} \text{ triggers})\&(\text{single lepton triggers})\&(\text{selection cuts for region X})}{\sum_i w_i \ \text{passing (single lepton triggers) AND (selection cuts for region X)}} \tag{5.18}$$

where w_i is the total event weight for event i ($w_i = 1$ in the case of data). See Section 4.2.2 for a detailed discussion of weights that are assigned to the MC simulated events. Correction scale factors, dependent on the p_{T} and η of the final-state lepton in each event, are included in the MC event weights in Eq. 5.18 to account for the $< 100\%$ trigger efficiency of the single lepton triggers.

Table 5.16: Summary of single muon triggers from the ATLAS trigger menu used for the search, along with the associated data collection period for each trigger. The minimum muon p_{T} threshold of each trigger is also listed.

Periods	**Single Muon Trigger**	**Muon p_{T} threshold**
2015	HLT_MU20_ILOOSE_L1MU15	20 GeV
2016 (A, B-D3, D4-E, F-G2, G3-I3, I4-), 2017 (B-), 2018	HLT_MU50	50 GeV
2016	HLT_MU24_ILOOSE	24 GeV
2015, 2016 (A)	HLT_MU40	40 GeV
2016 (B-D3, D4-E)	HLT_MU24_IVARMEDIUM	24 GeV
2016 (D4-E, F-G2, G3-I3, I4-), 2017 (B-), 2018	HLT_MU26_IVARMEDIUM	26 GeV

Figure 5.18 compares the $E_{\mathrm{T}}^{\mathrm{miss}}$ trigger efficiency defined in Eq. 5.18 for MC simulated events and ATLAS data for the region defined with the baseline selections, with the following modifications:

- A range of lower bounds on the $E_{\mathrm{T}}^{\mathrm{miss}}$ are considered, from $\sim$ 100 GeV to $\sim$ 500 GeV.
- The single charged lepton is required to be an electron (a.k.a. the "electron channel") in Figure 5.18a and a muon (a.k.a. the "muon channel") in Figure 5.18b.

Comparing the trigger efficiencies in the electron channel (Figure 5.18a) and the muon channel (Figures 5.18b and 5.18c), the efficiency in the electron channel converges to 100% for $E_{\mathrm{T}}^{\mathrm{miss}} > 200$ GeV, but in the muon channel it instead converges to $\sim 97\%$ for $E_{\mathrm{T}}^{\mathrm{miss}} > 200$ GeV. After some investigation, the inefficiency in the muon channel was found to be due to events with large $E_{\mathrm{T}}^{\mathrm{miss}}$ arising from high-p_{T} muons. This is because high-p_{T} muons leave very little energy in the ATLAS calorimeter and are detected instead by the muon spectrometer. As a result, such high-p_{T} muon events can be missed by the $E_{\mathrm{T}}^{\mathrm{miss}}$ triggers, which don't use information from the muon spectrometer (see Section 3 of Ref. [160] for details of the construction of $E_{\mathrm{T}}^{\mathrm{miss}}$ for the

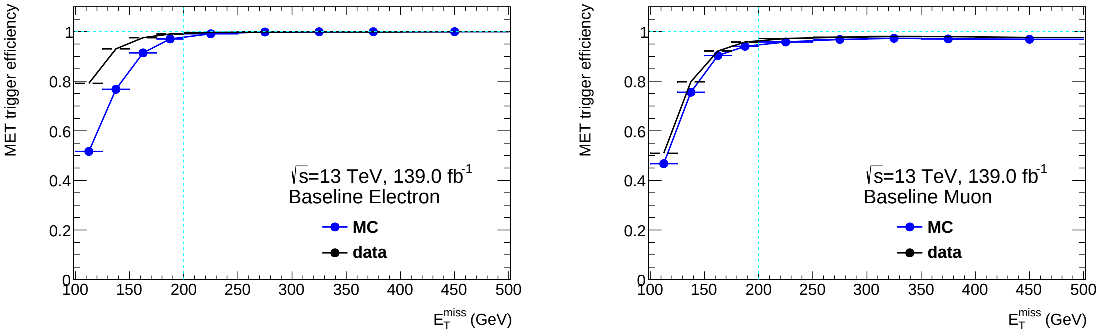

(a) Electron Channel

(b) Muon Channel

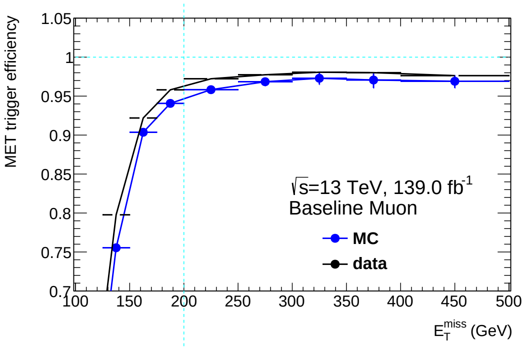

(c) Muon Channel (y-axis range reduced)

Figure 5.18: Comparison of the $E_{\mathrm{T}}^{\mathrm{miss}}$ trigger efficiency defined in Eq. 5.18, as a function of the $E_{\mathrm{T}}^{\mathrm{miss}}$ lower bound in the event selection, between MC simulated events and ATLAS data in a region defined by the baseline selection. The event selection is separated into electron (top left) and muon (top right and bottom center) channels.

Table 5.17: Summary of single electron triggers from the ATLAS trigger menu used for the study presented in Section 5.3, along with the associated data collection period for each trigger. The minimum electron p_{T} threshold of each trigger is also listed.

Periods	**Single Muon Trigger**	**Electron p_{T} threshold**
2015	HLT_e24_lhmedium_L1EM20VH	24 GeV
2015	HLT_e60_lhmedium	60 GeV
2015	HLT_e120_lhloose	120 GeV
2016 (A, B-D3)	HLT_e24_lhtight_nod0_ivarloose	24 GeV
2016 (A, B-D3, D4-F, G-), 2017 (B-), 2018	HLT_e60_lhmedium_nod0	60 GeV
2016 (A, B-D3, D4-F, G-)	HLT_e60_medium	60 GeV
2016 (A, B-D3, D4-F, G-), 2017 (B-), 2018	HLT_e300_etcut	300 GeV
2016 (A, B-D3, D4-F, G-), 2017 (B-), 2018	HLT_e140_lhloose_nod0	140 GeV
2016 (D4-F, G-), 2017 (B-) 2018	HLT_e26_lhtight_nod0_ivarloose	26 GeV

ATLAS $E_{\mathrm{T}}^{\mathrm{miss}}$ trigger). This can be seen by plotting the $E_{\mathrm{T}}^{\mathrm{miss}}$ trigger efficiency using a calculation of $E_{\mathrm{T}}^{\mathrm{miss}}$ in the event selection that ignores the muon p_{T} (a.k.a. "muon invisible") in Figure 5.19, and observing that in this case the efficiency converges to 100% for $E_{\mathrm{T}}^{\mathrm{miss}}$ (muon invisible) > 200 GeV.

It was found that high-$E_{\mathrm{T}}^{\mathrm{miss}}$ events in the muon channel that fail the $E_{\mathrm{T}}^{\mathrm{miss}}$ trigger do, however, pass the muon trigger with high efficiency. For this reason, the efficiency of a logical OR of the $E_{\mathrm{T}}^{\mathrm{miss}}$ and single muon triggers is studied in the muon channel. The ($E_{\mathrm{T}}^{\mathrm{miss}}$ OR single muon) trigger efficiency is calculated as follows for MC simulated events in a given region "X":

$$\mathrm{eff}_{E_{\mathrm{T}}^{\mathrm{miss}}\text{ OR single muon, MC, region X}} = \frac{\sum_i w_i \text{ passing } (E_{\mathrm{T}}^{\mathrm{miss}} \text{ OR single muon triggers) AND (in region X)}}{\sum_i w_i \text{ in region X}} \tag{5.19}$$

where the event weight w_i in the numerator includes the scale factors to correct for

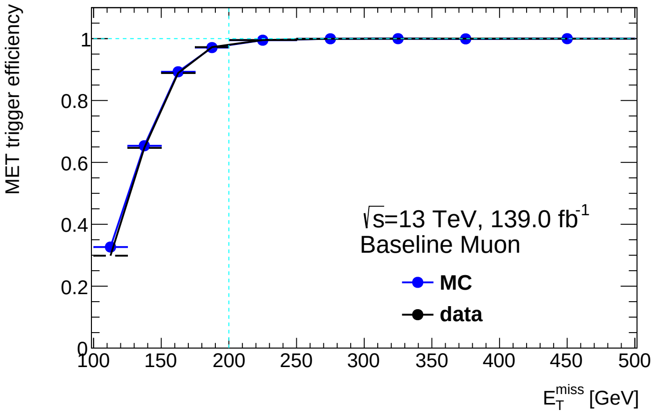

Figure 5.19: $E_{\mathrm{T}}^{\mathrm{miss}}$ trigger efficiency, as a function of the $E_{\mathrm{T}}^{\mathrm{miss}}$ lower bound with the baseline event selection applied in the muon channel, with muons treated as invisible in the calculation of $E_{\mathrm{T}}^{\mathrm{miss}}$.

the known $< 100\%$ trigger efficiency of the single muon trigger. Note that since Eq. 5.19 is evaluated only for MC simulated events, there is no need for an independent trigger in the numerator and denominator such as the single lepton trigger included in Eq. 5.18. As shown in Figure 5.20, the $E_{\mathrm{T}}^{\mathrm{miss}}$ OR single muon trigger is found to be effectively 100% efficient, given the application of appropriate scale factors for the single muon trigger, in the muon channel with the baseline event selection for all lower bounds on the $E_{\mathrm{T}}^{\mathrm{miss}}$ down to ~ 100 GeV.

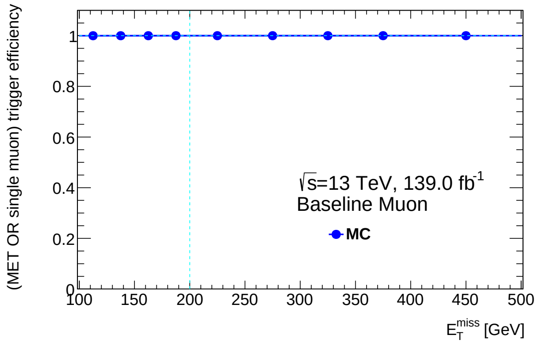

Figure 5.20: Efficiency of the $E_{\mathrm{T}}^{\mathrm{miss}}$ OR single muon trigger, as a function of the $E_{\mathrm{T}}^{\mathrm{miss}}$ lower bound, for the baseline event selection in the muon channel.

Based on the analysis presented in this section, it is concluded that, if all events considered in the analysis are explicitly required to have passed the ($E_{\mathrm{T}}^{\mathrm{miss}}$ OR single muon) trigger, the trigger efficiency is known to be 100% for all events, except for the small subset of events with a high-p_{T} muon that pass the muon trigger but fail the $E_{\mathrm{T}}^{\mathrm{miss}}$ trigger. For these events, scaling factors are included in the event weight to correct for the known $< 100\%$ efficiency of the single muon trigger. An additional "trigger-matching" requirement is applied for events that fail the $E_{\mathrm{T}}^{\mathrm{miss}}$ trigger but pass the single muon trigger. This requirement ensures that the final state muon object that activated the single muon trigger can be identified as the same muon object (i.e. as having originated from the same muon) that was used to reconstruct the signal muon used in the search.

Chapter 6

Systematic Uncertainties

In order to properly assess the significance of any discrepancies between predicted yields of signal and SM background and of the observed collision data, it is important to assign uncertainties to all sources that may limit the precision and accuracy of yield predictions. In addition to a limited precision arising from statistical uncertainty[1], there may be inaccuracies in the values of various parameters input to the simulation due to a limited precision with which their values are known. These inaccuracies can systematically shift predicted production rates and kinematic properties of the simulated processes. Systematic uncertainties aim to quantify the uncertainty of predicted yields of signal and SM background processes within each region and bin[2] used in the search that could result from each source of potential inaccuracy in the modelling.

Systematic uncertainties (or simply "systematics") are broadly classified into two categories according to their origin: theoretical and experimental. Theoretical systematics account for inaccuracies that could result from a limited knowledge of parameters involved in modelling the production and decay mechanisms resulting from *pp* collision events at the LHC. Experimental systematics are evaluated to account for the limited accuracy and precision involved with the highly detailed model used to simulate the operation of the ATLAS detector. In addition to the limited precision of the measured LHC beam luminosity, uncertainties arise from a wide range of sources involved with simulating the detection and reconstruction of collision events. These include limitations associated with the Geant4 model [124] used to simulate the passage of particles through the detector, with modelling the data acquisition

---

[1] See Chapter 4.1 for a discussion of the origin of statistical uncertainty in MC simulations.

[2] See Section 7.2 for details of the binning in $\min(m_s)$ performed in the SR

and readout systems employed by each sub-detector[3], and with simulating the reconstruction and identification of physics objects[4] using the simulated readouts from all the sub-detectors. Additional uncertainties arise from time-dependent modifications to the simulation, such as the reweighting of simulated events to account for time-varying pileup[5] conditions in the detector.

Experimental systematics are generally constrained in the process of calibrating particular physics objects reconstructed in the ATLAS detector using the ATLAS collision data, and as a result are generally considered quite well-defined and robust. In contrast, the choice of uncertainty to assign to theoretical parameters can be much less clear, as constraints from experimental results may be sparse, or in some cases such as appropriate choice of renormalization scale in perturbative QCD calculations, essentially non-existent (see Section 9.1 of Ref. [22] for a review of running coupling and the renormalization scale).

Experimental and theoretical systematic uncertainties are evaluated in all analysis regions and bins for the SM background processes. Due to the negligible yield of the DH signal process in the CRs, systematic uncertainties are only evaluated for the signal process in the SRs.

6.1 Experimental Systematics

Experimental systematics are evaluated for all physics objects considered in the search, and for the LHC beam luminosity.

The integrated luminosity $\mathcal{L}_{\text{int}}$ recorded by the ATLAS detector for the full data set considered in this search is known with a precision of 1.7% [161]. Since, from Eq. 1.2, the total number of recorded collision events scales linearly with the integrated beam luminosity, propagating this ±1.7% systematic to the yields results in coherent 1.7% up and down shifts of the predicted yield for each process across all analysis regions and bins.

For a given systematic uncertainty on a parameter k used in the reconstruction of physics objects, the general procedure for propagating the systematic uncertainty to the predicted yield N_p of a process p in a bin j is as follows:

---

[3] See Section 3.4 for a description of the ATLAS sub-detectors.

[4] See Section 5.1 for a presentation of the reconstructed physics objects used in this search.

[5] See Section 4.2.2 for a discussion of the pileup reweighting weight used to account for time-varying pileup conditions in the detector.

- Repeat the reconstruction with k shifted up by one standard deviation: k up $= k + \sigma_k$.
- Evaluate the predicted yield in the bin $N_{p,\ k\ \mathrm{up},\ \mathrm{bin}\ j}$ with updated simulation. The "up" systematic yield uncertainty is:

  $$\mathrm{syst}(\mathrm{exp},\ p,\ k\ \mathrm{up},\ \mathrm{bin}\ j) = N_{p,\ k\ \mathrm{up},\ j} - N_{p,\ \mathrm{nom},\ j} \tag{6.1}$$

  where $N_{p,\ \mathrm{nom},\ j}$ is the nominal yield.
- Repeat the above process with k shifted down by one standard deviation to evaluate the "down" systematic uncertainty.

Due to statistical uncertainties arising from the limited number of MC events available to evaluate shifted yields, asymmetries between the up and down yield shifts in the above procedure can occur simply due to statistical fluctuations in the number of events that fall into each bin, rather than from actual asymmetries in the underlying distribution being sampled. For this reason, the propagated yield systematics are symmetrized in each bin as follows:

$$\mathrm{syst}(\mathrm{exp},\ p,\ k\ \mathrm{symm},\ \mathrm{bin}\ j) = \pm\left(\frac{N_{p,\ k,\ \mathrm{up},\ j} - N_{p,\ k,\ \mathrm{down},\ j}}{2}\right) \tag{6.2}$$

Table 6.1 summarizes the sources of experimental systematics considered for all physics objects in the search.

Figure 6.1 shows the envelope of all symmetrized shifts in the total predicted yield of all SM backgrounds in the SRs due to the sources of experimental systematics considered for each type of physics object. Figure 6.2 shows the same set of envelopes for a sample signal point at $(m_s, m_{Z'}) = (210, 2100)$ GeV. Comparing the yield shifts associated with the reconstruction of the various physics objects, the experimental systematics are dominated by sources of uncertainty associated with the reconstruction of $R = 0.4$ jets and $R = 0.2$ TAR subjets in the merged SR. The $R = 0.2$ TAR subjets uncertainties produce relatively small yield shifts in the resolved SR because TAR jets are not used in this region. Shifts in predicted yield are also notably smaller for the signal model compared with the SM background processes.

Tables 6.2 and 6.3 show a sample breakdown of systematic uncertainties associated with the total predicted yield of SM background processes in the SRs and CRs,

Table 6.1: Sources of experimental systematic uncertainty considered for all physics objects used in the search.

Physics Object	**Systematic Uncertainties Considered**
Electrons	– Reconstruction, ID and isolation efficiency – Energy scale and resolution
Muons	– Reconstruction, ID and isolation efficiency – Trigger efficiency – Energy scale and resolution – Track-to-vertex association
$R = 0.4$ Jets	– Energy scale and resolution – Quark flavour composition – Jet-vertex association – Pileup – b-tagging efficiency
TAR jets	– $R = 0.2$ subjets input to TAR algo (consider same sources as for $R = 0.4$ jets) – Uncertainties associated with tracks input to TAR algo
$E_{\mathrm{T}}^{\mathrm{miss}}$	– Soft terms used in $E_{\mathrm{T}}^{\mathrm{miss}}$ calculation (note that uncertainties associated with other objects used in the $E_{\mathrm{T}}^{\mathrm{miss}}$ calculation are propagated to $E_{\mathrm{T}}^{\mathrm{miss}}$, so are not classified as $E_{\mathrm{T}}^{\mathrm{miss}}$ systematics)

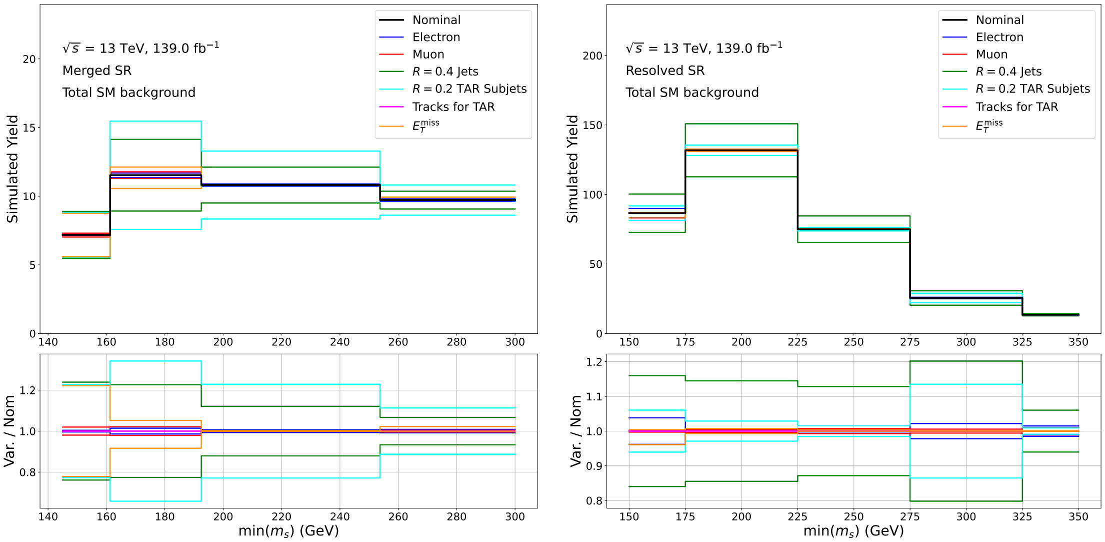

(a) Merged SR (b) Resolved SR

Figure 6.1: Envelope of shifts in the total predicted yield of SM background processes in the merged (left) and resolved (right) SRs due to experimental systematics associated with each physics object considered in the search. The predicted yield is binned in min(m_s) using the binning strategy employed in the fit used to search for evidence of the DH signal model in the data (see Chapter 7 for details). Bottom panel shows ratio of the shifts relative to the nominal yield.

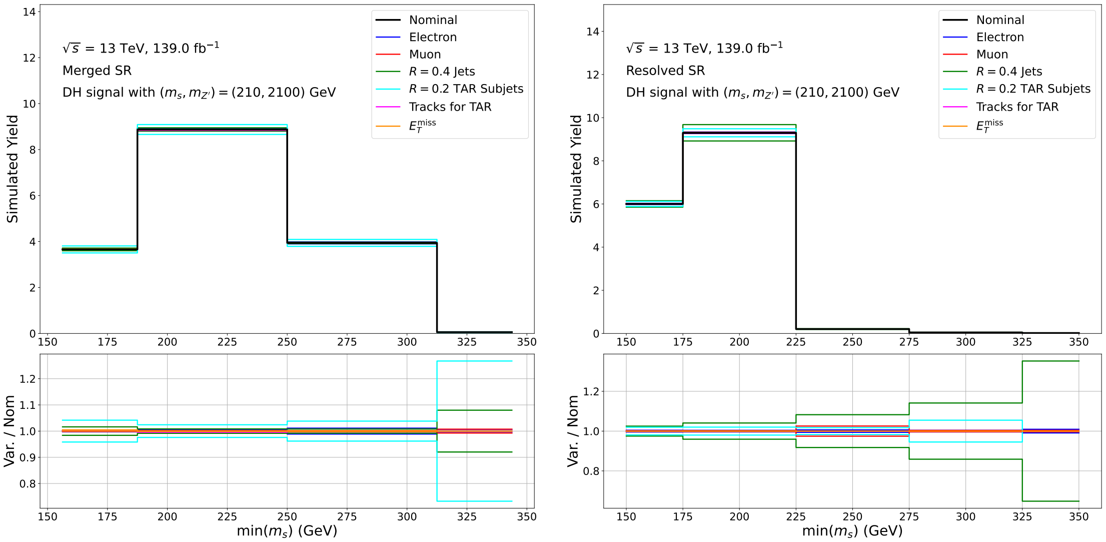

(a) Merged SR

(b) Resolved SR

Figure 6.2: Envelope of shifts in the predicted yield of the DH signal process at $(m_s, m_{Z'}) = (210, 2100)$ in the merged (left) and resolved (right) SRs due to experimental systematics associated with each physics object considered in the search. The predicted yield is binned in $\min(m_s)$ using the binning strategy employed in the fit used to search for evidence of the DH signal model in the data (see Chapter 7 for details). Bottom panel shows ratio of the shifts relative to the nominal yield.

respectively, which arise from shifting uncertain parameters associated with the reconstructed jet energy resolution (JER) of $R = 0.4$ jets by $\pm\sigma$. The $R = 0.4$ JER systematics are shown because they produce relatively large shifts in predicted yields compared with other experimental sources.

Table 6.2: Symmetrized uncertainties in the total predicted yields of all SM background processes in the merged and resolved SRs due to varying parameters associated with jet energy resolution (JER) by $\pm 1\sigma$. Uncertainties are reported as percent shift relative to nominal yield.

Name of JER parameter	**Mgd SR**	**Res SR**
JET_JER_DataVsMC_MC16	±2.92%	±0.85%
JET_JER_EffectiveNP_10	±0.29%	±0.11%
JET_JER_EffectiveNP_11	±0.62%	±1.41%
JET_JER_EffectiveNP_12restTerm	±0.78%	±1.30%
JET_JER_EffectiveNP_1	±1.80%	±0.10%
JET_JER_EffectiveNP_2	±0.25%	±2.48%
JET_JER_EffectiveNP_3	±0.46%	±2.33%
JET_JER_EffectiveNP_4	±0.29%	±0.55%
JET_JER_EffectiveNP_5	±1.94%	±2.62%
JET_JER_EffectiveNP_6	±1.05%	±1.64%
JET_JER_EffectiveNP_7	±0.42%	±1.46%
JET_JER_EffectiveNP_8	±0.73%	±0.01%
JET_JER_EffectiveNP_9	±0.86%	±0.49%

6.2 Theoretical Systematics

The sources of theoretical uncertainty considered in this search, as well as the methods used to evaluate the resulting uncertainties in predicted yields for the various processes relevant to the search, are discussed in the following sections. Some sources are only evaluated for a subset of the processes considered in the search.

Table 6.4 summarizes the theoretical uncertainties that are evaluated for each

Table 6.3: Symmetrized up and down uncertainties in total predicted yield of all SM background processes in the merged and resolved CRs due to varying parameters associated with jet energy resolution (JER) by $\pm 1\sigma$. Uncertainties are reported as percent shift relative to nominal yield.

Name of JER parameter	**Mgd CRW**	**Res CRW**	**Mgd CRTT**	**Res CRTT**
JET_JER_DataVsMC_MC16	±0.27%	±0.24%	±12.07%	±15.00%
JET_JER_EffectiveNP_10	±0.17%	±0.32%	±12.07%	±22.03%
JET_JER_EffectiveNP_11	±0.17%	±0.65%	±12.07%	±18.64%
JET_JER_EffectiveNP_12restTerm	±0.42%	±1.02%	±12.07%	±2.92%
JET_JER_EffectiveNP_1	±0.63%	±0.21%	±12.07%	±4.31%
JET_JER_EffectiveNP_2	±1.03%	±0.25%	±12.07%	±6.03%
JET_JER_EffectiveNP_3	±0.44%	±0.14%	±12.07%	±23.77%
JET_JER_EffectiveNP_4	±0.92%	±1.24%	±0.00%	±39.84%
JET_JER_EffectiveNP_5	±0.01%	±0.06%	±12.07%	±20.10%
JET_JER_EffectiveNP_6	±0.54%	±1.24%	±12.07%	±6.32%
JET_JER_EffectiveNP_7	±0.21%	±0.30%	±0.00%	±5.43%
JET_JER_EffectiveNP_8	±0.05%	±1.04%	±0.00%	±10.51%
JET_JER_EffectiveNP_9	±0.86%	±0.61%	±12.07%	±13.51%

process[6].

6.2.1 Use of Acceptance for Evaluating Theoretical Systematics of the DH Signal Model

For the SM background processes, the systematic uncertainties of predicted yields due to theoretical sources are in general evaluated directly using yield shifts induced by varying the uncertain parameter. Following ATLAS guidelines, theoretical uncertainties associated with the modelling of the DH signal process are instead evaluated in a given bin by calculating the relative shift in the so-called “acceptance”. The acceptance is defined for a given process p as the ratio of yield in the given bin with all analysis selection applied, relative to the inclusive yield of the process with no selections applied:

---

[6] Due the relatively low yield and small number of MC simulated events admitted into the analysis regions for the Z+jets process and the similarity in the production mechanisms for the W+jets and Z+jets processes, theoretical uncertainties are not explicitly calculated for the Z+jets process. Instead, all relative theoretical uncertainties evaluated in each bin j for the W+jets process syst(theo unc, W+jets, j)$/N_{W+\text{jets, nominal, } j}$ are also assigned to the Z+jets process.

Table 6.4: Summary of theoretical uncertainties evaluated for each process considered in the search.

Source	**W+jets**	**Diboson**	**Triboson**	**Z+jets**	**$t\bar{t}$**	**Single Top**	**DH Signal**
PDF	✓	✓	✓	✓	✓	✓	✓
α_s (PDF)	✓	✓	✓	✓	×	×	×
α_s (ISR)	×	×	×	×	✓	✓	×
μ_R and μ_F	✓	✓	✓	✓	✓	✓	✓
ME	×	×	×	×	✓	✓	×
PS	✓	✓	✓	✓	✓	✓	✓
$Wt/t\bar{t}$ Int.	×	×	×	×	×	✓	×

$$\text{acc(p, bin j)} = \frac{N(p,j)}{N(p,\text{inclusive})} \tag{6.3}$$

The uncertainty in the predicted yield in each bin is then evaluated by multiplying the relative shift in acceptance by the nominal yield in the bin:

$$\text{syst}(p,\,\text{up},\,\text{bin }j) = N_{p,\text{ nom},\ j}\left(\frac{\text{acc}(p,\,\text{up},\,j) - \text{acc}(p,\,\text{nom},\,j)}{\text{acc}(p,\,\text{nom},\,j)}\right) \tag{6.4}$$

Unless a given uncertainty applies exclusively to the signal model, the methods used to evaluate the uncertainties in the yield associated with each theoretical source are for the sake of brevity presented in their direct application to the yield, as would be used for background processes. In general, the presented methods would be applied rather to the acceptance when considering the DH signal process, and the yield uncertainty would subsequently be derived from the relative acceptance uncertainty using Eq. 6.4.

6.2.2 Modelling the Parton Distribution Function

Uncertainties associated with the parton distribution function[7] (PDF) used to model the substructure of protons involved in LHC collisions can affect the predicted cross sections of production and decay processes at the LHC. Following ATLAS guidelines and recommendations from the *PDF4LHC* [158] working group, generator weights[8] of events simulated for all processes are re-evaluated for 100 replicas of the nominal PDF. Each replica is obtained by randomly re-sampling all uncertain inputs to the PDF model and re-evaluating the PDF with the new inputs [162]. The yield in each region and bin is re-evaluated with each set of generator weights, and the uncertainty of the yield in each bin for a given process is estimated as the standard deviation over all yield variations [158].

6.2.3 Strong Coupling Constant α_s

The nominal PDF is produced with the strong coupling constant α_s set to its currently accepted value of $\alpha_s(m_Z^2) = 0.1180 \pm 0.0015$ [158] at a momentum scale m_Z.

---

[7] See Section 3.1 for an introduction to the parton model and parton distribution functions.

[8] See discussion of generator weights in Section 4.2.2

α_s in PDF Modelling

For the W+jets, diboson and triboson processes generated using SHERPA 2.2, alternative generator weights are produced using PDFs re-evaluated with α_s varied up or down by its ±0.0015 uncertainty. Following the *PDF4LHC* prescription, the yield N_p for a given process p is re-evaluated in each bin j with the alternative generator weights, and the uncertainty is evaluated as:

$$\text{syst}(\alpha_s,\, p,\, \text{bin } j) = \pm\left(\frac{N_{p,\, \alpha_s+1\sigma,\, j} - N_{p,\, \alpha_s\text{-}1\sigma,\, j}}{2}\right) \tag{6.5}$$

and added in quadrature with the PDF uncertainties discussed in Section 6.2.2.

Strong Coupling Constant in the Modelling of Initial State Radiation (ISR)

For the single-top and $t\bar{t}$ processes generated using the POWHEG BOX matrix element generator interfaced with the PYTHIA 8 parton shower generator, the effect of varying the strong α_s used to model initial state radiation (ISR) from $\alpha_{s,\,\text{ISR}} = 0.1$ to $\alpha_{s,\,\text{ISR}} = 0.15$ is evaluated using the up and down Var3c A14 tune variation [163], and the associated yield uncertainty in each bin is evaluated as half the resulting difference of yields, as in Eq. 6.5.

6.2.4 Renormalization and Factorization Scales (μ_R and μ_F) in QCD

In the framework of perturbative QCD, the strong coupling constant is expressed as a function of the "renormalization scale" μ_R, which is unphysical in the sense that the values of physical observables should be independent of μ_R. However, the choice of μ_R can impact the calculated values of observables in perturbative QCD calculations due to missing higher-order terms in truncated expansions. See Section 9.1 of Ref. [22] for a review of running coupling and the renormalization scale. A similar effect is seen with the "factorization scale" μ_F used in calculations of the proton PDF (see, for example, Section 9.2 of Ref. [22]), which effectively quantifies the resolution with which the proton is probed in a collision. As with μ_R, the choice of μ_F has no physical meaning, but affects the calculated values of observables due to missing higher-order terms in truncated QCD expansions.

To account for the unphysical impact of the choice of μ_R and μ_F on simulated observables, generator weights are re-evaluated for each process with μ_R and μ_F varied by factors of either $\frac{1}{2}$ or 2 in pairwise combinations (i.e. $(\mu_R, \mu_F) \rightarrow \{(\frac{1}{2}\mu_R, \mu_F), (\mu_R, 2\mu_F)\},$

etc.) from their values used for the nominal event generation. Following ATLAS guidelines, the systematic uncertainty in the yield in each bin is evaluated as the envelope of yield variations over all pairwise combinations of μ_R and μ_F variations, excluding the extreme off-diagonals $\{(\frac{1}{2}\mu_R, 2\mu_F), (2\mu_R, \frac{1}{2}\mu_F)\}$:

$$\text{syst}(\text{scale, up, } p\text{, bin } j) = \max\left[0, \max_{k\in\{\mu_R,\mu_F \text{ var'ns}\}} \left\{N_{p,\, k,\, j} - N_{p,\, \text{nom},\, j}\right\}\right] \tag{6.6}$$

where “max”→“min” for the “down” variation.

6.2.5 Matrix Element (ME) Generator Comparison

For the $t\bar{t}$ and single-top processes, for which separate generators are used to calculate the ME (Powheg Box) for the hard scatter process and model the subsequent parton shower (Pythia 8), an uncertainty associated with the choice of using Powheg Box to calculate the ME is obtained by comparing the nominal yield predictions with those obtained using an alternate MadGraph5_aMCNLO [130] generator. The associated uncertainty in the predicted yield for a given process p ($t\bar{t}$ or single-top) in bin j is evaluated using the difference in yield obtained with the alternate ME calculator:

$$\text{syst}(\text{ME, } p\text{, bin } j) = \pm\Big(N_{p,\, \text{ME=MadGraph5\_aMCNLO},\, j} - N_{p,\, \text{nom},\, j}\Big) \tag{6.7}$$

6.2.6 Parton Showering (PS)

Uncertainties associated with the modelling of the PS are evaluated for all processes. The approach used to evaluate these uncertainties for a given process differs depending on which package, or set of packages, was used to generate the nominal set of MC simulated events for the process.

Alternate PS Generator

For the $t\bar{t}$, single-top and DH signal processes for which separate packages are used to calculate the ME and to model the subsequent PS, an uncertainty associated with the choice of PS generator is evaluated by comparing the predicted yields obtained with the nominal Pythia 8 PS generator with an alternate Herwig 7 [164, 165] generator. In analogy with the evaluation of ME uncertainty described in Section 6.2.5 above, the associated uncertainty in yield is evaluated for the $t\bar{t}$ and single-top processes as:

$$\text{syst(PS, } p\text{, bin } j) = \pm\Big(N_{p,\ \text{PS=H}\textsc{erwig}\,7,\ j} - N_{p,\ \text{nom},\ j}\Big) \tag{6.8}$$

For the DH signal model, MC simulated samples are generated with the alternate HERWIG 7 PS generator at three sample points in m_s and $m_{Z'}$:

- $(m_s, m_{Z'}) = (160, 1000)$ GeV
- $(m_s, m_{Z'}) = (160, 2100)$ GeV
- $(m_s, m_{Z'}) = (310, 1000)$ GeV

For each choice of PS generator - nominal or alternate - all three sets of samples generated at the mass points listed above are statistically combined, with the cross section excluded from the event weights[9]. The cross section is excluded when combining the samples to prevent the signal points at m_s = 160 GeV with larger cross sections from dominating the shape of the combined sample. Using the combined DH sample, the relative uncertainty in the predicted acceptance associated with the alternate PS generator is evaluated as:

$$\text{(rel. syst)(PS, comb. DH, bin } j) = \pm\left(\frac{\text{acc}_{\text{comb. DH, PS=H}\textsc{erwig}\,7,\ j} - \text{acc}_{\text{comb. DH, nom},\ j}}{\text{acc}_{\text{comb. DH, nom},\ j}}\right) \tag{6.9}$$

This relative uncertainty is then applied to the DH signal yields at all m_s and $m_{Z'}$:

$$\text{syst}_{(\text{PS},\ (m_s,\ m_{Z'}),\ \text{bin } j)} = \pm\Big[\text{(rel. syst)(PS, combined DH, } j)\Big] \times \Big[N_{(m_s,\ m_{Z'}),\ \text{nom},\ j}\Big] \tag{6.10}$$

CKKW and QSF PS Systematics

For the W+jets, diboson and triboson processes, the SHERPA 2.2 generator is used to model both the ME calculation and the PS. Since it is not in general possible to disentangle the ME and PS components of the SHERPA 2.2 event simulation, the uncertainty associated with the PS shower generation is instead evaluated by varying

---

[9] see Section 4.2.2 for a detailed discussion of event weights

the following theoretical parameters in the parton showering model implemented in Sherpa 2.2:

- The "merging scale" Q_{cut} is used to merge the matrix element associated with partonic emissions with the ensuing parton shower evolution in the CKKW scheme [166, 132]. This merging scale is set to 20 GeV for the nominal event generation. Following ATLAS guidelines, the uncertainty associated with the choice of Q_{cut} is evaluated by producing alternate MC simulated samples with Q_{cut} varied to either $Q_{\text{cut, down}} = 15$ GeV or $Q_{\text{cut, up}} = 30$ GeV.
- The "resummation scale" μ_{QSF} is used in modelling parton shower evolution (see Section 9.2.3.3 of Ref. [22] for a review of resummation in QCD calculations). Following ATLAS guidelines, the uncertainty associated with the choice of μ_{QSF} is evaluated producing alternate samples with μ_{QSF} varied by factors of either $\frac{1}{2}$ or 2.

Evaluation Strategy for the W+jets Process

For the W+jets process, event weights associated with up and down variations of the Q_{cut} and μ_{QSF} scales are evaluated by the method described in Ref. [167] using truth-level[10] MC simulated samples that were generated with each scale variation. These event weights are used to re-evaluate the predicted yield of W+jets events in all regions and bins for each scale variation, and the associated uncertainty is calculated as half the difference in yields between up and down variations:

$$\text{syst}_{(\text{CKKW (QSF)},\ W+\text{jets, bin } j)} = \pm\left(\frac{N_{W+\text{jets},\ Q_{\text{cut}}\ \text{up}\ (\mu_{\text{QSF, up}}),\ j} - N_{W+\text{jets},\ Q_{\text{cut}}\ \text{down}\ (\mu_{\text{QSF, down}}),\ j}}{2}\right) \tag{6.11}$$

Evaluation Strategy for Diboson and Triboson Processes

For the diboson and triboson processes, predicted yields are evaluated for each truth-level sample of MC simulated diboson events generated with variations of the Q_{cut} and μ_{QSF} scales, and for the nominal truth-level sample, in a single "inclusive" region defined by the following selection on truth-level observables:

---

[10] See Section 4.2 for information on the distinction between truth-level and reconstruction-level simulation

- (1 signal muon) or (1 signal electron)
- (1 or more $R = 1.0$ large-R jet[11]) or (2 or more $R = 0.4$ jets)
- $E_{\mathrm{T}}^{\mathrm{miss}} > 150$ GeV
- $m_{\mathrm{T}}(\ell, E_{\mathrm{T}}^{\mathrm{miss}}) > 150$ GeV

The inclusive region is designed to contain all of the analysis regions used in the search, with the lower bounds on $E_{\mathrm{T}}^{\mathrm{miss}}$ and $m_{\mathrm{T}}(\ell, E_{\mathrm{T}}^{\mathrm{miss}})$ placed as high as possible in order to reflect the kinematics of events in the analysis regions, while still admitting enough simulated events to ensure that statistical yield fluctuations are sub-dominant in comparison to the yield shifts resulting from varying Q_{cut} and μ_{QSF}. Within this inclusive region, the relative uncertainty in yield is evaluated for each set of scale variations as:

$$(\text{rel. syst})_{(\text{CKKW (QSF), diboson})} = \pm\left(\frac{N_{\text{diboson (tr.)}, Q_{\text{cut}}\text{ up }(\mu_{\text{QSF, up}}), \text{incl.}} - N_{\text{diboson (tr.)}, Q_{\text{cut}}\text{ down }(\mu_{\text{QSF, down}}), \text{incl.}}}{2 \times N_{\text{diboson (tr.), nom, incl.}}}\right) \tag{6.12}$$

The relative uncertainty $(\text{rel. syst})_{(\text{CKKW (QSF), diboson})}$ is applied to the yield in each analysis region and bin in the reconstruction level diboson and triboson[12] samples:

$$\text{syst}_{(\text{CKKW (QSF), diboson (triboson), bin } j)} = \pm\left[(\text{rel. syst})_{(\text{CKKW (QSF), diboson})}\right] \times \left[N_{\text{diboson (triboson), nom, } j}\right] \tag{6.13}$$

Combination of CKKW and QSF Systematics

For each process, the CKKW and QSF systematic uncertainties are combined in quadrature to obtain an overall estimate of the total uncertainty associated with the parton shower modelling.

---

[11] The TAR jets used in the search are by default built at reconstruction level. At truth level, the TAR jets are approximated by $R = 1.0$ jets constructed using the anti-k_t algorithm [118].

[12] The relative CKKW and QSF uncertainty evaluated for the diboson process is also applied to the triboson process because there are currently no MC simulated samples available for the triboson process with Q_{cut} and μ_{QSF} varied.

6.2.7 Interference Between single-top Wt and $t\bar{t}$ Processes at NLO

Interference between the mechanisms for single-top (Wt) and $t\bar{t}$ production (details of which can be found in Ref. [168]) is accounted for when simulating the single-top process to obtain an accurate prediction of the combined production rate for the two processes. Two theoretical schemes, diagram removal (DR) and diagram subtraction (DS) have been developed to handle this interference. The DR scheme is used to generate the nominal MC simulated samples for the single-top process, and an uncertainty associated with the choice of interference handling scheme is evaluated by generating alternate samples for the single-top process using the DS scheme. The associated uncertainty in the predicted yield of the single-top process is evaluated in each bin j as:

$$\text{syst}(Wt/t\bar{t},\text{ single-top, bin } j) = \pm\Big(N_{\text{single-top, DS, } j} - N_{\text{single-top, nom, } j}\Big) \qquad (6.14)$$

6.2.8 Shifts in Predicted Yields due to Theoretical Systematic Uncertainties

Figure 6.3 shows yield variations associated with all sources of theoretical uncertainty presented in this section in the merged SR for sample processes.

Tables 6.5 and 6.6 summarize the uncertainties associated with the total predicted yield from all theoretical sources for each background process in the SRs and CRs, respectively.

6.3 Relative Impact of Statistical and Systematic Uncertainties in Analysis Regions

Table 6.9 compares the statistical uncertainty associated with the total MC simulated yield of all background processes in each analysis region with the combined statistical+systematic uncertainty. The combination of systematic uncertainties from all sources is done within the HistFitter framework used to perform the statistical analysis for the search (see Chapter 7 for details). Table 6.10 shows the same comparison for the DH signal model at a sample mass point. As discussed in Section 7.1.2, shifts in the predicted yield of a given process induced by varying a given systematic source are treated as correlated between all regions and bins in the fit. Yield shifts associated with experimental sources are additionally treated as correlated between all

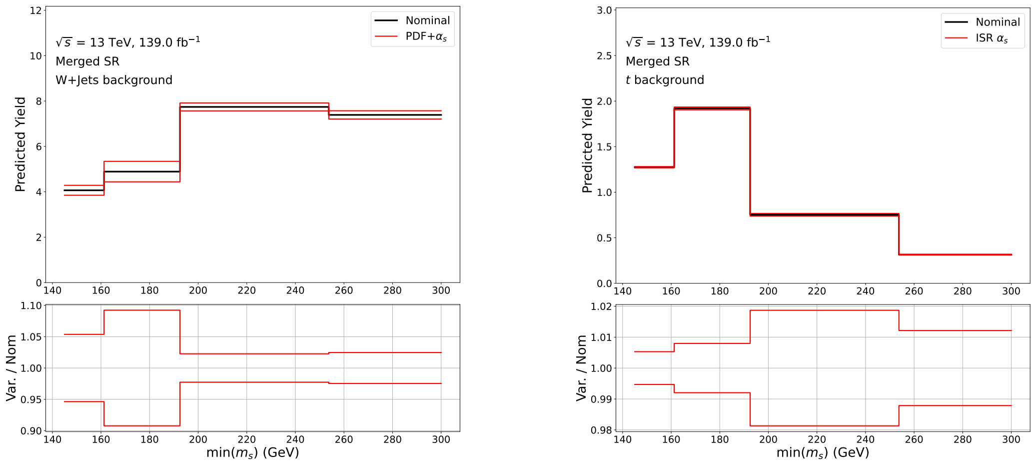

(a) PDF+α_s for W+jets background

(b) ISR α_s for $t\bar{t}$ background

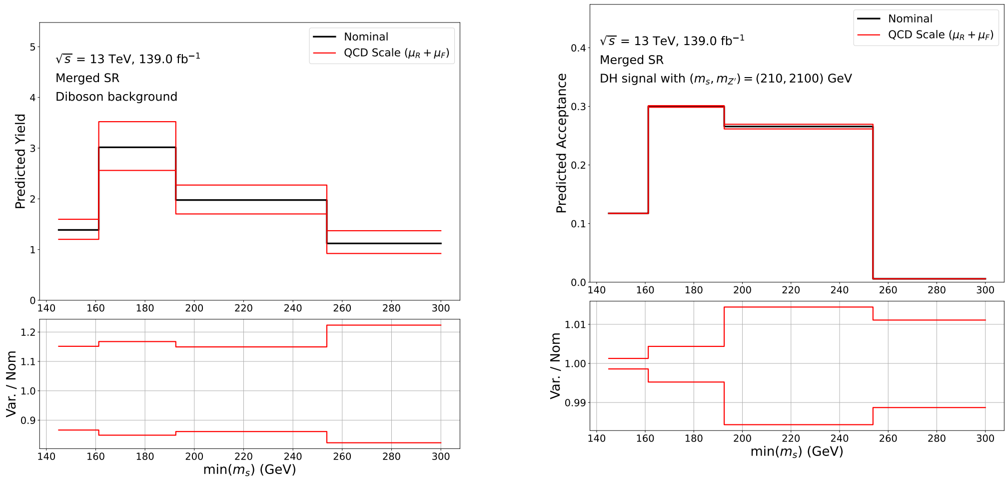

(c) $\mu_R + \mu_F$ for diboson background

(d) $\mu_R + \mu_F$ for DH signal at $(m_s, m_{Z'}) = (210, 2100)$ GeV

Figure 6.3: Shifts in the predicted yield of various processes considered in the search in the merged SRs due to theoretical systematic uncertainties. The predicted yield is binned in min(m_s) using the binning strategy employed in the fit used to search for evidence of the DH signal model in the data (see Chapter 7 for details). Bottom panel shows ratio of the shifts relative to the nominal yield.

processes.

For the SM background, the combined systematic uncertainty is comparable in size to the statistical uncertainty in the merged SR, but all other analysis regions the combined systematic uncertainty is dominant. For the DH signal process, the statistical uncertainty dominates in the merged SR, but is comparable to the combined

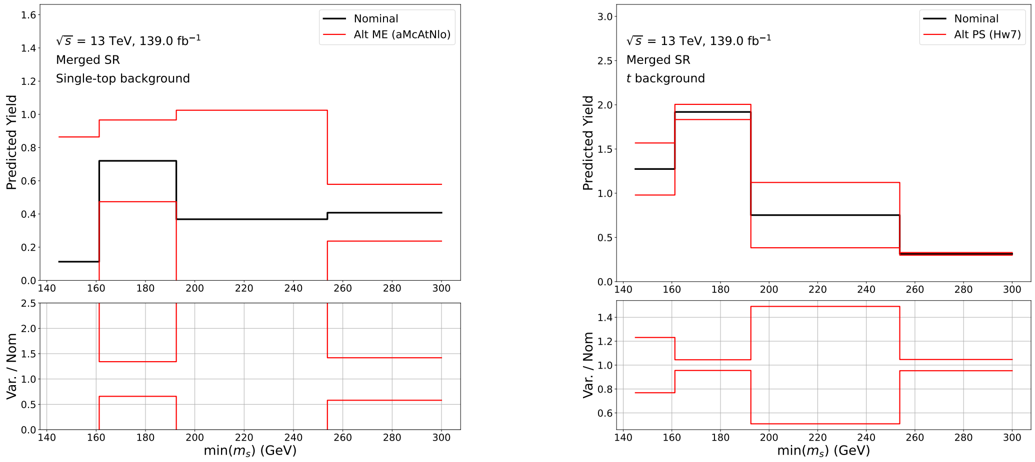

(e) ME for single-top background

(f) PS for $t\bar{t}$ background

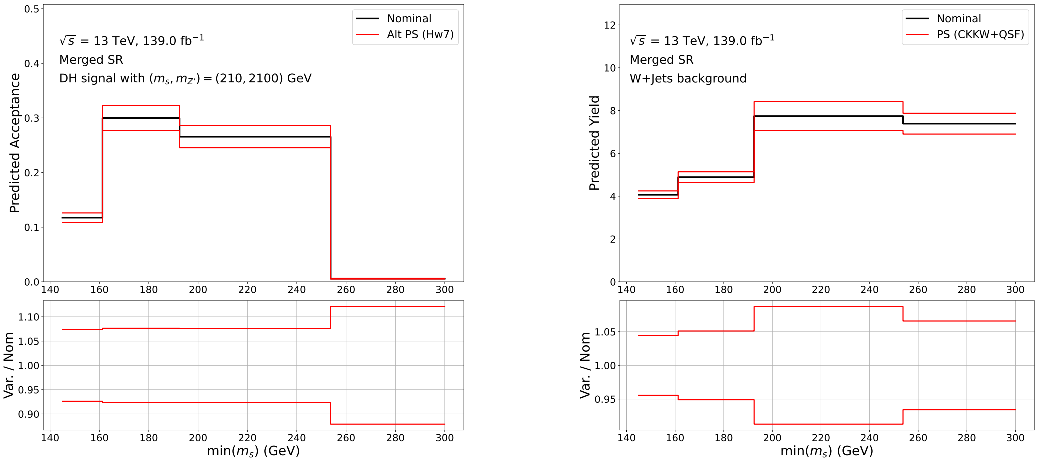

(g) PS for DH signal at $(m_s, m_{Z'}) = (210, 2100)$ GeV

(h) PS (CKKW+QSF) for W+jets background

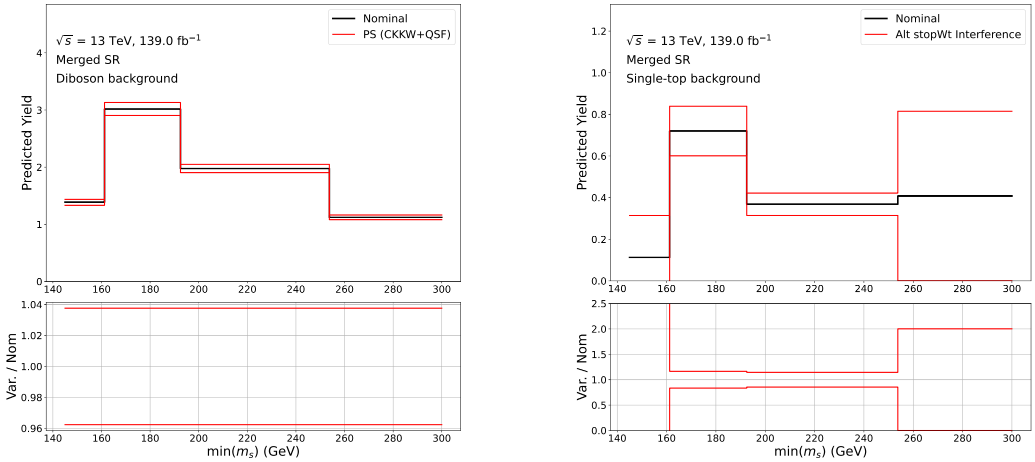

(i) PS (CKKW+QSF) for diboson background

(j) $Wt/t\bar{t}$ Interference for single-top background

Figure 6.3: Shifts in the predicted yield due to theoretical systematic uncertainties (continued)

systematic uncertainties in the resolved SR.

Table 6.5: Theoretical systematic uncertainties associated with predicted yields of dominant backgrounds in the SRs, reported both in terms of absolute yield, and (in parentheses) as percent relative to nominal yield.

Bkg and Syst.	**Mgd SR**	**Res SR**
W+Jets μ_R+μ_F	$^{+4.85}_{-2.65}\left(^{+20.15\%}_{-10.99\%}\right)$	$^{+33.92}_{-42.77}\left(^{+14.33\%}_{-18.07\%}\right)$
W+Jets PDF+α_s	±1.03 (±4.27%)	±3.18 (±1.34%)
W+Jets PS	±1.25 (±6.22%)	±16.31 (±7.54%)
diboson μ_R+μ_F	$^{+1.26}_{-1.11}\left(^{+16.82\%}_{-14.85\%}\right)$	$^{+7.62}_{-6.61}\left(^{+15.22\%}_{-13.19\%}\right)$
diboson PDF+α_s	±2.50 (±33.35%)	±16.30 (±32.55%)
diboson PS	±0.28 (±3.77%)	±1.89 (±3.77%)
$t\bar{t}$ PS	±0.76 (±17.94%)	±1.82 (±8.64%)
$t\bar{t}$ ME	±2.15 (±50.36%)	±4.91 (±23.26%)
$t\bar{t}$ PDF	±0.03 (±0.80%)	±0.09 (±0.43%)
$t\bar{t}$ μ_R+μ_F (ME)	$^{+0.16}_{-0.21}\left(^{+3.74\%}_{-4.91\%}\right)$	$^{+0.59}_{-0.86}\left(^{+2.79\%}_{-4.08\%}\right)$
$t\bar{t}$ ISR	±0.04 (±0.94%)	±0.24 (±1.13%)
$t\bar{t}$ μ_R+μ_F (FSR)	±0.60 (±14.12%)	±0.73 (±3.44%)
stop PS	±1.04 (±64.74%)	±3.00 (±80.10%)
stop ME	±1.82 (±113.45%)	±3.07 (±82.10%)
stop $Wt/t\bar{t}$	±0.78 (±48.58%)	±2.33 (±62.20%)
stop PDF	±0.04 (±2.58%)	±0.09 (±2.54%)
stop μ_R+μ_F (ME)	$^{+0.15}_{-0.11}\left(^{+9.24\%}_{-7.02\%}\right)$	$^{+0.39}_{-0.33}\left(^{+10.45\%}_{-8.78\%}\right)$
stop ISR	±0.15 (±9.04%)	±0.48 (±12.87%)
stop μ_R+μ_F (FSR)	±1.19 (±74.13%)	±1.59 (±42.47%)
triboson μ_R+μ_F	$^{+0.04}_{-0.04}\left(^{+3.58\%}_{-3.11\%}\right)$	$^{+0.12}_{-0.11}\left(^{+4.39\%}_{-3.83\%}\right)$
triboson PDF+α_s	±0.02 (±1.78%)	±0.04 (±1.37%)
triboson PS	±0.07 (±6.22%)	±0.21 (±7.54%)
Z+Jets μ_R+μ_F	$^{+0.32}_{-0.18}\left(^{+20.15\%}_{-10.99\%}\right)$	$^{+2.49}_{-3.14}\left(^{+14.33\%}_{-18.07\%}\right)$
Z+Jets PDF+α_s	±0.07 (±4.27%)	±0.23 (±1.34%)
Z+Jets PS	±0.07 (±6.22%)	±1.30 (±7.54%)

Table 6.6: Theoretical systematic uncertainties associated with predicted yields of dominant backgrounds in the CRs, reported both in terms of absolute yield, and (in parentheses) as percent relative to nominal yield.

Bkg and Syst.	**Mgd CRW**	**Res CRW**	**Mgd CRTT**	**Res CRTT**
W+Jets μ_R+μ_F	$^{+35.90}_{-23.55}\left(^{+21.89\%}_{-14.36\%}\right)$	$^{+42.02}_{-60.43}\left(^{+7.03\%}_{-10.10\%}\right)$	$^{+3.50}_{-0.87}\left(^{-278.89\%}_{+68.98\%}\right)$	$^{+4.83}_{-0.57}\left(^{+319.96\%}_{-37.98\%}\right)$
W+Jets PDF+α_s	±3.38 (±2.06%)	±13.10 (±2.19%)	±0.68 (±-54.00%)	±0.30 (±19.81%)
W+Jets PS	±12.17 (±8.02%)	±35.66 (±6.86%)	±0.19 (±8.44%)	±0.18 (±10.77%)
diboson μ_R+μ_F	$^{+1.09}_{-4.20}\left(^{+4.06\%}_{-15.66\%}\right)$	$^{+18.37}_{-15.45}\left(^{+17.40\%}_{-14.64\%}\right)$	$^{+0.03}_{-0.02}\left(^{+20.96\%}_{-15.84\%}\right)$	$^{+0.13}_{-0.10}\left(^{+22.80\%}_{-16.85\%}\right)$
diboson PDF+α_s	±8.62 (±32.18%)	±33.34 (±31.59%)	±0.05 (±32.59%)	±0.17 (±29.12%)
diboson PS	±1.00 (±3.77%)	±3.99 (±3.77%)	±0.00 (±3.77%)	±0.02 (±3.77%)
$t\bar{t}$ PS	±0.02 (±0.20%)	±0.20 (±0.98%)	±3.14 (±4.46%)	±4.93 (±7.68%)
$t\bar{t}$ ME	±2.74 (±27.66%)	±0.13 (±0.64%)	±1.39 (±1.97%)	±9.00 (±14.02%)
$t\bar{t}$ PDF	±0.03 (±0.33%)	±0.06 (±0.30%)	±0.29 (±0.41%)	±0.14 (±0.22%)
$t\bar{t}$ μ_R+μ_F (ME)	$^{+0.28}_{-0.21}\left(^{+2.83\%}_{-2.10\%}\right)$	$^{+1.27}_{-0.87}\left(^{+6.35\%}_{-4.38\%}\right)$	$^{+2.42}_{-3.76}\left(^{+3.44\%}_{-5.34\%}\right)$	$^{+0.98}_{-1.57}\left(^{+1.52\%}_{-2.44\%}\right)$
$t\bar{t}$ ISR	±0.03 (±0.28%)	±0.11 (±0.53%)	±0.89 (±1.26%)	±0.04 (±0.07%)
$t\bar{t}$ μ_R+μ_F (FSR)	±0.95 (±9.60%)	±0.46 (±2.31%)	±5.97 (±8.47%)	±2.89 (±4.49%)
stop PS	±2.10 (±77.12%)	±1.18 (±36.86%)	±1.97 (±36.44%)	±4.57 (±41.68%)
stop ME	±0.21 (±7.65%)	±2.03 (±63.64%)	±1.80 (±33.28%)	±2.05 (±18.72%)
stop $Wt/t\bar{t}$	±3.05 (±112.13%)	±1.09 (±34.30%)	±3.85 (±71.16%)	±7.90 (±71.98%)
stop PDF	±0.05 (±2.02%)	±0.22 (±6.90%)	±0.08 (±1.44%)	±0.25 (±2.31%)
stop μ_R+μ_F (ME)	$^{+0.25}_{-0.18}\left(^{+9.08\%}_{-6.72\%}\right)$	$^{+0.48}_{-0.34}\left(^{+14.99\%}_{-10.61\%}\right)$	$^{+0.37}_{-0.27}\left(^{+6.89\%}_{-4.98\%}\right)$	$^{+1.58}_{-1.08}\left(^{+14.44\%}_{-9.87\%}\right)$
stop ISR	±0.02 (±0.75%)	±0.28 (±8.65%)	±0.17 (±3.09%)	±0.43 (±3.91%)
stop μ_R+μ_F (FSR)	±0.24 (±8.87%)	±0.24 (±7.67%)	±0.05 (±0.99%)	±1.57 (±14.32%)
triboson μ_R+μ_F	$^{+0.11}_{-0.10}\left(^{+5.86\%}_{-4.99\%}\right)$	$^{+0.34}_{-0.29}\left(^{+6.05\%}_{-5.20\%}\right)$	$^{+0.00}_{-0.00}\left(^{+6.16\%}_{-5.27\%}\right)$	$^{+0.00}_{-0.00}\left(^{+10.12\%}_{-8.51\%}\right)$
triboson PDF+α_s	±0.02 (±1.12%)	±0.06 (±1.12%)	±0.00 (±1.76%)	±0.00 (±3.98%)
triboson PS	±0.07 (±3.77%)	±0.21 (±3.77%)	±0.00 (±3.77%)	±0.00 (±3.77%)
Z+Jets μ_R+μ_F	$^{+3.34}_{-2.19}\left(^{+21.89\%}_{-14.36\%}\right)$	$^{+1.21}_{-1.73}\left(^{+7.03\%}_{-10.10\%}\right)$	$^{+0.00}_{-0.00}\left(^{-278.89\%}_{+68.98\%}\right)$	$^{+0.00}_{-0.00}\left(^{+319.96\%}_{-37.98\%}\right)$
Z+Jets PDF+α_s	±0.31 (±2.06%)	±0.38 (±2.19%)	±0.00 (±-54.00%)	±0.00 (±19.81%)
Z+Jets PS	±0.95 (±8.02%)	±1.24 (±6.86%)	±0.00 (±8.44%)	±0.00 (±10.77%)

Table 6.7: Theoretical systematic uncertainties associated with predicted yields of the DH signal model at several m_s and $m_{Z'}$ in the merged SR, reported both in terms of absolute yield, and (in parentheses) as percent relative to nominal yield.

Signal Point (m$_{Z'}$, m$_s$)	**PDF**	μ_R+μ_F	**PS**
(500, 260) GeV	±0.71%	$^{+1.76\%}_{-1.70\%}$	±4.74%
(1000, 335) GeV	±1.58%	$^{+1.64\%}_{-1.48\%}$	±4.74%
(1700, 235) GeV	±1.29%	$^{+0.98\%}_{-1.04\%}$	±4.74%
(2100, 210) GeV	±1.05%	$^{+1.13\%}_{-1.23\%}$	±4.74%

Table 6.8: Theoretical systematic uncertainties associated with predicted yields of the DH signal model at several m_s and $m_{Z'}$ in the resolved SR, reported both in terms of absolute yield, and (in parentheses) as percent relative to nominal yield.

Signal Point (m$_{Z'}$, m$_s$)	**PDF**	μ_R+μ_F	**PS**
(500, 260) GeV	±0.73%	$^{+1.35\%}_{-1.21\%}$	±8.23%
(1000, 335) GeV	±1.30%	$^{+1.40\%}_{-1.27\%}$	±8.23%
(1700, 335) GeV	±1.33%	$^{+0.49\%}_{-0.52\%}$	±8.23%
(2100, 210) GeV	±0.67%	±0.37%	±8.23%

Table 6.9: Comparison of the statistical uncertainties associated with the total predicted yield of SM background events in each analysis region with the total combined statistical+systematic uncertainties.

Analysis Region	**Predicted SM Bkg Yield**	**Stat Unc**	**Stat+Sys Unc**
Merged SR	39.74	±7.29 (18%)	±11.05 (28%)
Resolved SR	331.73	±23.92 (7%)	±64.68 (19%)
Merged CRW	220.62	±24.48 (11%)	±45.12 (20%)
Resolved CRW	749.53	±31.03 (4%)	±110.68 (15%)
Merged CRTT	77.27	±2.28 (3%)	±11.32 (15%)
Resolved CRTT	77.28	±2.75 (4%)	±16.57 (21%)

Table 6.10: Comparison of the statistical uncertainties associated with the predicted yield of the DH signal process at $(m_s, m_{Z'}) = (210, 2100)$ GeV in each analysis region with the total combined statistical+systematic uncertainties.

Analysis Region	**Predicted SM Bkg Yield**	**Stat Unc**	**Stat+Sys Unc**
Merged SR	16.19	±2.89 (18%)	±3.00 (18%)
Resolved SR	15.86	±1.49 (9%)	±2.11 (13%)

Chapter 7

Statistical Framework

This chapter presents the statistical framework used to search for evidence of new physics in the ATLAS collision data and, if no such evidence is found, establish the range of parameters over which the DH model is excluded by the search. Evidence of new physics would take the form of a statistically significant discrepancy between distributions of the observed collision data in the SRs compared with distributions of the predicted yield of SM background processes.

Owing to the observation of m_s-dependent peaks in the $\min(m_s)$ distribution of the DH signal model in the SRs[1], the sensitivity of the search was found to be dramatically boosted by binning all data - MC simulated and ATLAS collision events - in the SRs into several bins of $\min(m_s)$ prior to performing the statistical analysis. Details of the binning strategy are presented in Section 7.2. Within each analysis region and bin, the statistical analysis is performed by fitting the predicted yields of background and signal processes to the ATLAS collision data with the aim of maximizing the likelihood function presented in the following section.

The computational construction and analysis of the likelihood function is performed within the HistFitter [1] statistical analysis framework.

7.1 Likelihood Function

The likelihood function that lies at the heart of the statistical framework is a product of Poisson distributions of event counts in all regions and bins:

---

[1] See Section 5.1.7 for details.

$$
\begin{aligned}
L(\boldsymbol{n}, \boldsymbol{\theta}^0 | \mu_{\text{Sig}}, \boldsymbol{s}, \boldsymbol{\mu}, \boldsymbol{b}, \boldsymbol{\theta}) &= P_{\text{SR}} \times P_{\text{CRs}} \times C_{\text{syst}} \\
&= \prod_{i \in \text{SR bins}} P(n_{S,i} | \lambda_{S,i}(\mu_{\text{Sig}}, \boldsymbol{\mu_i}, s_i, \boldsymbol{b_i}, \boldsymbol{\theta})) \times \\
&\quad \prod_{j \in \text{CRs}} P(n_j | \lambda_j(\mu_{\text{Sig}}, \boldsymbol{\mu_j}, s_j, \boldsymbol{b_j}, \boldsymbol{\theta})) \times \\
&\quad C_{\text{syst}}(\boldsymbol{\theta}^0, \boldsymbol{\theta})
\end{aligned}
\tag{7.1}
$$

where:

- $\boldsymbol{n} \in n_{S,i}, n_j$ is the set of all observed event counts in each region and bin.
- $n_{S,i}$ and n_j are the number of observed events in the i^{th} bin of the SR and in the j^{th} CR, respectively.
- The signal strength μ_{Sig} is an overall factor that scales the predicted yield of collision events produced by the DH signal model in all regions and bins.
- $\boldsymbol{\mu}_{i(j)}$ represents the normalization factors in each bin i or region j, which scale the $W+$jets and $t\bar{t}$ backgrounds in all regions and bins of the fit. Separate normalization factors are used in the merged and resolved categories. The normalization factors are treated as unconstrained nuisance parameters (NPs) in the fit. They are initialized as 1, with an uncertainty of ±1.
- $s_{i(j)}$ is the yield of the signal process in each bin i or region j predicted by MC simulation. Likewise, $\boldsymbol{b}_{i(j)}$ is the set of yield predictions for all SM background processes in each bin i or region j.
- $\boldsymbol{\theta}$ represents the set of NPs that parametrize all uncertainties associated with the MC simulated yields. For each uncertainty source k, the corresponding NP θ_k continuously interpolates between the nominal value of the predicted yield and the up/down shifts associated with varying the given uncertainty source by $\pm 1\sigma$, as discussed in Section 4.4 of Ref. [1]. For systematic sources, the NPs are normalized in the HistFitter framework such that $\theta_k = 0$ for the nominal yield and $\theta_k = \pm 1$ corresponds to $\pm 1\sigma$ variations of the uncertainty source. NPs associated with statistical uncertainty of the predicted yields are instead normalized such that $\theta = 1$ represents the nominal yield in the given bin and $\theta_k = 1 \pm 1\sigma_{\text{stat}}/N$ represents $\pm 1\sigma$ yield shifts, where N and σ_{stat} are the expected yield in the bin and its statistical uncertainty, respectively.

- $C_{\text{syst}}(\boldsymbol{\theta}^0, \boldsymbol{\theta})$ is a composite function of Gaussian priors, which is used to constrain the floating NPs $\boldsymbol{\theta}$ in the fit based on their central values $\boldsymbol{\theta^0}$ and uncertainties $\boldsymbol{\kappa}$:

$$C_{\text{syst}}(\boldsymbol{\theta}^0, \boldsymbol{\theta}) = \prod_{k \in S} \frac{1}{\kappa_k \sqrt{2\pi}} e^{-\frac{1}{2}(\frac{\theta_k^0 - \theta_k}{\kappa})^2} \tag{7.2}$$

  where S is the full set of uncertainties considered in the fit.

- The Poisson expectation functions $\lambda_{S,i}(\mu_{\text{Sig}}, \boldsymbol{\mu_i}, s_i, \boldsymbol{b_i}, \boldsymbol{\theta})$ and $\lambda_j(\mu_{\text{Sig}}, \boldsymbol{\mu_j}, s_j, \boldsymbol{b_j}, \boldsymbol{\theta})$, represent the total expected yield in each SR bin i and CR bin j, respectively. The Poisson expectation function is discussed in further detail in the following section.

7.1.1 Poisson Expectation Function

Within a given SR bin or CR k, the Poisson expectation function λ_k in Eq. 7.1 is given by:

$$\lambda_k(\mu_{\text{Sig}}, \boldsymbol{\mu_k}, s_k, \boldsymbol{b}_k, \boldsymbol{\theta}) = \mu_{\text{Sig}} s_k \eta_{k,\text{Sig}}(\boldsymbol{\theta}) + \sum_{p \in \{\text{SM bkg processes}\}} \mu_{k,p} b_{k,p} \eta_{k,p}(\boldsymbol{\theta}) \tag{7.3}$$

where s_k ($b_{k,p}$) is the yield of the signal process (SM background process p) predicted by MC simulation, as discussed in Section 4.2. $\eta_{i,s}(\boldsymbol{\theta})$ is a scaling factor, nominally set to 1, which parametrizes the variations in expected yield induced by varying the NPs $\boldsymbol{\theta}$ in the fit:

$$\eta_{k,p}(\boldsymbol{\theta}) = 1 + \sum_{s \in \text{all systematics}} I(\theta_s(k,p), N_{\text{down}}(k,p), N_{\text{up}}(k,p)) \tag{7.4}$$

where $I(\theta_p, \sigma_{\text{down}}(i,s), \sigma_{up}(i,s))$ is a continuous function of $\theta_s(k,p)$ that interpolates[2] the relative shift in predicted yields between the up $N_{\text{up}}(k,p)$ and down $N_{\text{down}}(k,p)$ extrema, associated with varying the given uncertainty source by $\pm 1\sigma$.

---

[2] HistFitter employs a 6th-order polynomial to interpolate between $\sigma_{\text{down}}(i,s)$ and $\sigma_{\text{up}}(k,p)$ using a linear extrapolation beyond these extrema. See Section 4.1 of Ref. [169] for details.

7.1.2 Nuisance Parameter Nomenclature and Correlations

Many of the NPs that appear in the likelihood function are correlated between bins, categories, and/or processes. For example, if a given NP is correlated between all bins in the fit, the value of the NP will be the same within all bins: $\theta_s(k,p) \to \theta_s(p)$. The names given to NPs in the HistFitter framework reflect the presence of any such correlations by omitting the correlated information in the NP name. Taking the above example of an NP that is correlated between all bins, this correlation will be reflected by the omission of any bin number specification (eg. `_bin1`).

The background normalization factors $\boldsymbol{\mu}$ and uncertainty-related NPs $\boldsymbol{\theta}$ are broken down as follows:

$$\boldsymbol{\mu} \in \{\mu_{W+\text{jets, merged}}, \mu_{W+\text{jets, resolved}}, \mu_{t\bar{t}\text{, merged}}, \mu_{t\bar{t}\text{, resolved}}\} \tag{7.5}$$

and

$$\boldsymbol{\theta} \in \{\boldsymbol{\theta}_{\text{statistical}}, \boldsymbol{\theta}_{\text{sys, experimental}}, \boldsymbol{\theta}_{\text{sys, theory}}\} \tag{7.6}$$

Table 7.1 summarizes the correlations present for each type of NP, and the scheme used by HistFitter to assign names to each.

Table C.1 (C.2) summarizes the scheme used to name NPs associated with the experimental (theoretical) uncertainty sources presented in Chapter 6.

7.2 Binning Strategy

As shown in Figure 7.1, the min(m_s) variable presented in Section 5.1.7 has a m_s-dependent peaked distribution, which for most m_s values is distinct in shape from the distribution of SM background processes in this variable. This shape discrimination between the signal and background processes is exploited when performing the likelihood fit by binning the MC simulated events and collision data into several min(m_s) bins.

The exact placement of bin edges in min(m_s) used when performing the fit was optimized with the aim of maximizing the projected exclusion of the DH signal model for a background-only hypothesis using the limit-setting strategy presented in Section 7.3.3, while maintaining a total predicted yield of > 5 SM background events in each bin to justify the use of the asymptotic approximation during limit-setting (see Section 7.3.3 for details).

Table 7.1: Summary of naming scheme and correlation information for nuisance parameters in the likelihood function. See Tables C.1 and C.2 for details of the names assigned to NPs associated with individual sources of systematic uncertainty.

NP Type	**Description**	**Correlation Info**	**Naming Scheme**
– $\mu_{W+\text{jets, mgd}}$ – $\mu_{W+\text{jets, res}}$ – $\mu_{t\bar{t}\text{, mgd}}$ – $\mu_{t\bar{t}\text{, res}}$	Normalization factor that scales the $W+\text{jets}$ ($t\bar{t}$) background in all analysis regions and bins of the merged (resolved) category.	Correlated between all analysis regions and bins for the $W+\text{jets}$ ($t\bar{t}$) background in the merged (resolved) category. Each normalization factor scales one process ($t\bar{t}$ or $W+\text{jets}$) - i.e. no correlation between processes.	– μ_Wjets_mgd – μ_Wjets_res – μ_ttbar_mgd – μ_ttbar_res
$\boldsymbol{\theta}_{\text{statistical}}$	NPs that parametrize the statistical uncertainty associated with the predicted yield in each region and bin from MC simulation.	Correlated between all processes. Not correlated between regions or bins.	γ_{region}_{category}_{bin type}_bin_{bin index} $\text{bin type} = \begin{cases} \text{“mS_bin”} & \text{in SR bins} \\ \text{“cuts”} & \text{in CRs} \end{cases}$
$\boldsymbol{\theta}_{\text{sys, experimental}}$	NPs that parametrize systematic uncertainties from experimental sources.	Correlated between all processes, regions and bins.	α_{uncertainty source}
$\boldsymbol{\theta}_{\text{sys, theory}}$	NPs that parametrize systematic uncertainties for each process from theoretical sources.	Correlated between all regions and bins. Not correlated between processes.	α_process_{uncertainty source}

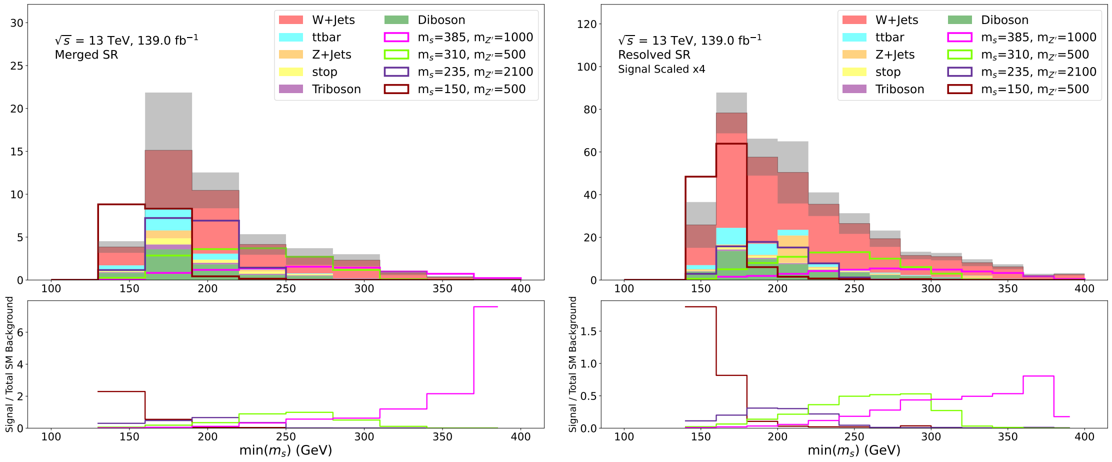

(a) Merged SR (b) Resolved SR

Figure 7.1: Predicted yields of SM background processes (stacked filled) and the DH signal model (unfilled lines) at several mass points in the merged (left) and resolved (right) SRs, binned in min(m_s). The lower panel shows the ratio of yields predicted for the DH signal process over the sum of MC background processes. Grey bands show the statistical uncertainty of the background estimate.

Distributions of $\min(m_s)$ are shown with the optimized binning in Figure 7.2. In the merged SR, binning the data into four $\min(m_s)$ bins with non-equidistant bin edges was found to provide maximal sensitivity while maintaining > 5 predicted SM background events per bin. In the resolved SR, binning into five $\min(m_s)$ bins was found to be optimal, and equidistant bin edges are used because no appreciable sensitivity improvements were found with non-equidistant edges.

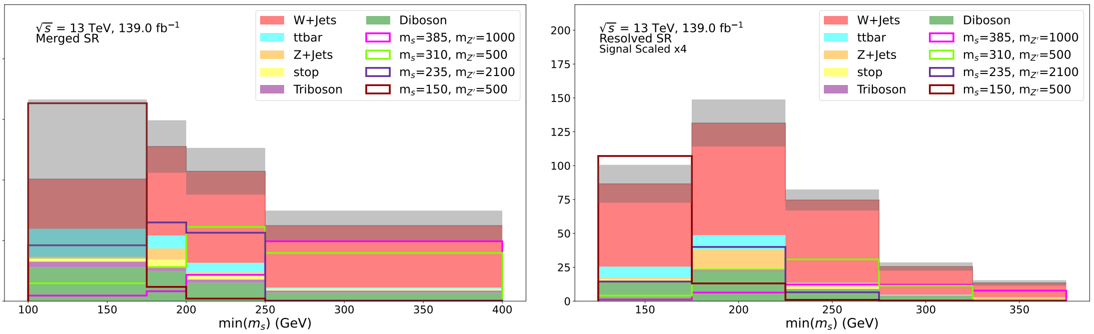

(a) Merged SR

(b) Resolved SR

Figure 7.2: Predicted yield of SM background processes (stacked filled) and the DH signal model (unfilled lines) at several mass points in the merged (left) and resolved (right) SRs, binned in $\min(m_s)$ with the optimized bin edges presented in Table 7.2. Grey bands show the statistical uncertainty of the background estimate.

The CRs are left unbinned in the fit to provide constraints on the overall yield of the W+jets and $t\bar{t}$ processes in each kinematic category. Table 7.2 summarizes the binning strategy in all analysis regions.

Table 7.2: Binning used in the analysis regions.

Region	**Binning in Merged Category**	**Binning in Resolved Category**
SR	4 non-equidistant bins in m_s bin edges: [125, 165, 190, 225, 375] GeV	5 equidistant bins in m_s bin edges: [125, 175, 225, 275, 325, 375] GeV
W+jets CR	none	none
$t\bar{t}$ CR	none	none

7.3 Fit Setup

With the MC simulated yields and ATLAS collision data binned into CRs and $\min(m_s)$ bins within the SRs, as detailed in Section 7.2 above, the statistical analysis is performed by fitting the simulated yields to the collision data in all regions and bins. The fits are performed within the HistFitter framework by varying the signal strength parameter μ_{Sig} and all floating NPs $\{\boldsymbol{\mu}, \boldsymbol{\theta}\}$ in the likelihood function presented in Eq. 7.1, until the set of parameter values that maximizes the likelihood is determined.

7.3.1 Pruning of Systematics

Prior to performing a fit, NPs associated with systematic uncertainties are pruned within the HistFitter framework at a user-defined threshold. The pruning is done as follows: for a given source of systematic uncertainty, HistFitter compares the relative up and down yield shifts due to a given NP within each analysis region and bin. If the relative shift in both directions is below the user-defined threshold in all regions and bins, the given NP is 'pruned', which means that it is not included in fit. Pruning helps to reduce fitting time, as well as minimizing numerical instabilities in the fit.

For this search, a 1% pruning threshold is applied. Dedicated studies were done to ensure that pruning systematics at a 1% threshold has no appreciable impact on the overall fit behaviour or search results.

7.3.2 Background-only Fit and Signal Region Extrapolation

To initially check for an excess of data in the SRs, a "background-only" fit of the SM background yield prediction to the observed collision data is performed in the CRs to constrain the normalization factors (eg. $\mu_{W+\text{jets, mgd}}$) for the $W+$jets and $t\bar{t}$ backgrounds within each category, along with all other NPs $\boldsymbol{\theta}$ that affect yields expectations in the CRs. The likelihood function presented in Eq. 7.1 is modified such that μ_{Sig} is fixed to 0 (i.e. "background-only"), and the SR component P_{SR} is fixed to 1 (i.e. "CR-only").

The values of normalization factors and other NPs that are constrained in the background-only fit to maximize this modified likelihood function are subsequently extrapolated to the SR to incorporate these constraints into the predicted yields of background processes in the SR. The updated distributions of the total predicted SM background yield in the SR are compared with distributions of the observed collision data to check for the presence of any discrepancies that, if statistically significant considering all statistical and systematic uncertainties, would be indicative of new physics in the data.

The extrapolation to the SR is performed by building the total expected yield of SM background events in each SR bin using the Poisson expectation formula in Eq. 7.3 with the constrained NPs, and with μ_{Sig} still set to 0. Any NPs that are specific to the SR and thus not constrained in the background-only fit are maintained at their nominal pre-fit values when constructing the extrapolated Poisson expectations. Further details of the extrapolation method and its implementation within the HistFitter framework can be found in Section 5.2 of Ref. [1].

Evaluation of Systematic Uncertainties by Means of the Transfer Factor

After the values of all background normalization factors $\boldsymbol{\mu}$ are constrained in the background-only fit, the total yield $\big((b_{\text{fit}})_{p,\text{ mgd CRW}} + (b_{\text{fit}})_{p,\text{ mgd CRTT}}\big)$ of a process p (either $W+$jets or $t\bar{t}$) in the merged CRs whose normalization factor $\mu_{p,\text{mgd}}$ is constrained in the fit can be expressed using the formalism of Eq. 7.3 (neglecting for now the $\boldsymbol{\theta}$ constraints) as:

$$(b_{\text{fit}})_{p,\text{ mgd CRW}} + (b_{\text{fit}})_{p,\text{ mgd CRTT}} = \mu_{p,\text{mgd}}\Big[b_{p,\text{ mgd CRW}} + b_{p,\text{ mgd CRTT}}\Big] \tag{7.7}$$

where an equivalent formula would apply in the resolved CRs with "mgd"→"res".

Extrapolating the constrained normalization factor $\mu_{p,\text{mgd}}$ to any region or bin j in the merged category scales the predicted yield of the process p in a bin j of the merged SR as follows:

$$\begin{aligned}(b_{\text{fit}})_{p,\ j} &= \mu_{p,\text{mgd}} \times b_{p,\ j} \\ &= \Big[(b_{\text{fit}})_{p,\text{ mgd CRW}} + (b_{\text{fit}})_{p,\text{ mgd CRTT}}\Big] \times \left[\frac{b_{p,\ j}}{b_{p,\text{ mgd CRW}} + b_{p,\text{ mgd CRTT}}}\right]\end{aligned} \tag{7.8}$$

The ratio of raw MC yields in brackets, which extrapolates the fitted yield $\big((b_{\text{fit}})_{p,\text{ mgd CRW}} + (b_{\text{fit}})_{p,\text{ mgd CRTT}}\big)$ of process p in the merged CRs to the estimated yield $(b_{\text{fit}})_{p,\ j}$ in a given region or bin j, is referred to as the "transfer factor" TF.

When considering how the systematic uncertainties, which are correlated between regions and bins, can be expected to impact the predicted yields $(b_{\text{fit}})_{p,\ j}$, the fitted yield of the process $p \in \{W+\text{jets}, t\bar{t}\}$ in the CRs will be predominantly set by the observed yield of collision data, and consequently should be effectively unshifted when systematic uncertainty sources are varied. As a result, the primary impact of systematic uncertainty sources on the predicted yields $(b_{\text{fit}})_{p,\ \text{SR bin}\ j}$ in the SR will take the form of correlated shifts of the predicted yields on the top and bottom of the TF ratio. For this reason, relative systematic uncertainties associated with the post-fit predicted yields in all regions are evaluated for the W+jets and $t\bar{t}$ backgrounds using systematic shifts in the TF rather than in the pre-fit yields. In a given SR bin or CR j in the merged category:

$$\begin{aligned}\text{rel. syst(TF, sys up, } p,\ j \text{ (mgd)} &= \frac{TF(\text{sys up, } p,\ j \text{ (mgd))}}{TF_{\text{nom}}} \\ &= \left[\frac{b_{p,\ \text{sys up},\ j\ \text{(mgd)}}}{b_{p,\ j\ \text{(mgd)}}}\right] \times \\ &\quad \left[\frac{b_{p,\ \text{mgd CRW}} + b_{p,\ \text{mgd CRTT}}}{b_{p,\ \text{sys up, mgd CRW}} + b_{p,\ \text{sys up, mgd CRTT}}}\right] - 1\end{aligned} \tag{7.9}$$

where an analogous equation holds in the resolved category with ”mgd”→”res”.

If yield shifts associated with a given systematic source are positively correlated between the region or bin j and the CRs and comparable in size relative to the nominal yield, then the relative systematic uncertainty of the transfer factor can be significantly reduced compared with that of the raw yields due to cancellation between the two terms in square brackets in Eq. 7.9.

Table 7.3 compares the total relative systematic uncertainty associated with the predicted yield of the $W+$jets process in the SRs (bins combined) and $W+$jets CRs, evaluated using either the systematic yield uncertainties alone (first term in square brackets in Eq. 7.9) or using the TF. The $t\bar{t}$ CRs are excluded from the comparison due to the relatively small predicted yield of W+jets events in these CRs. The combination of systematic uncertainties from all sources is performed within the HistFitter framework. The relative systematic uncertainties are reduced in all regions when evaluated using the TF rather than the yield. In the W+jets CR (CRW), much of the reduction comes from the fact that most of the W+jets events in the combined CRW+CRTT are contained within the CRW, so systematic shifts in the combined CRW+CRTT yield are guaranteed to be highly correlated with those in the CRW.

Table 7.3: Comparison of total relative systematic uncertainty associated with the predicted yield of the W+jets process in the SRs and W+jets CRs (CRW), evaluated using either the predicted yield (second column) or the TF (third column). The relative statistical uncertainty is shown in the first column for comparison.

Analysis Region	**Stat**	**Total Sys (yield)**	**Total Sys (TF)**
Merged SR	±14%	±31%	±27%
Resolved SR	±7%	±24%	±14%
Merged CRW	±11%	±24%	±12%
Resolved CRW	±4%	±16%	±4%

7.3.3 Exclusion Hypothesis Test and Limit Setting

In the event that no significant discrepancy is seen in the comparison of SM background yield predictions to the ATLAS collision data in the SR following the background-only fit and extrapolation of constraints to the SR, an exclusion hypothesis test of the DH signal model is performed at each simulated m_s and $m_{Z'}$ to assess the range, or "limits", of model parameters that can be excluded by the search. This procedure is referred to as "limit setting".

The exclusion hypothesis test is performed using "signal+background fits", which incorporate all regions and bins in the likelihood function presented in Eq. 7.1, and allow for a nonzero signal strength μ_{Sig}. The ultimate product of the hypothesis test at each m_s and $m_{Z'}$ of the DH model is a "CL$_s$ value". A CL$_s$ value below 0.05 is considered to exclude the signal+background hypothesis at a 95% confidence level (CL).

Typical approaches to evaluating a CL associated with an alternative hypothesis directly consider the level of agreement between the observed data and the expectation of the alternative hypothesis. In the context of a search for new phenomena in experimental particle physics, this amounts to evaluating the confidence level CL$_{s+b}$ associated with the signal+background hypothesis. The CL$_{s+b}$ approach encounters issues when one considers a regime in which the data is expected to be predominantly comprised of background events ($s << b$). In this regime, CL$_{s+b}$ becomes increasingly similar to the confidence level CL$_b$ associated with the null background-only hypothesis; this effect tends to diminish the ability of the search to exclude the signal+background hypothesis at a fixed reference CL (eg. 95%). To address this issue, the CL_s method considers instead the CL_s ratio:

$$\mathrm{CL}_s = \frac{\mathrm{CL}_{s+b}}{\mathrm{CL}_b} \tag{7.10}$$

which compares the confidence with which the observed data can be explained by the alternative signal+background hypothesis relative to the null background-only hypothesis. The CL_s is generally found to provide more powerful exclusion than the CL_{s+b} in the high-background regime.

CL_s Evaluation Strategy

For a given value of the hypothesized signal strength μ_{Sig}, a "profiled log-likelihood ratio" $q_{\mu_{\mathrm{Sig}}}$ is constructed as follows:

$$q_{\mu_{\mathrm{Sig}}} = -2\log\left(\frac{L(\mu_{\mathrm{Sig}}, \hat{\hat{\boldsymbol{\theta}}})}{L(\hat{\mu}_{\mathrm{Sig}}, \hat{\boldsymbol{\theta}})}\right) \tag{7.11}$$

where $\hat{\mu}_{\mathrm{Sig}}$ and $\hat{\boldsymbol{\theta}}$ are the values of μ_{Sig} and of the NPs $\boldsymbol{\theta}$ that maximize the likelihood function with all parameters left floating (i.e. profiled over) in the signal+background fit. $\hat{\hat{\boldsymbol{\theta}}}$ is the set of floating NP values that maximize the likelihood function for a given fixed μ_{Sig} in the fit. Note that the background normalization parameters $\boldsymbol{\mu}$ are folded into the set of NPs $\boldsymbol{\theta}$ in Eq. 7.11, and in all equations that follow in this section.

Two p-values are evaluated to quantify the CL_{s+b} (CL_b) by integrating the distribution $f(q_{\mu_{\mathrm{Sig}}}|\mu_{\mathrm{Sig}}, \boldsymbol{\theta})$ above (below) the value $q_{\mu_{\mathrm{Sig}},\,\mathrm{obs}}$ evaluated for $\mu_{\mathrm{Sig}} = 1$ ($\mu_{\mathrm{Sig}} = 0$) with the observed ATLAS collision data and the central NP values input to the fit:

$$\mathrm{CL}_{s+b} = p_{\mu_{\mathrm{Sig}}=1} = \int_{q_{1,\,\mathrm{obs}}}^{\infty} f(q_1|\mu_{\mathrm{Sig}} = 1, \boldsymbol{\theta})dq_1 \tag{7.12}$$

$$\mathrm{CL}_b = p_{\mu_{\mathrm{Sig}}=0} = \int_{q_{0,\,\mathrm{obs}}}^{\infty} f(q_0|\mu_{\mathrm{Sig}} = 0, \boldsymbol{\theta})dq_0 \tag{7.13}$$

The distribution $f(q_{\mu_{\mathrm{Sig}}}|\mu_{\mathrm{Sig}}, \boldsymbol{\theta})$ can be obtained by throwing pseudo-experiments that randomize the number of observed events and the central values of the NPs $\boldsymbol{\theta}$, and re-calculating $q_{\mu_{\mathrm{Sig}}}$ for each pseudo-experiment. However, for sufficiently high statistics in the analysis regions - typically taken to be at least $\mathcal{O}(5)$ expected SM background events per region or bin - $f(q_{\mu_{\mathrm{Sig}}}|\mu_{\mathrm{Sig}}, \boldsymbol{\theta})$ is known to follow a χ^2 distribution according to Wilks' theorem [170]. In this "asymptotic regime", asymptotic formulae [171] are used to evaluate the p-value, thus avoiding the need to generate pseudo-experiments. The CL_s value is then evaluated using Eq. 7.10 to test the exclusion of the DH signal hypothesis at the given m_s and $m_{Z'}$. In addition to the "observed" CL_s value $\mathrm{CL}_{s,\,\mathrm{obs}}$ obtained with the observed ATLAS collision data, an additional "expected" CL_s value $\mathrm{CL}_{s,\,\mathrm{exp}}$ is evaluated by replacing the observed collision data with the background-only "Asimov data set", which is simply set to be equal to the predicted yield of SM background processes in each region and bin.

Visualization and Limit Setting

Having obtained a $\mathrm{CL}_{s,\,\mathrm{obs}}$ and $\mathrm{CL}_{s,\,\mathrm{exp}}$ for each m_s and $m_{Z'}$ by the above procedure, interpolation is performed with respect to both sets of CL_s values within the (m_s, $m_{Z'}$) plane to obtain an expected (observed) "exclusion contour", which corresponds with $\mathrm{CL}_{s,\,\mathrm{exp}} = 0.05$ ($\mathrm{CL}_{s,\,\mathrm{obs}} = 0.05$). The $\mathrm{CL}_{s,\,\mathrm{exp}} = 0.05$ contour is evaluated with a $\pm 1\sigma$ uncertainty band, and a fine-grained colour-coded distribution of the $\mathrm{CL}_{s,\,\mathrm{exp}}$ is plotted within the modelled range of m_s and $m_{Z'}$. The interpolation is performed internally by HistFitter using a radial basis interpolation function[3].

---

[3] Interpolation is performed using the interpolate.Rbf() class function in python's scipy module. This work uses the 'linear' (r) interpolation function rather than the default 'multiquadratic', because linear interpolation was found to provide a smoother interpolation of the signal grid.

Chapter 8

Results

This chapter presents the results of applying the statistical analysis presented in Chapter 7 to the MC simulated and observed yields of ATLAS collision events in all analysis regions and bins[1] to search for evidence of new physics in the SRs. No significant discrepancy is found between the predicted yields of SM background processes and the collision data in the SRs, so the exclusion hypothesis test described in Section 7.3.3 is used to determine the parameter space of the DH model that is excluded by the search.

8.1 Background-only Fit

This section presents the results of performing the "background-only" fit of the predicted yields of SM background processes obtained from MC simulation to the observed yields of ATLAS collision events in the CRs, as described in Section 7.3.2, with the goal of obtaining data-driven constraints for the normalizations of the W+jets and $t\bar{t}$ backgrounds within each kinematic category.

8.1.1 Pre- and Post-Fit Yields of MC Simulated Background Events

Figure 8.1 compares the total predicted yield of all SM background processes considered in the CRs with the yield of observed events in the ATLAS collision data, both before and after the background-only fit in the CRs. The observed yield of ATLAS collision events is consistent with the pre-fit predicted yield of SM background events within the combined statistical and systematic uncertainties in all CRs, with the exception of the merged CRTT. In the merged CRTT, a slight overprediction of the SM

---

[1] See Section 5.2 for details of the selections applied to define the regions used for the search, and Section 7.2 for details of the strategy used to bin data in the SRs.

background yield is observed.

The uncertainty of the total expected yield of SM background processes is reduced in all CRs after the fit, as the post-fit uncertainty is predominantly set by the Poisson uncertainty associated with the observed event counts.

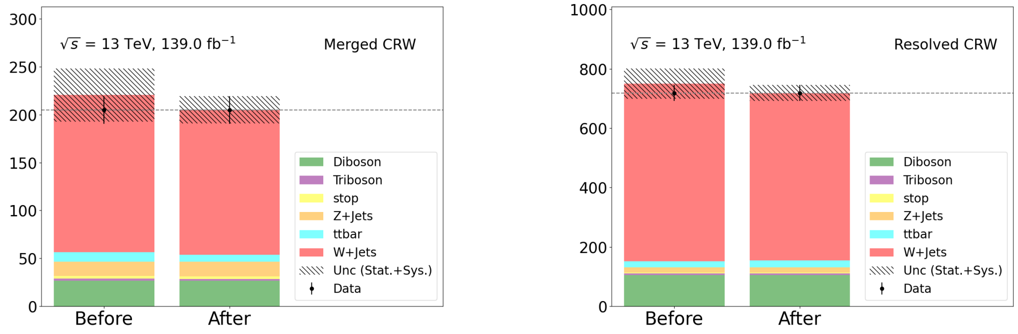

(a) Merged CRW (b) Resolved CRW

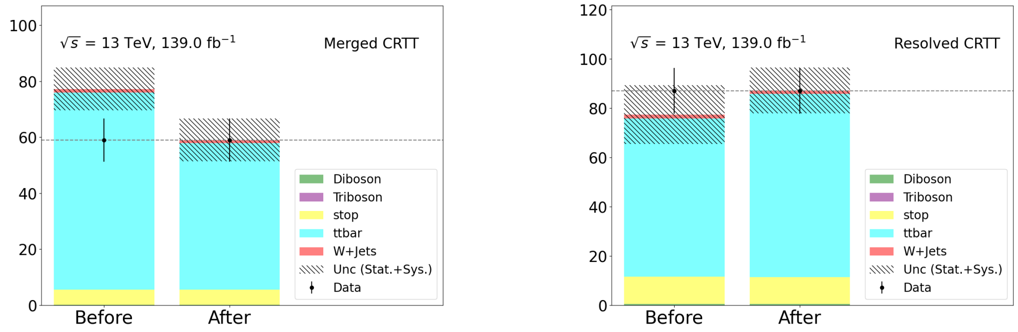

(c) Merged CRTT (d) Resolved CRTT

Figure 8.1: Comparison between the predicted yields of SM background processes and observed yields of ATLAS collision data in the CRs, before and after the background-only fit. Hatched band shows the combined statistical and systematic uncertainty of the total yield prediction of SM background processes. Black error bars represent the Poisson uncertainty associated with the observed event count in each CR.

8.1.2 Nuisance Parameter Pulls and Correlations

Figure 8.2 summarizes the post-fit shifts (a.k.a. "pulls") of the values of all NPs included in the background-only fit, as well as their post-fit uncertainties. Both the values and uncertainties of the $\boldsymbol{\mu}$ normalization factors, which scale the W+jets and

$t\bar{t}$ backgrounds separately in the merged and resolved categories, are constrained by the fit to obtain the post-fit agreement seen in Figure 8.1 between the total predicted yield of SM background processes and the observed yields in the ATLAS collision data. The values of all other NPs, which parametrize sources of statistical and systematic uncertainty, receive negligible pulls in the fit, since agreement with data can be obtained in all CRs just by varying the $W+$jets and $t\bar{t}$ normalization factors. The uncertainties of the γ_* parameters[2] that parametrize the statistical uncertainty associated with the MC simulated yield predictions in each CR are reduced by the fit to data, which results in the reduction seen in Figure 8.1 of the uncertainty associated with the post-fit expected yield of SM background events.

Figure 8.3 shows the Pearson correlation coefficient r between NPs in the fit. There is some appreciable correlation ($|r| \gtrsim 0.2$) between separate background normalization factors μ_*, and between normalization factors and a few of the γ_* NPs - for example, $r = -0.7$ between μ_Wjets_mgd and γ_stat_CRW_Merged_cuts_bin_0. However, there is in general very little cross correlation ($r < 0.01$) between the γ_* and α_* NPs, which collectively parametrize all uncertainty sources in the fit due to the negligible shifts induced on these parameters by the background-only fit (see Figure 8.2).

8.2 Comparison of SM Background Expectation and Data in the Signal Region

After performing the background-only fit in the CRs, the constraints on the background normalization factors $\boldsymbol{\mu}$ and the other NPs $\boldsymbol{\theta}$ summarized in Figure 8.2 are extrapolated to the SR following the procedure described in Section 7.3.2. Figure 8.4 compares the predicted yields of SM background processes in the SR - binned in $\min(m_s)$ using the binning strategy presented in Section 7.2 - before and after the background-only fit and extrapolation procedure. Table 8.1 summarizes the total predicted and observed yields in the merged SRs, combined over all bins within each SR.

Both before and after the background-only fit extrapolation, Figures 8.4a and 8.4b, respectively, show an excess of observed ATLAS collision events compared with the predicted yield of SM background processes in the first three bins of the merged SR. However, the difference is within uncertainty in all three bins, and a comparison of the combined yields reported in the first row of Table 8.1 reveals that the overall

---

[2] See Table 7.1 for a description of the scheme used to name NPs.

Table 8.1: Comparison of the total observed yields of events in the SRs with the predicted yield of SM background processes, either before (pre-fit) or after (post-fit) extrapolation of constraints from the background-only fit in the CRs.

Region	**Observed Yield**	**SM Bkg Prediction (Pre-fit)**	**SM Bkg Prediction (Post-fit)**
Merged SR	51	39.7 ± 11	36.8 ± 10
Resolved SR	285	331.7 ± 65	321.2 ± 40

yield of ATLAS collision data in the merged SR a factor of 1.3 larger than the total post-fit uncertainty associated with the expected yield of SM background processes (a.k.a. a 1.3σ excess). If the distribution of measured discrepancies between the predicted yield of SM background processes and the observed yield of collision data is assumed to be reasonably approximated as Gaussian, the observed 1.3σ discrepancy corresponds to a two-sided p-value of 0.18 (see, for example, Section 11 of [172] for an introduction to the p-value and its use in hypothesis testing). If a p-value below 0.05 is taken to represent a statistically significant deviation from the null hypothesis, the observed p-value of 0.18 implies that the observed yield of ATLAS collision events in the merged SR is statistically compatible with the null hypothesis that all events observed in the SR were produced by SM background processes.

Figures 8.4c and 8.4d show an over-prediction of the SM background yield compared with the observed number of ATLAS collision events in all bins of the resolved SR, both before and after NP constraints from the background-only fit are extrapolated to the SRs. Comparing the observed yield of collision events from Table 8.1 in the resolved SR with the post-fit predicted yield of SM background events reveals a -0.8σ discrepancy. The resulting two-sided Gaussian p-value of 0.42 indicates that, as in the merged SR, the observed yields are statistically compatible with the null background-only hypothesis.

8.3 Exclusion of the Dark Higgs Signal Model

Given the absence of any statistically significant discrepancy between the observed yields of ATLAS collision events in the SRs and the predicted yields of events from SM background processes, the exclusion hypothesis test presented in Section 7.3.3 is used to determine the range of m_s and $m_{Z'}$ for which the DH signal model can be confidently excluded by the search for the fixed choices of the DM mass m_χ, mixing angle $\sin\theta$ and coupling choices g_q and g_χ in the DH model used for the search[3]:

- $m_\chi = 200$ GeV
- $g_q = 0.25$
- $g_\chi = 1$
- $\sin\theta = 0.01$

8.3.1 Signal+Background Fit

Figures 8.5, 8.6 and 8.7 compare the observed yield of ATLAS collision events in the SRs, binned in $\min(m_s)$, with the predicted yields for the SM background and DH signal processes at the three sample combinations of m_s and $m_{Z'}$ in the signal model. The sample m_s and $m_{Z'}$ combinations, listed below, are chosen to cover the range of production cross sections for the DH model considered in the search:

- $(m_s, m_{Z'}) = (160, 1000)$ GeV (cross section: 93.3 fb^{-1})
- $(m_s, m_{Z'}) = (210, 2100)$ GeV (cross section: 3.9 fb^{-1})
- $(m_s, m_{Z'}) = (310, 2900)$ GeV (cross section: 0.31 fb^{-1})

As shown in Figure 8.5, the DH signal model at $(m_s, m_{Z'}) = (160, 1000)$ GeV with a cross section of 93.3 fb^{-1} has a sufficiently large production rate that the signal+background fit constrains the signal strength parameter to $\mu_{\text{Sig}} = 0.09 \pm 0.08$. Therefore, the signal+background hypothesis ($\mu_{\text{Sig}} = 1$) is excluded with a high degree of confidence.

Figure 8.6 shows the results of the signal+background fit for $(m_s, m_{Z'}) = (210, 2100)$ GeV in the signal model, with an intermediate cross section of 3.9 fb^{-1}. The predicted yield of the signal process is comparable in the first three bins of the merged SR to the discrepancy between the observed yield of data and the predicted yield of SM background processes, which results in a fitted signal strength close to 1 ($\mu_{\text{Sig}} = 0.88$). However, since the predicted yield of the signal and background processes are still consistent with the background-only prediction, there is a large (nearly 100%) uncertainty associated with the fitted signal strength. As a result, the fit can neither support nor confidently exclude the signal+background hypothesis at this mass point.

---

[3] See Sections 2.2.1 and 2.3.2 for a presentation and discussion of the choices for the m_χ, $\sin\theta$ and coupling parameters in the DH model.

Further reduced exclusion power is observed for the fit shown in Figure 8.7d, which considers the signal model at the mass combination $(m_s, m_{Z'}) = (310, 2900)$ GeV with the lowest cross section of the three combinations considered. The signal yields are so small compared with the uncertainty of the total yield prediction that the fitted signal strength could range from -3.82 to 5.06 within its post-fit uncertainty. As a result, the search can neither meaningfully support nor exclude the DH signal model at this mass point.

Figure 8.8 summarizes the post-fit value and uncertainty of the signal strength parameter μ_{Sig} for the signal+background fit performed with the DH signal model at all m_s and $m_{Z'}$ considered in the search. The fitted value and uncertainty vary depending on the production cross section and the shape of the signal distribution with respect to $\min(m_s)$. The size of the uncertainty for a given m_s and $m_{Z'}$ combination reflects the exclusion power of the search at the given mass combination, where a larger uncertainty generally implies less exclusion power. In general, the fitted values of μ_{Sig} are consistent with 0 within 1.5σ, in agreement with the null background-only hypothesis.

Nuisance Parameter Pulls and Correlations

Figure 8.9 summarizes the pulls and uncertainties of all NPs included in the signal+background fit using the DH signal model at the sample mass point $(m_s, m_{Z'}) = (210, 2100)$ GeV. In contrast with the background-only fit, the pulls of some γ_* and α_* NPs, which constrain the statistical and systematic uncertainties associated with MC simulated yields, can be appreciably shifted (i.e. pulled) relative to their pre-fit values. This is due to differences in the shapes of $\min(m_s)$ distributions in the SRs between the observed ATLAS collision data and the predicted yields of the SM background and signal processes, which cannot be corrected by varying the μ_* normalization parameters alone. Particularly large pulls are seen for the NPs α_JET_JER_* and α_JET_R02_JER_*, which parametrize the systematic jet energy resolution (JER) uncertainties associated with the $R = 0.4$[4] and $R = 0.2$[5] jets, respectively (see Tables C.1 and C.2 for descriptions of individual NPs used to parametrize systematic uncertainties). As shown in Figures 6.1 and 6.2, the JER systematic uncertainties induce

---

[4] See Section 5.1.2 for a description of the $R = 0.4$ jets, and Section 5.1.3 for a description of the method used to reconstruct the W boson candidate in the resolved category.

[5] See Section 5.1.4 for a description of the algorithm used to construct TAR jets using input $R = 0.2$ jets.

the largest yield shifts in the SRs relative to other systematic sources. Therefore, it is reasonable to expect that these NPs would in general receive relatively strong pulls in the signal+background fit to help correct for the observed differences between expected and observed event yields in the SRs.

Figure 8.10 shows the Pearson correlation coefficient r between NPs in the signal+background fit for the sample mass point $(m_s, m_{Z'}) = (210, 2100)$ GeV in the DH signal model. As with the background-only fit, there is appreciable correlation ($|r| \gtrsim 0.2$) between separate background normalization factors μ_*, and between normalization factors and several of the γ_* NPs that parametrize the statistical uncertainties associated with MC simulated yield predictions. In contrast to the background-only fit, some of the α_* parameters also have non-negligible correlations ($|r|$ up to ~ 0.3) with one another and with γ_* and μ_* NPs. The introduction of correlations involving α_* NPs in the signal+background fit compared with the background-only fit is attributed to the non-negligible post-fit shifts of these NPs observed in Figure 8.9 for the signal+background fit.

Ranking of Systematic Uncertainties

Figure 8.11 shows the pre- and post-fit values and impacts of NPs in the signal+background fit on the fitted signal strength μ_{Sig}. The 30 leading NPs are ranked from top to bottom in order of the size of their impact. The pre- and post-fit impact of a given NP θ is measured as follows:

- **Pre-fit impact:** Shift the value of θ to the upper bound $\theta_0 + \Delta\theta$ of its pre-fit uncertainty. Perform the signal+background fit with θ fixed to this upper value, and all other NPs left floating. Repeat with the value of θ fixed to the lower bound $\theta_0 + \Delta\theta$ of its pre-fit uncertainty. The resulting shifts $\Delta_{\text{up/down}}\widehat{\mu_{\text{Sig}}}$ of the best-fit μ_{Sig} are shown as unfilled white boxes with black borders in Figure 8.11.

- **Post-fit impact:** As above, but with the value of θ shifted instead to the upper and lower bounds of its post-fit uncertainty. The resulting shifts $\Delta_{\text{up/down}}\widehat{\mu_{\text{Sig}}}$ are shown as filled boxes, where the colour of the box indicates whether μ_{Sig} is correlated (blue) or anti-correlated (green) with the value of the NP.

The highest-ranked NPs are associated with systematic JER uncertainties, which also receive some of the largest pulls in the fit (see Figure 8.9 and related discussion in Section 8.3.1). Following in rank are some of the statistical γ_* NPs.

8.3.2 Hypothesis Testing and Model Exclusion

Hypothesis testing is performed following the method presented in Section 7.3.3 to determine the range of m_s and $m_{Z'}$ that can be confidently excluded by the search. The colour map in Figure 8.12 shows the expected CL_s value evaluated over the range of m_s and $m_{Z'}$ considered in the search. Interpolated contours are drawn at $\text{CL}_s = 0.05$ for the expected (grey dashed) and observed (solid red) values, and the contained areas represent the expected and observed range of m_s and $m_{Z'}$ that are excluded by the search for the assumed DM mass and coupling choices.

Figure 8.13 summarizes the excluded range of m_s and $m_{Z'}$ in the DH model - for the fixed choices of the DM mass, DH mixing angle and couplings presented at the beginning of this section - by this and all other searches presented in Section 2.3.2 that place constraints on the model by targeting various decay modes of the DH boson s. This search (blue) extends the excluded range for on-shell WW decays ($m_s > 160$ GeV). By additionally probing off-shell WW decays in the range $m_s < 160$, this search largely closes the pre-existing gap in coverage (150 GeV $< m_s <$ 160 GeV) between searches in the $s \to WW$ and $s \to bb$ DH decay channels.

8.3.3 Dependence of Sensitivity on Signal Strength

Neglecting slight changes to the width of the Z' mediator, the production rate of the DH model would be expected to scale in proportion to g_q^2 and g_χ^2 [12] if the values of the g_q and g_χ coupling strength parameters, respectively, are varied, since both correspond to a single annihilation (g_q) or decay (g_χ) vertex in the model (see Figure 2.1). As noted in Section 2.2.1, upper bounds are placed on the coupling strength g_q between the Z' mediator and quarks in the DH model by dijet searches, which range from approximately 0.04 to 0.2 depending on the value of $m_{Z'}$, and on the methods the assumptions involved in placing the constraints. However, the actual value of g_χ in the model is unknown, and is not currently constrained by dijet or other searches.

Given the dependence of the production rate on the choices of g_q and g_χ, a test was done following recommendations in Ref. [173] to evaluate the impact of reducing the production rate of the DH process on the sensitivity of the search. Implicit in this test is a simplifying assumption that the modified values of g_q and g_χ associated with reducing μ will result in the same distributions of kinematic variables as the benchmark choices, such that the predicted yields of the signal model in all regions and bins of the search scale linearly with μ. Figure D.1 compares the range of m_s and $m_{Z'}$ excluded by the search with the value of a "signal strength" parameter μ, which coherently scales the production rate of the DH signal process at all m_s and $m_{Z'}$ considered in the search. The search is able to exclude phase space in the m_s vs. $m_{Z'}$ plane for μ down to 0.3, with the excluded range successively diminished as μ is reduced.

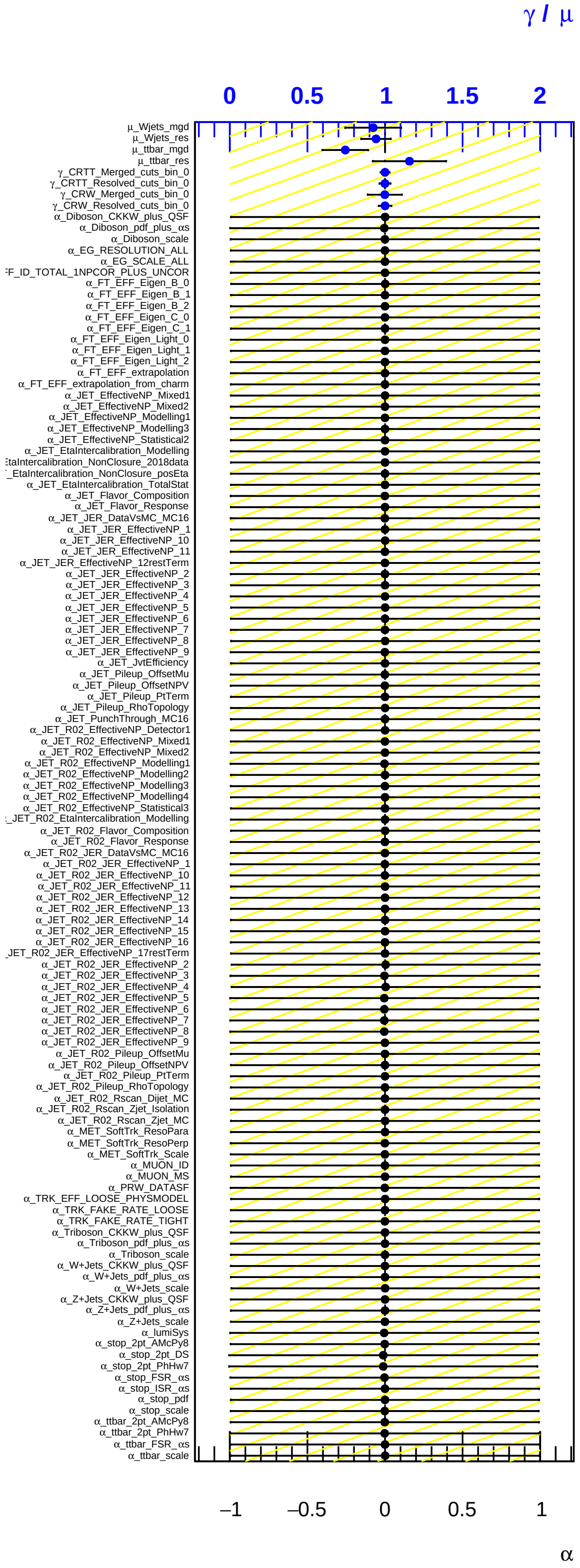

Figure 8.2: Post-fit values and uncertainties of all NPs in the background-only fit. See Tables 7.1, C.1 and C.2 for details of the scheme used to name the NPs. Yellow hatched band shows the pre-fit uncertainty for each NP, and black horizontal error bars show the post-fit uncertainty.

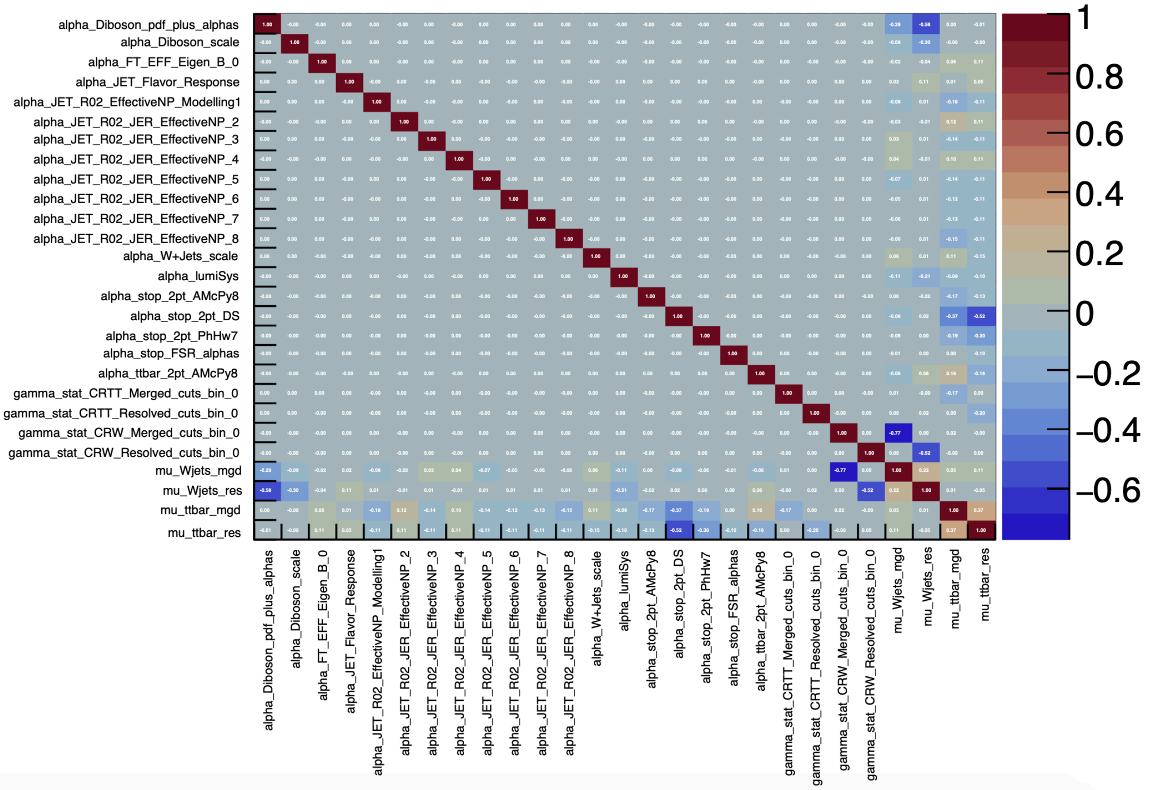

Figure 8.3: Correlation matrix for all NPs considered in the background-only fit for which at least one coefficient of cross-correlation with another NP is larger than 0.1. See Tables 7.1, C.1 and C.2 for details of the scheme used to name the NPs.

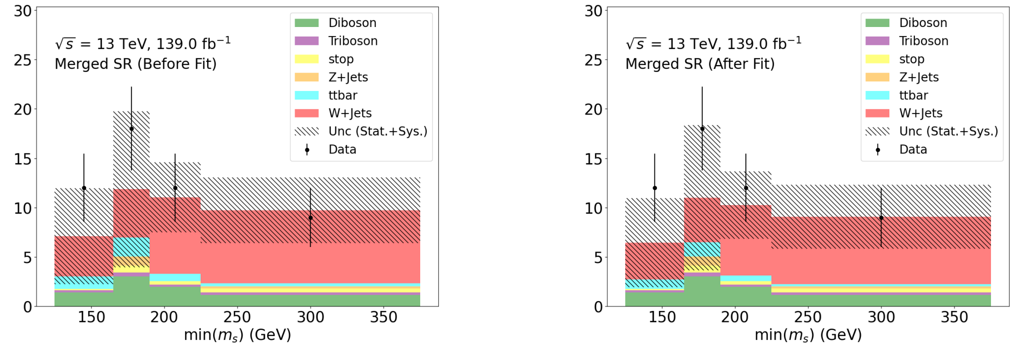

(a) Merged SR (Before Fit) (b) Merged SR (After Fit)

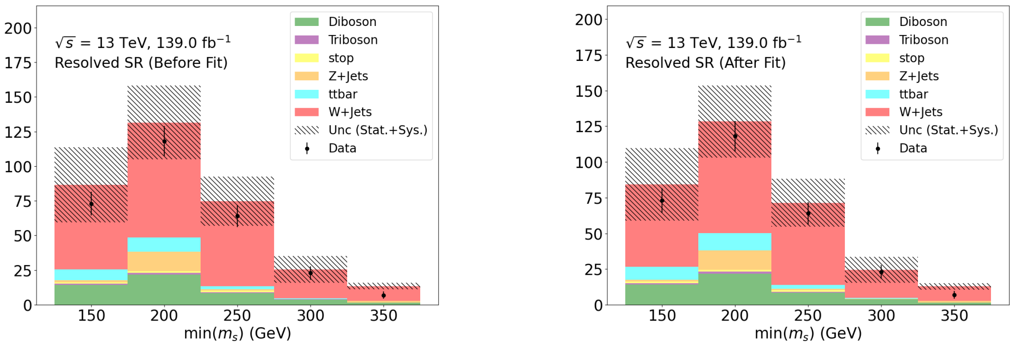

(c) Resolved SR (Before Fit) (d) Resolved SR (After Fit)

Figure 8.4: Comparison between predicted yields of SM background processes and observed yields in the SRs, before (left) and after (right) the background-only fit and extrapolation to the SR. Yields are binned in min(m_s) using the binning strategy presented in Section 7.2.

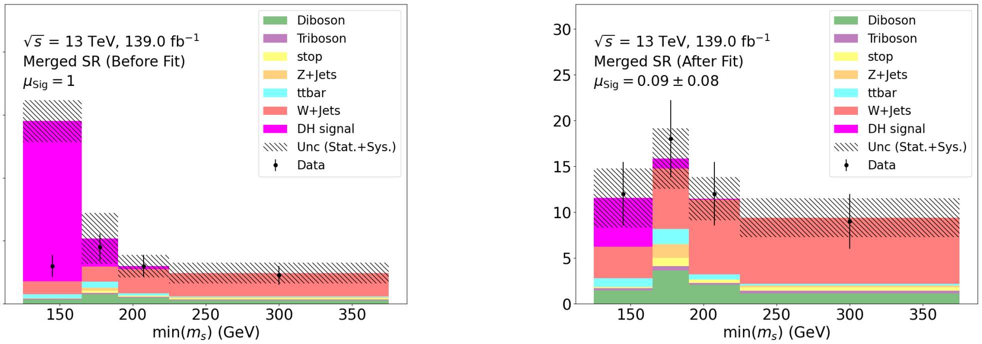

(a) Merged SR (Before Fit)   (b) Merged SR (After Fit)

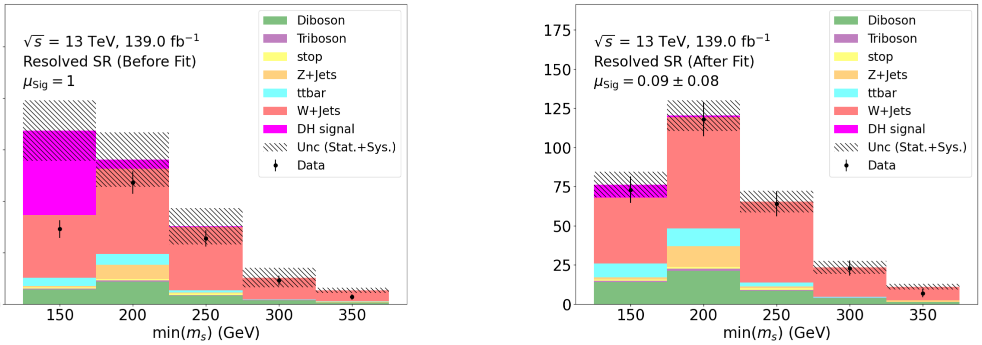

(c) Resolved SR (Before Fit)   (d) Resolved SR (After Fit)

Figure 8.5: Comparison between predicted yields of SM background processes, the DH signal process at $(m_s, m_{Z'}) = (160, 1000)$ GeV and observed yields in the SRs. Yields are shown before (left) and after (right) the signal+background fit. The pre- and post-fit values of the signal strength μ_{Sig} are also reported. Yields are binned in $\min(m_s)$ using the binning strategy presented in Section 7.2.

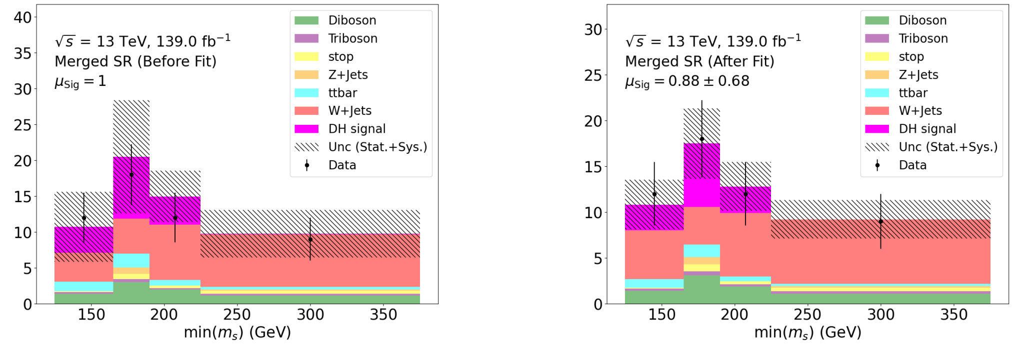

(a) Merged SR (Before Fit)

(b) Merged SR (After Fit)

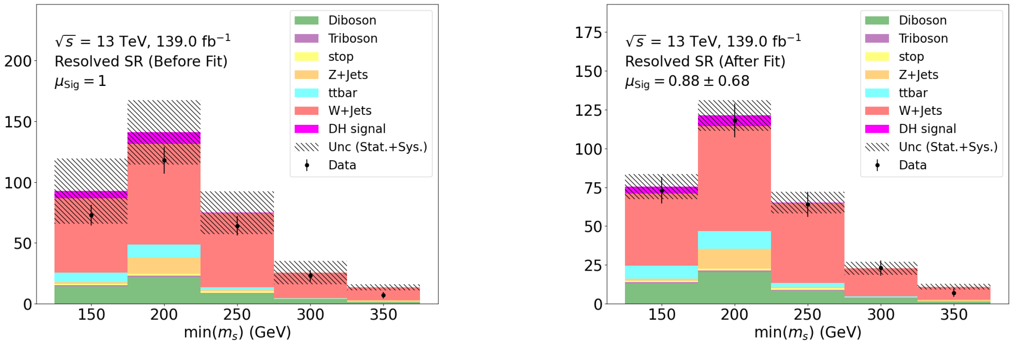

(c) Resolved SR (Before Fit)

(d) Resolved SR (After Fit)

Figure 8.6: Comparison between predicted yields of SM background processes, the DH signal process at $(m_s, m_{Z'}) = (210, 2100)$ GeV and observed yields in the SRs. Yields are shown before (left) and after (right) the signal+background fit. The pre- and post-fit values of the signal strength μ_{Sig} are also reported. Yields are binned in $\min(m_s)$ using the binning strategy presented in Section 7.2.

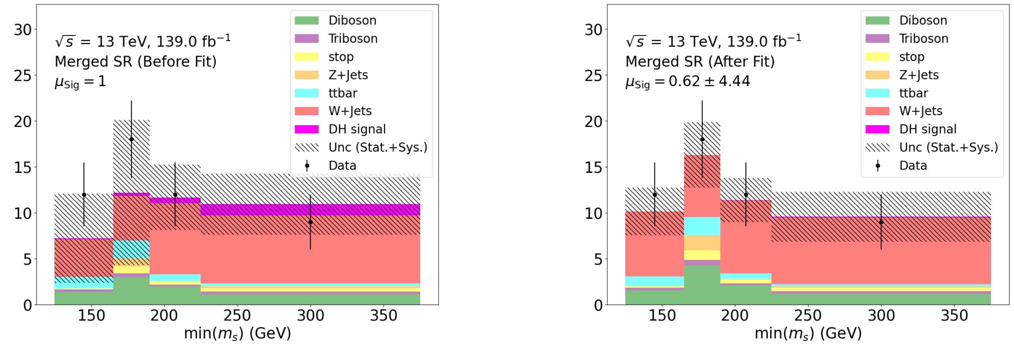

(a) Merged SR (Before Fit) (b) Merged SR (After Fit)

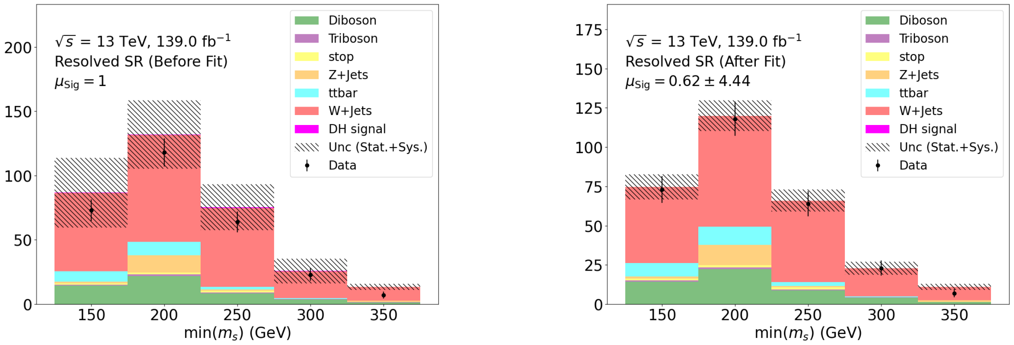

(c) Resolved SR (Before Fit) (d) Resolved SR (After Fit)

Figure 8.7: Comparison between predicted yields of SM background processes, the DH signal process at $(m_s, m_{Z'}) = (310, 2900)$ GeV and observed yields in the SRs. Yields are shown before (left) and after (right) the signal+background fit. The pre- and post-fit values of the signal strength μ_{Sig} are also reported. Yields are binned in $\min(m_s)$ using the binning strategy presented in Section 7.2.

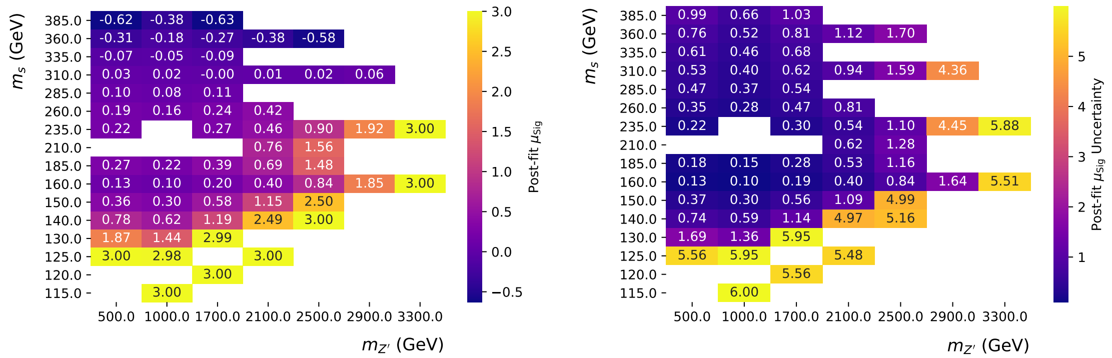

(a) Post-fit $\mu_{\rm Sig}$

(b) Post-fit $\mu_{\rm Sig}$ uncertainty

Figure 8.8: Post-fit value (left) and uncertainty (right) of the signal strength parameter $\mu_{\rm Sig}$ in the signal+background fit ($\mu_{\rm Sig}$ left floating) for each m_s and $m_{Z'}$ in the DH signal model considered in the search.

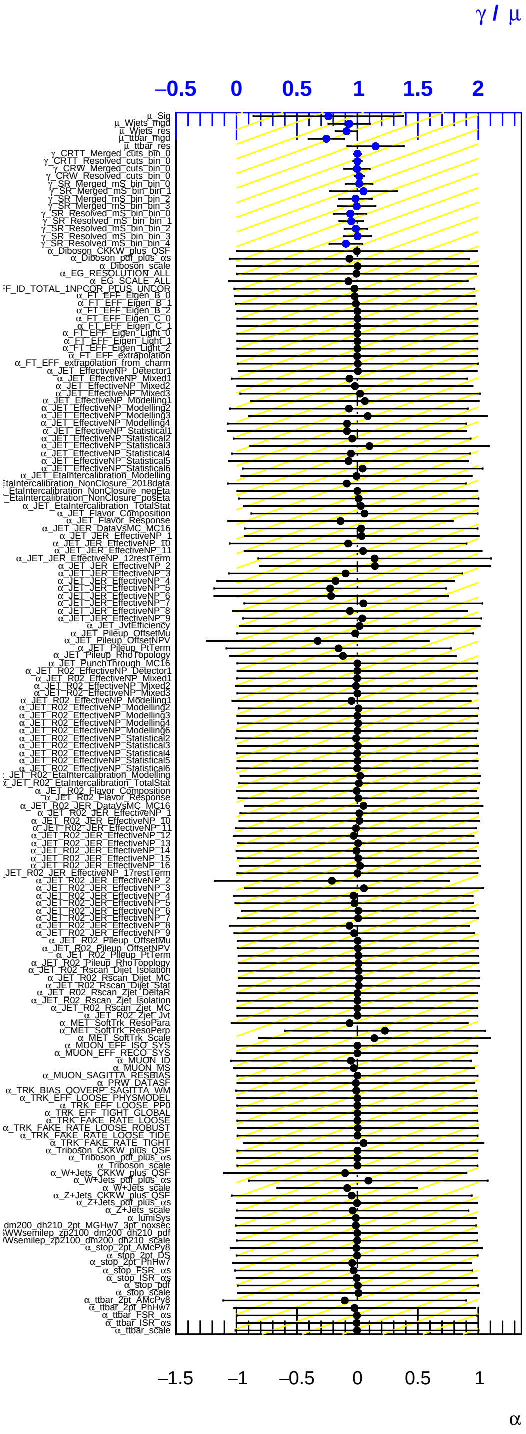

Figure 8.9: Post-fit values of all NPs in the signal+background fit using the DH signal model at $(m_s, m_{Z'}) = (210, 2100)$ GeV. See Tables 7.1, C.1 and C.2 for details of the scheme used to name the NPs. Yellow hatched band shows the pre-fit uncertainty for each NP, and black horizontal error bars show the post-fit uncertainty.

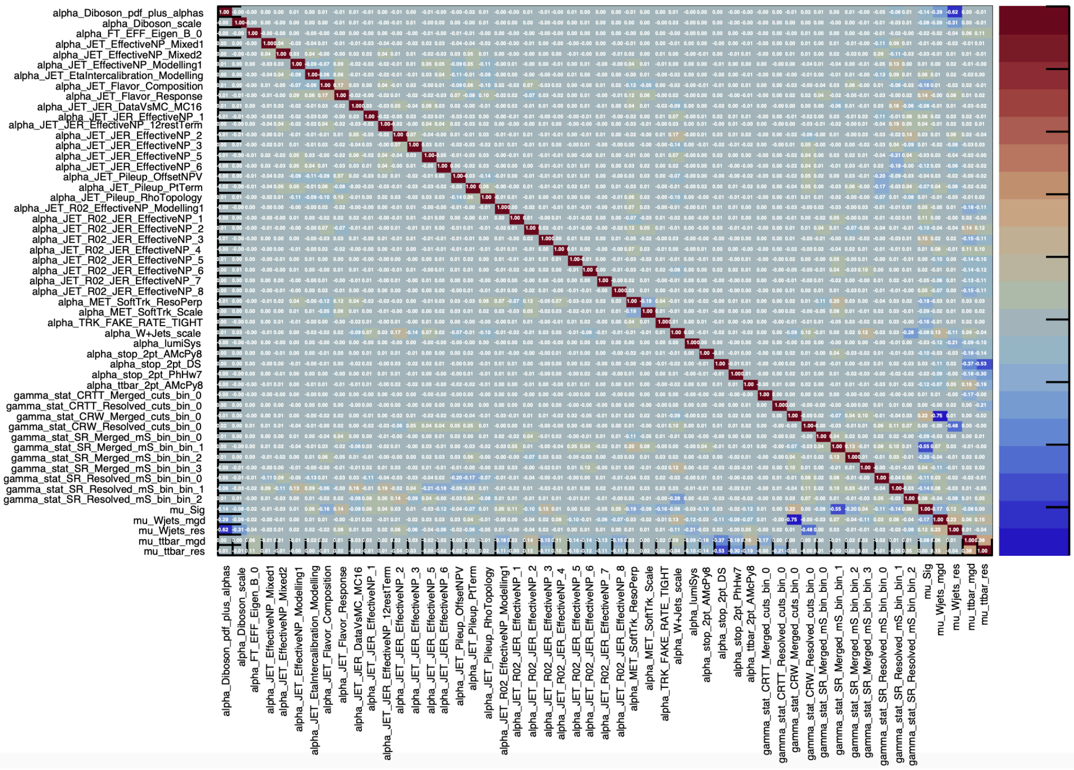

Figure 8.10: Correlation matrix for all NPs considered in the signal+background fit at a sample signal point of $(m_s, m_{Z'}) = (210, 2100)$ GeV, for which at least one coefficient of cross-correlation with another NP is larger than 0.1. See Tables 7.1, C.1 and C.2 for details of the scheme used to name the NPs.

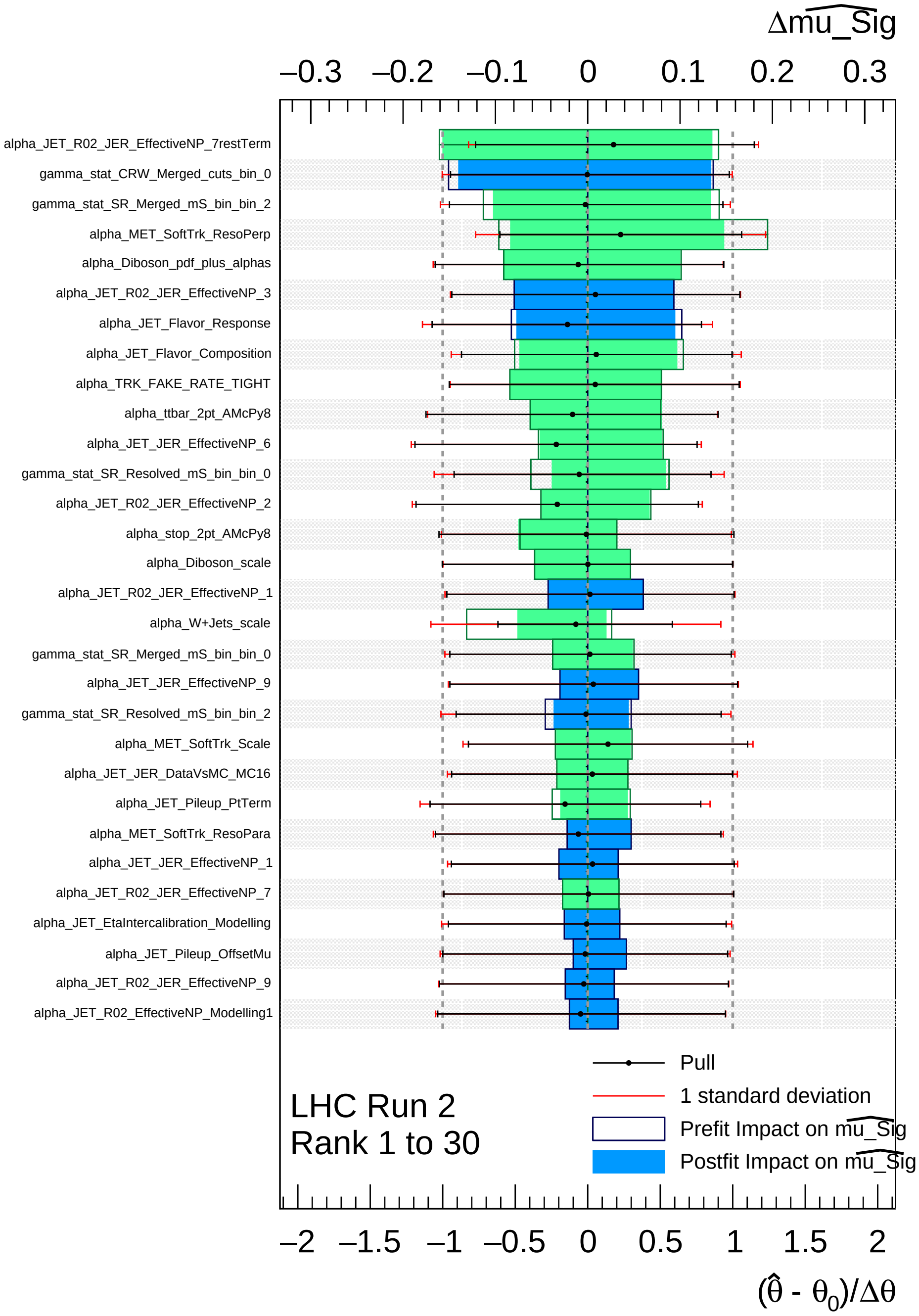

Figure 8.11: Leading 30 pre-and post-fit impacts on μ_{Sig} for NPs associated with experimental and theoretical uncertainties in the signal+background fit at the sample signal point $(m_s, m_{Z'})$=(210, 2100) GeV. NPs are ranked from top to bottom in order of the size of their impact on μ_{Sig}. Blue (green) colouring of post-fit impacts indicates positive (negative) correlation with the signal strength. Post-fit values of the NPs (a.k.a. “pulls”) are also shown as black circles, where red (black) error bars show the size of the pre-fit (post-fit) uncertainty.

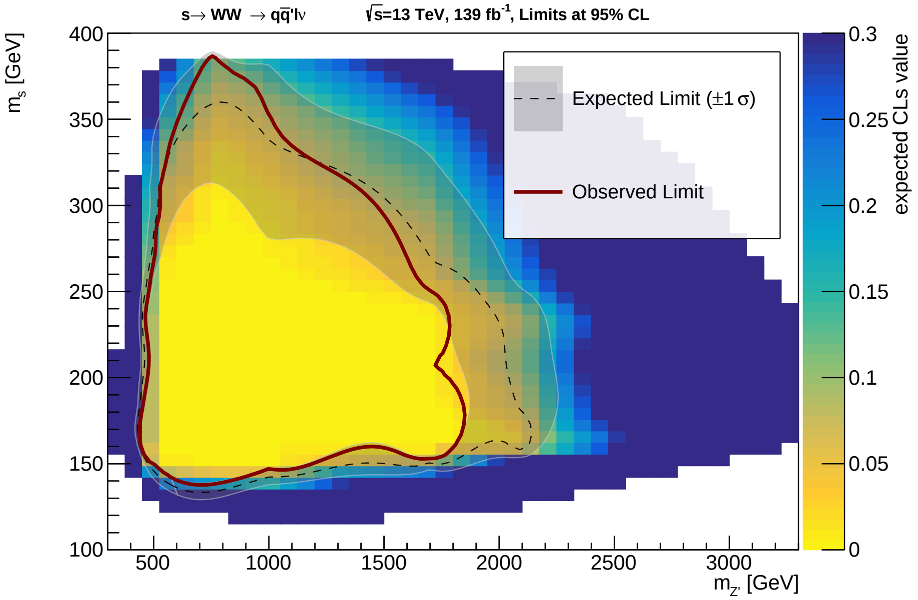

Figure 8.12: Expected (grey dashed with ±1σ uncertainty band) and observed (solid red) range of m_s and $m_{Z'}$ in the DH model excluded by this search. All m_s and $m_{Z'}$ contained within the solid red line are excluded by the search for the choice of $m_\chi = 200$ GeV, $\sin\theta = 0.01$, $g_\chi = 1.0$ and $g_q = 0.25$.

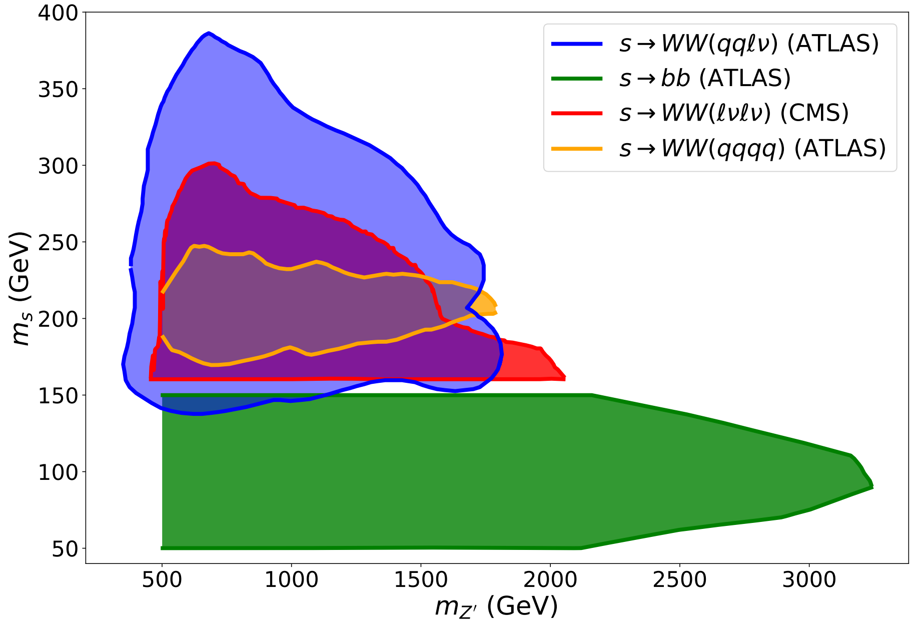

Figure 8.13: Summary of m_s and $m_{Z'}$ parameters in the DH model excluded by all searches for the model by ATLAS and CMS. All values of m_s and $m_{Z'}$ contained within a coloured area are excluded. The range excluded by the search presented in this thesis is shown in blue.

Chapter 9

Conclusion

The study presented in this thesis is part of a worldwide programme to search for dark matter using particle physics detectors, and focusses in particular on dark matter production at the LHC. Given the potential for yet-unconceived mechanisms by which the hypothetical interactions between dark matter and the Standard Model could occur, the search programme at the LHC emphasizes a comprehensive coverage of the possible final states that could result in the detector from dark matter production in the high-energy pp collisions, with searches guided by and interpreted using simplified models for the dark matter production mechanisms. While there could be many possible dark matter production mechanisms that would predict a signature in the $E_{\mathrm{T}}^{\mathrm{miss}} + WW$ final state studied in this thesis, the construction and interpretation of the search are guided by the Dark Higgs model [40]. No statistically significant deviation was found between distributions of ATLAS collision events in the signal regions and Standard Model predictions. The search places exclusion limits on the Dark Higgs model for masses of the Dark Higgs mediator in the approximate range of 150 GeV to 350 GeV. As shown in the summary plot in Figure 8.13, the parameter space of the Dark Higgs model excluded by this search extends the reach of existing searches for the model performed by the ATLAS and CMS collaborations [100, 101, 98], which targeted different final states.

The semileptonic $WW(qq\ell\nu)$ final state studied by this search presented a number of opportunities compared with alternative WW decay modes to develop targeted data selections and analysis strategies that enhance the sensitivity of the search in this final state. The requirement of a single energetic lepton in the final state allows for a significant reduction of SM background processes relative to the fully hadronic channel, and the W+jets process that dominates the Standard Model background in this semileptonic final state is massively reduced by the application of a lower bound on the transverse mass between the final-state lepton and the $E_{\mathrm{T}}^{\mathrm{miss}}$. In addition, the distinct decay modes of the two W bosons enable a detailed reconstruction of the hadronically decaying W. This reconstruction is facilitated in the boosted merged regime by a modification to the basic TAR algorithm [2] used to reconstruct hadronic activity in the final state within one or more large-radius jets, where the modification additionally disentangles the final-state lepton from the hadronic activity. Targeted selections involving the reconstructed hadronically decaying W further reduce the background of SM processes in the search. Although the final-state neutrino prevents a full reconstruction of the Dark Higgs boson, the $\min(m_s)$ strategy allows for an approximate reconstruction, which provides valuable shape discrimination between the DH signal model and SM background processes in the signal regions.

While the searches that target the WW final state were optimized to probe the Dark Higgs model, it is important to acknowledge that appreciable constraints on the Dark Higgs model were also obtained in the bb final state [98] by re-interpreting an existing dark matter search [102] that targeted the same final state, but which was optimized to probe a different model. The impressive sensitivity of the re-interpreted search in the bb final state to the Dark Higgs model highlights the value of ensuring that searches in this $E_{\mathrm{T}}^{\mathrm{miss}} + WW$ final state can also be re-interpreted in the future to constrain any alternative models that may predict a signature in the same final state. This search has been preserved for future re-interpretation using the RECAST framework [3] developed within the ATLAS collaboration. More generally, given the vast multitude of mechanisms by which dark matter could be produced at the LHC, and the tremendous amount of human effort and computing resources involved in developing searches to probe new final states, it will be important moving forward to ensure that all new searches for dark matter can be efficiently re-interpreted to constrain alternative models, thus maximizing the potential impact of each search.

Despite longstanding evidence from observational astronomy for the abundance of dark matter in the universe, its composition remains one of the open mysteries of modern physics. Each time that a new model is tested or new parameter space is probed, a collective step is taken towards cracking the mystery of what makes up the most abundant form of matter in the universe.

Bibliography

[1] M. Baak et al., *HistFitter software framework for statistical data analysis*, Eur. Phys. J. C **75** (2015) (cit. on pp. xvi, 141, 142, 149).

[2] ATLAS Collaboration, *Track assisted techniques for jet substructure*, ATL-PHYS-PUB-2018-012, 2018, URL: `https://cds.cern.ch/record/2630864` (cit. on pp. xvi, 51, 75, 78, 175).

[3] K. Cranmer et al., *RECAST - extending the impact of existing analyses*, JHEP **04** (2011) 038, arXiv: `1010.2506 [hep-ex]` (cit. on pp. xvii, 35, 36, 175).

[4] T. Šimko et al., *Scalable Declarative HEP Analysis Workflows for Containerised Compute Clouds*, Frontiers in Big Data **04** (2021) (cit. on p. xvii).

[5] ATLAS Collaboration, *Search for new phenomena in events with an energetic jet and missing transverse momentum in pp collisions at* $\sqrt{s} = 13$ *TeV with the ATLAS detector*, Phys. Rev. D **103** (11 2021) 112006, arXiv: `2102.10874 [hep-ex]` (cit. on pp. xvii, 22).

[6] ATLAS Collaboration, *Observation of a new particle in the search for the Standard Model Higgs boson with the ATLAS detector at the LHC*, Phys. Lett. B **716** (1 2012) 1–29, arXiv: `1207.7214 [hep-ex]` (cit. on pp. 1, 45).

[7] CMS Collaboration, *Observation of a new boson at a mass of 125 GeV with the CMS experiment at the LHC*, Phys. Lett. B **716** (1 2012) 30–61, arXiv: `1207.7235 [hep-ex]` (cit. on pp. 1, 45).

[8] A. Einstein, *Relativity: The Special and General Theory*, New York: Holt, 1921 (cit. on pp. 1, 2).

[9] Super-Kamiokande Collaboration,
Evidence for Oscillation of Atmospheric Neutrinos,
Phys. Rev. Lett. **81** (1998) 1562–1567, arXiv: `hep-ex/9807003 [hep-ex]`
(cit. on p. 1).

[10] L. Canetti et al., *Matter and antimatter in the universe*,
New Journal of Physics **14** (2012) 095012, arXiv: `1204.4186 [hep-ph]`
(cit. on p. 1).

[11] MissMJ (Wikipedia user), *Standard Model of Elementary Particles*,
[Online; accessed March 9, 2021], 2021,
URL: `https://en.wikipedia.org/wiki/File:Standard_Model_of_Elementary_Particles.svg` (cit. on p. 2).

[12] D. Griffiths, *Introduction to Elementary Particles*,
Weinheim: Wiley-VCH Verlag GmbH & Co., 2008
(cit. on pp. 3, 6–9, 14, 161).

[13] F. Englert et al., *Broken Symmetry and the Mass of Gauge Vector Mesons*,
Phys. Rev. Lett. **13** (9 1964) 321–323 (cit. on pp. 4, 9, 23).

[14] P. W. Higgs, *Broken Symmetries and the Masses of Gauge Bosons*,
Phys. Rev. Lett. **13** (16 1964) 508–509 (cit. on pp. 4, 9, 23).

[15] G. S. Guralnik et al., *Global Conservation Laws and Massless Particles*,
Phys. Rev. Lett. **13** (20 1964) 585–587 (cit. on pp. 4, 9, 23).

[16] G. Breit et al., *Capture of Slow Neutrons*, Phys. Rev. **49** (7 1936) 519–531
(cit. on p. 5).

[17] M. Vogel,
Concepts in particle physics: a concise introduction to the standard model,
Contemporary Physics **59** (2018) 327–328 (cit. on p. 7).

[18] G. Costa et al., *Symmetries and group theory in particle physics: An introduction to space-time and internal symmetries*, vol. 823,
Springer Science & Business Media, 2012 (cit. on p. 8).

[19] W. Greiner et al., *Quantum Chromodynamics*, Berlin: Springer-Verlag, 2007
(cit. on p. 8).

[20] A. Pich, *The Standard Model of Electroweak Interactions*, 2012,
arXiv: `1201.0537 [hep-ph]` (cit. on p. 9).

[21] C. N. Yang et al.,
Conservation of Isotopic Spin and Isotopic Gauge Invariance,
Phys. Rev. **96** (1 1954) 191–195 (cit. on p. 9).

[22] P. Zyla et al., *Review of Particle Physics*, PTEP **2020** (8 2020)
(cit. on pp. 9, 12, 13, 15, 17, 30, 39, 68, 72, 73, 85, 119, 128, 131).

[23] S. Weinberg, *A Model of Leptons*, Phys. Rev. Lett. **19** (21 1967) 1264–1266
(cit. on p. 10).

[24] V. C. Rubin et al., *Extended rotation curves of high-luminosity spiral galaxies. IV. Systematic dynamical properties, Sa → Sc.*,
Astrophys. J. **225** (1978) L107–L111 (cit. on p. 11).

[25] L. Bergström,
Non-baryonic dark matter: observational evidence and detection methods,
Rep. Prog. Phys. **63** (2000) 793–841, arXiv: `hep-ph/0002126 [hep-ph]`
(cit. on p. 11).

[26] M. Persic et al., *Rotation Curves of 967 Spiral Galaxies*,
Astrophys. J. **99** (1995) 501, arXiv: `astro-ph/9502091 [astro-ph]`
(cit. on pp. 11, 12).

[27] M. Milgrom, *A modification of the Newtonian dynamics as a possible alternative to the hidden mass hypothesis.*, Astrophys. J. **270** (1983) 365–370
(cit. on p. 12).

[28] W. H. Tucker et al., *A Search for "Failed Clusters" of Galaxies*,
Astrophys. J. **444** (1995) 532 (cit. on p. 12).

[29] D. Landry et al., *Chandra measurements of a complete sample of X-ray luminous galaxy clusters: the gas mass fraction*,
Mon. Not. R. Astron. Soc. **433** (2013) 2790–2811,
arXiv: `1211.4626 [astro-ph.CO]` (cit. on p. 12).

[30] J.-P. Uzan, *The big-bang theory: construction, evolution and status*, 2016,
arXiv: `1606.06112 [astro-ph.CO]` (cit. on p. 12).

[31] A. A. Penzias et al.,
A Measurement of Excess Antenna Temperature at 4080 Mc/s.,
Astrophys. J. **142** (1965) 419–421 (cit. on p. 13).

[32] Planck Collaboration, *Planck 2018 results*, Astron. Astrophys. **641** (2020), arXiv: `1807.06209 [astro-ph.CO]` (cit. on pp. 13, 14).

[33] B. Famaey et al., *Modified Newtonian Dynamics (MOND): Observational Phenomenology and Relativistic Extensions*, Living Rev. Relativ. **15** (2012) (cit. on p. 13).

[34] C. Skordis et al., *New Relativistic Theory for Modified Newtonian Dynamics*, Phys. Rev. Lett. **127** (16 2021) 161302, arXiv: `2007.00082 [astro-ph.CO]` (cit. on p. 13).

[35] S. D. M. White et al., *Clustering in a neutrino-dominated universe*, Astrophys. J. **274** (1983) L1–L5 (cit. on p. 14).

[36] H. Baer et al., *Dark matter production in the early Universe: Beyond the thermal WIMP paradigm*, Physics Reports **555** (2015) 1–60, arXiv: `1407.0017 [hep-ph]` (cit. on p. 15).

[37] L. Roszkowski et al., *WIMP dark matter candidates and searches – current status and future prospects*, Rep. Prog. Phys. **81** (2018) 066201, arXiv: `1707.06277 [hep-ph]` (cit. on p. 15).

[38] M. Pospelov et al., *Secluded WIMP dark matter*, Phys. Lett. B **662** (1 2008) 53–61, arXiv: `0711.4866 [hep-ph]` (cit. on p. 15).

[39] M. Duerr et al., *How to save the WIMP: global analysis of a dark matter model with two s-channel mediators*, JHEP **09** (2016) 042, arXiv: `1606.07609 [hep-ph]` (cit. on pp. 15, 26, 28–30).

[40] M. Duerr et al., *Hunting the dark Higgs*, JHEP **04** (2017) 143, arXiv: `1701.08780 [hep-ph]` (cit. on pp. 15, 22, 23, 29, 30, 174).

[41] J. Billard et al., *Direct Detection of Dark Matter – APPEC Committee Report*, 2021, arXiv: `2104.07634 [hep-ex]` (cit. on pp. 15–17).

[42] M. Cirelli, *Indirect searches for dark matter*, Pramana **79** (2012) 1021–1043, arXiv: `1912.12739 [hep-ph]` (cit. on pp. 15, 17).

[43] A. Boveia et al., *Dark Matter Searches at Colliders*, Annu. Rev. Nucl. Part. Sci. **68** (2018) 429–459 (cit. on pp. 16, 17).

[44] I. Lawson et al., *The SNOLAB Deep Underground Research Facility and Its Science Program*, Nuclear Physics News **23** (2013) 5–9 (cit. on p. 16).

[45] D. Baxter et al., *Recommended conventions for reporting results from direct dark matter searches*, Eur. Phys. J. C **81** (2021), arXiv: `2105.00599 [hep-ex]` (cit. on p. 16).

[46] M. Ibe et al., *Migdal effect in dark matter direct detection experiments*, JHEP **03** (2018) 003, arXiv: `1707.07258 [hep-ph]` (cit. on p. 17).

[47] J. Billard et al., *Assessing the discovery potential of directional detection of dark matter*, Phys. Rev. D **85** (2012), arXiv: `1110.6079 [astro-ph.CO]` (cit. on p. 17).

[48] J. Billard et al., *Implication of neutrino backgrounds on the reach of next generation dark matter direct detection experiments*, Phys. Rev. D **89** (2014), arXiv: `1307.5458 [hep-ph]` (cit. on p. 17).

[49] J. Conrad, *Indirect Detection of WIMP Dark Matter: a compact review*, (2014), arXiv: `1411.1925 [hep-ph]` (cit. on p. 17).

[50] N. ArkaniaHamed et al., *The hierarchy problem and new dimensions at a millimeter*, Phys. Lett. B **429** (1998) 263, arXiv: `hep-ph/9803315 [hep-ph]` (cit. on p. 18).

[51] P. Brax et al., *LHC signatures of scalar dark energy*, Phys. Rev. D **94** (2016), arXiv: `1604.04299 [hep-ph]` (cit. on p. 18).

[52] L. Evans et al., *LHC Machine*, JINST **03** (2008) S08001 (cit. on pp. 19, 40).

[53] ATLAS Collaboration, *The ATLAS Experiment at the CERN Large Hadron Collider*, JINST **03** (2008) S08003 (cit. on pp. 19, 43, 44, 46, 49, 52).

[54] CMS Collaboration, *The CMS experiment at the CERN LHC*, JINST **03** (2008) S08004 (cit. on pp. 19, 43).

[55] LHCb Collaboration, *The LHCb Detector at the LHC*, JINST **03** (2008) S08005 (cit. on pp. 19, 44).

[56] N. Trevisani, *Collider Searches for Dark Matter (ATLAS + CMS)*, Universe **04** (2018) 131 (cit. on p. 19).

[57] T. Mombacher, *Dark matter searches at LHCb*, 2021, arXiv: `2111.00306 [hep-ex]` (cit. on p. 19).

[58] BABAR collaboration, *The BABAR detector*, Nucl. Instrum. Methods Phys. Res. A **479** (2002) 1–116, arXiv: `hep-ex/0105044 [hep-ex]` (cit. on p. 19).

[59] Belle Collaboration, *The Belle detector*, Nucl. Instrum. Methods Phys. Res. A **479** (2002) 117, Detectors for Asymmetric B-factories (cit. on p. 19).

[60] I. Adachi et al., *Detectors for extreme luminosity: Belle II*, Nucl. Instrum. Meth. A **907** (2018) 46 (cit. on p. 19).

[61] K. Akai et al., *SuperKEKB collider*, Nucl. Instrum. Methods Phys. Res. A **907** (2018) 188–199, arXiv: `1809.01958 [physics.acc-ph]` (cit. on p. 19).

[62] M. Campajola, *Dark Sector first results at Belle II*, Phys. Scripta **96** (2021) 084005 (cit. on p. 19).

[63] H. Ray, *The MiniBooNE Experiment: An Overview*, 2007, arXiv: `hep-ex/0701040 [hep-ex]` (cit. on p. 20).

[64] A. Habig, *The NOvA Experiment*, Nucl. Phys. B Proc. Suppl. **229-232** (2012) 460, ed. by G. S. Tzanakos (cit. on p. 20).

[65] MiniBooNE collaboration, *Dark matter search in nucleon, pion, and electron channels from a proton beam dump with MiniBooNE*, Phys. Rev. D **98** (2018), arXiv: `1807.06137 [hep-ex]` (cit. on p. 20).

[66] P. deNiverville et al., *Hunting sub-GeV dark matter with the NOvA near detector*, Phys. Rev. D **99** (2019), arXiv: `1807.06501 [hep-ph]` (cit. on p. 20).

[67] NA64 Collaboration, *Dark Matter Search in Missing Energy Events with NA64*, Phys. Rev. Lett. **123** (2019), arXiv: `1906.00176 [hep-ex]` (cit. on p. 20).

[68] G. Jungman et al., *Supersymmetric dark matter*, Phys. Rept. **267** (1996) 195, arXiv: `hep-ph/9506380` (cit. on p. 20).

[69] O. Buchmueller et al.,
Beyond Effective Field Theory for Dark Matter Searches at the LHC,
JHEP **01** (2014) 025, arXiv: `1308.6799 [hep-ph]` (cit. on p. 21).

[70] D. Abercrombie et al., *Dark Matter benchmark models for early LHC Run-2 Searches: Report of the ATLAS/CMS Dark Matter Forum*,
Physics of the Dark Universe **27** (2020) 100371,
arXiv: `1507.00966 [hep-ex]` (cit. on p. 21).

[71] C. Csaki, *The Minimal Supersymmetric Standard Model (MSSM)*,
Mod. Phys. Lett. A **11** (1996) 599, arXiv: `hep-ph/9606414 [hep-ex]`
(cit. on p. 20).

[72] CMS collaboration,
Search for new particles in events with energetic jets and large missing transverse momentum in proton-proton collisions at $\sqrt{s} = 13$ *TeV*,
JHEP **11** (2021) 153, arXiv: `2107.13021 [hep-ex]` (cit. on p. 22).

[73] CMS Collaboration, *Search for dark matter produced in association with heavy-flavor quark pairs in proton-proton collisions at* $\sqrt{s} = 13$ *TeV*,
Eur. Phys. J. C **77** (2017), arXiv: `1706.02581 [hep-ex]` (cit. on p. 22).

[74] ATLAS Collaboration, *Search for dark matter produced in association with bottom or top quarks in* $\sqrt{s} = 13$ *TeV pp collisions with the ATLAS detector*,
Eur. Phys. J. C **78** (2018), arXiv: `1710.11412 [hep-ex]` (cit. on p. 22).

[75] ATLAS Collaboration,
Search for associated production of a Z boson with an invisibly decaying Higgs boson or dark matter candidates at $\sqrt{s} = 13$ *TeV with the ATLAS detector*,
(2021), arXiv: `2111.08372 [hep-ex]` (cit. on p. 22).

[76] CMS Collaboration, *Search for dark matter produced in association with a leptonically decaying Z boson in proton-proton collisions at* $\sqrt{s} = 13$ *TeV*,
Eur. Phys. J. C **81** (2021), arXiv: `2008.04735 [hep-ex]` (cit. on p. 22).

[77] CMS Collaboration, *Search for dark matter particles produced in association with a Higgs boson in proton-proton collisions at* $\sqrt{s} = 13$ *TeV*,
JHEP **03** (2020) 025, arXiv: `1908.01713 [hep-ex]` (cit. on p. 22).

[78] ATLAS Collaboration, *Search for Dark Matter produced in association with a Standard Model Higgs boson decaying to b-quarks using the full Run 2 collision data with the ATLAS detector*, (2021), arXiv: `2108.13391 [hep-ex]` (cit. on p. 22).

[79] ATLAS Collaboration, *Search for dark matter in events with missing transverse momentum and a Higgs boson decaying into two photons in pp collisions at* $\sqrt{s} = 13\,TeV$ *with the ATLAS detector*, JHEP **10** (2021) 013, arXiv: `2104.13240 [hep-ex]` (cit. on p. 22).

[80] A. Alves et al., *Dark matter complementarity and the* Z' *portal*, Phys. Rev. D **92** (2015), arXiv: `1501.03490v2 [hep-ph]` (cit. on p. 25).

[81] M. Fairbairn et al., *Constraints on* Z' *models from LHC dijet searches and implications for dark matter*, JHEP **09** (2016) 018, arXiv: `1605.07940v2 [hep-ph]` (cit. on pp. 25–27).

[82] M. Chala et al., *Constraining dark sectors with monojets and dijets*, JHEP **07** (2015) 089, arXiv: `1503.05916 [hep-ph]` (cit. on pp. 25–27).

[83] M. T. Frandsen et al., *LHC and Tevatron bounds on the dark matter direct detection cross-section for vector mediators*, JHEP **07** (2012) 123, arXiv: `1204.3839v2 [hep-ph]` (cit. on p. 29).

[84] P. J. Fitzpatrick et al., *New Pathways to the Relic Abundance of Vector-Portal Dark Matter*, 2020, arXiv: `2011.01240 [hep-ph]` (cit. on p. 29).

[85] M. Blennow et al., *Neutrino portals to dark matter*, Eur. Phys. J. C **79** (2019), arXiv: `1903.00006 [hep-ph]` (cit. on p. 29).

[86] G. Arcadi et al., *Dark Matter through the Higgs portal*, Physics Reports **842** (2020) 1–180 (cit. on p. 29).

[87] Y. Nomura et al., *Dark matter through the axion portal*, Phys. Rev. D **79** (2009), arXiv: `0810.5397 [hep-ex]` (cit. on p. 29).

[88] A. Pais, *Remark on Baryon Conservation*, Phys. Rev. D **08** (6 1973) 1844–1846 (cit. on p. 30).

[89] J. Berger et al.,
Cosmological constraints on decoupled dark photons and dark Higgs,
J. Cosmol. Astropart. Phys. **11** (2016), arXiv: `1605.07195 [hep-ex]`
(cit. on p. 30).

[90] *A combination of measurements of Higgs boson production and decay using up to* 139 *fb*$^{-1}$ *of proton–proton collision data at* $\sqrt{s} = 13$ *TeV collected with the ATLAS experiment*, tech. rep. ATLAS-CONF-2020-027, CERN, 2020,
URL: `https://cds.cern.ch/record/2725733` (cit. on p. 31).

[91] *Combined Higgs boson production and decay measurements with up to 137 fb-1 of proton-proton collision data at* $\sqrt{s} = 13$ *TeV*,
tech. rep. CMS-PAS-HIG-19-005, CERN, 2020,
URL: `https://cds.cern.ch/record/2706103` (cit. on p. 31).

[92] S. Argyropoulos et al.,
Collider Searches for Dark Matter through the Higgs Lens,
Symmetry **13** (2021) 2406, arXiv: `2109.13597 [hep-ex]` (cit. on p. 31).

[93] CMS Collaboration, *Search for Narrow Resonances in the b-Tagged Dijet Mass Spectrum in Proton-Proton Collisions at* $\sqrt{s} = 8$ *TeV*,
Phys. Rev. Lett. **120** (2018), arXiv: `1802.06149 [hep-ex]` (cit. on p. 32).

[94] ATLAS Collaboration,
Search for Low-Mass Dijet Resonances Using Trigger-Level Jets with the ATLAS Detector in pp Collisions at $\sqrt{s} = 13$ *TeV*,
Phys. Rev. Lett. **121** (2018), arXiv: `1804.03496 [hep-ex]` (cit. on p. 32).

[95] CMS Collaboration, *Search for narrow and broad dijet resonances in proton-proton collisions at* $\sqrt{s} = 13$ *TeV and constraints on dark matter mediators and other new particles*, JHEP **08** (2018) 130,
arXiv: `1806.00843 [hep-ex]` (cit. on pp. 32, 37).

[96] ATLAS Collaboration, *Search for low-mass resonances decaying into two jets and produced in association with a photon using pp collisions at* $\sqrt{s} = 13$ *TeV with the ATLAS detector*, Phys. Lett. B **795** (2019) 56–75,
arXiv: `1901.10917 [hep-ex]` (cit. on p. 32).

[97] ATLAS Collaboration,
Search for new phenomena in dijet events using 37 fb^{-1} *of pp collision data collected at* $\sqrt{s} = 13$ *TeV with the ATLAS detector*,
Phys. Rev. D **96** (5 2017) 052004, arXiv: `1703.09127 [hep-ex]`
(cit. on p. 32).

[98] *RECAST framework reinterpretation of an ATLAS Dark Matter Search constraining a model of a dark Higgs boson decaying to two b-quarks*,
tech. rep. ATL-PHYS-PUB-2019-032, CERN, 2019,
URL: `https://cds.cern.ch/record/2686290` (cit. on pp. 34–37, 174, 175).

[99] D. Abercrombie et al., *Dark Matter benchmark models for early LHC Run-2 Searches: Report of the ATLAS/CMS Dark Matter Forum*,
Physics of the Dark Universe **27** (2020) 100371,
arXiv: `1507.00966 [hep-ex]` (cit. on p. 35).

[100] ATLAS Collaboration, *Search for Dark Matter Produced in Association with a Dark Higgs Boson Decaying into* $W^{\pm}W^{\mp}$ *or* ZZ *in Fully Hadronic Final States from* $\sqrt{s} = 13$ *TeV pp Collisions Recorded with the ATLAS Detector*,
Phys. Rev. Lett. **126** (12 2021) 121802, arXiv: `2010.06548 [hep-ex]`
(cit. on pp. 35, 38, 39, 174).

[101] *Search for dark matter particles produced in association with a dark Higgs boson decaying into* W^+W^- *in proton-proton collisions at* $\sqrt{s} = 13$ *TeV with the CMS detector*, tech. rep. CMS-PAS-EXO-20-013, CERN, 2021,
URL: `https://cds.cern.ch/record/2776774` (cit. on pp. 36, 38, 39, 174).

[102] *Search for Dark Matter Produced in Association with a Higgs Boson decaying to* $b\bar{b}$ *at* $\sqrt{s} = 13$ *TeV with the ATLAS Detector using 79.8* fb^{-1} *of proton-proton collision data*, tech. rep. ATLAS-CONF-2018-039,
CERN, 2018, URL: `https://cds.cern.ch/record/2632344`
(cit. on pp. 36, 37, 175).

[103] H. T. Edwards,
The Tevatron Energy Doubler: A Superconducting Accelerator,
Annu. Rev. Nucl. Part. Sci. **35** (1985) 605–660 (cit. on p. 40).

[104] T.-M. Yan et al., *The parton model and its applications*,
Int. J. Mod. Phys. A **29** (2014) 1430071, arXiv: `1409.0051 [hep-ph]`
(cit. on p. 41).

[105] S. Bailey et al., *Parton distributions from LHC, HERA, Tevatron and fixed target data: MSHT20 PDFs*, Eur. Phys. J. C **81** (2021), arXiv: `2012.04684 [hep-ph]` (cit. on p. 41).

[106] *Standard Model Summary Plots June 2021*, tech. rep. ATL-PHYS-PUB-2021-032, CERN, 2021, URL: `http://cds.cern.ch/record/2777014` (cit. on p. 42).

[107] *Performance of the ALICE experiment at the CERN LHC*, Int. J. Mod. Phys. A **29** (2014) 1430044, arXiv: `1402.4476 [nucl-ex]` (cit. on p. 44).

[108] R Alkofer et al., *Quark confinement: the hard problem of hadron physics*, J. Phys. G **34** (2007), arXiv: `hep-ph/0610365 [hep-ph]` (cit. on p. 44).

[109] P. Braun-Munzinger et al., *Colloquium: Phase diagram of strongly interacting matter*, Rev. Mod. Phys. **81** (3 2009) 1031–1050, arXiv: `0801.4256 [hep-ph]` (cit. on p. 44).

[110] *ATLAS inner detector: Technical Design Report, 1*, Technical design report. ATLAS ATLAS-TDR-4, CERN-LHCC-97-016, Geneva: CERN, 1997, URL: `https://cds.cern.ch/record/331063` (cit. on p. 47).

[111] L. D. Landau et al., *The cascade theory of electronic showers*, Proc. R. Soc. Lond. A **166** (1938) 213–228 (cit. on p. 47).

[112] C. Leroy et al., *Physics of cascading shower generation and propagation in matter: Principles of high-energy, ultrahigh-energy and compensating calorimetry*, Rep. Prog. Phys. **63** (2000) 505–606 (cit. on pp. 47, 49).

[113] H. Zhang et al., *The ATLAS Liquid Argon Calorimeter: Overview and Performance*, J. Phys. Conf. Ser. **293** (2011) 012044 (cit. on p. 48).

[114] V Grassi, *The Atlas Liquid Argon Calorimeter at the CERN Large Hadron Collider: General Performance and Latest Developments of the High Voltage System*, tech. rep. ATL-LARG-PROC-2013-013, CERN, 2013, URL: `https://cds.cern.ch/record/1628748` (cit. on p. 48).

[115] ATLAS Collaboration,
Electron reconstruction and identification in the ATLAS experiment using the 2015 and 2016 LHC proton-proton collision data at $\sqrt{s} = 13$ *TeV*,
Eur. Phys. J. C **79** (2019), arXiv: `1902.04655 [physics.ins-det]`
(cit. on p. 48).

[116] S. Schramm, *ATLAS Jet Reconstruction, Calibration, and Tagging of Lorentz-boosted Objects*, tech. rep. ATL-PHYS-PROC-2017-236,
CERN, 2017, URL: `https://cds.cern.ch/record/2291608` (cit. on p. 50).

[117] ATLAS Collaboration, *Topological cell clustering in the ATLAS calorimeters and its performance in LHC Run 1*, Eur. Phys. J. C **77** (2017),
arXiv: `1603.02934 [hep-ex]` (cit. on p. 50).

[118] M. Cacciari et al., *The anti-*k_t *jet clustering algorithm*, JHEP **04** (2008) 063,
arXiv: `0802.1189 [hep-ph]` (cit. on pp. 50, 72, 132).

[119] *ATLAS muon spectrometer: Technical Design Report*,
Technical design report. ATLAS ATLAS-TDR-10, CERN-LHCC-97-022,
Geneva: CERN, 1997, URL: `https://cds.cern.ch/record/331068`
(cit. on p. 51).

[120] ATLAS Collaboration, *Muon reconstruction and identification efficiency in ATLAS using the full Run 2 pp collision data set at* $\sqrt{s} = 13$ *TeV*,
Eur. Phys. J. C **81** (2021), arXiv: `2012.00578 [hep-ex]`
(cit. on pp. 51, 52, 81).

[121] ATLAS Collaboration,
Performance of missing transverse momentum reconstruction with the ATLAS detector using proton-proton collisions at $\sqrt{s} = 13$ *TeV*,
Eur. Phys. J. C **78** (2018) (cit. on p. 52).

[122] M. zur Nedden,
The Run-2 ATLAS Trigger System: Design, Performance and Plan,
tech. rep. ATL-DAQ-PROC-2016-039, CERN, 2016,
URL: `https://cds.cern.ch/record/2238679` (cit. on pp. 53, 54).

[123] ATLAS Collaboration, *The ATLAS Simulation Infrastructure*,
Eur. Phys. J. C **70** (2010) 823–874, arXiv: `1005.4568 [physics.ins-det]`
(cit. on p. 58).

[124] S. Agostinelli et al., *Geant4–a simulation toolkit*, Nucl. Instrum. Methods Phys. Res. A **506** (2003) 250–303 (cit. on pp. 58, 118).

[125] Z. Marshall et al., *Simulation of Pile-up in the ATLAS Experiment*, J. Phys. Conf. Ser. **513** (2014) 022024 (cit. on pp. 59, 72).

[126] H. Wiedemann, *Particle Accelerator Physics*, 4th ed., Springer, 2015, URL: `https://doi.org/10.1007/978-3-319-18317-6` (cit. on p. 59).

[127] A. Haas, *ATLAS Simulation using Real Data: Embedding and Overlay*, J. Phys. Conf. Ser. **898** (2017) 042004 (cit. on p. 60).

[128] Novak, Tadej, *New techniques for pile-up simulation in ATLAS*, EPJ Web Conf. **214** (2019) 02044 (cit. on p. 60).

[129] J. Alwall et al., *MadGraph 5: going beyond*, JHEP **06** (2011) 128, arXiv: `1106.0522 [hep-ph]` (cit. on p. 62).

[130] J. Alwall et al., *The automated computation of tree-level and next-to-leading order differential cross sections, and their matching to parton shower simulations*, JHEP **07** (2014) 079, arXiv: `1405.0301 [hep-ph]` (cit. on pp. 62, 129).

[131] T. Sjöstrand et al., *An introduction to PYTHIA 8.2*, Comput. Phys. Commun. **191** (2015) 159, arXiv: `1410.3012 [hep-ph]` (cit. on pp. 63, 66, 67).

[132] T. Gleisberg et al., *Event generation with SHERPA 1.1*, JHEP **02** (2009) 007, arXiv: `0811.4622 [hep-ph]` (cit. on pp. 64, 131).

[133] C. Varni, *Tracking and flavour-tagging performance at ATLAS*, tech. rep. ATL-PHYS-PROC-2020-085, CERN, 2020, URL: `https://cds.cern.ch/record/2742644` (cit. on p. 66).

[134] S. Frixione et al., *A positive-weight next-to-leading-order Monte Carlo for heavy flavour hadroproduction*, JHEP **09** (2007) 126, arXiv: `0707.3088 [hep-ph]` (cit. on p. 66).

[135] P. Nason, *A new method for combining NLO QCD with shower Monte Carlo algorithms*, JHEP **11** (2004) 040, arXiv: `hep-ph/0409146` (cit. on pp. 66, 67).

[136] S. Frixione et al., *Matching NLO QCD computations with parton shower simulations: the POWHEG method*, JHEP **11** (2007) 070, arXiv: `0709.2092 [hep-ph]` (cit. on pp. 66, 67).

[137] S. Alioli et al., *A general framework for implementing NLO calculations in shower Monte Carlo programs: the POWHEG BOX*, JHEP **06** (2010) 043, arXiv: `1002.2581 [hep-ph]` (cit. on pp. 66, 67).

[138] E. Re, *Single-top Wt-channel production matched with parton showers using the POWHEG method*, Eur. Phys. J. C **71** (2011) 1547, arXiv: `1009.2450 [hep-ph]` (cit. on p. 67).

[139] S Xella, *Physics objects reconstruction in the ATLAS experiment*, tech. rep. ATL-GEN-PROC-2013-001, CERN, 2013, URL: `https://cds.cern.ch/record/1519113` (cit. on p. 68).

[140] *Measurement of the tau lepton reconstruction and identification performance in the ATLAS experiment using pp collisions at $\sqrt{s} = 13\ TeV$*, tech. rep. ATLAS-CONF-2017-029, CERN, 2017, URL: `https://cds.cern.ch/record/2261772` (cit. on p. 69).

[141] ATLAS Collaboration, *Electron and photon reconstruction and performance in ATLAS using a dynamical, topological cell clustering-based approach*, ATL-PHYS-PUB-2017-022, 2017, URL: `https://cds.cern.ch/record/2298955` (cit. on p. 69).

[142] ATLAS Collaboration, *Electron reconstruction and identification in the ATLAS experiment using the 2015 and 2016 LHC proton–proton collision data at $\sqrt{s} = 13\ TeV$*, Eur. Phys. J. C **79** (2019) 639, arXiv: `1902.04655 [hep-ex]` (cit. on pp. 70, 71).

[143] ATLAS Collaboration, *Electron and photon energy calibration with the ATLAS detector using 2015–2016 LHC proton–proton collision data*, JINST **14** (2019) P03017, arXiv: `1812.03848 [hep-ex]` (cit. on p. 70).

[144] ATLAS Collaboration, *Muon reconstruction performance of the ATLAS detector in proton–proton collision data at $\sqrt{s} = 13\ TeV$*, Eur. Phys. J. C **76** (2016) 292, arXiv: `1603.05598 [hep-ex]` (cit. on p. 71).

[145] S. Rettie, *Muon identification and performance in the ATLAS experiment*, tech. rep. ATL-PHYS-PROC-2018-052, CERN, 2018, URL: `https://cds.cern.ch/record/2626330` (cit. on p. 71).

[146] ATLAS Collaboration, *Jet reconstruction and performance using particle flow with the ATLAS Detector*, Eur. Phys. J. C **77** (2017) 466, arXiv: `1703.10485 [hep-ex]` (cit. on p. 71).

[147] ATLAS Collaboration, *Monte Carlo Calibration and Combination of In-situ Measurements of Jet Energy Scale, Jet Energy Resolution and Jet Mass in ATLAS*, ATLAS-CONF-2015-037, 2015, URL: `https://cds.cern.ch/record/2044941` (cit. on p. 72).

[148] ATLAS Collaboration, *Selection of jets produced in* 13 *TeV proton–proton collisions with the ATLAS detector*, ATLAS-CONF-2015-029, 2015, URL: `https://cds.cern.ch/record/2037702` (cit. on p. 72).

[149] ATLAS Collaboration, *Tagging and suppression of pileup jets with the ATLAS detector*, ATLAS-CONF-2014-018, 2014, URL: `https://cds.cern.ch/record/1700870` (cit. on p. 72).

[150] ATLAS Collaboration, *Calibration of light-flavour b-jet mistagging rates using ATLAS proton–proton collision data at* $\sqrt{s} = 13$ *TeV*, ATLAS-CONF-2018-006, 2018, URL: `https://cds.cern.ch/record/2314418` (cit. on p. 73).

[151] M. Cacciari et al., *The catchment area of jets*, JHEP **04** (2008) 005 (cit. on p. 75).

[152] ATLAS Collaboration, *Performance of missing transverse momentum reconstruction with the ATLAS detector using proton–proton collisions at* $\sqrt{s} = 13$ *TeV*, Eur. Phys. J. C **78** (2018) 903, arXiv: `1802.08168 [hep-ex]` (cit. on p. 80).

[153] ATLAS Collaboration, *Object-based missing transverse momentum significance in the ATLAS Detector*, ATLAS-CONF-2018-038, 2018, URL: `https://cds.cern.ch/record/2630948` (cit. on p. 80).

[154] W. Buttinger et al., *Formulae for Estimating Significance*, tech. rep. ATL-COM-GEN-2018-026, CERN, 2018, URL: `https://cds.cern.ch/record/2643488` (cit. on p. 90).

[155] A. J. Larkoski et al., *Energy Correlation Functions for Jet Substructure*, JHEP **06** (2013) 108, arXiv: `1305.0007 [hep-ph]` (cit. on p. 94).

[156] A. J. Larkoski et al., *Analytic boosted boson discrimination*, JHEP **05** (2016) 117, arXiv: `1507.03018 [hep-ph]` (cit. on p. 94).

[157] S. Forte et al., *Progress in the Determination of the Partonic Structure of the Proton*, Annu. Rev. Nucl. Part. Sci. **63** (2013) 291–328, arXiv: `1301.6754 [hep-ph]` (cit. on p. 98).

[158] J. Butterworth et al., *PDF4LHC recommendations for LHC Run II*, J. Phys. G **43** (2016) 023001, arXiv: `1510.03865 [hep-ph]` (cit. on pp. 98, 127).

[159] ATLAS Collaboration, *Performance of the missing transverse momentum triggers for the ATLAS detector during Run-2 data taking*, JHEP **08** (2020) 080, arXiv: `2005.09554 [hep-ex]` (cit. on p. 111).

[160] M. Ronzani, *ATLAS Transverse Missing Energy Trigger Performance*, tech. rep. ATL-DAQ-PROC-2019-028, CERN, 2019, URL: `https://cds.cern.ch/record/2693457` (cit. on pp. 111, 113).

[161] ATLAS Collaboration, *Luminosity determination in pp collisions at* $\sqrt{s} = 13$ *TeV using the ATLAS detector at the LHC*, ATLAS-CONF-2019-021, 2019, URL: `https://cds.cern.ch/record/2677054` (cit. on p. 119).

[162] R. D. Ball et al., *A determination of parton distributions with faithful uncertainty estimation*, Nuclear Physics B **809** (2009) 1–63, arXiv: `0808.1231 [hep-ph]` (cit. on p. 127).

[163] *ATLAS Pythia 8 tunes to 7 TeV data*, tech. rep. ATL-PHYS-PUB-2014-021, CERN, 2014, URL: `https://cds.cern.ch/record/1966419` (cit. on p. 128).

[164] M. Bähr et al., *Herwig++ physics and manual*, Eur. Phys. J. C **58** (2008) 639, arXiv: `0803.0883 [hep-ph]` (cit. on p. 129).

[165] J. Bellm et al., *Herwig 7.0/Herwig++ 3.0 release note*, Eur. Phys. J. C **76** (2016) 196, arXiv: `1512.01178 [hep-ph]` (cit. on p. 129).

[166] S. Höche et al., *QCD matrix elements and truncated showers*, JHEP **05** (2009) 053, arXiv: `0903.1219 [hep-ph]` (cit. on p. 131).

[167] J. K. Anders et al., *V+Jets theoretical uncertainties estimation via a parameterisation method*, tech. rep. ATL-COM-PHYS-2016-044, CERN, 2016, URL: `https://cds.cern.ch/record/2125718` (cit. on p. 131).

[168] C. D. White et al., *Isolating Wt production at the LHC*, JHEP **11** (2009) 074, arXiv: `0908.0631 [hep-ph]` (cit. on p. 133).

[169] K. Cranmer et al., *HistFactory: A tool for creating statistical models for use with RooFit and RooStats*, tech. rep. CERN-OPEN-2012-016, New York U., 2012, URL: `https://cds.cern.ch/record/1456844` (cit. on p. 143).

[170] S. S. Wilks, *The Large-Sample Distribution of the Likelihood Ratio for Testing Composite Hypotheses*, Ann. Math. Stat. **09** (1938) 60–62 (cit. on p. 152).

[171] G. Cowan et al., *Asymptotic formulae for likelihood-based tests of new physics*, Eur. Phys. J. C **71** (2011), arXiv: `1007.1727 [physics.data-an]` (cit. on p. 153).

[172] D. M. Lane, *Online Statistics Education: A Multimedia Course of Study*, [Online; accessed March 11, 2021], Rice University, URL: `http://onlinestatbook.com/` (cit. on p. 157).

[173] *Recommendations on presenting LHC searches for missing transverse energy signals using simplified s-channel models of dark matter*, Physics of the Dark Universe **27** (2020) 100365, arXiv: `1603.04156 [hep-ex]` (cit. on p. 161).

Appendix A

Kinematic Distributions (N-1) in Signal Regions

Figures A.1 and A.2 show N-1 plots with the finalized selections for the variables listed in Table 5.3 that are used to define the analysis regions that are not shown in Figures 5.10 and A.2, respectively, in Section 5.2.3. The placements of cuts is also shown using red arrows.

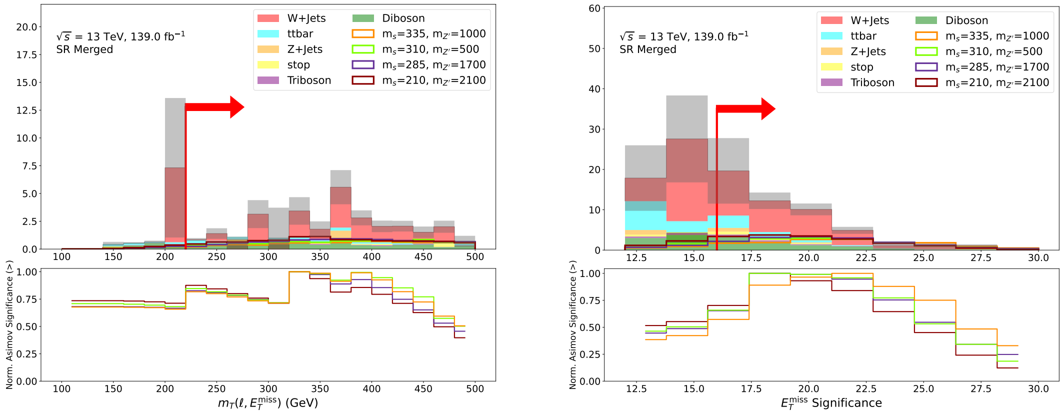

(a) $m_{\mathrm{T}}(\ell, E_{\mathrm{T}}^{\mathrm{miss}})$ (b) $\mathcal{S}$

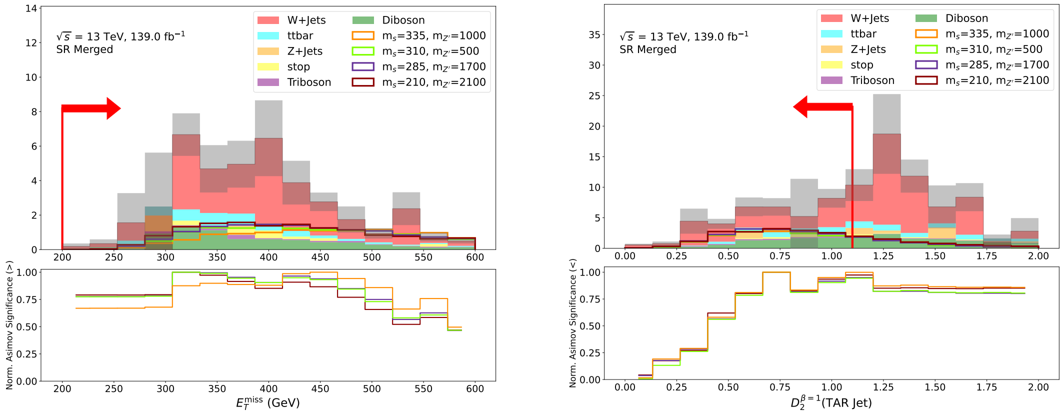

(c) $E_{\mathrm{T}}^{\mathrm{miss}}$ (d) $D_2^{\beta=1}$(TAR Jet)

Figure A.1: N-1 Distributions for variables used in the merged signal region definition. Grey bands show statistical uncertainty on background estimate. The lower panel shows the cumulative Asimov significance normalized to unit peak, where the direction (> or <) specified in the y label indicates whether the significance is being summed from above (>) or from below (<). Red vertical line and arrow show placement and direction of selection on the given variable in this region.

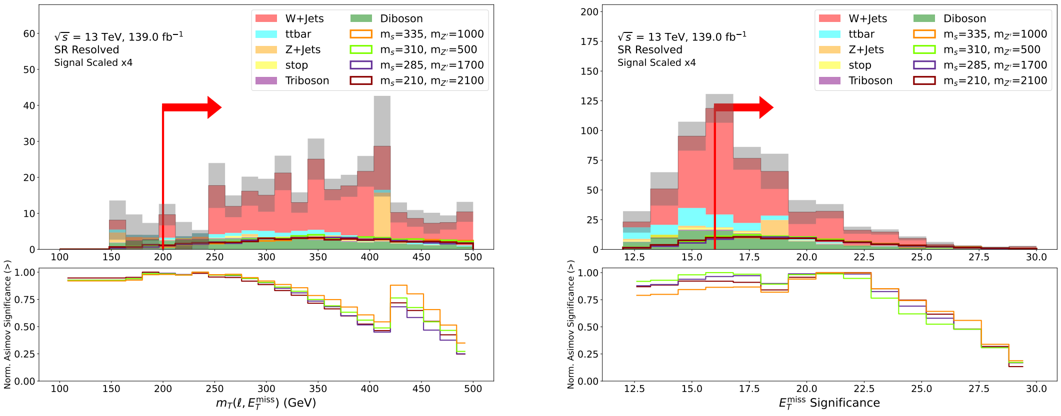

(a) $m_{\mathrm{T}}(\ell, E_{\mathrm{T}}^{\mathrm{miss}})$ (b) $\mathcal{S}$

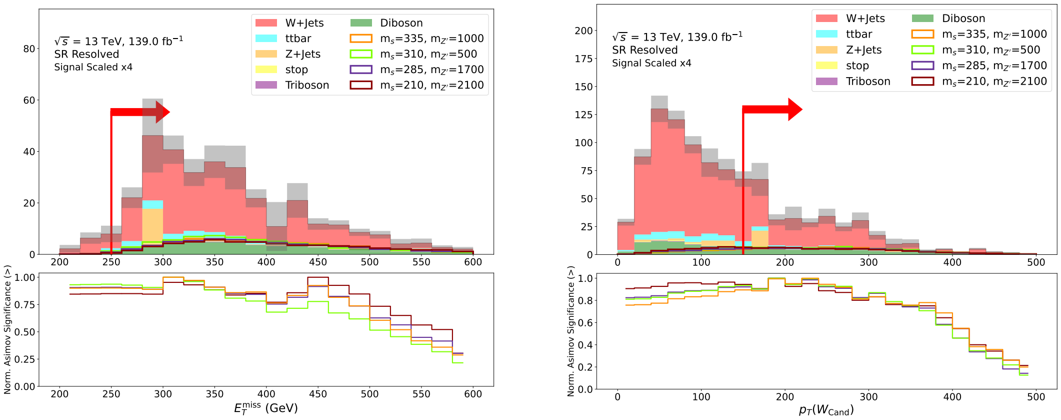

(c) $E_{\mathrm{T}}^{\mathrm{miss}}$ (d) $p_{\mathrm{T}}(W_{\mathrm{Cand}})$

Figure A.2: N-1 Distributions for variables used in the resolved signal region definition. Grey bands show statistical uncertainty on the background estimate. The lower panel shows the cumulative Asimov significance normalized to unit peak, where the direction (> or <) specified in the y label indicates whether the significance is being summed from above (>) or from below (<). Red vertical line and arrow show placement and direction of selection on the given variable in this region.

Appendix B

Kinematic Distributions in Signal and Control Regions

This appendix documents comparisons of the distributions of kinematic variables of interest for the search between the signal region (SR) and each control region (CR), considering the merged and resolved categories separately. The aim of these comparisons is to validate that, within each of the merged and resolved categories, the kinematic properties of events in the CRs are sufficiently similar to those in the corresponding SR that the data-driven normalization factors for the $W+$jets and $t\bar{t}$ background processes, which are evaluated primarily by comparison with the observed yield of ATLAS collision data in the CRs, can be reasonably applied to scale the predicted yields of these processes in the SR as well.

B.1 Signal region vs. $W+$jets control region

Figure B.1 compares distributions of kinematic variables of interest for the analysis between the merged SR and the W+jets CR. Figure B.2 presents the same comparison between the resolved SR and the $W+$jets CR.

B.2 Signal region vs. $t\bar{t}$ control region

Figure B.3 compares distributions of kinematic variables of interest for the analysis between the merged SR and the $t\bar{t}$ CR. Figure B.4 presents the same comparisons between the resolved SR and the $t\bar{t}$ CR.

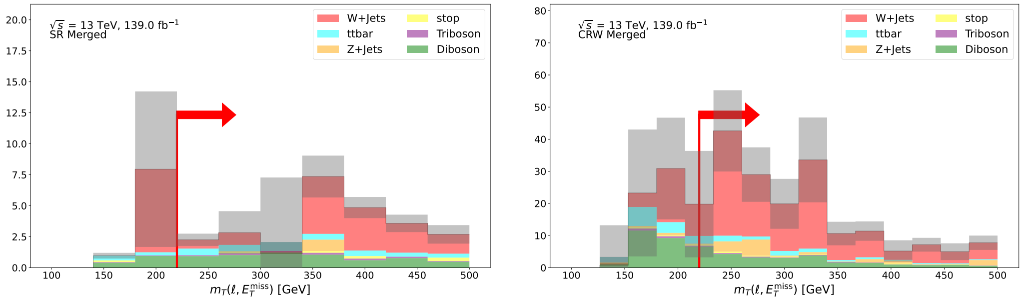

(a) $m_{\mathrm{T}}(\ell, E_{\mathrm{T}}^{\mathrm{miss}})$ (merged SR) (b) $m_{\mathrm{T}}(\ell, E_{\mathrm{T}}^{\mathrm{miss}})$ (merged W+jets CR)

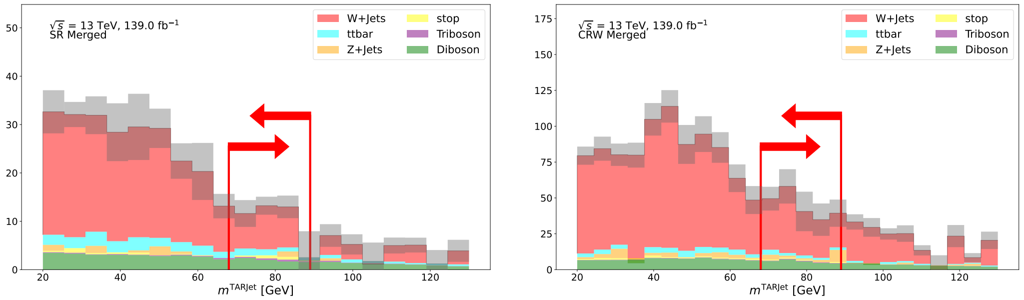

(c) $m^{\text{TAR Jet}}$ (merged SR) (d) $m^{\text{TAR Jet}}$ (merged W+jets CR)

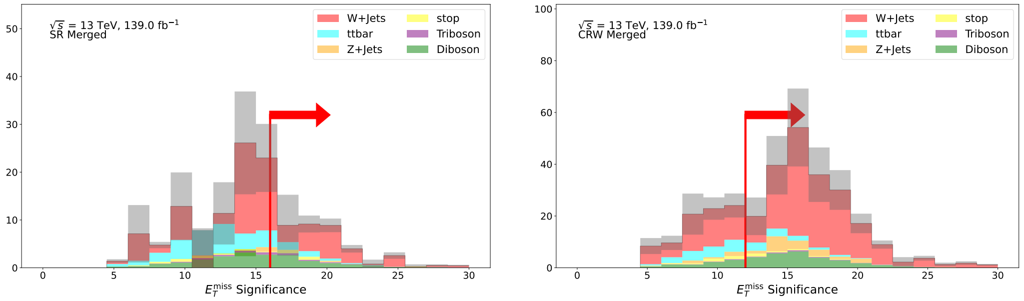

(e) $\mathcal{S}$ (merged SR) (f) $\mathcal{S}$ (merged W+jets CR)

Figure B.1: Comparison of N-1 distributions for kinematic variables of interest between the SR and the W+jets CR in the merged category. Grey bands show statistical uncertainty on the background estimate.

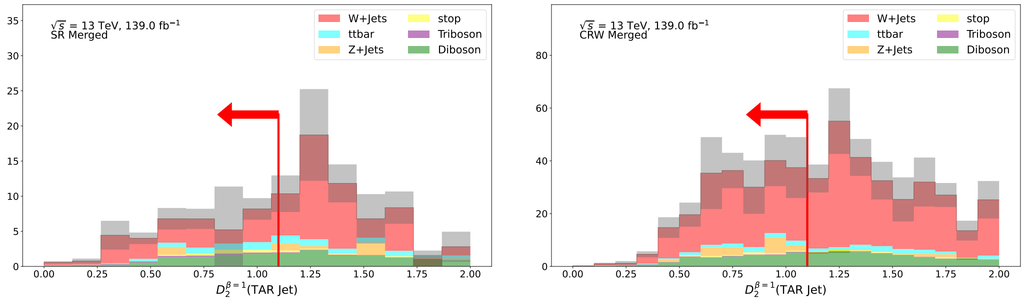

(g) $D_2^{\beta=1}$(TAR Jet) (merged SR) (h) $D_2^{\beta=1}$(TAR Jet) (merged W+jets CR)

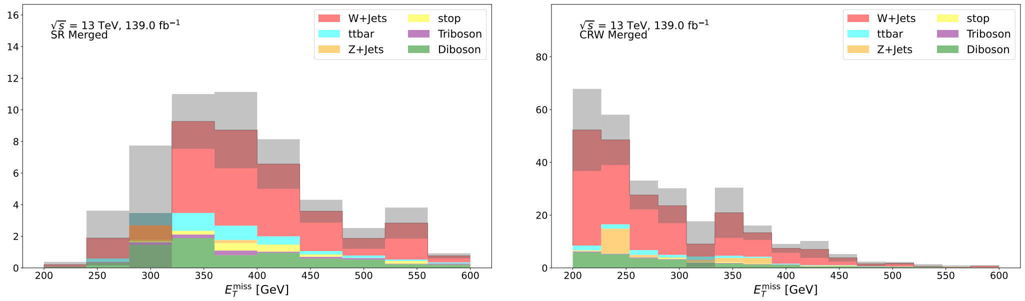

(i) $E_{\mathrm{T}}^{\mathrm{miss}}$ (merged SR) (j) $E_{\mathrm{T}}^{\mathrm{miss}}$ (merged W+jets CR)

Figure B.1: Comparison of N-1 distributions for kinematic variables of interest between the SR and the W+jets CR in the merged category (continued).

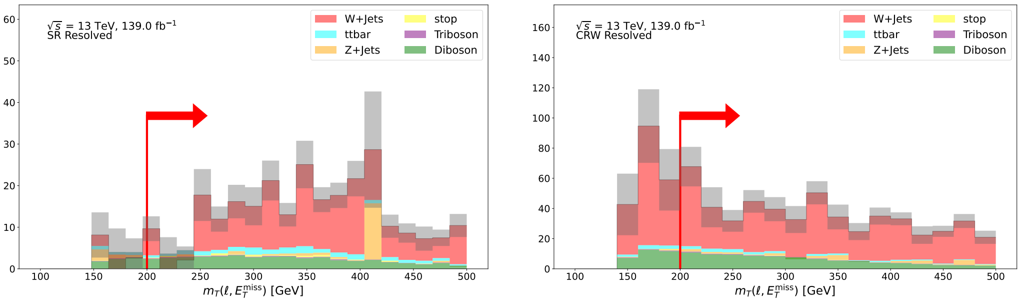

(a) $m_{\mathrm{T}}(\ell, E_{\mathrm{T}}^{\mathrm{miss}})$ (resolved SR) (b) $m_{\mathrm{T}}(\ell, E_{\mathrm{T}}^{\mathrm{miss}})$ (resolved W+jets CR)

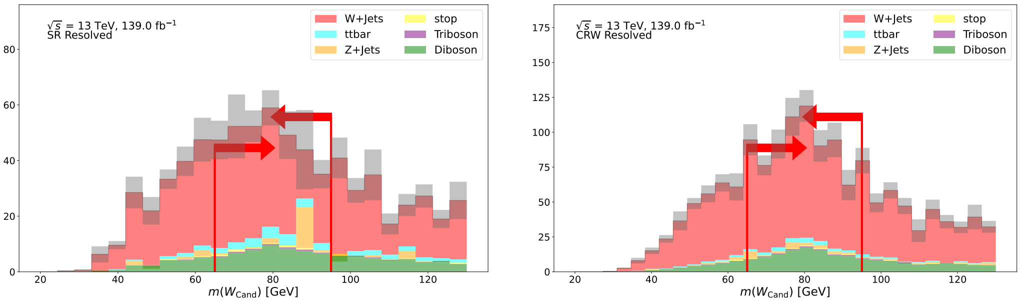

(c) $m(W_{\mathrm{Cand}})$ (resolved SR) (d) $m(W_{\mathrm{Cand}})$ (resolved W+jets CR)

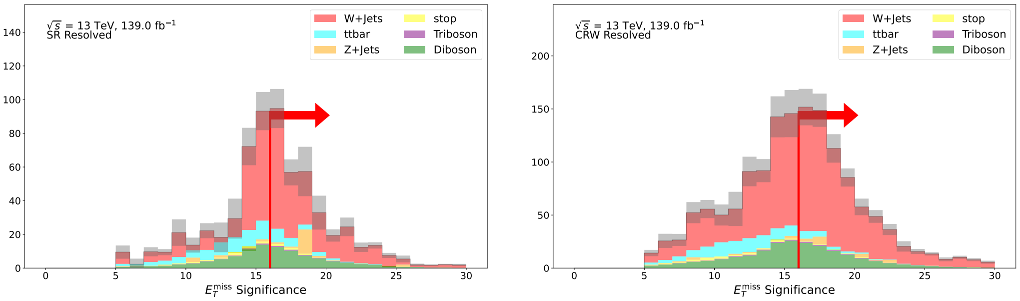

(e) $\mathcal{S}$ (resolved SR) (f) $\mathcal{S}$ (resolved W+jets CR)

Figure B.2: Comparison of N-1 distributions for kinematic variables of interest between the SR and the W+jets CR in the resolved category. Grey bands show statistical uncertainty on the background estimate.

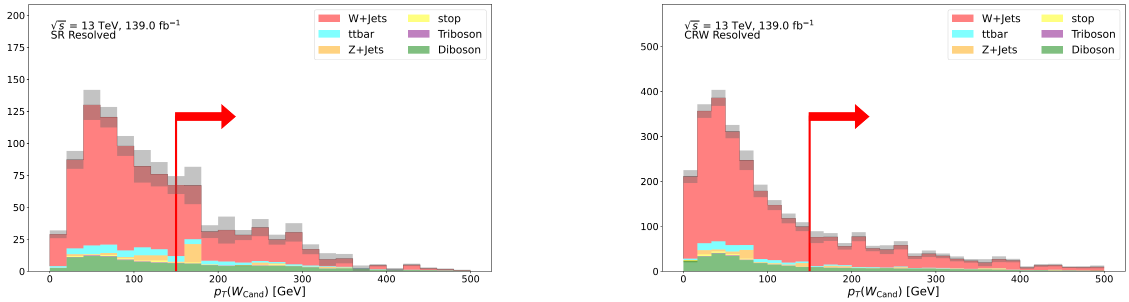

(g) $p_{\mathrm{T}}(W_{\mathrm{Cand}})$ (resolved SR) (h) $p_{\mathrm{T}}(W_{\mathrm{Cand}})$ (resolved W+jets CR)

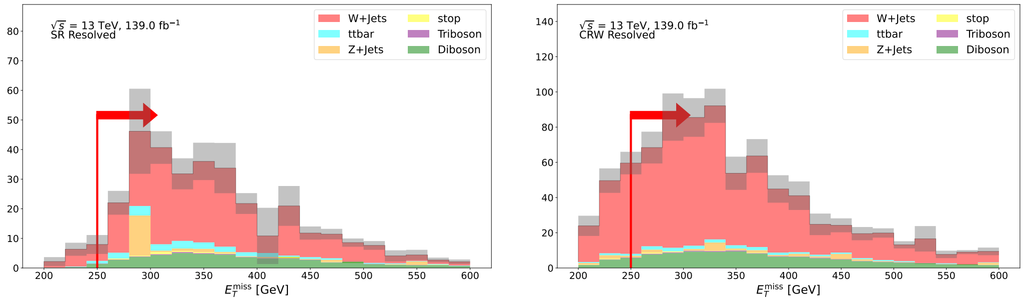

(i) $E_{\mathrm{T}}^{\mathrm{miss}}$ (resolved SR) (j) $E_{\mathrm{T}}^{\mathrm{miss}}$ (resolved W+jets CR)

Figure B.2: Comparison of N-1 distributions for kinematic variables of interest between the SR and the W+jets CR in the resolved category (continued).

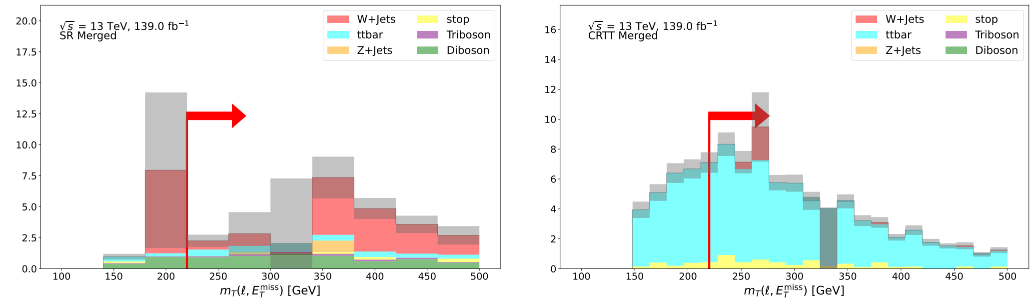

(a) $m_{\mathrm{T}}(\ell, E_{\mathrm{T}}^{\mathrm{miss}})$ (merged SR)

(b) $m_{\mathrm{T}}(\ell, E_{\mathrm{T}}^{\mathrm{miss}})$ (merged $t\bar{t}$ CR)

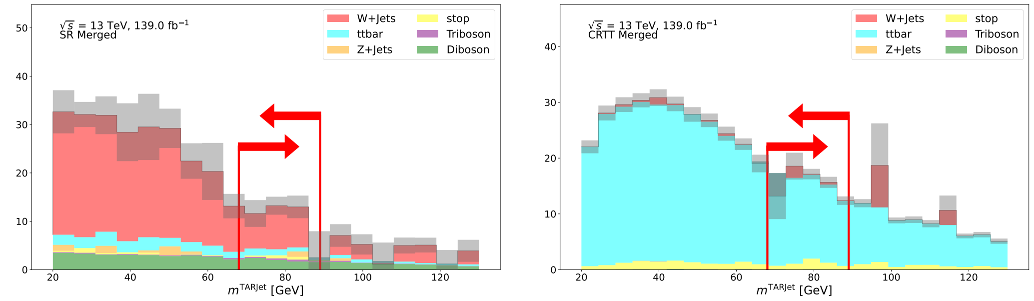

(c) $m^{\mathrm{TAR\ Jet}}$ (merged SR)

(d) $m^{\mathrm{TAR\ Jet}}$ (merged $t\bar{t}$ CR)

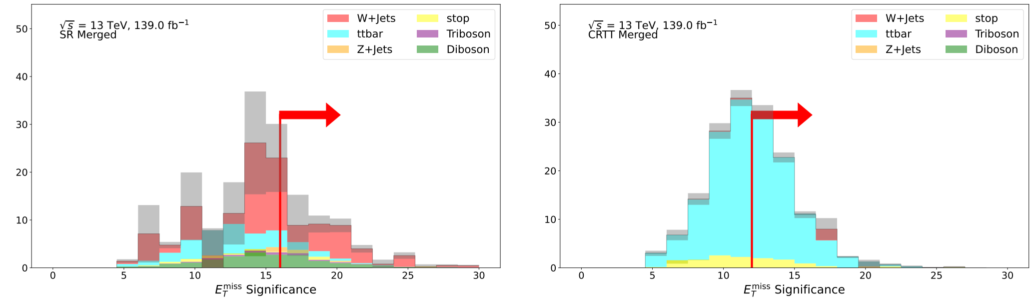

(e) $\mathcal{S}$ (merged SR)

(f) $\mathcal{S}$ (merged $t\bar{t}$ CR)

Figure B.3: Comparison of N-1 distributions for kinematic variables of interest between the SR and the $t\bar{t}$ CR in the merged category. Grey bands show statistical uncertainty on the background estimate.

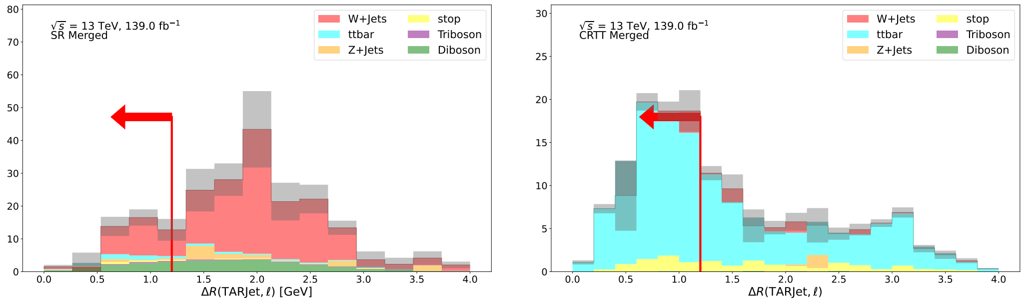

(g) $\Delta R(\text{TAR Jet}, \ell)$ (merged SR)
(h) $\Delta R(\text{TAR Jet}, \ell)$ (merged $t\bar{t}$ CR)

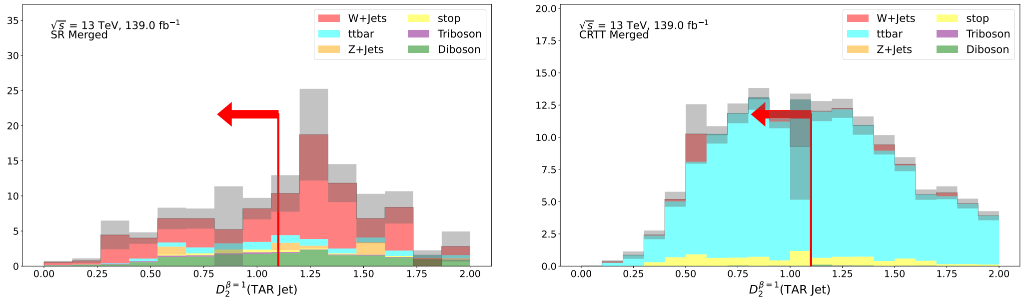

(i) $D_2^{\beta=1}(\text{TAR Jet})$ (merged SR)
(j) $D_2^{\beta=1}(\text{TAR Jet})$ (merged $t\bar{t}$ CR)

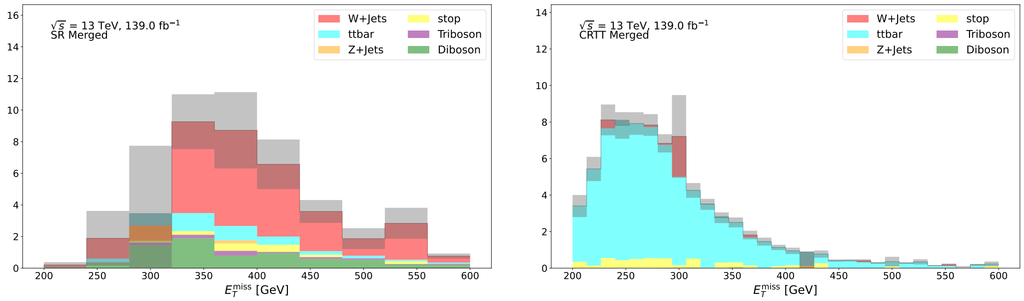

(k) $E_{\mathrm{T}}^{\mathrm{miss}}$ (merged SR)
(l) $E_{\mathrm{T}}^{\mathrm{miss}}$ (merged $t\bar{t}$ CR)

Figure B.3: Comparison of N-1 distributions for kinematic variables of interest between the SR and the $t\bar{t}$ CR in the merged category (continued).

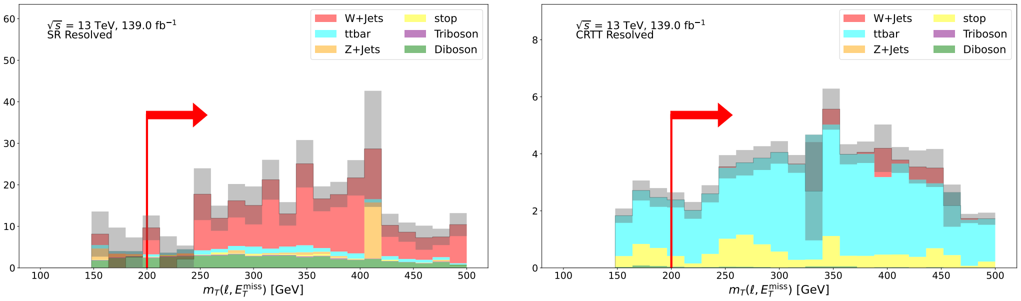

(a) $m_{\mathrm{T}}(\ell, E_{\mathrm{T}}^{\mathrm{miss}})$ (resolved SR) (b) $m_{\mathrm{T}}(\ell, E_{\mathrm{T}}^{\mathrm{miss}})$ (resolved $t\bar{t}$ CR)

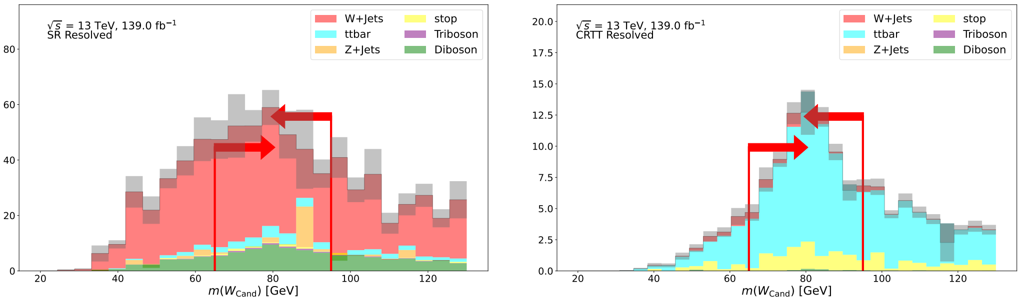

(c) $m(W_{\mathrm{Cand}})$ (resolved SR) (d) $m(W_{\mathrm{Cand}})$ (resolved $t\bar{t}$ CR)

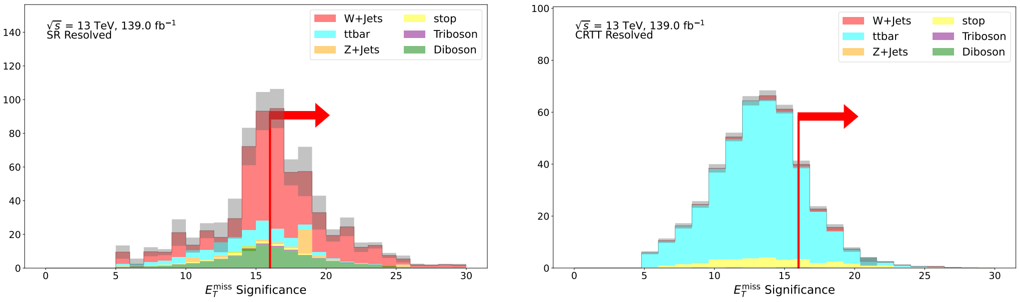

(e) $\mathcal{S}$ (resolved SR) (f) $\mathcal{S}$ (resolved $t\bar{t}$ CR)

Figure B.4: Comparison of N-1 distributions for kinematic variables of interest between the SR and the $t\bar{t}$ CR in the merged category. Grey bands show statistical uncertainty on the background estimate.

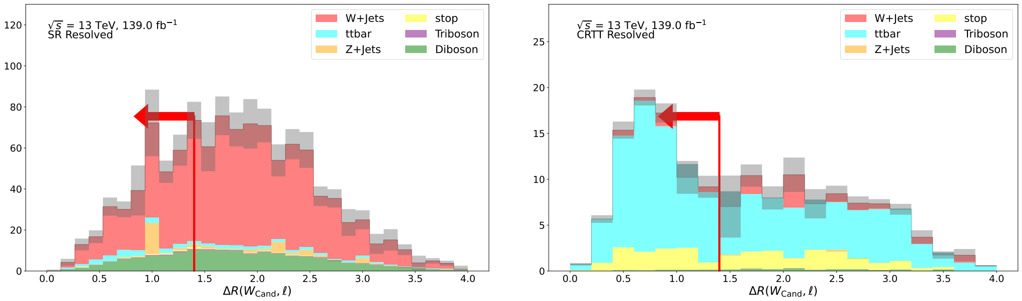

(g) $\Delta R(W_{\mathrm{Cand}}, \ell)$ (resolved SR) (h) $\Delta R(W_{\mathrm{Cand}}, \ell)$ (resolved $t\bar{t}$ CR)

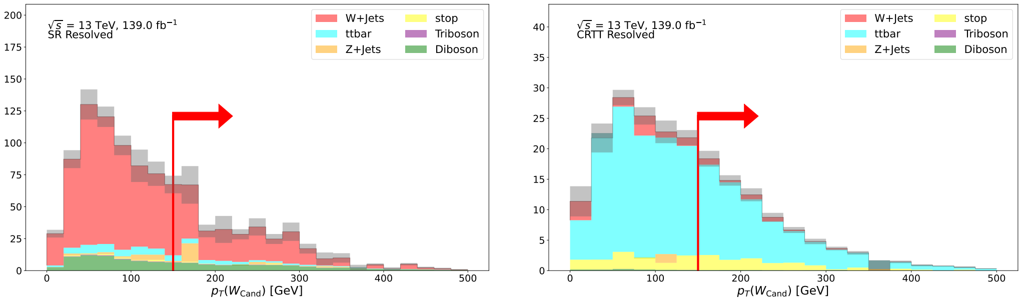

(i) $p_{\mathrm{T}}(W_{\mathrm{Cand}})$ (resolved SR) (j) $p_{\mathrm{T}}(W_{\mathrm{Cand}})$ (resolved $t\bar{t}$ CR)

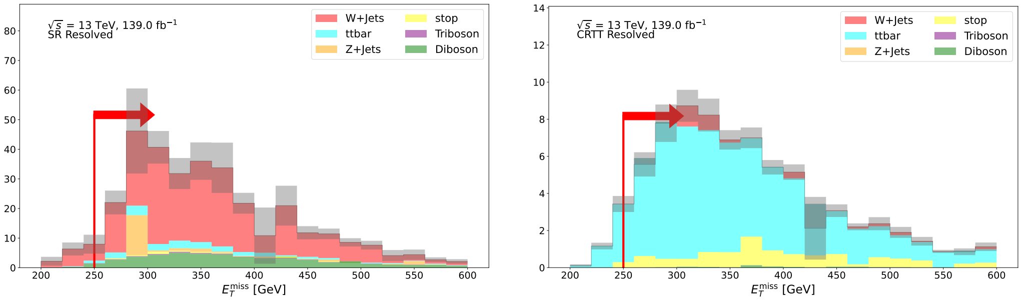

(k) $E_{\mathrm{T}}^{\mathrm{miss}}$ (resolved SR) (l) $E_{\mathrm{T}}^{\mathrm{miss}}$ (resolved $t\bar{t}$ CR)

Figure B.4: Comparison of N-1 distributions for kinematic variables of interest between the SR and the $t\bar{t}$ CR in the merged category (continued)

Appendix C

Nuisance Parameter Descriptions for Systematics

Tables C.1 and C.2 provide qualitative descriptions of the NPs used to parametrize systematic uncertainties in the likelihood function presented in Section 7.1. Details of the systematic uncertainty sources can be found in Chapter 6.

Table C.1: Qualitative description of NPs associated with sources of experimental systematic uncertainty considered in the search.

Nuisance Parameter	**Short Description**
Event	
α_lumiSys	uncertainty on the total integrated luminosity
α_PRW_DATASF	pileup reweighting uncertainty
Electrons	
α_EL_EFF_Reco_TOTAL_1NPCOR_PLUS_UNCOR	reconstruction efficiency uncertainty
α_EL_EFF_ID_TOTAL_1NPCOR_PLUS_UNCOR	ID efficiency uncertainty
α_EL_EFF_Iso_TOTAL_1NPCOR_PLUS_UNCOR	isolation efficiency uncertainty
α_EG_SCALE_ALL	energy scale uncertainty
α_EG_RESOLUTION_ALL	energy resolution uncertainty
Muons	
α_MUON_EFF_TrigSystUncertainty	trigger efficiency uncertainties
α_MUON_EFF_TrigStatUncertainty	
α_MUON_EFF_RECO_STAT	reconstruction and ID efficiency uncertainty for $p_{\mathrm{T}} > 15$ GeV
α_MUON_EFF_RECO_SYS	
α_MUON_EFF_RECO_STAT_LOWPT	reconstruction and ID efficiency uncertainty for $p_{\mathrm{T}} < 15$ GeV
α_MUON_EFF_RECO_SYS_LOWPT	
α_MUON_EFF_ISO_STAT	isolation efficiency uncertainty
α_MUON_EFF_ISO_SYS	
α_MUON_EFF_TTVA_STAT	track-to-vertex association efficiency uncertainty
α_MUON_EFF_TTVA_SYS	
α_MUON_SCALE	energy scale uncertainty
α_MUON_ID	energy resolution uncertainty from inner detector
α_MUON_MS	energy resolution uncertainty from muon system
α_MUON_SAGITTA_RESBIAS	uncertainty in the momentum scale

α_MUON_SAGITTA_RHO	uncertainty in the momentum scale
anti-k_t $R = 0.4$ jets	
α_JET_EffectiveNP_Detector	JES uncertainty: detector effects (2 components)
α_JET_EffectiveNP_Mixed	JES uncertainty: mixed effects (3 components)
α_JET_EffectiveNP_Modelling	JES uncertainty: modelling effects (5 components)
α_JET_EffectiveNP_Statistical	JES uncertainty: statistical uncertainty (6 components)
α_JET_EtaIntercalibration_Modelling	uncertainties in scale calibration of forward / central jets
α_JET_EtaIntercalibration_NonClosure_2018data	
α_JET_EtaIntercalibration_NonClosure_highE	
α_JET_EtaIntercalibration_NonClosure_negEta	
α_JET_EtaIntercalibration_NonClosure_posEta	
α_JET_EtaIntercalibration_TotalStat	
α_JET_BJES_Response	flavour-related uncertainties
α_JET_Flavor_Composition	
α_JET_Flavor_Response	
α_JET_JER_EffectiveNP	jet energy resolution uncertainty (12 components)
α_JET_JER_DataVsMC_MC16	jet energy resolution uncertainty (data vs. MC)
α_JET_JvtEfficiency	jet-vertex-tagger efficiency uncertainty
α_JET_Pileup_OffsetMu	Pileup uncertainties
α_JET_Pileup_OffsetNPV	
α_JET_Pileup_PtTerm	
α_JET_Pileup_RhoTopology	
α_JET_PunchThrough_MC16	punch through uncertainty
Tagging efficiency (using anti-k_t $R = 0.4$ jets)	
α_FT_EFF_EIGEN_B	b-tagging efficiency uncs (medium eigenvector decomp. of flavour tagging uncs)
α_FT_EFF_EIGEN_C	3 components for b-jets, 4 for c-jets and 5 for light jets
α_FT_EFF_EIGEN_L	
α_FT_EFF_EIGEN_extrapolation	b-tagging efficiency uncertainty on the extrapolation on high p_{T}-jets
α_FT_EFF_EIGEN_extrapolation_from_charm	b-tagging efficiency uncertainty on τ-jets
Rscan $R = 0.2$ jets used for TAR jet construction	
α_JET_R02_EffectiveNP_Detector	JES uncertainty: detector effects (2 components)
α_JET_R02_EffectiveNP_Mixed	JES uncertainty: mixed effects (3 components)
α_JET_R02_EffectiveNP_Modelling	JES uncertainty: modelling effects (5 components)
α_JET_R02_EffectiveNP_Statistical	JES uncertainty: statistical uncertainty (6 components)
α_JET_R02_EtaIntercalibration_Modelling	uncertainties in scale calibration of forward / central jets
α_JET_R02_EtaIntercalibration_NonClosure_highE	
α_JET_R02_EtaIntercalibration_NonClosure_negEta	
α_JET_R02_EtaIntercalibration_NonClosure_posEta	
α_JET_R02_EtaIntercalibration_TotalStat	
α_JET_R02_BJES_Response	flavour-related uncertainty
α_JET_R02_Flavor_Composition	
α_JET_R02_Flavor_Response	
α_JET_R02_JER_EffectiveNP	jet energy resolution uncertainty (17 components)
α_JET_R02_JER_DataVsMC_MC16	jet energy resolution uncertainty (data vs. MC)
α_JET_R02_Pileup_OffsetMu	Pileup uncertainty
α_JET_R02_Pileup_OffsetNPV	
α_JET_R02_Pileup_PtTerm	
α_JET_R02_Pileup_RhoTopology	

α_JET_R02_PunchThrough_MC16	punch through uncertainty
α_JET_R02_SingleParticle_HighPt	High pT term (2012 version)
α_JET_R02_Rscan_Dijet_DeltaR	Dijet Direct matching, delta R between Rscan and Ref jets
α_JET_R02_Rscan_Dijet_Isolation	Dijet Rscan isolation requirement
α_JET_R02_Rscan_Dijet_Jvt	Dijet Rscan LAr JVT
α_JET_R02_Rscan_Dijet_MC	Dijet Rscan MC generator difference
α_JET_R02_Rscan_Dijet_Stat	Dijet Rscan comb. of stat. components
α_JET_R02_Rscan_NonClosure	Non closure observed at low p_{T} in the Z+jets calibration method
α_JET_R02_Rscan_Zjet_DeltaR	Zjet Direct matching, ΔR between Rscan and Ref jets
α_JET_R02_Rscan_Zjet_Isolation	Zjet Rscan isolation requirement
α_JET_R02_Rscan_Zjet_MC	Zjet Rscan MC generator difference
α_JET_R02_Rscan_Zjet_stat	Zjet Rscan comb. of stat. components
α_JET_R02_Zjet_Jvt	Zjet Rscan LAr JVT
Tracks used for TAR jet construction	
α_TRK_BIAS_D0_WM	d_0 residual alignment tracking uncertainties
α_TRK_BIAS_Z0_WM	z_0 residual alignment uncertainties
α_TRK_BIAS_QOVERP_SAGITTA_WM	p_{T} residual alignment tracking uncertainties
α_TRK_EFF_LOOSE_GLOBAL	tracking efficiency (loose working point) uncertainty
α_TRK_EFF_LOOSE_IBL	tracking efficiency (loose working point) uncertainty
α_TRK_EFF_LOOSE_PHYSMODEL	tracking efficiency (loose working point) uncertainty
α_TRK_EFF_LOOSE_PP0	tracking efficiency (loose working point) uncertainty
α_TRK_EFF_LOOSE_TIDE	tracking in dense environments efficiency (loose working point) uncertainty
α_TRK_FAKE_RATE_LOOSE	tracking uncertainties on fake rate
α_TRK_FAKE_RATE_LOOSE_ROBUST	tracking uncertainties on fake rate
α_TRK_FAKE_RATE_LOOSE_TIDE	tracking uncertainties on fake rate in dense environments
α_TRK_RES_D0_DEAD	tracking uncertainties associated with IP d_0 resolution
α_TRK_RES_D0_MEAS	tracking uncertainties associated with IP d_0 resolution
α_TRK_RES_Z0_DEAD	tracking uncertainties associated with IP z_0 resolution
α_TRK_RES_Z0_MEAS	tracking uncertainties associated with IP z_0 resolution
$\boldsymbol{E_{\mathrm{T}}^{\mathrm{miss}}}$	
α_MET_SoftTrk_ResoPerp	track-based soft term related to transversal resolution uncertainty
α_MET_SoftTrk_ResoPara	track-based soft term related to longitudinal resolution uncertainty
α_MET_SoftTrk_Scale	track-based soft term related to longitudinal scale uncertainty
α_MET_JetTrk_Scale	track MET scale uncertainty due to tracks in jets

Table C.2: Qualitative description of NPs associated with sources of theoretical systematic uncertainty considered in the search.

Nuisance Parameter	Short Description
α_W+jets_scale	QCD scale (μ_R+μ_F) for W+jets process
α_W+jets_pdf_plus_alphas	combined PDF + α_s for W+jets process
α_W+jets_CKKW_plus_QSF	combined CKKW + QSF PS for W+jets process
α_Z+jets_scale	uncertainty of QCD scale (μ_R+μ_F) for Z+jets process
α_Z+jets_pdf_plus_alphas	combined PDF + α_s for Z+jets process

α_Z+jets_CKKW_plus_QSF	combined CKKW + QSF PS for Z+jets process
α_Diboson_pdf_plus_alphas	combined PDF + α_s for diboson process
α_Diboson_scale	QCD scale $(\mu_R+\mu_F)$ for diboson process
α_Diboson_CKKW_plus_QSF	combined CKKW + QSF PS for diboson process
α_Triboson_pdf_plus_alphas	combined PDF + α_s for diboson process
α_Triboson_scale	QCD scale $(\mu_R+\mu_F)$ for diboson process
α_Triboson_CKKW_plus_QSF	combined CKKW + QSF PS for diboson process
α_ttbar_scale	QCD scale $(\mu_R+\mu_F)$ for $t\bar{t}$ process
α_ttbar_pdf	PDF for $t\bar{t}$ process
α_ttbar_2pt_PhHw7	comparison with alternate PS generator for $t\bar{t}$ process
α_ttbar_2pt_AMcPy8	comparison with alternate ME generator for $t\bar{t}$ process
α_ttbar_ISR_alphas	ISR α_s for $t\bar{t}$ process
α_ttbar_FSR_alphas	FSR α_s $(\mu_R+\mu_F)$ for $t\bar{t}$ process
α_stop_scale	QCD scale $(\mu_R+\mu_F)$ for single top process
α_stop_pdf	PDF for single top process
α_stop_2pt_PhHw7	comparison with alternate PS generator for single top process
α_stop_2pt_AMcPy8	comparison with alternate ME generator for single top process
α_stop_ISR_alphas	ISR α_s for single top process
α_stop_FSR_alphas	FSR α_s $(\mu_R+\mu_F)$ for single top process
α_stop_2pt_DS	$t\bar{t}$/Wt interference at NLO for single top process
α_monoSww_*_zp*_dm200_dh*_scale	QCD scale $(\mu_R+\mu_F)$ for DH signal process
α_monoSww_*_zp*_dm200_dh*_pdf	PDF for DH signal process
α_monoSww_*_zp*_dm200_dh*_2pt_MGHw7_3pt_noxsec	comparison with alternate PS generator for DH signal process

Appendix D

Dependence of Sensitivity on Signal Strength

To assess the impact of varying the production rate of the DH signal model on the sensitivity of the search, Figure D.1 compares the range of m_s and $m_{Z'}$ excluded by the search with the value of the signal strength parameter μ, which coherently scales the production rate of the DH signal process at all m_s and $m_{Z'}$ considered in the search.

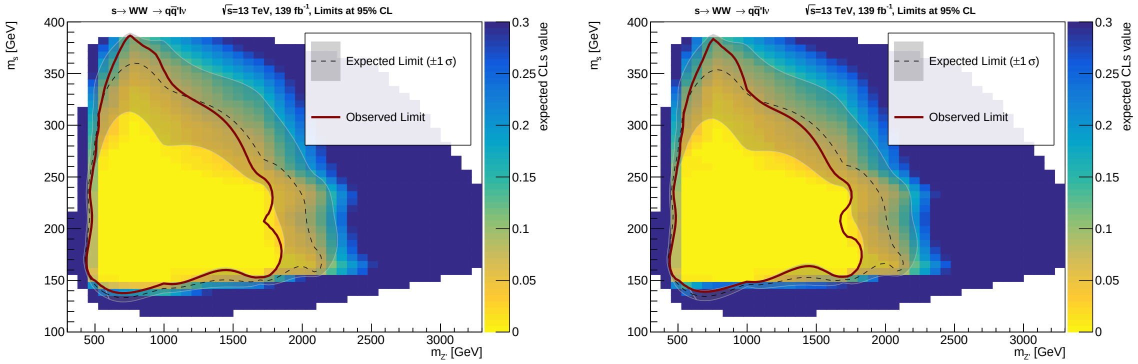

(a) $\mu = 1.0$ (b) $\mu = 0.95$

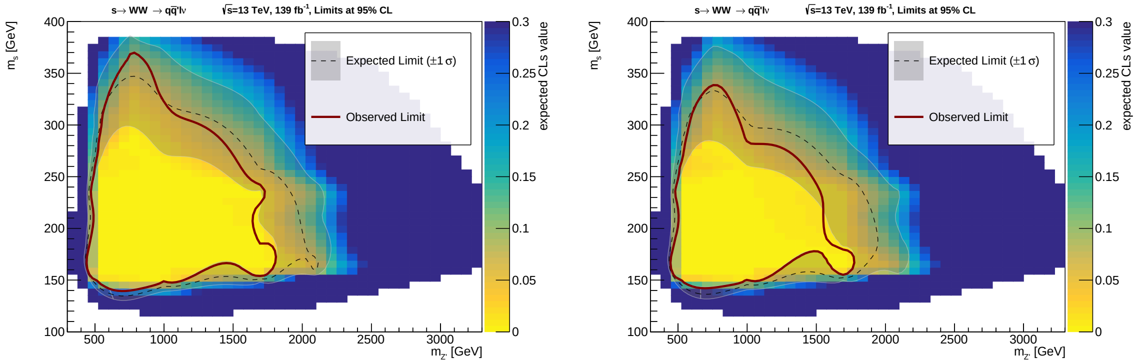

(c) $\mu = 0.9$ (d) $\mu = 0.8$

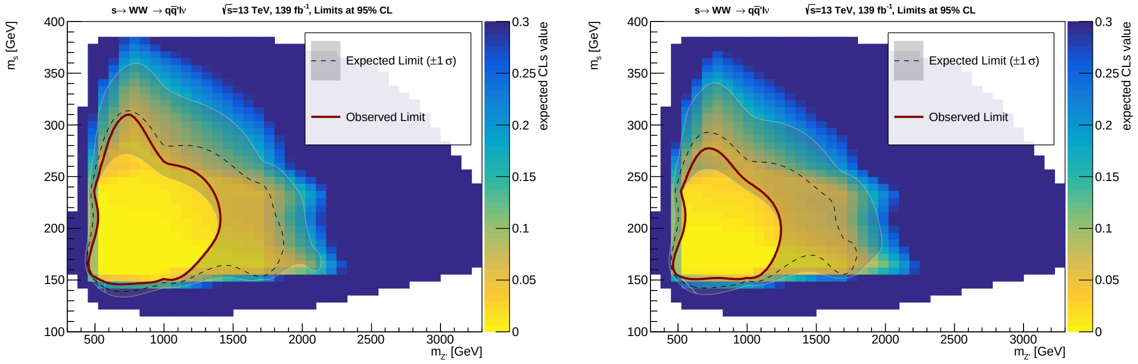

(e) $\mu = 0.7$ (f) $\mu = 0.6$

Figure D.1: Range of m_s and $m_{Z'}$ in the DH signal model excluded by the search for various choices of the signal strength μ which coherently scales the production rate of the signal model at all m_s and $m_{Z'}$. Note that the variation with μ assumes changes to coupling combinations yield the same kinematic distributions as the benchmark choices.

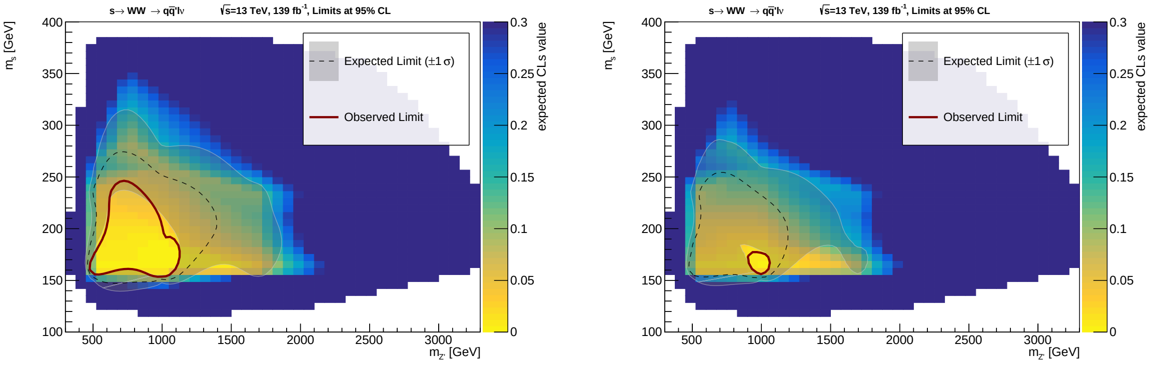

(g) $\mu = 0.5$ (h) $\mu = 0.4$

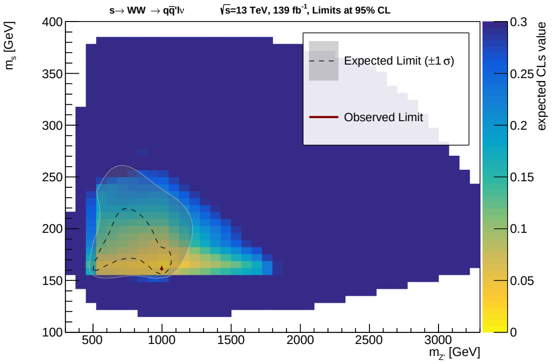

(i) $\mu = 0.3$

Figure D.1: Range of m_s and $m_{Z'}$ in the DH signal model excluded by the search for various choices of the signal strength μ (continued).